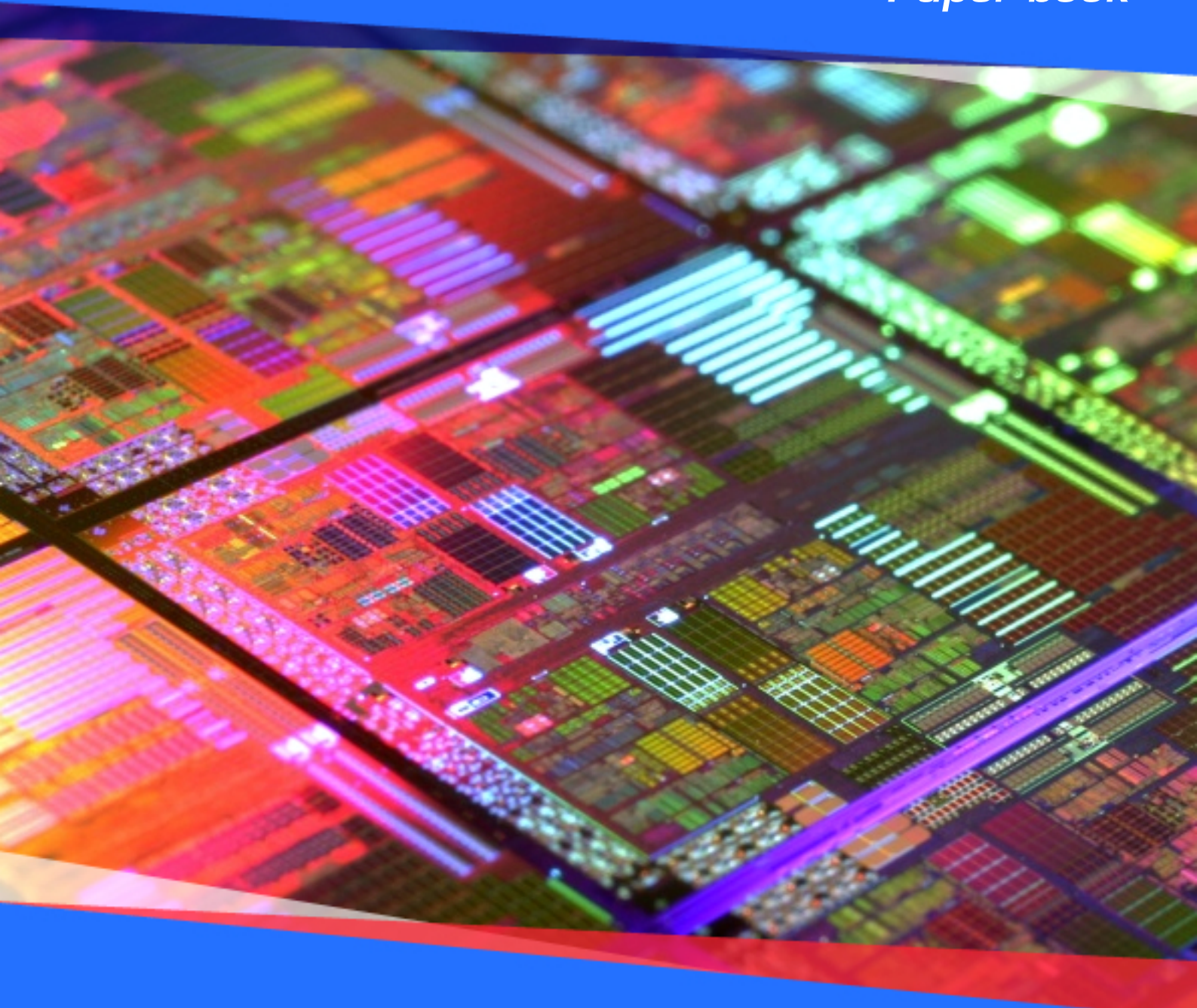# IEET–2015

Instrumentation Engineering, Electronics and Telecommunications – 2015

1st International Forum held within the framework of the XI International Scientific–Technical Conference "Instrumentation Engineering in the XXI Century. Integration of Science, Education and Production" (November, 25–27, 2015, Izhevsk, Russia)

Министерство образования и науки Российской Федерации
ФГБОУ ВО «Ижевский государственный технический университет имени М.Т. Калашникова»

«ПРИБОРОСТРОЕНИЕ, ЭЛЕКТРОНИКА И ТЕЛЕКОММУНИКАЦИИ – 2015»

Сборник статей I Международного форума IEET-2015, проводимого в рамках XI Международной научно-технической конференции «Приборостроение в XXI веке. Интеграция науки, образования и производства» (25–27 ноября 2015 года, Ижевск, Россия)

УДК 681.2(06)

Сборник содержит прошедшие рецензирование статьи по широкому кругу вопросов в областях приборостроения, электроники, связи и смежных им, которые обсуждались на I Международном форуме IEET-2015. Статьи могут быть полезны ученым, специалистам, молодым исследователям, аспирантам и студентам.

"INSTRUMENTATION ENGINEERING, ELECTRONICS AND TELECOMMUNICATIONS – 2015"

Paper book of the I International Forum IEET-2015
held within the framework of the
XI International Scientific-Technical Conference
"Instrumentation Engineering in the XXI Century.
Integration of Science, Education and Production"
(November 25–27, 2015, Izhevsk, Russia)

UDC 681.2(06)

Organizing Committee Chairmans

Boris Yakimovich – Chairman, DSc, Prof., Rector of Kalashnikov ISTU;
Alexandr Korshunov – Vice-chairman, DSc, Prof.;
Vladimir Khvorenkov – Vice-chairman, DSc, Prof.;
Vladimir Alexeev – Vice-chairman, DSc, Prof.;
Albert Abilov – Vice-chairman, , CSc, Executive organizer;
Alexandr Tyurin – Vice-chairman, DCs, Prof.;
Vladimir Zabolotskih – Vice-chairman, DSc, Senior Researcher

Scientific Committee

Albert Abilov – CSc, Kalashnikov ISTU, Russian Federation;
Alexandr Homchenko – DSc, assoc. prof., Belarusian-Russian University, Mogilev, Republic of Belarus;
David Kubanek – PhD, Brno University of Technology, Czech Republic;
Dmitrij Marandin – PhD, CommAgility Ltd., Federal Republic of Germany;
Jaroslav Kotton – PhD, Brno University of Technology, Czech Republic;
Martin Ayvazyan – DSc, National Polytechnic University of Armenia, Republic of Armenia;
Mohamed M. A. Moustafa – PhD, Egyptian Russian University, Arab Republic of Egypt;
Olga Muravieva – DSc, prof., Kalashnikov ISTU, Russian Federation;
Pavel Reichert – Ing., Techniserv Ltd., Czech Republic;
Petr Machník – PhD, VŠB – Technical University of Ostrava, Czech Republic;
Petr Münster – PhD, Brno University of Technology, Czech Republic;
Radim Burget – PhD, Brno University of Technology, Czech Republic;
Sergey Murashov – CSc, Kalashnikov ISTU, Russian Federation;
Sergey Sergeev – DSc, prof., Belarusian-Russian University, Mogilev, Republic of Belarus;
Vasilii Borisov – DSc, prof., Belarusian-Russian University, Mogilev, Republic of Belarus;
Vladimir Emelianov – CSc, Kalashnikov ISTU, Russian Federation;
Vladimir Khvorenkov – DSc, prof., Kalashnikov ISTU, Russian Federation

Editorial Board

Albert Abilov – CSc, chief editor;
Sergey Murashov – CSc, technical editor

Instrumentation engineering, electronics and telecommunications – 2015 : Paper book of the I International Forum IEET-2015 held within the framework of the XI International Scientific-Technical Conference "Instrumentation Engineering in the XXI Century. Integration of Science, Education and Production" (November, 25–27, 2015, Izhevsk, Russia). – Izhevsk : Publishing House of Kalashnikov ISTU, 2016. – 208 p. – 7 MB.

ISBN 978-5-7526-0734-9 (Electronic Edition)

This volume contains peer-reviewed papers on wide range of problems in fields of instrumental engineering, electronics, telecommunications and related areas discussed during the I International Forum IEET-2015. The papers could be useful for scientists, professionals, young researchers, post graduate and under graduate students.

TABLE OF CONTENTS

Powerline Communications Channel: Modeling and Noise Monitoring

R. Abenov [1], D. Pokamestov [1], A. Geltser [1],
Ya. Kryukov [1], E. Rogozhnikov [1], A. Shibelgut [1,2]

[1] Department of telecommunications and radio engineering fundamentals, Tomsk state university of control systems and radioelectronics, Tomsk, Russia
E-mail: abenov.rr@gmail.com
[2] Department of computer measuring systems and metrology, Tomsk polytechnic university, Tomsk, Russia

Abstract. The research of a low frequency channel of the Power Line Communications (PLC) systems was performed. A mathematical model of the channel was obtained. The model takes into account the multipath signal propagation over power lines of typical buildings. An amplitude-frequency characteristic of the channel was measured. The noise monitoring in a power network of the university academic building was fulfilled.

Keywords: PLC, multipath channel, modeling, noise measurement

INTRODUCTION

In the modern world the development of telecommunication technologies goes to direction of growth of the traffic and amount increasing of connected devices. By estimation of experts an era of the global Internet will became to 2020, when every household appliance will practically have an access to the Internet and an ability to remote control [1-3]. Therefore, a need of creation of combined networks is increasing. These combined networks have to include both wired and wireless technologies for connection to various kinds of devices. A number of standards for wired communication over power lines (power line communication – PLC) has been recently developed. This technology is above all attractive that it is possible to use the existing power line without the need to deploy an additional physical network. PLC systems can be divided into a high and a low frequency systems [4, 5]. High frequency systems operate in the range up to 100 MHz. They are used to provide PC users by access to the Internet with speed up to several hundreds of megabits per second. Low frequency PLC systems are typically used to exchange data between the sensors and for automation of industrial processes. Among the standards describing these technologies can be picked out a recently appeared European standard "G3-PLC" and an American "PRIME" [6]. In systems that work with using of these standards are applied OFDM technology on a physical level. Such systems work in the frequency range of up to 150 kHz (predominantly a range of up to 100 kHz). A correct operation of the PLC systems depends directly on the state of the transmission channel. The multipath effect, caused by a complex branched topology of network, and interferences, appeared by other connected devices, have the greatest impact on

the channel [7]. In this paper these factors are studied. A mathematical model of the multipath channel which takes into account the network topology and the signal attenuation is considered. A series of measurement experiments of the frequency response of the channel and a monitoring of noises in the laboratory of academic building are performed.

MODELING

The communication channel is depicted in Fig. 1, where τ_i – time delay in i-th path, l_i – length of i-th path, ν – propagation velocity of wave in medium, k_i – attenuation along i-th path. This typology can be described as [8]:

$$H(f) = \sum_{i=0}^{N-1} k_i e^{-2\pi f \tau_i},\qquad(1)$$
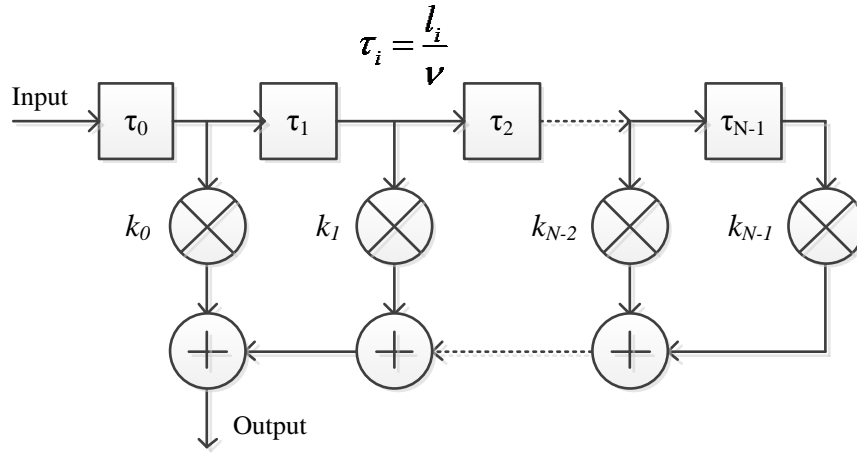
Figure 1. Multipath PLC topology

If we add a frequency-dependent attenuation of a signal along the path to (1), we have:

$$H(f) = \sum_{i=0}^{N-1} g_i e^{-\left(a_0 + a_1 f^k\right)d_i} \cdot e^{-j2\pi f \frac{d_i}{v_p}},\qquad(2)$$

where a_0 – an initial attenuation, a_1 – an attenuation increase with increase of frequency, N – total number of paths, k – coefficient of attenuation decrease, d_i – a length of the data transmission path for various path numbers (in meters), g_i – an attenuation coefficient of i-th path [9].

This approach was simulated in MATLAB and represents three models of multipath channel.

Main parameters of model:
- $a_0 = 0$ – an attenuation shift;
- $a_1 = 7.8 \cdot 10^{-10}$ – a long attenuation;
- $k = 1$ – a coefficient of attenuation decrease;
- $v_p = 1.5 \cdot 10^8$ – propagation velocity.

The propagation velocity is calculated as:

$$v_p = \frac{c}{\sqrt{\varepsilon_r}} = \frac{3 \cdot 10^8}{\sqrt{4}} = 1.5 \cdot 10^8 \text{ m/s.}$$

Fig. 2 shows the modeling results of transfer functions of these channels in the range of up to 1 MHz. The characteristic of channel 1 in the given frequency range is close to linear and has relatively low attenuation. It can be explained due to a small time delay between the direct and the reflected signals [10]. Channel 2 has a similar transfer function but the characteristic is non-linear due to a longer time delay. Channel 3 is characterized by a larger number of reflection paths and longer delays, so the given frequency range has deep fades.
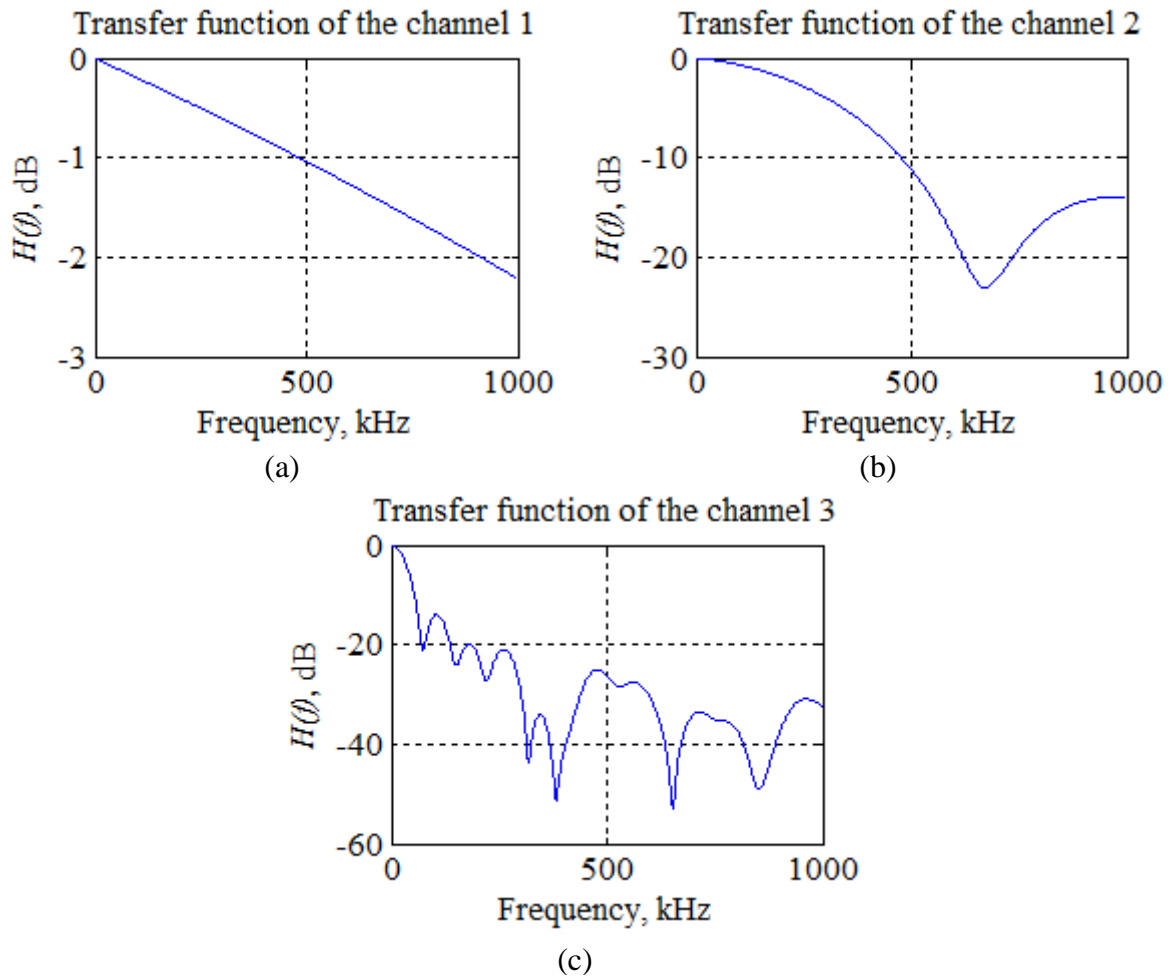
Figure 2. Frequency characteristics of paths in the range of 0–1 MHz: channel 1 (a); channel 2 (b); channel 3 (c)

NOISE MONITORING IN PLC-NETWORK

The experimental measurement of noises has been performed by a voltage converter which is presented a transformer within-series capacitor [11]. During experiment was used LeCroy WaveRunner 6100A oscilloscope. The device has been connected with the MATLAB environment to automate the registration process of the signal.

The control was carried out in MATLAB. Every five minutes an oscilloscope was keeping an input signal and transmitting it over the LAN to a computer. Then the Fourier transformation was performed and the result was stored in the computer memory as a matrix form. Further the influence of the voltage converter is eliminated by dividing the Fourier transform on a pre-measured amplitude-frequency characteristic of the voltage converter. The

registration of the signal was continued during 24 hours, from 7:35 p.m. till 7:45 p.m. of next day. According to the received results was built a spectrogram in the range of 10–100 kHz shown in Fig. 3. The spectrogram is represented by way of a three-dimensional picture of distribution of noise amplitudes (dBV) on the frequency-time axis.
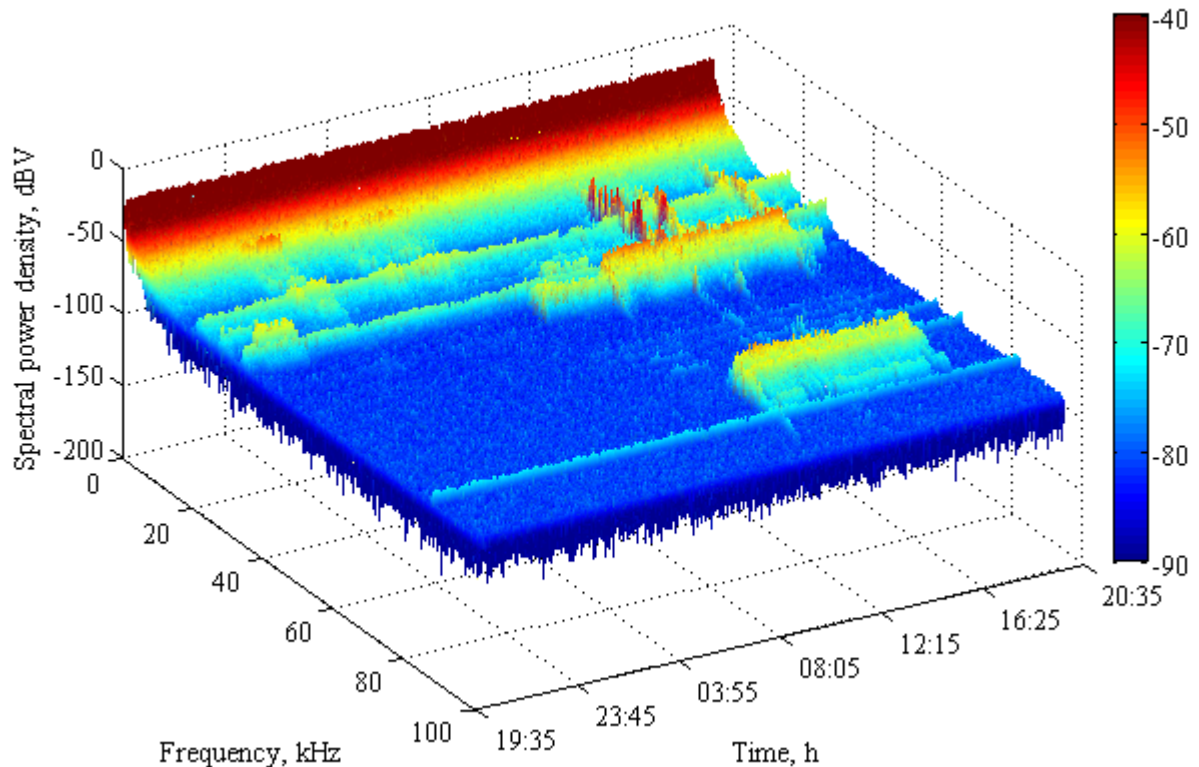
Figure 3. Spectrogram of the noise signal

The presented spectrogram enables us to evaluate the level of noises at different times of day. The measurement was performed in the laboratory of university which has about 10 working places. Every place is equipped with a computer. There are also measuring equipment (oscilloscopes, spectrum analyzers) and soldering stations in some working places. In addition, there are also a printer and a cooler of drinking water in the laboratory. At evening and night (till 9:00 a.m.) one computer, an oscilloscope and a cooler were working in the laboratory. During the day the working places were occupied by staff of the laboratory. About 12:30 p.m. students were in the laboratory with two laptops which have been also connected to the network.

This result suggests that working computers generate interferences in the frequency range of 35–45 kHz and 70–90 kHz. However, the spectrogram has broadband noises which are very different from the rest. These noises are shown in Fig. 4. Here a fragment of the frequency-time plane of the spectrogram is depicted. The spectrum of such interferences takes the band up to 50 kHz. The time of interference occurrence coincides with the connecting laptops to the network. Probably a power supply of the laptop during charging of the battery creates impulse noises in this range. The noise spectrum at different times is shown in Fig. 5. As can be seen from Fig. 5, a level of noises in non-working hours does not exceed −70 dBV. Connection of computers and measuring devices to the power line network causes the noises on a level −60…−65 dBV in above mentioned frequency range. During the maximal load the level of noises achieves a value −43…−45 dBV.

10
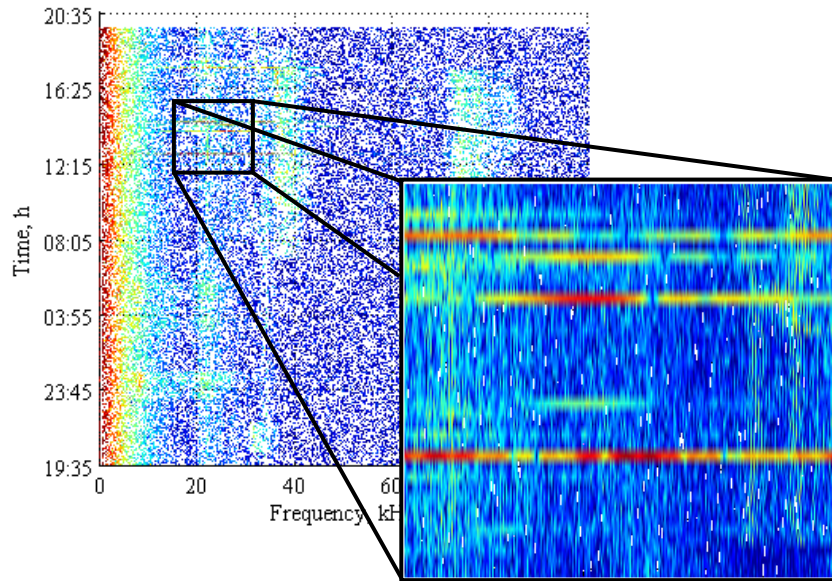
Figure 4. Short broadband interferences in spectrogram
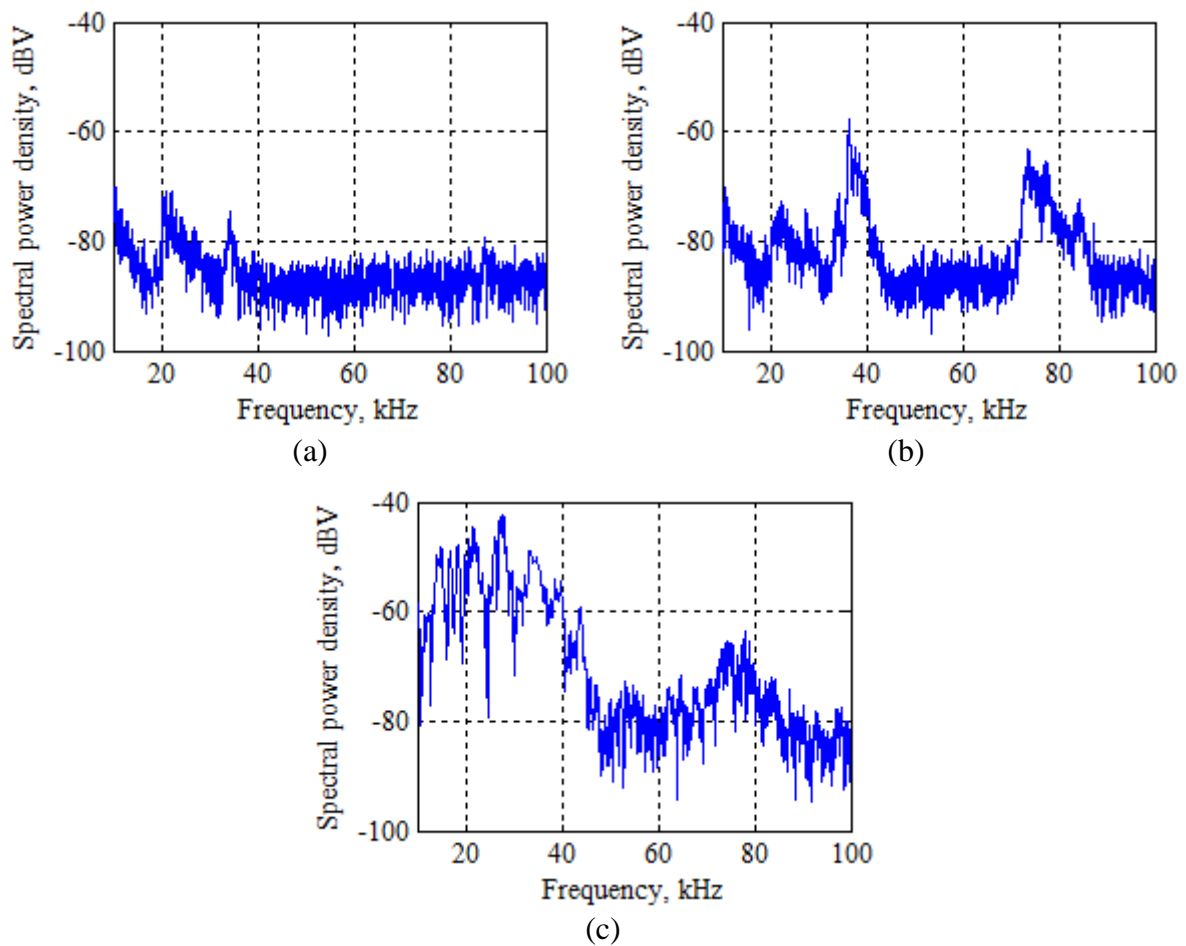
Figure 5. Spectrum of noise signal: a) night-time (04:00); b) working time (10:35); c) peak (12:45)

THE MEASUREMENT OF THE TRANSFER FUNCTION OF PLC CHANNEL

The measurement of the transfer function of PLC channel was carried out in the laboratory of university building. During the measurement were used Agilent DSO-X 2002A oscillator and LeCroy WaveRunner 6100A oscilloscope. The protection circuit was used in the operational amplifier for oscillator protection against interferences. A schematic diagram of the experimental setup is shown in Fig. 6.
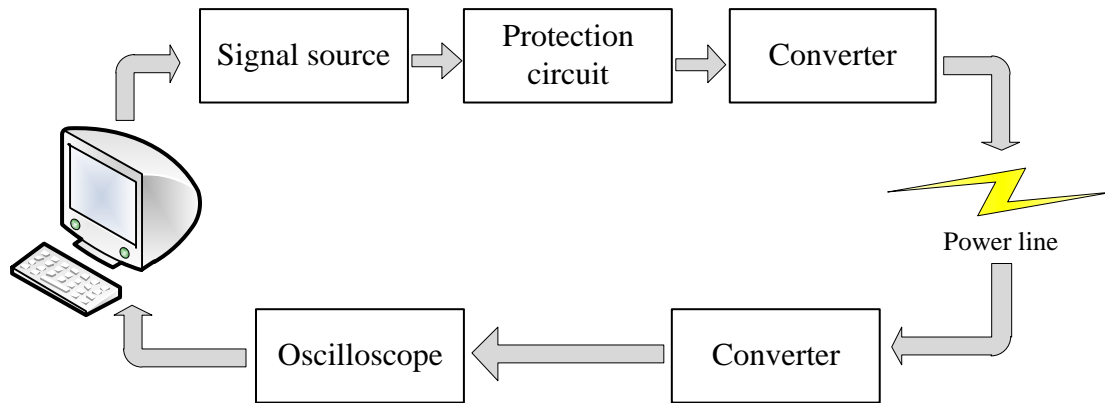
Figure 6. Schematic diagram of the experimental setup

The obtained transfer function is shown in Fig. 7. The oscillator and the oscilloscope were connected to a power supply in various parts of the laboratory. The measurements were fulfilled in two modes: non-working time and working time. Non-working time (see Fig. 7b) is characterized by a small number of devices connected to the network such as the oscillator, the oscilloscope and the PC which is used for recording and signal processing. At working time (see Fig. 7a) the devices connected to the network greatly complicate the topology of the network which will be become heterogeneous. Thus a plurality of reflecting loads are appeared in the network. It leads to multiple reflections and strong signal attenuation.

| (a) | (b) |
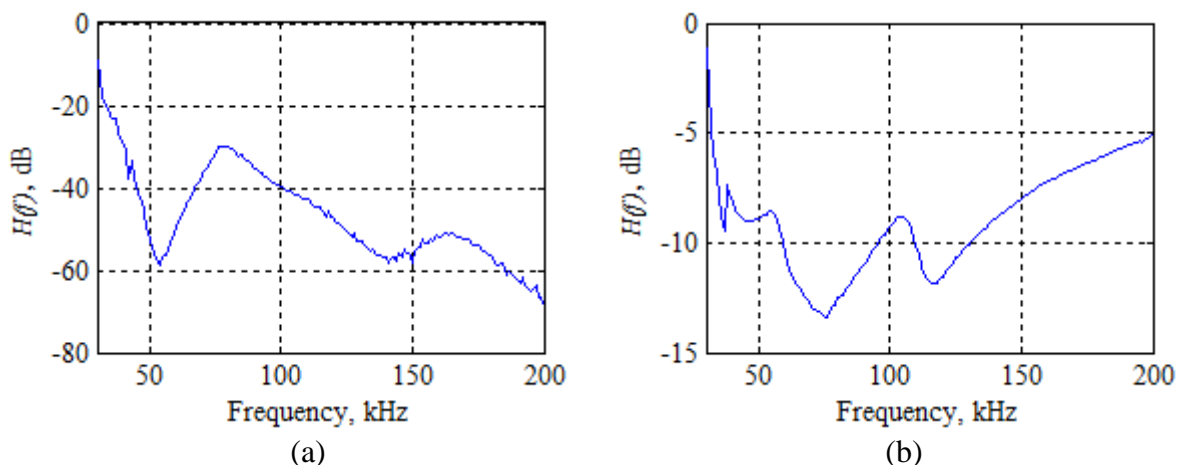
Figure 7. Transfer function of the PLC channel: a) in working hours; b) in non-working hours

CONCLUSION

PLC network deployed in a house implies that the distance between a distribution box and apartments is not more than several tens of meters. In this case according to the results we can conclude that the channel is quite stable in the range of 1 MHz. However, it should be

noted that the communication channel in such networks is highly dependent on the complexity of the network organization and on the subscriber's numbers. In certain cases the multipath effect leads to deep fade.

The obtained model allows predicting the channel state under different conditions of the multipath effect and parameters of the channel attenuation. The model can be used in engineering and deployment of real PLC networks.

The measurement results allow concluding that by modeling of the PLC networks we should take into account multipath effects in a channel as well as different appliances which generate various noises in the range of up to 1 MHz. Any devices connected to the power line can be sources of these noises. The observed noises are random in character as the number and the type of network-linked devices are constantly changed. The level and the type of noises can be also changed during the day and it depends on power line load. It should be noted that the connection of household appliances to the power line causes power line surges.

The measured transfer functions can be used in modeling of various low frequency PLC systems, for example, to quality assessment of data transmission. They can be also used to perform check of the signal processing algorithms used in these systems.

REFERENCES

1. M. Pavlyuk, A. Nazarov, and Yu. Sakhno, "Automated energy accounted PLC and ZigBee communication modules," Electronics: science, technology, business, Issue 7, pp. 38–46, 2014.

2. S. Singh and P. Singh, "Key concepts and network architecture for 5G mobile technology," International Journal of Scientific Research Engineering & Technology (IJSRET), vol. 1, No. 5, pp. 165–170, 2012.

3. K. Ashton, "That 'internet of things' thing," RFiD Journal, vol. 22, No. 7, pp. 97–114, 2009.

4. N. Pavlidou, A.J. Han Vinck, J. Yazdani, and B. Honary, "Power line communications: state of the art and future trends," IEEE Communications Magazine, vol. 41, No. 4, pp. 34–40, April 2003.

5. S. Galli and O. Logvinov, "Recent developments in the standardization of power line communications within the IEEE," IEEE Communications Magazine, vol. 46, No. 7, pp. 64–71, July 2008.

6. M. Hoch, "Comparison of PLC G3 and PRIME," IEEE Int. Symposium on Power Line Communications and Its Applications (ISPLC 2011), pp. 165–169, April 2011.

7. M. Qiang, C. Qimei, and L. Bo, "Predictive schemes for future power line communication. Part two: PLC channel analysis and model," Automation of Electric Power Systems, vol. 4, p. 016, 2003.

8. H.C. Ferreira, L. Lampe, J. Newbury, and T.G. Swart, Power Line Communications: theory and applications for narrowband and broadband communications over power lines, John Wiley & Sons, 2010.

9. M. Zimmermann and K. Dostert, "A multipath model for the powerline channel," IEEE Trans. Commun., vol. 50, No. 4, pp. 553–559, Apr 2002.

10. H. Philipps, "Modeling of powerline communication channels," Proc. Int. Symp. Power Line Commun. and Its Appl., pp. 14–21, 1999.

11. A. Emleh, H.C. Ferreira, A.J. Han Vinck, and A. Snyders, "Received noise on powerline communications where the in-building wiring acts as an antenna," IEEE Africon Conference – Zambia, pp. 1–6, September 2011.

Border-Collision Bifurcations in Automatic Control Systems with Two-Side Sinusoidal Unipolar Reversible Pulse-Width Modulation

A.I. Andriyanov

Department of Electronics, Radioelectronic and Electrotechnical Systems, Bryansk State Technical University, Bryansk, Russia
E-mail: mail@ahaos.ru

Abstract. This paper considers nonlinear dynamics of automatic control system based on two-side sinusoidal unipolar reversible modulation. Mathematical simulation of the considered system is carried out. The first bifurcation borders in two-parameter state space has been analyzed, that is relevant to the practical side. The paper demonstrates, that in the considered system the first bifurcation borders are critical, as they are related to hard bifurcations. A bifurcation, which corresponds to the variation of the widely-known border-collision bifurcation, was detected at large control signal values. Being characterized by its unique features this bifurcation variation is of great theoretical interest.

Keywords: automatic control system, sinusoidal pulse-width modulation, power inverter, bifurcation, nonlinear dynamics

INTRODUCTION

Single-phase sinusoidal pulse-width modulation inverters are rather widely used owing to their capability to provide high quality AC output voltage and reasonable weight and size. Their common applications are computer uninterruptable power supply units, AC-motor variable speed control, induction heats, etc. [1].

Sinusoidal pulse-width modulation inverters have significant differences in principle of output voltage formation as compared to DC/DC converters [1]. In particular, the systems under analysis are characterized by additional low-frequency periodic action (sinusoidal control signal), which brings about specific characteristics of the nonlinear dynamics of such systems. Currently a small number of works [2] is devoted to the study of bifurcations in systems with sinusoidal modulation, with works devoted to two-side unipolar reversible modulation (URM) missing, which makes this study topical.

CONTROL SYSTEM DESCRIPTION

Equivalent circuit of the closed-loop control system based on two-side unipolar reversible modulation is shown in Fig. 1. The symbols in Fig. 1 correspond to the following: U_{in} – input voltage, L – inductor inductance, C – capacitor capacity, R_L – load resistance, FA – feedback

amplifier with gain value K_{fb}, CON – controller, MC – master clock, $RMP1$, $RMP2$ – ramp generators, $CM1$, $CM2$ – comparators, $XOR1$, $XOR2$ – XOR-gates, $VT1$–$VT4$ – power switches, $VD1$–$VD4$ – power diodes, $K1$, $K2$ – bi-directional switches, TV – power transformer, U_{ref} – sinusoidal reference signal, U_{con} – control signal, U_{err} – error signal, U_{rm1}, U_{rm2} – ramp generators output signals, U_{cm1}, U_{cm2} – comparators output signals, U_{mc} – master clock output signal.

The specialty of the control system shown in Fig. 1 is two sweep generators, producing respectively rising ramp and falling ramp signals. It also includes two pulse-width modulators, each controlling the corresponding bridge leg composed of two power transistors [3]. When control signal is modified, control pulse of the left bridge leg shifts to the right by the phase angle α, meanwhile control pulse of the right bridge leg shifts to the left by the phase β, where α=β. The power circuit, which is a part of the described control system, is known as a phase-shifted URM-inverter [3].
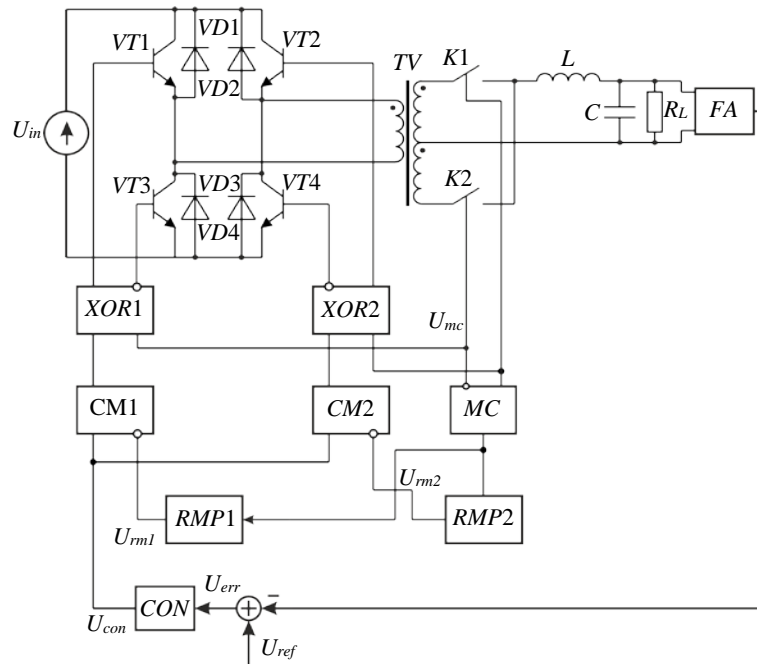
Figure 1. Functional block diagram of closed automatic control system based on URM

Signal waveforms on a modulation period of the system considered are shown in Fig. 2. The symbols in Fig. 2 correspond to the following: z_{ki} – i-th moment of switching in relative time.

The moment of switching in relative time is calculated as:

$$z_{ki} = \frac{t_{ki} - (k-1)T}{T},$$

where t_{ki} – the moment of switching in absolute time, k – the modulation period number, T – the modulation period duration.

Waveform analysis demonstrates that the modulation period can be divided into three intervals of system constancy:

1) interval 1: $0 < z < z_{k1}$. Transistors $VT1$, $VT2$ or $VT3$, $VT4$ and bi-directional switch $K1$ or $K2$ are in ON-state. Zero voltage is applied to the power filter input: $U_{inf} = 0$;

2) interval 2: $z_{k1} < z < z_{k2}$. Transistors $VT1$, $VT4$ or $VT2$, $VT3$ and bi-directional switch K1 or K2 are in ON-state. In this case voltage across the power filter input (U_{inf}) is respectively positive or negative (Fig. 2);

3) interval 2: $z_{k2} < z < 1$. This interval is similar to interval 1.

The automatic control system dynamics on each constancy interval is presented by the corresponding linear differential equation system. The subdivision smooth curves of different intervals are interconnected by fitting procedure. The mathematical model of the system described is given in [4].
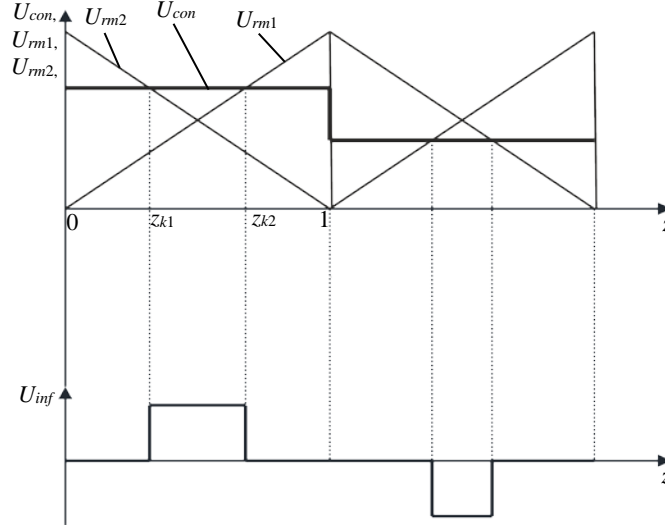
Figure 2. Signal waveforms on a modulation period of the full bridge phase-shifted URM power inverter

The set of linear differential equations that describe the system dynamics on every interval of power circuit structure constancy can be presented in matrix form as:

$$\frac{d\mathbf{X}}{dt} = \mathbf{A}_i \mathbf{X} + \mathbf{B}_i, \tag{1}$$

where $\mathbf{A}_i$ – matrix of constant factors on the i-th interval of power circuit structure constancy, $\mathbf{B}_i$ – vector of forcings on the i-th interval of power circuit structure constancy, $i = 1, 2,$

$$\mathbf{A}_1 = \mathbf{A}_2 = \mathbf{A}_3 = \begin{bmatrix} -\dfrac{R}{L} & -\dfrac{1}{L} \\ \dfrac{1}{C} & -\dfrac{1}{CR_L} \end{bmatrix}, \mathbf{B}_2 = \begin{bmatrix} U_{in}/L \\ 0 \end{bmatrix}, \mathbf{B}_1 = \mathbf{B}_3 = \begin{bmatrix} 0 \\ 0 \end{bmatrix}, \ \mathbf{X} = [x_1, x_2] = [i_L, u_C] - \text{vector}$$

of state variables, i_L – inductor current, u_c – capacitor voltage.

The integration results (1) are presented in analytical form with transition from one interval to another implemented by curve fitting technique.

Hereafter the author demonstrates that the system behavior on the k-th modulation period can be described by the function of stroboscopic maps as follows:

$$\mathbf{X}_k = \Psi(\mathbf{X}_{k-1}) = e^{\mathbf{A}a}\mathbf{X}_{k-1} + (e^{\mathbf{A}a} - e^{\mathbf{A}(1-z_k)a})\mathbf{A}^{-1}\mathbf{B}, \tag{2}$$

where $\mathbf{X}_{k-1}$ – vector of state variables at the beginning of the k-th modulation period.

In the case of sinusoidal URM control signal period contains integral number of modulation periods q, where q is quantization ratio. Therewith the function of stroboscopic maps for the system with sinusoidal URM can be defined as follows:

$$\mathbf{X}_p = \Psi^{(q)}(\mathbf{X}_{p-1}) \equiv \underbrace{\Psi \circ \Psi \circ \Psi \circ \Psi \circ ... \circ \Psi}_{q \ times}, \tag{3}$$

where p – stroboscopic maps iteration number.

Switching moments z_{k1} and z_{k2} on the k-th modulation period can calculated from the equation of switching varifold $\xi(\mathbf{X}, z_{k1})=0$, where switching function is given by [2]:

$$\xi(\mathbf{X}, z_k) = \alpha\big(U_{ref}(k) - \beta u_c(k)\big) - U_{rgm} z_k,$$

where $u_c(k)$ – capacitor voltage at the beginning of the k-th modulation period, U_{rgm} – ramp signal amplitude, $U_{ref}(k) = U_{rgm}/2 + U_{rm}\sin(\omega_c(k-1)T)$, U_{rm} – reference signal amplitude.

As can be seen in Fig. 2 on account of modulation period symmetry $z_{k2} = 1 - z_{k1}$.

MATHEMATICAL SIMULATION

Mathematical simulation of inverter operation with two-side unipolar reversible modulation was carried out as part of the study. The following set of parameters was selected as part of the calculations: $U_{in}=50$ V, quantization ratio $q=10$, $R_L=45$ Ohm, quantization frequency $f_{qu}=10$ kHz, $R=1$ Ohm, $L=4$ mH, $C=3.5$ µF, ramp signal $U_{rmpm}=\pm10$ V, coefficient of proportional regulator $K=50$, feedback gain $K_{fb}=0.015$.

Fig. 3a (U_{rm} – reference signal amplitude) shows a dynamical modes map with marked areas of existence of different modes in the space of two parameters: reference signal amplitude of voltage output U_{rm} and input voltage U_{in}.
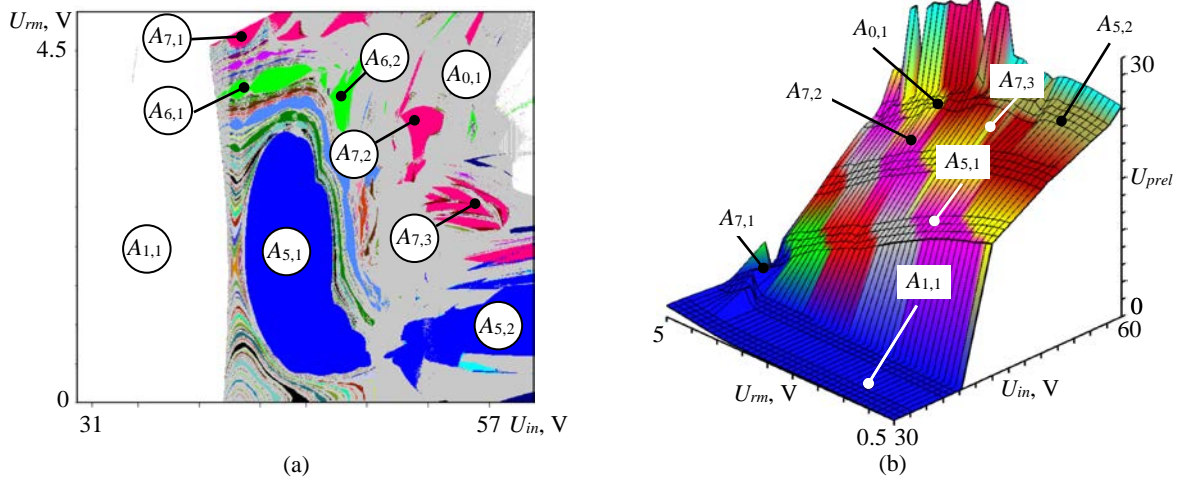
Figure 3. Two-parameter diagrams: dynamical modes map (a);
relative RMS-value of output voltage parasitic harmonics (b)

Fig. 4 shows the bifurcation diagram and monodromy matrix large multiplier module diagram of mode $R^s_{1,1}$ (i_L – inductor current). This mode corresponds to the area $A_{1,1}$ in Fig. 3a.

The map has areas of existence of different dynamical modes marked with symbols $A_{i,j}$ (i is an m-cycle peculiar to this area, therewith, when $i=0$, the area corresponds to a region of existence of chaotic oscillations; j is a number of the area on the dynamical modes map). Fig. 3b shows a two-parameter diagram of relative RMS-value of output voltage parasitic harmonics (U_{prel}), that can be calculated as:

$$U_{prel} = \frac{U_p}{U_{1max}},$$

where U_p – RMS-value of output voltage parasitic harmonics, U_{1max} – maximum RMS-value of the wanted harmonic in the area of the design mode.

17

(a)

(b)
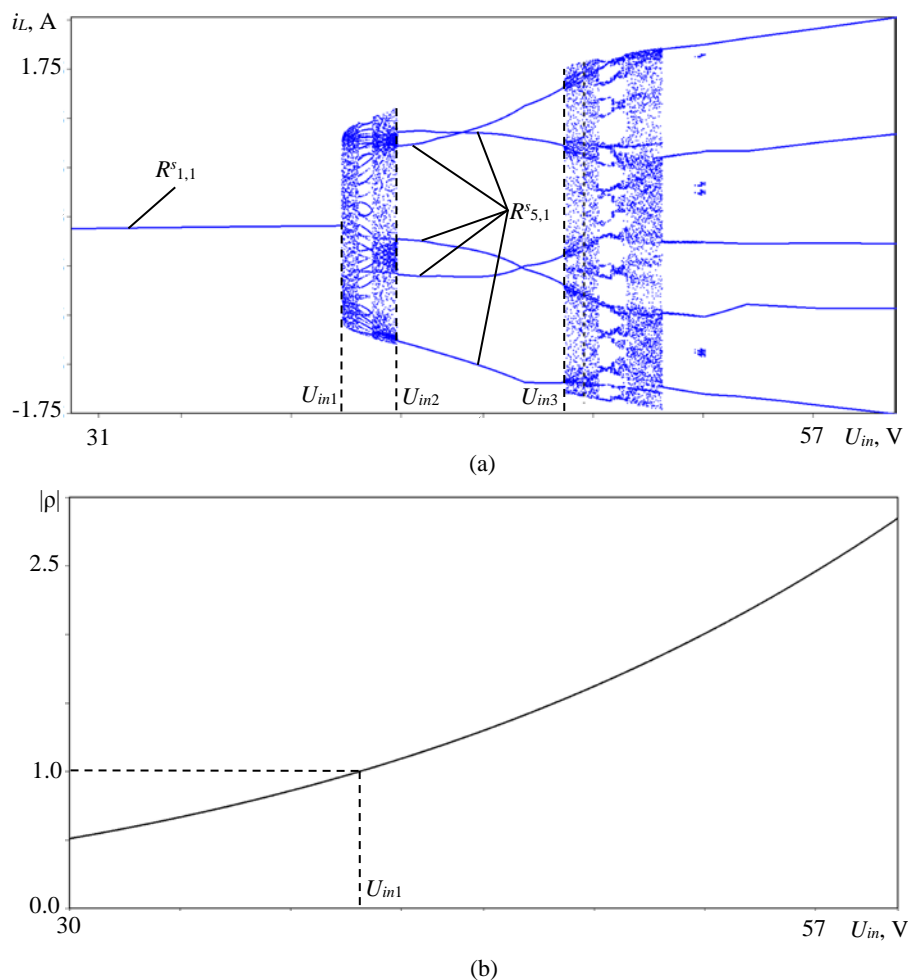
Figure 4. Diagrams at U_{rm}=1 V: bifurcation diagram (a); large multiplier module diagram (b)
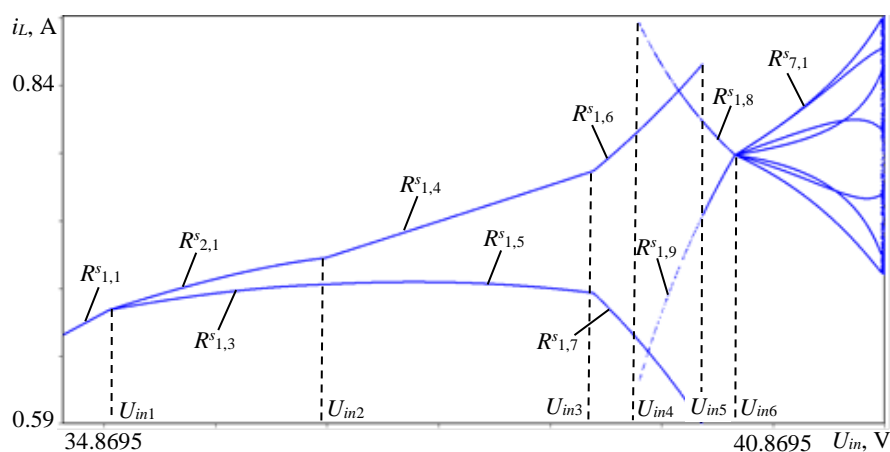
Figure 5. Bifurcation diagram at U_{rm}=4.75 V

The analysis of these diagrams shows that the first bifurcation point (U_{in1}=39.846 V) is due to Neumark-Sacker subcritical bifurcation (complex large multiplier module at the bifurcation point intersects the unity). This bifurcation is obscure and determines the segment AB of the first bifurcation border.

Fig. 5 shows a bifurcation diagram with U_{rm} =4.75 V, corresponding to dynamical modes map (Fig. 3a).

The first bifurcation point U_{in1}=34.917 V is associated with a border-collision bifurcation of pitch-fork type (Fig. 6, where u_c – capacitor voltage), with two stable 1-cycles $R^s_{1,2}$ and $R^s_{1,3}$ following the bifurcation, and 1-cycle $R^s_{1,1}$ transition to unstable 1-cycle $R^u_{1,5}$ with another symbolic characteristics. The definition of a symbolic characteristic is given in [5].

The bifurcation point U_{in2}=36.848 V (Fig. 5) features a bifurcation of a simple change of the solution type for a pair of 1-cycles. The symbolic characteristic of the first 1-cycle is changed during transition from $R^s_{1,2}$ to $R^s_{1,4}$, and the symbolic characteristic of the second 1-cycle is changed during transition from $R^s_{1,3}$ to $R^s_{1,5}$.

The bifurcation point U_{in3}=39.25 V (Fig. 5) features another change of symbolic characteristics for the pair of 1-cycles. The symbolic characteristic of the one 1-cycle is changed during transition from $R^s_{1,4}$ to $R^s_{1,6}$, and the symbolic characteristic of the other 1-cycle is changed during transition from $R^s_{1,5}$ to $R^s_{1,7}$.
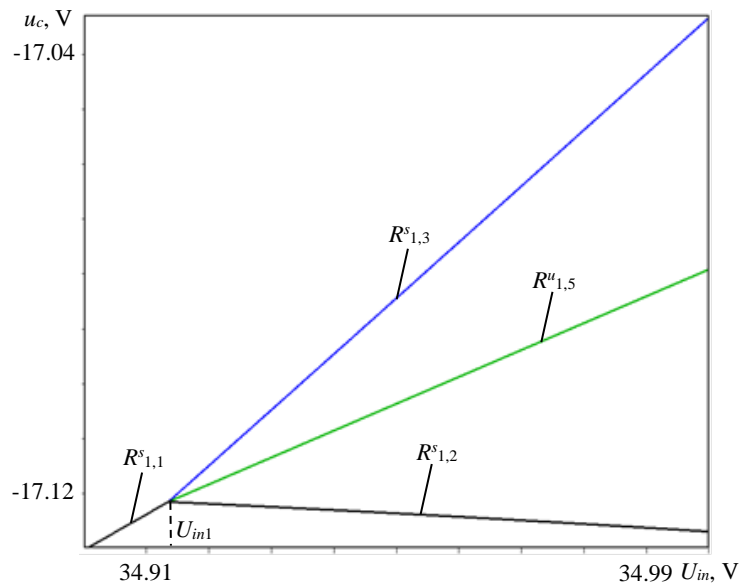
Figure 6. Detalization 1 of the bifurcation diagram at U_{rm}=4.75 V
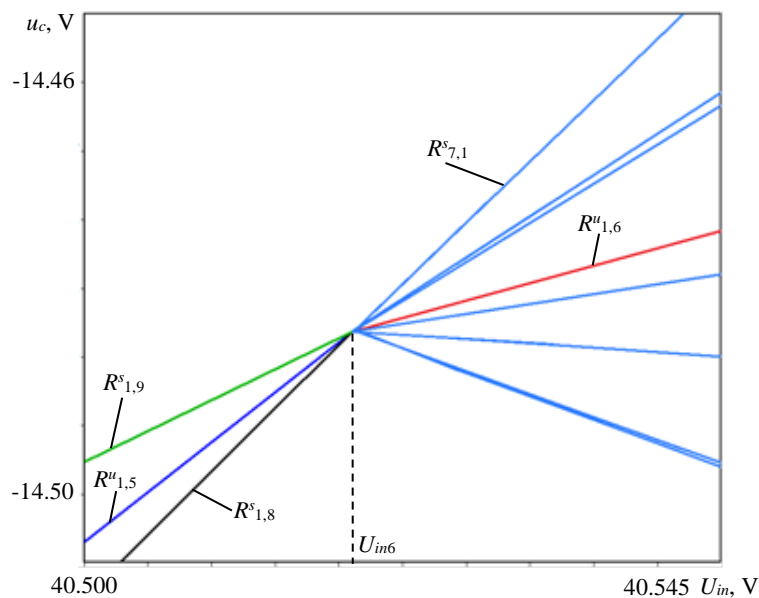
Figure 7. Detalization 2 of bifurcation diagram at U_{rm}=4.75 V

The bifurcation point U_{in4}=39.656 V features a pair of saddle-node border-collision bifurcations. The bifurcation point U_{in4} features the merge of two pairs of 1-cycles with different symbolic characteristics, which corresponds to saddle-node border-collision bifurcations.

A specific bifurcation occurs at the point U_{in6}=40.521 V (it corresponds to BC segment of the first bifurcation border (Fig. 3a)). In this case, the merge of two stable 1-cycles $R^s_{1,8}$ and $R^s_{1,9}$ and an unstable $R^u_{1,5}$ with different symbolic characteristics takes place, followed by the subsequent soft emergence of a stable 7-cycle $R^s_{7,1}$ together with an unstable 1-cycle $R^u_{1,6}$ (Fig. 7). This bifurcation is a kind of border-collision bifurcation. A bifurcation with similar principle is described in [6], but in this case, the bifurcation involves the cycles with the same periodicity equal to 1, thus bearing evidence of the novelty of the observed phenomenon.

CONCLUSION

The bifurcation analysis conducted shows specific behavior of the system with variation of its parameters. A characteristic feature of automatic control pulse-width modulation systems is the presence of a great variety of border-collision bifurcations. It imposes specific requirements to the design mode of SPWM systems. In particular, the design mode of such systems means 1-cycle [4, 5], where all the duty factors on the period of sinusoidal reference voltage must be less than unity and greater than zero. The findings will further allow to create control algorithms for nonlinear dynamics of SPWM systems.

REFERENCES

1. B. Ismail, S.T. Mieee, A.R. Mohd, M.I. Saad and C.M. Hadzer, "Development of a Single Phase SPWM Microcontroller-Based Inverter," in First International Power and Energy. Conference Pecon 2006 November 28-29, Putrajaya, and Malasia, pp. 437–440, 2006.

2. Zh.T. Zhusubaliyev, E. Mosekilde, A.I. Andriyanov and V.V. Shein, "Phase Synchronized Quasiperiodicity in Power Electronic Inverter Systems," Physica D: Nonlinear Phenomena, vol. 268, pp.14–24, 2014.

3. A.V. Kobzev, G.Ya. Michal'chenko and N.M. Muzhitchenko, Modulating Power Supplies of Radioelectronic Devices, Tomsk: U.S.S.R.: Radio i Svyaz, 1990.

4. A.I. Andriyanov and G.Ya. Mikhalchenko, "Problems of mathematical modeling of the closed-loop systems of automatic control on the basis of unipolar reversible modulation," Mekhatronika, avtomatizaciya, upravlenie, No. 1, pp. 11–19, 2005.

5. Zh.T. Zhusubaliyev and Yu. V. Kolokolov, Bifurcations and chaos in relay and pulse-width automatic control systems, Moscow: Mashinostroenie-1, 2001.

6. Zh. T. Zhusubaliev, E.A. Soukhoterin and E. Mosekilde, "Border-collision bifurcations and chaotic oscillations in a piecewise-smooth dynamical system," Int. J. Bifurcation Chaos, vol. 11, No. 12, pp. 2977–3001, 2001.

Application of Nanostructured Silver-Palladium Resistance Films for Measuring of Power and Frequency of Laser Radiation Pulses

V.A. Aleksandrov, D.G. Kalyuzhnyi, V.V. Besogonov, I.N. Skvortsova

Institute of Mechanics UB RAS, Izhevsk, Russia
E-mail: ava@udman.ru

Abstract. It is shown that the electric signal taking off probe electrodes placed on a silver-palladium resistive film surface, at the effect by laser radiation essentially depends on power and frequency of radiation pulses. The irradiated area of a sensitive element gets an electric charge, due to originating of temperature gradient and charge carriers thermodiffusion current, as result the potential difference, recorded in the form of generated voltage signal, is created.

Keywords: resistive film, silver-palladium resistive films, laser, thermodiffusion, nanostructured, sensor

Introduction

Development of laser technics is accompanied not only increase the laser radiation power, but also occurrence of the automated laser complexes both in manufacture and applied science field, and in basic researches. The parameters of laser sources of radiation are still the subject of research and scientific development. Spatial, temporal, spectral and energy parameters allow you to judge the nature of the laser radiation. For carrying out of experimental works with laser radiation use it is necessary to solve a number of problems on control and measuring of the laser beam parametres, considering that applied detectors should stand powerful laser pulses effect without damage.

The photovoltaic effect has been detected during studying of silver-palladium resistive films obtained by the thick-film technology [1].

Experimental Research

Research of photovoltaic effects in thick-film Ag-Pd resistors at pulse laser effect has permitted to find out sufficiently quick electric response of these resistors to laser pulse effect. Resistive films with silver electrodes are made on ceramic substrates BK-94 by repeated cauterizing to a substrate semiconductor ink at the temperature 815 °C and resistive ink at the 605 °C in the conveyor furnace in the air atmosphere. Powder component Ag-Pd of resistive inks contains Ag_2O, Pd and C-660a glass. During thermal treatment of these inks there are the

redox reaction resulting in resistive film forming which functional material consists from nanodimensional particles of Ag-Pd alloy and palladium oxide PdO [2].

Because of a high processing temperature on air the external surface of a resistive film contains PdO which thin layer is formed besides on a surface of Ag-Pd particles alloy. As Ag-Pd is metal, and PdO is the p-type semiconductor, during resistor forming on its surface the set nanodimensional areas with transient the metal-semiconductor layers, having property of Schottky barrier is created. Accordingly, the Ag-Pd thick-film resistor surface can have the properties similar to the properties of Shottki photo diodes, what causes their high-speed performance of the photo-electric response. PdO content on Ag-Pd thick-film resistors surface is also confirmed that on a surface of these resistors thermo-EMF originating is detected [3, 4]. When heated copper electrode contacts with a thick-film resistor surface which is at a room temperature, between an electrode and any resistor electrode appears a negative sign thermo-EMF (on the heated electrode), that indicates p-type conductivity of a the resistor surface [5].

The received resistors had resistance ~60 Ω at the size of a resistive film 6×6×0.02 mm and 300 Ω at the size 2×2×0.02 mm. The resistors contacts located along opposite sides of a rectangle between a ceramic substrate and a film, were formed from silver semiconductor ink PP-3 (Figure 1).
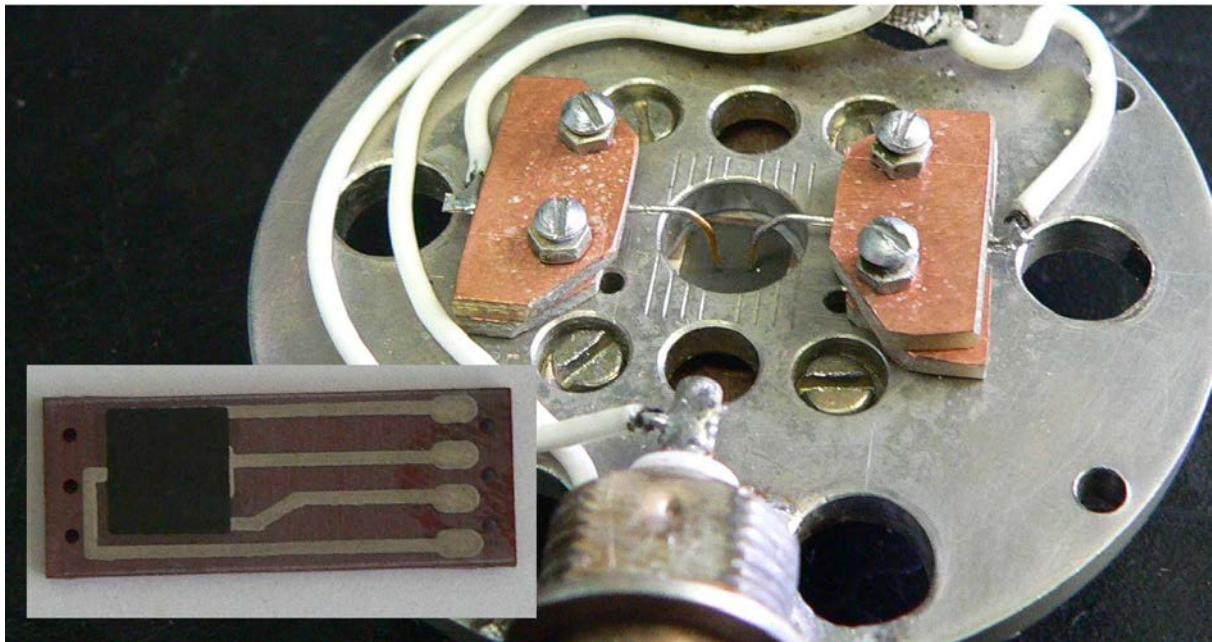
Figure 1. Exterior thick film silver-palladium resistor and probe electrodes on its surface

Researches were carried out with application as a source of radiation pulse CO_2 laser with radiation wavelength of 10.6 microns. In order to reduce external noise resistor placed in a shielding metal case. Immersion heaters with painted surface to the probe electrode was placed on the XY table. The distance from the focusing lens of the laser to the surface of the resistor was 70 mm. Focal length of the lens is 50 mm. Thus the surface of the resistor fell partially defocused bunch. This avoids modifying the surface of the resistor from the powerful heat of the laser radiation. The diameter of the laser beam normally incident on the surface of the resistor is approximately 1 mm. Exposure time of the laser to the surface of the resistor is 10 seconds. Electrical signals induced in the resistor on its surface, were recorded after amplification oscilloscope. Thus a fixed maximum value of EMF occurring between electrodes. Summing up the signal is taken from the surface of the resistor electrodes and electrodes on the edge of the resistor. After each measurement point of impact of the laser

pulses on the surface of the resistor is moved over a distance of 0.2 mm increments using the screws XY table.

Laser radiation incidents normally to a resistive film surface. The film, being a sensitive element, possesses property of electric charges division on a surface during a laser radiation local exposure, due to forming of a temperature gradient and a thermodiffusion current of charge carriers, and forming in irradiated area of a spatial charge, differing on a sign from a charge of non-irradiated part of a film surface. Thus the spatial charge originating in the irradiated part of a surface creates a potential difference on non-irradiated part and at edges of this surface. The potential difference in the form of EMF signal can be taken off using the electrodes placed at its edges of a resistive film, and by means of probe electrodes, positioned to a surface. At irradiation of a sensitive element surface by laser pulses repeated by determined frequency there are charge fluctuations of an irradiated surface part, and accordingly, a potential difference created by this charge by the frequency corresponding to laser pulses frequency. The electric signal value on electrodes is thus proportional to laser pulses power, and frequency is equal to laser impulses frequency.

The signal value directly taken off a resistive film does not exceed several mkV. For registration the electric signal supplies to an oscilloscope through the amplifier. The power and frequency of laser pulses is determined by the amplitude and frequency of control signals.
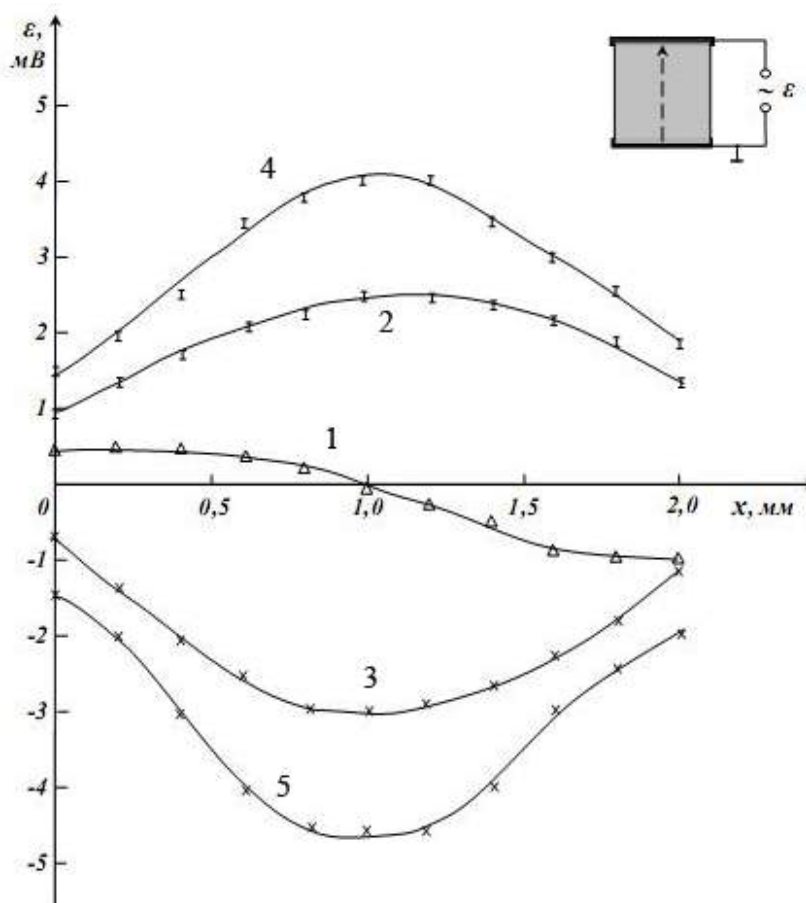
Figure 2. The amplitude of the EMF pulse bias voltage to Ag-Pd 300 Ω resistor by irradiating pulses of the laser: 1 – without applying a bias voltage; 2, 3 – a bias voltage + 0.5 V and −0.5 V, respectively; 4, 5 – offset voltage of +1.0 V and −1.0 V, respectively

For sensitivity increase to the electrodes located at edges of a sensitive element surface, voltage 1.5 and 3 V was applying constantly what created the electric field in a sensitive

element internally, having an effect on a spatial charge in an irradiated part of a sensitive element surface. Due to it a spatial charge current appears in a sensitive element which creates on electrodes additional EMF, 10 times exceeding EMF on value, caused by a potential difference created by it (Figure 2).

The value of the constant EMF between electrodes depends on the point of impact of the laser pulses to the surface of the resistor. As seen in figure 2, its sign is reversed, when passing the point is the midpoint of the distance between electrodes.

The size of EMF between electrodes depends on the point of impact of the laser pulses to the surface of the resistor and the applied bias voltage. As seen in Figure 2, the sign of the EMF is reversed, when passing the point is the midpoint of the distance between the electrodes (curve 1). The bias voltage changes the nature of the relationship (curves 3, 4). Changing the polarity of the bias voltage dependence of the mirror displays rented signal (curves 3, 5).

In the Figure 3 typical oscillograms of EMF signals received from probe electrodes, positioned the Ag-Pd resistors surface at their surface irradiation by laser pulses of the frequency 1 kHz and from thick-film electrodes at resistor edges at laser pulses irradiation with frequency of 700 Hz are presented. Signals pulses are unipolar, have sharp front and shallow recession. As the laser generates radiation in the form of a pulses package with the set frequency, that, evidently, front duration of separate electric impulses is equal to duration of one package of laser radiation. On frequency 1 kHz, one can see from the oscillogram, impulses front duration is ~0.1 ms, on frequency of 700 Hz is ~0.2 ms.
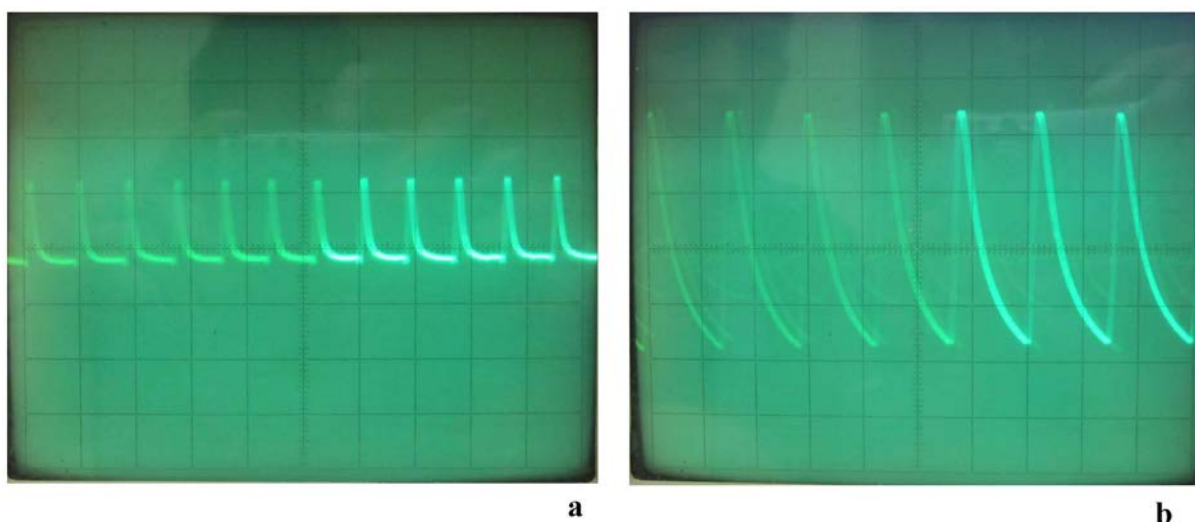
Figure 3. EMF oscillograms on Ag-Pd resistors surface at an irradiation by the CO_2 laser pulses when frequency is: 1 kHz (a); 700 Hz (b)

CONCLUSION

Pulse laser radiation effect on a surface of thick-film silver-palladium resistors result in thermo-EMF originating. Measuring the surface voltage in the Ag-Pd resistors when irradiated pulses of CO_2 laser shows patterns of change in the nature of EMF on the location of the point of impact of the laser beam on the surface of the resistor. The amplitude of the pulse and the polarity sign of the signal are significantly dependent on the coordinates of the laser irradiation. Pulse EMF component carrying information about the frequency and duration of the laser pulses, provides information on relevant parameters of the laser radiation.

Thus, the effects of pulsed laser radiation on the surface of the thick-film silver-palladium resistors leads to a thermo-EMF, which is detected by simple means of measurement. The

dependence of the magnitude and polarity of the thermoelectric voltage between the electrodes on the surface of the resistors from the coordinates of the point of the laser radiation indicates the semiconducting properties of the surface of the p-type resistors. Occurrence of EMF on the surface when exposed resistors normally incident laser radiation may be explained fad carriers thermal phonons resulting in local heating and the occurrence of a temperature gradient on the surface of the resistors. The studies point to the use of silver-palladium thick film resistors as sensors for monitoring parameters of high-power pulsed laser radiation.

Thermo-EMF signal parameters relation between electrodes on a resistors surface from amplitude and pulse repetition frequency of laser radiation allows using silver-palladium thick-film resistors as detectors for the parameters control of powerful pulse laser radiation.

REFERENCES

1. V.A. Aleksandrov, D.G. Kaluzhny and R.G. Zonov, "Laser-Induced Surface Vortex Current in a Thick Film Resistor," Technical Physics Letters, vol. 36, issue 7, pp. 663–664, 2010. DOI: 10.1134/S1063785010070230.

2. V.I. Smirnov, Physical and chemical bases of technology of electronic means, Ulyanovsk: Ulyanovsk State Technical University, 2005.

3. V.A. Alexandrov, "Surface thermopower in the silver-palladium thick film resistors," Bulletin of Udmurt University Physics and chemistry, No. 4, pp 18–21, 2012.

4. V.A. Aleksandrov, D.G. Kalyuzhnyi and E.V. Aleksandrovich, "The Effect of Hydrogen on the Conductivity of Ag-Pd Thick Film Resistors," Technical Physics Letters, vol. 39, No. 1, pp. 95–97, 2013. DOI: 10.1134/S1063785013010021.

5. V.L. Bonch-Bruevich and S.G. Kalashnikov, Physics of semiconductors, Moscow: MIR, 1977.

Complex Automated Electrolysis Unit for Wastewaters Treatment and Drinking Water Purification

E. Arakcheev [1], V. Brunman [2], M. Brunman [3], A. Konyashin [3], A. Petkova [2]

[1] GC "Spetsmash", Dzerzhinsk, Russia
E-mail: info@specmach.ru
[2] Laboratory "Mechatronics", Peter the Great Saint-Petersburg Polytechnic University, St. Petersburg, Russia
[3] Department "Automats", Peter the Great Saint-Petersburg Polytechnic University, St. Petersburg, Russia
E-mail: automats@inbox.ru

Abstract. Article describes construction principles and design of comprehensive electrolysis unit that produces simultaneously chlorinated anolyte and sodium ferrate. Anolyte will permit to carry on water treatment at the municipal water supplies or enterprise territory and the ferrates – the treatment of industrial wastewaters, so the unit will ensure that treated wastewaters discharged into the environment without any harm. Integrated electrolysis unit for the production of reagents for drinking water purification and wastewaters treatment does not have any domestic analogues, and can ensure the competitiveness of the domestic water treatment processing systems compared to foreign made analogues by price, productiveness and energy efficiency.

Keywords: Water, industrial wastewaters, disinfection, anolyte, ferrates, electrolysis unit, energy efficiency

INTRODUCTION

A new approach to water treatment is a creation of an ecologically safe and economically effective integrated electrolysis unit (IEU), generating anolyte (mainly Cl_2) from the solution of salt in water and liquid ferrates (NaOH) from the waste of anolyte electrolytic production [1]. At this, the anolyte and the ferrates are used directly at the place of production: anolyte for disinfection of drinking and industrial water for own needs of the enterprise, and the ferrates for processing of industrial wastewaters.

A membrane electrolysis was chosen as a promising method for obtaining chlorine-containing anolyte for disinfection of drinking and industrial water, and for production of sodium ferrate for wastewater treatment [2]. Proposed by authors an environmentally sound and economically efficient integrated electrolysis unit (IEU) allows to combine two electrolysis processes (obtaining of anolyte and production of ferrates) in one unit with an adaptive performance management system.

Such an approach, which includes intelligent control of the electrolysis process for both products at the same time, gives a possibility to avoid violations of regulations and legislative acts in the field of water treatment, improve the quality and increase the energy efficiency of the overall process.

DESIGN OF AN INTEGRATED ELECTROLYSIS UNIT

The IEU combines modules for production of anolyte and ferrates with the systems of gas outlet and recirculation of anolyte and catholyte and automated unit control system (Fig. 1).
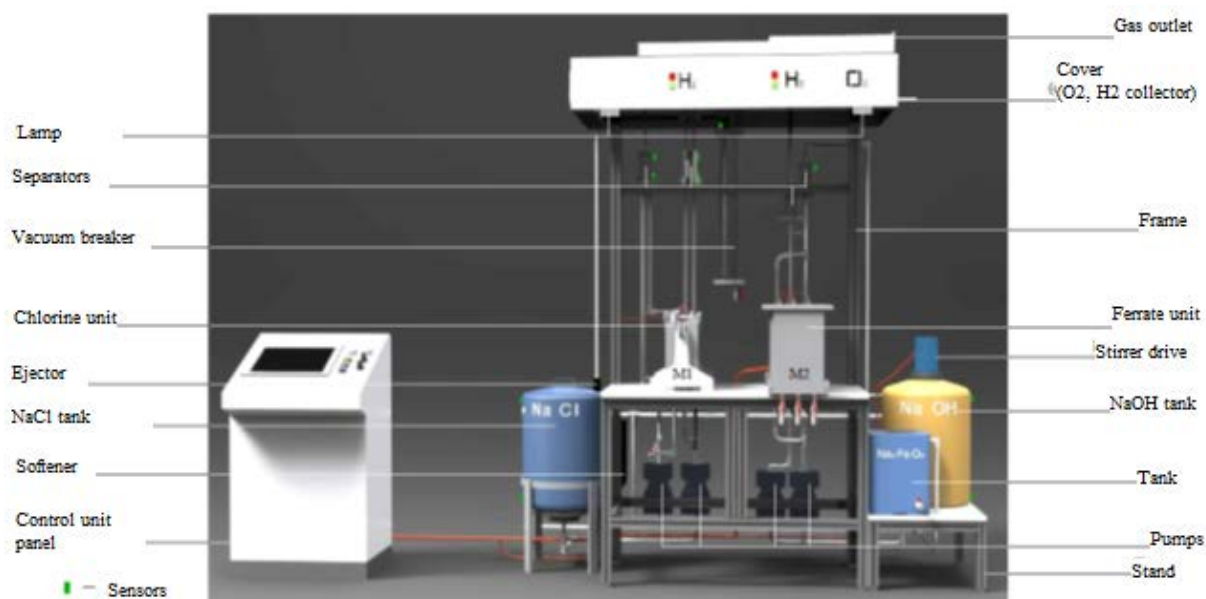
Figure 1. General view of experimental integrated electrolysis unit

Module M1 for producing anolyte (Fig. 2) consists of a DC power supply 1, a tank for preparing the salt solution 2, cell E1, which is divided for anode and cathode compartments by ion-exchanging membrane 4, with two electrodes – cathode 5 and anode 6, pumps for dispensing the salt solution in the anode chamber and water in the cathode chamber, an ejector for dispensing anolyte in water, tanks to store water 8 and alkali 9, separators of hydrogen 10 and chlorine 11 from cathode and anode chambers, sensors controlling the amount of chlorine in water and gas, and alarm annunciators of contamination of premises with chlorine/hydrogen.

Module M2 for production of ferrates (Fig. 2) contains a DC power supply source 12, the cell E2, with the at least one consumable iron-containing anode 14 and the cathode 15, pumps for dispensing alkali in the anode and the cathode chambers, a tank 17 for the accumulation of the ferrates, the hydrogen (18) and oxygen (19) separators from cathode and anode chambers, and the device for ferrates dosing.

All the styles used in this template are described in Table 1. Most of styles should be applied on a whole paragraph. Please try to avoid creating new styles because it can lead to difficulties in proceedings book assembly.

The unit also contains diaphragm pumps for feeding and dosing of reagents in the cells and a control unit with sensors for monitoring production parameters of anolyte and ferrates. The controlling unit operates in the specified mode and control the performance of the unit.

The case of the membrane cell E1 for the production of anolyte is divided into two chambers by a semi-permeable cation-exchange membrane. The cathode chamber is made of chlorine-resistant titanium, the anode chamber – of alkali with concentration of 30–35 % – resistant stainless steel. As cation exchange membranes operating at alkali concentrations of 30–35 %, membranes of Flemion 811 or Nafeon-2030 types can be used.
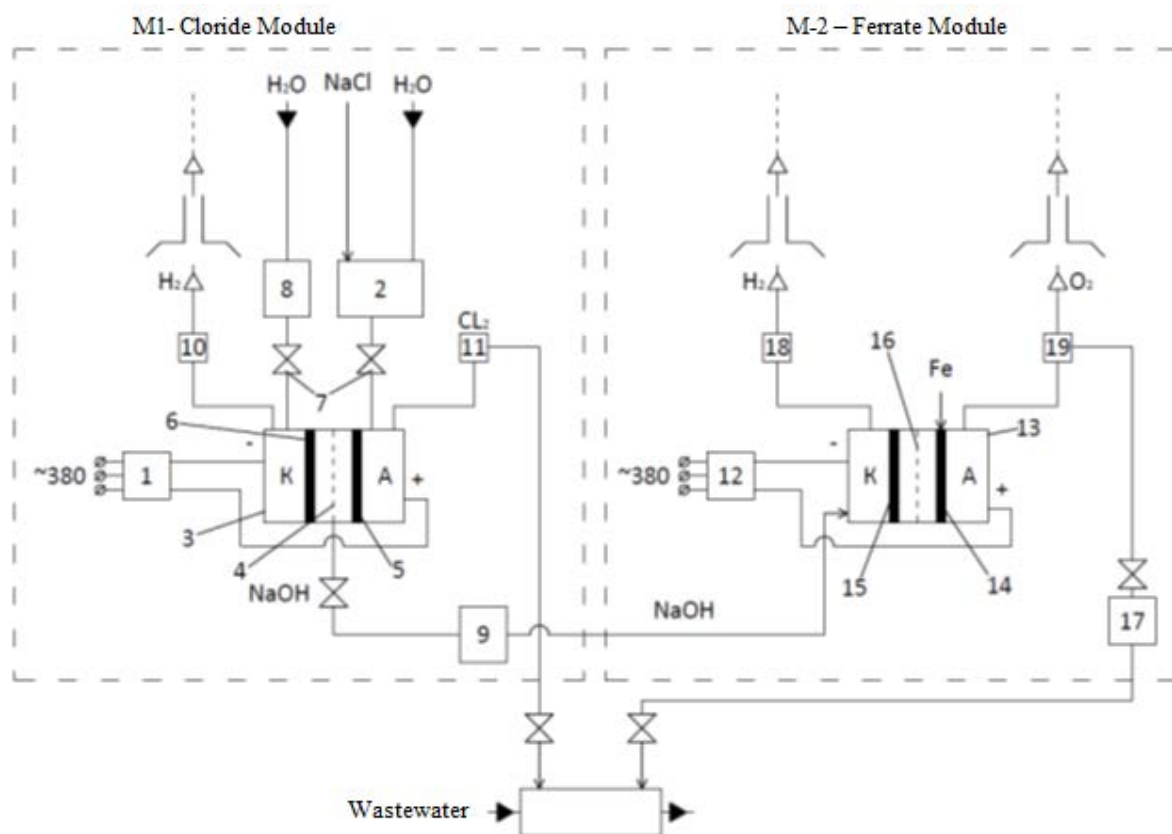
Figure 2. A schematic diagram of apparatus for integrated producing of chlorine-containing reagent and sodium ferrate: 1, 12 – electrolytic cells power supplies units; 2 – tank for brine preparation; 3,13 – cell E1 for the production of anolyte and E2 for the production of sodium ferrate; 4, 16 – cation-exchange membrane; 5, 15 – cathode; 6 – anode; 7 –valves controlling the feed of salt solution and water; 8 – can for water; 9 – intermediate tank with a solution of sodium hydroxide; 10, 18 – cathode separators; 11, 19 – anode separators; 14 – consumable anode; 17 – tank with sodium ferrate

The case of the membrane cell E2 for the production of ferrate is made of alkali-resistant polypropylene, and is divided into three chambers, separated by a semi-permeable cation exchange membrane. As cation exchange membranes operating at alkali concentrations of 30–35 %, membranes of Flemion 811 or Nafeon-2030 types can be used also.

The feedstock for the operation of the unit is tap water and salt for the brine. Salt is fed into the brine tank manually. Water and brine contains in the tanks, which filling is controlled by a floating mechanism. Then they are served into the first module by pumps. The recirculation loop of the first module contains separators to separate products of liquid and gaseous phase. The alkali produced of the first module reserves in a separate tank, from which it supplied to the second module by pumps.

Controlled rectifier with two independent outputs delivers a direct electric current on each of the modules. The by-produced hydrogen from both modules is displayed in a separate ventilation system, which has the pressure sensor for monitoring the pressure of hydrogen in the exhaust.

The integrated electrolysis unit automated control system (ACS) optimizes production process of anolyte and ferrates while minimizing energy consumption. The unit ACS controls the following parameters: the minimum level of liquid in tanks with water and brine; minimum and maximum liquid level in the alkali tank, both separators and in the second module; the chlorine concentration in the treated water; reduced pressure in the branch vacuum breaker; overpressure in the hydrogen exhaust system; temperature of the output liquids of each module; hydrogen and chloride permissible concentration exceeding alerts

from the air sensor (Fig. 1). ACS manages the following actuators: unit tap water supply valve; modules DC power supply; pumps for feedstocks supply to the modules; emergency extractor; automatic feeder system.
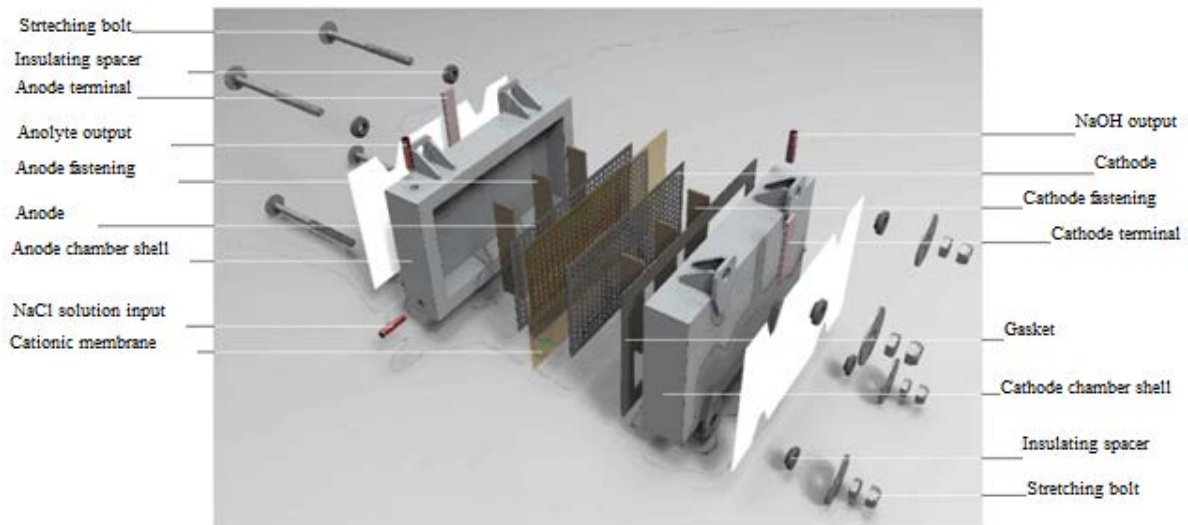
Figure 3. Device for producing chloride (anolyte) (as a part of IEU) layout scheme
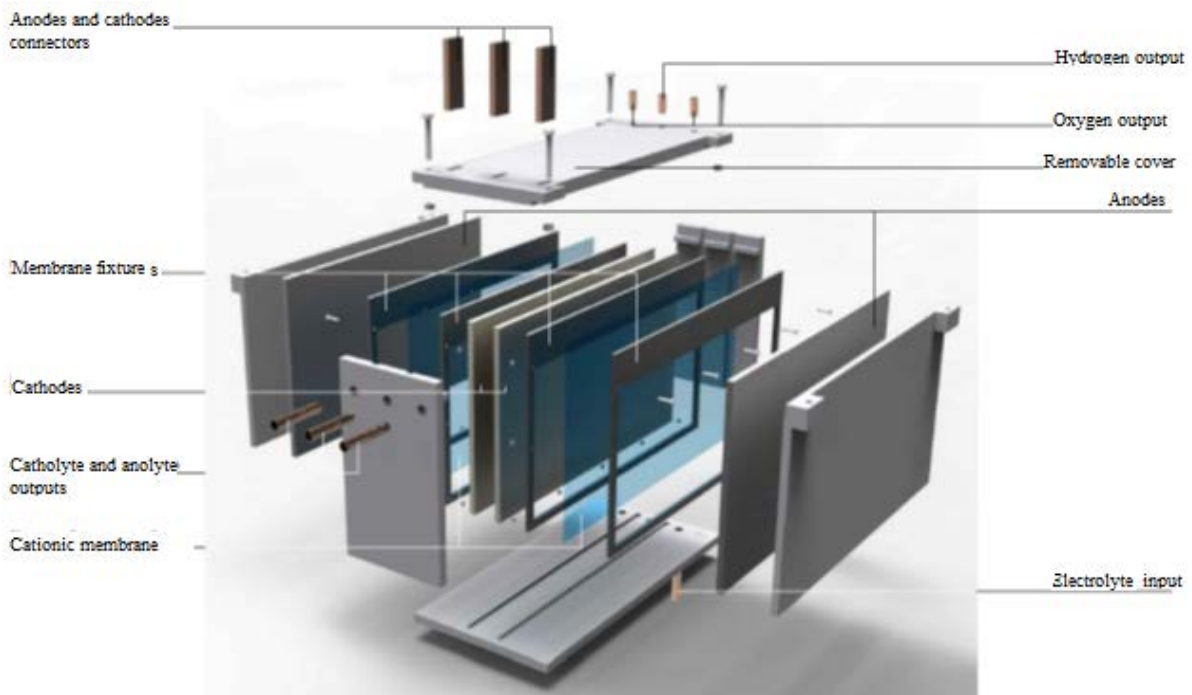
Figure 4. Device for producing ferrate (as a part of IEU) layout scheme

ACS supports following modes: unit launch, operation with automatic control, operation with manual control, regular stop and emergency stop. Automatic control of anolyte production carried out on a sensor readings of residual chlorine in the treated water feedback providing a residual chlorine content in the range 1.8–2.3 mg/l [3]. Ferrate production carried out by a given amount of wastewater, which is determined statistically. In case of exceeding the critical level in any of the monitored parameters of process safety ACS starts emergency ventilation, gives an audible alarm and starts emergency stop process by turning off modules power supply and terminating object water supply.

TECHNOLOGICAL PARAMETERS OF PROCESS

Experimental integrated electrolysis unit produces 65 g of chlorine and 25 g of sodium ferrate per hour. Cell E1 of the module M1, which produces chlorine-containing anolyte, is supplied by DC current of up to 60 amps, at a voltage of 3 to 4 V. The maximum specific power consumption of the module is 3.5 kWh / kg. Depending on the area of the electrodes (solid or perforated) maximum current density can vary respectively from 1400 to 1600 A/m^2. Thus, Flemion 811 or Nafeon-424 can be used as cation-exchange membrane.

Purified softened water is fed into the cathode chamber of the electrolytic cell E1. The saturated salt solution is fed to the anode chamber of E1. The electrolysis process takes place in cell E1 at the optimum temperature of 60-80 Co. Anolyte from the anode chamber through the chlorine separator is sucked by an ejector into the processed wastewaters transportation system.

Solution of sodium hydroxide with a concentration of 25 % to 35 % goes from the cathodic chamber through a hydrogen separator to the intermediate storage tank of alkali, and gaseous hydrogen is deflected. Then, the solution of sodium hydroxide is fed into the chamber of the cell E2, which is part of the module M2, for the production of sodium ferrate.

The cell E2 is fed by the DC power supply of 45A at a voltage of 3–3.5 V. The maximum specific power consumption of the module is 6 kWh / kg. The anode in the electrolytic cell E2 may be solid, perforated, or of expanded metal. At this, the current density does not exceed 250 A/m^2, which also allows the use Flemion 811 or Nafeon-424 type's membrane. Electrolysis in cell E2 runs at temperature less than 60 °C. Solution of sodium ferrate from the anode chamber through the oxygen separator is fed into the tank for accumulation of the product, and gaseous oxygen is deflected. Gaseous hydrogen is removed from the cathode chamber through the separator.

The separators of both modules are used for visual control of the boundary between liquid and gaseous media with separate removal of gaseous hydrogen and oxygen, and for control of chlorine inflow system for the absence of leakage in the unit.

SUMMARY

Proposed unit as feedstock uses tap water, salt and electricity, so it can easily be implemented into the production cycle. Such installation will permit to carry on water treatment at the municipal water supplies or enterprise territory and ensure that treated wastewaters be discharged into the environment without any harm.

The integrated electrolysis unit automatic control system allows real-time monitoring and managing of reagents production in automatic or manual mode, chose the necessary dosage ratio of the reagents, keep records of the unit operation and solve emergency problems.

The developed integrated electrolysis unit for producing reagents for purification of drinking water and wastewaters processing has no domestic analogues and can ensure the competitiveness of home wastewater processing systems compared to foreign made analogues by price, productiveness and energy efficiency.

Technology of anolyte (chlorine) production by membrane electrolysis is less energy-intensive as compared to the production of hypochlorite on consumption site method, which is used in foreign analogues [4]. The main advantage of using a membrane electrolysis for ferrate manufacturing is providing its larger output by used current, and, consequently, greater energy efficiency, than in diaphragmless electrolytic cells described in analogue projects. This is because in the absence of the separator, ferrate ions reach the cathode and are partially exposed to electrochemical recovery, including molecular hydrogen formed in the cathode area.

In addition, the presence of the membrane prevents the mixing of gaseous hydrogen and oxygen, generated by electrolysis in different cells. This increases the explosion safety of the entire installation and eliminates the need for purging the cell with inert gas, used by analogue projects, which, in turn, also reduces energy costs.

REFERENCES

1. V.E. Brunman, A.P. Petkova and M.V. Brunman, "Construction principles and design of autonomous mobile systems for water treatment and disinfection at the place of use of reagents," International Research Institute «EDUCATO», No. 6, pp 18-22, 2014.

2. E. N. Arakcheev, V. E. Brunman, M.V. Brunman, A.H. Volkov, V.A. Dyachenko, A.V. Kochetkov and A.P. Petkova, "Modern Advanced Technology for Disinfection of Water and Wastewater," Hygiene and Sanitation, vol. 94, No. 4, pp. 25-32, 2015.

3. GOST 51232-98 (1998). Drinking water. General requirements for the organization and methods of quality control.

4. Ballast water treatment. Unit and method of ferrate usage. Russian Federation Patent. KR101202765, MPK C02F1/461 (19 November 2012).

Multiscale Centroid Filtration of Noisy Graphics Image

I. Arkhipov, A. Murynov

Dept. of Computer Software, Kalashnikov Izhevsk State Technical University, Izhevsk, Russia
E-mail: aio1024@mail.ru

Abstract. Multiscale centroid filtration allows to allocate mass centers of graphics image structure elements. This work highlights insufficient reliability of multiscale centroid filtration while analysing noisy graphics image. The paper proposes a new scheme of multiscale centroid filtration graphics image by accumulating current values of structure element mass within the analysis window. The solution in question enables to considerably decrease relation between analysis result and image noise.

Keywords: structural elements, spatially chromatic parameters, multiscale centroid filtration, graphics image, image analysis

INTRODUCTION

Graphics images (GI) are distinguished by spatial and graphical distinctness. GI is created by plotting structural elements (SE) on image surface in accordance with a priori assigned imaging plan [1]. One can define maps, schemes, drafts, traffic sings and others among GI. The centroid filtration method [2] allows to efficiently solve the problems of detecting and recognising SE on GI. Multiscale centroid filtration may be carried out by calculating spatially chromatic parameters (SCP) [3–5]. SCP are based on calculating moment functions W_i of SE cross section $f(n)$ and makes it possible to evaluate coordinates, dimension and brightness of the object. The first two spatially chromatic parameters are valuable for the centroid filtration – mass and centroid. Mass $M = W_0$ defines SE mass, and the centroid $C = W_1/M$ points at its «mass center». SCP are calculated in inverse gray scale (0 is a code for white background). Multiscale centroid is performed as follows:

$$Z[n + C(n)] = Z[n + C(n)] + 1, \qquad (1)$$

meanwhile, accumulation of centroid information occurs.

Multiscale centroid filtration is performed iteratively. The first stage sees analysis window width $N = 2$. With each of the following iteration the window extends by 1 pixel up to some predefined maximum value N_{max}. Meanwhile, at each stage centroid image accumulates data about location of mass centers of image objects. The further threshold processing with threshold:

$$p = N_{max} - 1, \qquad (2)$$

allows to detect SE and GI. Figure 1a shows cross-section with two SE and its centroid image before threshold processing ($N_{max} = 10$). The centroid image function values are enlarged

tenfold for the ease of display. The threshold post-processing of the centroid image with threshold:

$$p = N_{\max} - 1 = 9,$$

reserves two discreet centroid impulses with coordinates corresponding to mass centers of structure elements.
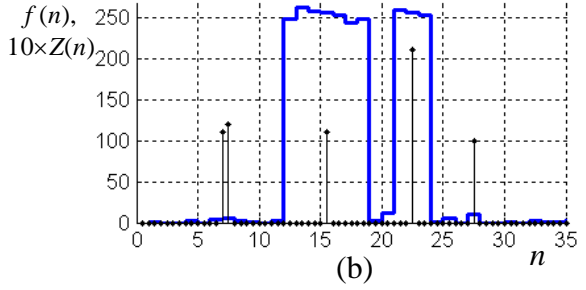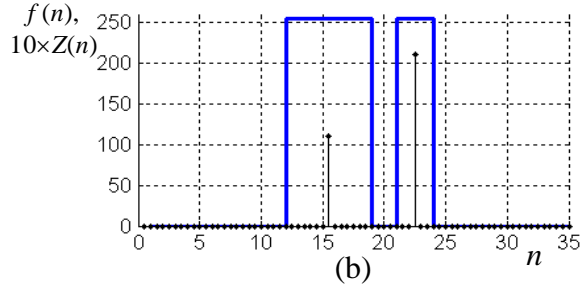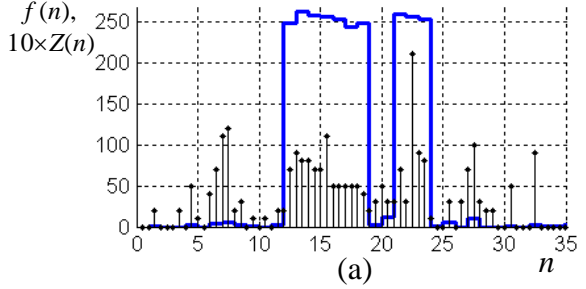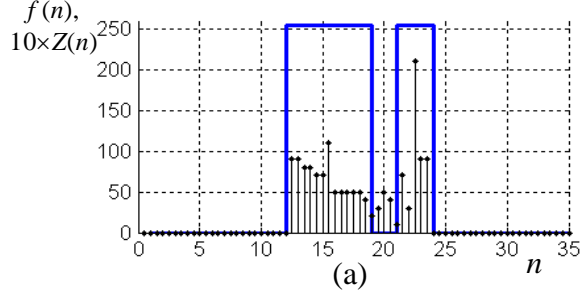
Figure 1. SE cross-section and its centroid image: without threshold processing (a); after threshold processing (b)

Figure 2. Noisy SE cross-section and its centroid image: without threshold processing (a); after threshold processing (b)

According to the work [6], noise occurrence on the GI corrupts substantially SCP. Figure 2 shows the result of multiscale centroid filtration of GI cross-section corrupted by additive gaussian noise with σ = 5. False centroid impulses conditioned by noise are shown in Figure 2b. However, basic centroid impulses correspond to mass centres of structure elements.

The data analysis in Figure 2b enables to draw conclusions as follows:

1. Coordinates of basic centroid impulses are robust to GI noise distortion.

2. Noise on GI results in multiple false centroid impulses on background GI spots and hinders gating out basic centroid impulses.

SUPPRESSING FALSE CENTROID IMPULSES

One of the disadvantages of the execution algorithm of multiscale centroid filtration described above is accumulating information with equal weighing about SE mass centers and information about GI element mass centers conditioned by noise. In other words, the expression (1) considers only image element location regardless of the element nature occurred in cross-section.

The paper in question proposes a new algorithm of centroid filtration in case of accumulating information with the usage of mass accumulation instead of expression (1):

$$Z[n + C(n)] = Z[n + C(n)] + M(n). \tag{3}$$

Expression (3) considers SE masses center as well as their mass. In this case it makes sense to point to mass-centroid image of SE cross-section.

Figure 3 shows noisy SE cross-section and its mass-centroid image before threshold processing and after threshold processing.
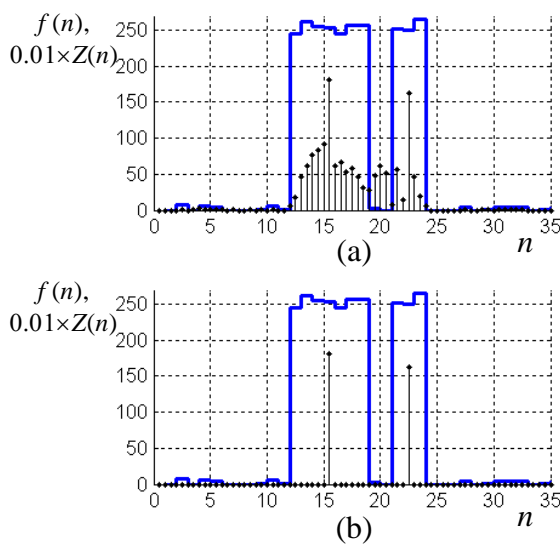
Figure 3. Noisy SE cross-section and its mass-centroid image: without threshold processing (a); after threshold processing (b)
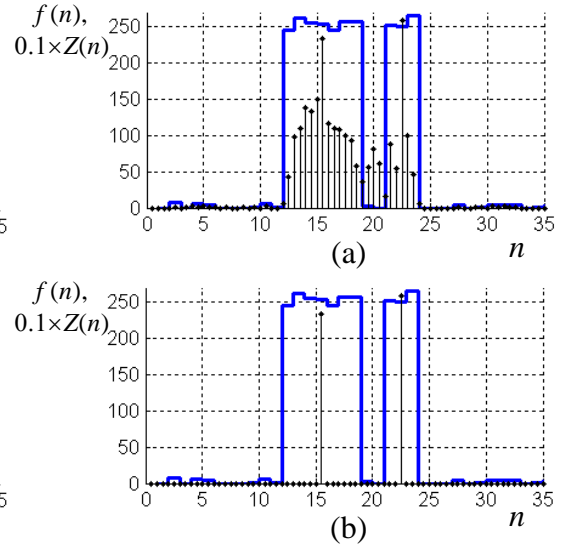
Figure 4. Noisy SE cross-section and its weighed mass-centroid image: without threshold processing (a); after threshold processing (b)

The mass-centroid image values are diminished hundredfold for the ease of display. It is evident that accumulating centroid information by mass value increases noise resistance of centroid filtration and it allowed to accurately define SE mass centers in Figure 3b.

The major disadvantage of mass centroid filtration is relation of mass centroid image values to maximum analysis window dimension N_{max}, which makes it difficult to choose objective threshold value in case of mass-centroid image post-processing.

Accumulating centroid information with the usage of weighed mass values enables to diminish the given relation:

$$Z[n+C(n)] = Z[n+C(n)] + \frac{M(n)}{N}, \qquad (4)$$

where N is dimension of analysis window on the current iteration.

Figure 4 shows icross-section of noisy SE and its weighed mass-centroid image before and after threshold processing.

Figure 4b shows, that weighed mass-cenroid image also increases noise resistance of centroid filtration. In addition, it simplifies a choice of post-processing threshold of weighed mass-cenroid image.

RESULTS

To analyse reliabity of various techniques of centroid filtration in dependence on noise degree of GI processed an experiment was carried out. Additive Gaussian noise with standard deviation range from 0.01 to 150 was added to a 1000 pixel long cross section. Centroid images were calculated for every noise level added in accordance with expressions (1), (3) and (4). After threshold post processing of centroid images false centroid impulses was calculated. Every experiment was repeated two hundred times. The experiment findings are summarized in Table 1.

I. Arkhipov, A. Murynov,
"Multiscale centroid filtration of noisy graphics image"

Table 1. Reliability of various techniques of noise centroid filtering

Root-mean-square error of additive noise, σ	The amount of false centroid impulses per 1000 pixels of cross section		
	Multiscale centroid filtration	Multiscale mass-centroid filtration	Multiscale weighed mass-centroid filtration
0.00	0	0.000	0.00
0.01	248	0.000	0.00
5.00	249	0.000	0.00
10.00	248	0.000	0.00
15.00	245	0.005	0.00
20.00	250	0.010	0.01
30.00	250	0.100	0.06
40.00	248	0.290	0.19
50.00	248	0.470	0.35
60.00	248	0.590	0.44
80.00	249	1.500	1.20
100.00	249	3.100	2.80
120.00	250	7.100	6.50
150.00	250	16.900	16.60

Table 1 shows, that the initial technique of accumulating centroid information sees any amount of small value of noise, which results in abrupt amount decrease of false impulses up to the maximam value. For its turn, mass-centroid and weighed mass-centroid filtration techniques are irresponsive to noises with standard deviations right up to the value $\sigma = 10$.

If we admit potential occurrence of false centroid impulses with frequency not exceeding one time per 1000 pixels of GI cross-section, permissible noise level may be increased up to the value $\sigma = 60$.

CONCLUSION

Based on the experiments carried out we can make conclusions as follows:

1. Multiscale centroid filtration in initial performance has low reliability in processing GI even with slight noise.

2. Multiscale mass-centroid and multiscale weighed mass-centroid filtration techniques are irresponsive to noises with standard deviations right up to the value $\sigma=10$ and weakly responsive to noises up to the value $\sigma = 60$.

3. Multiscale mass-centroid and multiscale weighed mass-centroid filtration techniques have equal antinoise proofness.

4. Multiscale weighed mass-centroid filtration sets less requirements to the choice of threshold value at post-processing stage of cross-section centroid image.

REFERENCES

1. L.N. Levickaya, "Modeling and analysis of the spatial structure of the graphic images on the basis of discrete-planimetric model hyperraster," Ph.D. Diss., Izhevsk, 2006.

2. A.I. Murynov, "Mathematical models and methods of analysis of spatial structures for expert intelligence systems," Doctoral Diss., Izhevsk, 2002.

3. I.O. Arkhipov, "Modeling and analysis of linear low-sized structural elements of graphics images on the basis of usage of spatially chromatic parameters," Bulletin of Izhevsk State Technical University, No. 2 (62), pp. 149–152, 2014.

4. I.O. Arkhipov, "Increase of evaluation accuracy of spatially chromatic parameters of low-sized structural elements of graphic image," Volga Scientific Bulletin, No. №7 (35), pp. 18–21, 2014.

5. I.O. Arkhipov, "Graphics image blurring analysis for evaluating spatially chromatic parameters," Volga Scientific Bulletin, No. 7(35), pp. 14–17, 2014.

6. I.O. Arkhipov and R.T. Akkuzin, "Measurement of the sizes of the structural elements of the noisy graphics image on the basis of its spatial chromatic model," Bulletin of Izhevsk State Technical University, No. 2 (66), pp. 100–102, 2015.

Influence of the Operating Damage on the Acoustic Parameters in the Railhead

A.V. Baiteryakov [1], V.V. Muraviev [2], R.S. Kazakov [3], A.I. Dedov [4]

Instrumentation engineering faculty, Kalashnikov Izhevsk State Technical University, Russia
**E-mail: [1] email1990@yandex.ru, [2] vmuraviev@mail.ru,
[3] kazakovromanvip@mail.ru, [4] superdedov@mail.ru**

Abstract. The experimental study on changes in the structural noise level and on propagation velocity of surface waves in rail samples before and after operation is performed. The study describes the effect of accumulated damage in the railhead on the measured acoustic parameters.

Keywords: acoustic structurescopy, accumulated damage, rails

INTRODUCTION

In the process of rails operation on the railhead surface plastic deformation occurs as a result of multiple impact of a train load.

Consequently, it leads to the accumulation of microdefects which form serious large defects and ultimately lead to disasters.

To prevent the possible destruction of the rail, it is necessary to perform immediate non-destructive control of the structure in overlay of the tread surface.

Sensitive to the structural state changes acoustic methods are based on measurement of the structural noises level and the velocity of the Rayleigh surface waves. In this case the correlation between the ultrasonic wavelength and metal grain size is important. Properly chosen ultrasound frequency is sensitive to even small structural changes in metal.

The work is devoted to the effect of accumulated operating damage in the railhead surface on the measured acoustic structural noises and the propagation velocity of surface waves.

MEASUREMENT PROCEDURE OF STRUCTURAL NOISES

To assess diversity in structural state it was accomplished estimation experiment of the structural noise level for two rails: after operation 40 million gross tons (the old rail was fabricated in 1996 year) and without operation (the new rail was fabricated in 2013 year). The measurements were carried out on prepared tread surface of the headrail samples with a length of 300 mm.

The measurements were carried out by angle beam double-crystal transducer P122-5,0-65-8-M with a step of 5 mm from the edge of the rail slice.
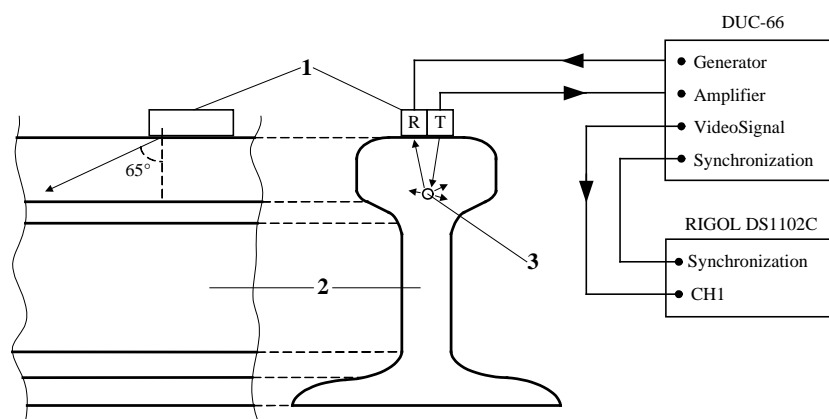
Figure 1. The schematic arrangement of measurement system: 1 – transducer, 2 – rail, 3 – grain structure

The ultrasonic defectoscope DUC-66 was used for excitation and reception of ultrasonic waves in the testing object. The digital oscilloscope RIGOL was connected to the output «Video Signal» of defectoscope by synchronization line for saving and the further processing of the electrical signal.

During installation of the transducer on the rail surface the oscilloscope digital screen displays the oscillogram (Fig. 2).
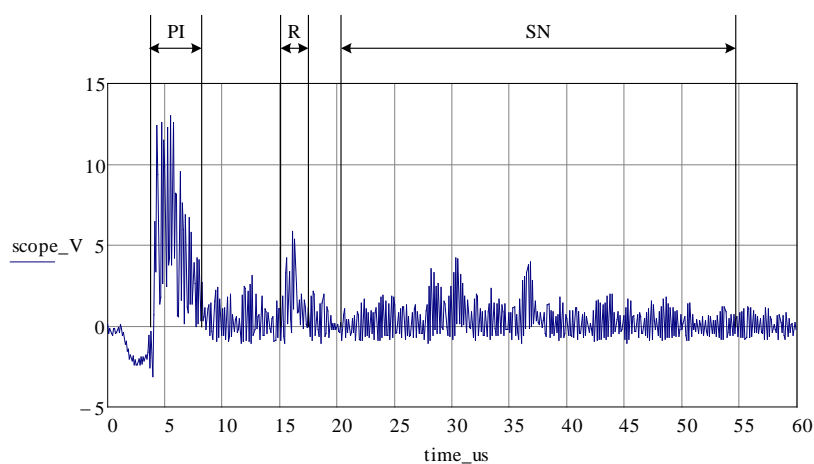
Figure 2. Oscillogram of the acoustic signal

As shown in Fig. 2, the waveform is divided into 3 areas:
- the first area corresponds to the probe pulse (PI);
- the second area corresponding to Rayleigh wave (R) appears in the double-crystal
- transducer protector [1];
- the third area corresponds to the zone of structural noise (SN).

The selected time period from 20 to 55 microseconds for the structural noise evaluating corresponds to the time of wave transmission from the headrail surface to the railhead bottom and back. Time domains contain interfering multipath ultrasonic waves from the fillet transition to the rail web.

To improve the accuracy of the dimension three measurements were taken from each of the 13 points on the rail. After that it was determined the average level of structural noise U_{SN} [1] and the Rayleigh wave level U_R for each dimension in the MathCAD program environment.

For the detuning from the quality of acoustic contact between ultrasonic transducer and rail surface it was calculated the ratio structural noise –Rayleigh wave U_{SN}/U_R.
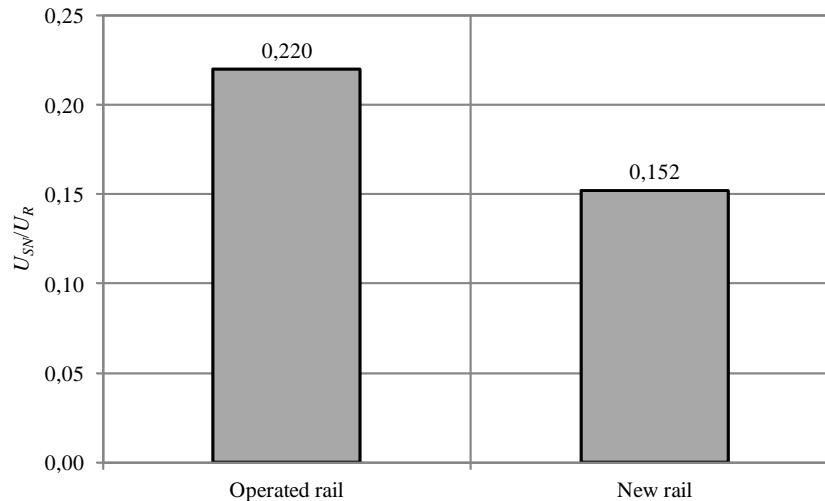
Figure 3. The level of structural noise in the old and new rails

Fig. 3 shows a chart demonstrating the difference in average levels of structural noise in the old and new rails. The data presented in Fig. 3 shows that the level of structural noise in the old rail exceeds the level of structural noise in the new rail by more than 40 %.

MEASUREMENT PROCEDURE OF THE SURFACE WAVES SPEED

Experimental assessment of the Rayleigh surface waves velocity in rail samples was performed by using electromagnetic acoustic structurescopy (SEA) and electromagnetic-acoustic (EA) transducer of surface waves at the frequency of 1.25 MHz.

EA transducer was mounted on surface in the middle part of the railhead. In this instance surface wave propagated along the rolled rail. Five measurements were taken on each rail. Fig. 4 shows the program window "the PRINCE VIII" displays the progress difference of surface waves in two rails.
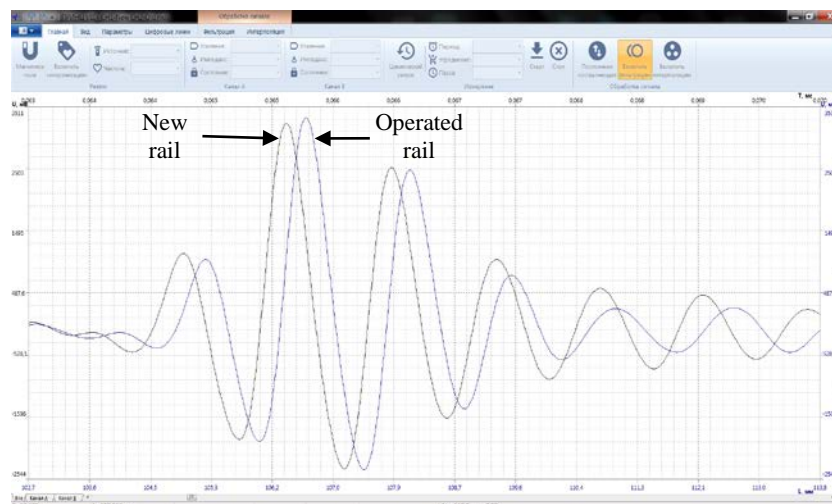
Figure 4. The program window "the PRINCE VIII"

The time difference of rays between two received signals of surface waves is $\Delta t_r = 168$ ns. This value approximately corresponds to the difference of the velocities of surface waves between the new and operated rail, which is 10.8 m/s. This fact can be

explained by damage accumulation and work hardening [2–4]. The reduction of Rayleigh wave propagation speed on the rail wheel thread after operation is 0.3 %.

CONCLUSION

The analysis of experimental results shows the difference in the structural noise levels for the operated and new rails. This effect is due to the accumulated structural damage as a result of long exploitation.

Rayleigh waves, which are sensitive to the surface defects, confirm the presence of work hardening and the accumulated defects in the railhead surface after long time operating.

REFERENCES

1.   V.V. Muravyev, O.V. Muravyeva, A.V. Bayteryakov and A.I. Dedov, "Method for determination of acoustic structural noise of metal," Intelligent systems in production, No. 1, pp. 143–149, 2013.

2.   V.V. Murav'ev, "Interrelationship of the velocity of an ultrasonic wave in steels and their heat treat cycles," Russian Journal of Nondestructive Testing, vol. 25, No. 2, pp. 135–137, 1989.

3.   V.V. Muraviev, L.B. Zuev, K.L. Komarov, V.B. Kharitonov and V.N. Chaplygin, "Evaluation of fatigue damage accumulation process by acoustic method," Journal of Machinery Manufacture and Reliability, No. 4, pp. 103–107, 1994.

4.   A.N. Smirnov, V.V. Muraviev, S.V. Folmer, "Structurally Phase State and Resource of Long-term Working Metal of Technical Devices of Dangerous Industrial Objects," Testing. Diagnostics, No. 1, pp. 22–32, 2009.

Visualization and Image Processing Techniques in the Evaluation of Ultrasonic Equipment Radiation Intensity

O.P. Bogdan [1], O.V. Muravieva [1], Yu.S. Dudina [1],
S.I. Maslennikov [2], V.N. Milich [2]

[1] "Measurements, Control, Diagnostics Instruments and Techniques" Department,
Kalashnikov Izhevsk State Technical University, Izhevsk, Russia
E-mail: pmkk@istu.ru
[2] Department of Research and Diagnostics of Spatial Structures,
Physical Technical Institute UB RAS, Izhevsk, Russia
E-mail: sergeymasle@gmail.com

Abstract. A method for evaluating the intensity of ultrasonic medical equipment radiation is presented in the paper. The capabilities of image processing of equilibrium gas bubbles under influence of acoustic field in fluid are described to determine the bubble radius and subsequently evaluate the ultrasonic radiation intensity.

Keywords: Bubble, ultrasound radiation intensity, image processing, ImageJ, iPython Notebook

INTRODUCTION

The use of ultrasonic (US) radiation in various fields of medicine (diagnostics, therapy, surgery, cosmetology) is largely determined by its intensity. Maximum permissible levels of US radiation intensity for each application are strictly regulated by international and Russian standards in order to avoid the negative effects of US treatment (thermal and mechanical effects). For example, according to the FDA [1] in US diagnostics the intensity $I < 720$ mW/cm^2, in US therapy (IEC 601-2-5-84) – $I < 1.2$ W/cm^2. Therefore, used in medical applications US equipment requires periodic calibration of its basic parameters, in particular, the radiation intensity.

Among different methods of measuring the US radiation intensity (calorimetric, interferometric, method of reciprocity [2]), the most common and available method is the measurement of radiation pressure. However, its existing implementations are generally applicable only for continuous radiation and do not allow to evaluate the intensity distribution in space.

The authors proposed a method for estimating the US radiation intensity and its spatial distribution and visualization of acoustic field and its orientation, based on the method of gravitational balancing the force of US waves radiation pressure and the buoyant force, acting on a gas bubble of a certain size [3]. Analyzing the equilibrium size of bubbles in a fluid in the US field makes it possible to evaluate the intensity and visualize its distribution at any point in space.

An air bubble in the fluid (water) can be represented in form of a compressible sphere, whose density ρ is much smaller than the density ρ_0 of the fluid: $\rho \ll \rho_0$. According to proposed physical model of US radiation interaction with air bubbles in a fluid [4], the bubbles are under influence of radiation pressure force, buoyant force, radiation pressure force of scattered wave. Furthermore, a gas bubble in a fluid, while in the US field, performs radial oscillations, acting as a secondary source and interacting with particles around it, including other bubbles. These oscillations in US field cause non-uniform motion of the fluid near bubbles, leading to the bubbles attraction in perpendicular to US waves propagation direction and the bubbles repulsion along the US field [5]. As a result of attraction force acting between bubbles, the bubbles approach each other deviating from their spherical shape.

Interaction effects stated lead to unstable behavior of bubbles in US field and appearance of artifacts in obtained images, which requires the development of new approaches to obtained images analysis and improvement of precision in inhomogeneities size evaluations.

EXPERIMENTAL SETUP FOR ULTRASONIC RADIATION INTENSITY EVALUATION
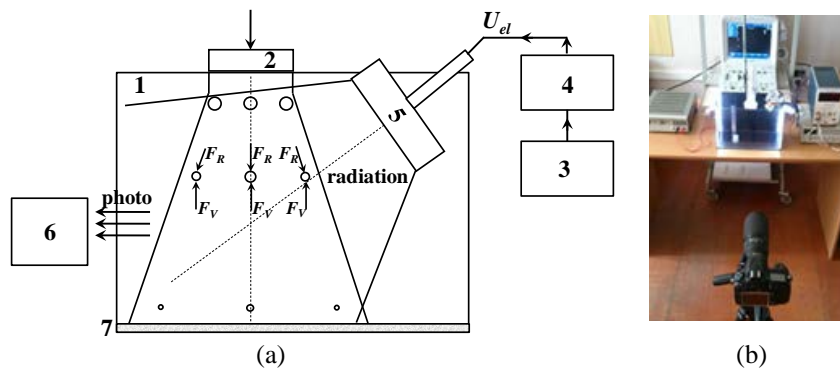
Figure 1. Block-scheme (a) and photo (b) of US transducer parameters evaluation setup:
1 – container with a fluid; 2 – investigated US transducer; 3 – sinusoidal signals generator;
4 – adjustable amplifier; 5 – bubbles generator; 6 – photography device; 7 – absorber

Scheme and photo of the experimental setup for the US radiation intensity evaluation and its distribution in space is presented in Fig. 1. Near the surface of container 1 with a transparent wall there are the investigated US emitting transducer 2, radiating into the fluid the wave normal to the surface, and a specialized low-frequency US transducer 5 that emits the US wave at an angle to the surface, acting as a gas bubbles generator. Formation of bubbles occurs by supplying the low frequency transducer from the sinusoidal signals generator 3 through an adjustable amplifier 4 with electrical voltage corresponding to the threshold level of stable cavitation [3]. The investigated US emitting transducer 2 at the operating frequency forms in the fluid an acoustic field with radiation intensity I, at the same time the superposition of bubbles generator and investigated emitting transducer fields is visualized. After shutting-down the bubbles generator, some bubbles of larger size float to the surface due to excess of the buoyant force over the radiation pressure force. Part of smaller sized bubbles moves in the opposite direction due to the excess of radiation pressure force over the buoyant force, gathering near the bottom surface. Bubbles with dimensions corresponding to the equilibrium condition (equality of buoyant and radiation pressure forces) are distributed in space according to intensity values in the transducer acoustic field. Distribution pattern formed of equilibrium state bubbles is recorded by the photography device 6. The registered photographic image is processed using a specialized software, allowing the bubble radius r measurement at any point of interest in the plane of photographic

image [3]. Evaluation of US radiation intensity is produced in accordance with the developed physical model of US radiation interaction with air bubbles in the fluid.
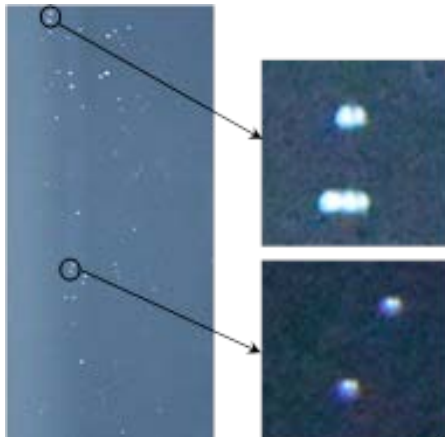
Figure 2. An example of equilibrium gas bubbles distribution recorded

To improve the quality of the resulting image and its resolution to increase the equilibrium gas bubbles size estimates precision, minimize error and improve the reliability of US radiation intensity evaluation, the conditions of the visualization and registration process are optimized.

It is recommended to use a full-frame photographic camera like Nikon D800 Body with resolution of not less than 36 megapixels, CMOS image sensor size 35.9x24.0 mm and a macro lens like 200mm f/4D ED-IF AF Micro-Nikkor with the following settings: manual lens focus, the minimum exposure (1/4000 s or faster), maximum ISO sensitivity ("Hi 1" mode) with noise suppression and automatic distortion control, manual white balance settings or white balance in direct sunlight mode. Higher stability and uniformity of generated bubbles size and reduced influence of artifacts on the image is also achieved through the use of 1.2 % glycerin solution in distilled water at a temperature of 30 °C ÷ 40 °C as the fluid to form bubbles. Fig. 2 illustrates the received equilibrium gas bubbles spatial distribution image and the enlarged view of individual bubbles.

IMAGE PROCESSING METHODS

The recorded images are subject to significant influence of artifacts caused by oscillating bubbles, deviations from the spherical shape during the approach of two bubbles, as well as distortions caused by photographing through a glass. Artifacts distort the initial information on the geometrical dimensions of the bubbles. The image processing software methods developed include localization and identification of bubbles, coupled bubbles detection, bubble boundaries delineation and size estimation, building the dependencies of the bubble size on observation point parameters. For detuning from artifacts, extracting the information about size of bubbles and subsequent analysis, the possibilities of various image processing methods are investigated.

Today, the use of computer technology for scientific data analysis is an accepted fact [6]. There are various software tools containing a lot of ready-made algorithms and methods for image processing. The open source software ImageJ [7] possesses significant set of ready-made algorithms as well as the ability to extend the functionality by implementing the necessary methods using embedded macro language or subroutines (plug-ins) written in Java. A grayscale image example of bubbles (a) and values of pixels intensity in three-dimensional space (b) in the ImageJ software are presented in Fig. 3.

For the tasks of bubbles localization in the image and their radius calculation the following algorithm is applied. The grayscale image is considered as a two-dimensional matrix of pixels, the values of which characterizes the color intensity of the corresponding picture element. The bubbles localization task is the identification of a pixel belonging to image background or bubble. The identification difficulty lies in the variability of background intensity values (Fig. 4, a). The exception of variability is achieved by applying a local threshold filter on the image areas of a size corresponding to the size of bubble. The result of this filter applying are selected areas of bubbles.

(a)   (b)
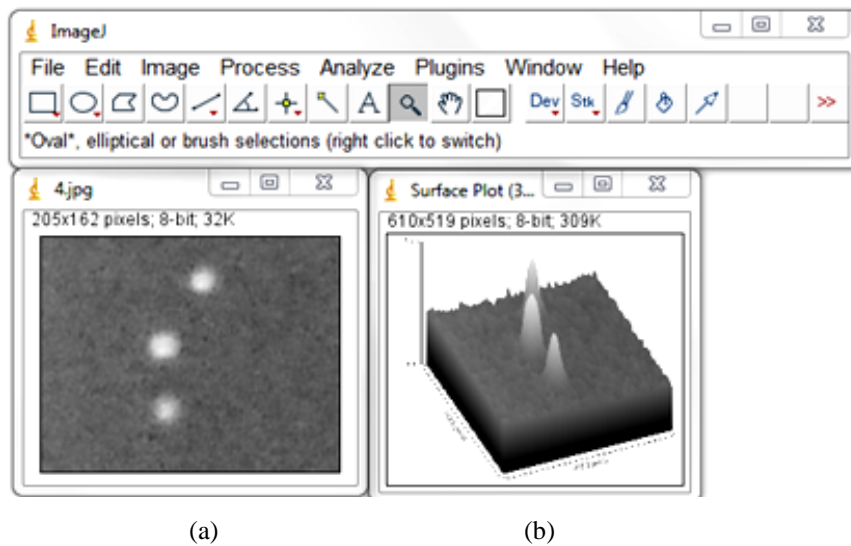
Figure 3. Image of bubbles in grayscale (a) and pixel intensity values in three-dimensional space (b) in open source software ImageJ

To determine the coupled bubbles radius (Fig. 4, b) the following algorithms can be used:

– approximation of the selected bubble using an ellipse and calculation of its equivalent radius, considering the equality of the ellipse area and the circle area (Fig. 5, a);

– calculation of the radius as the arithmetic mean of ellipse semi-axes a and b (Fig. 5, b);

– calculation of the radius as half of the bubble maximum size on the X axis.

The effectiveness of algorithms mentioned was evaluated on the basis of the standard deviation of measured radii from the calculated ones according to known data about the US radiation intensity and bubble sizes according to the physical model of US waves interaction with bubbles.

(a)   (b)
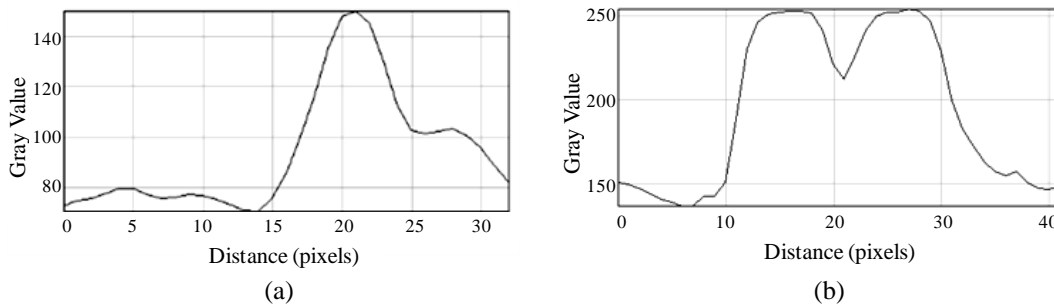
Figure 4. Graphs of intensity values of pixels with non-uniform background (a) and with the effect of coupled bubbles (b)

When processing the experimental images obtained with variable shooting conditions the ImageJ program showed the less practical efficiency in comparison to other image processing tools. Less efficiency lies in the fact that any changes in algorithm lead to necessity of making changes in subroutine (plug-in) code and subsequent compilation, which significantly increases processing time.

In such conditions, greater effectiveness has been shown by iPython Notebook software (Fig. 6, a), which is an interactive shell for the Python language [8]. Interactivity allows to observe the result of algorithm changes without recompiling the program.

Unlike localization by identifying the pixels belonging to background or bubble using a threshold filter, another localization method is based on determining the local maxima of

(a)   (b)
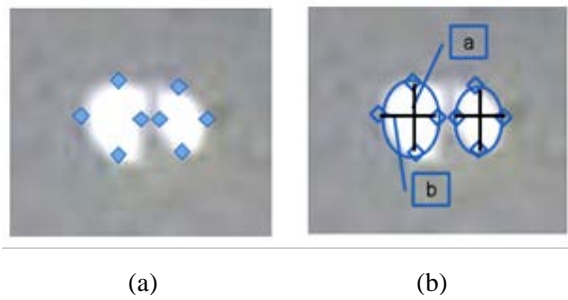
Figure 5. Bubble radius calculation technique

bubbles intensity values. The algorithm in iPython Notebook with new approach application includes the following steps:

1. Read the image (Fig. 6, a).

2. Selection of local area and conversion the color model of image to grayscale (Fig. 6, b). One of the most common problems in image processing is the presence of noise, which is mostly a variation of intensity and inhomogeneity of the background. To exclude noise and inhomogeneity the median and threshold filters are applied. The median filter eliminates the noise, the threshold filter divides image pixels in belonging to background or bubble by intensity. These filters are applied using the "sliding window", which size corresponds to desired bubble average size.

3. Determining the local maxima using the "sliding window" technique (Fig. 7, a).

4. Calculation of bubble radii using the approximation of bubble shape as an ellipse, considering the equality of ellipse and circle areas, and forming the result tables by depth (Fig. 7, b).

The image processing result obtained with use of the algorithm specified above is presented in Fig. 8.

The deviations of the bubbles radii from the mean values at a given depth are $6 \div 12 \, \mu m$ ($8 \div 15 \, \%$).

At the same time, with the increase in distance there is a decreasing in radii and their evaluation accuracy.

The bubbles image processing results are the equilibrium bubbles radius values in point of interest. Knowing the latter, it is possible to determine the US radiation intensity in accordance with the expression:

$$I = \frac{\rho_0 C_0 g \left((kr)^6 + \left[\frac{3\mu^2}{\delta} - (kr)^2 \right]^2 \right)}{3k^4 r^3}, \tag{1}$$

(a)   (b)
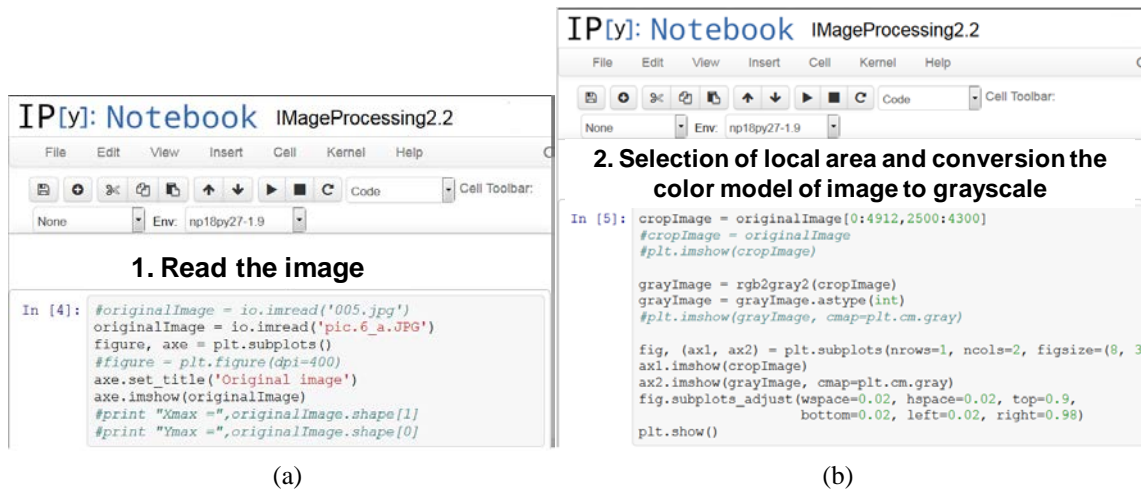
Figure 6. An example of image processing in iPython Notebook software: step 1: read the image (a); step 2: the selection of area to process and grayscale conversion (b)

(a)   (b)
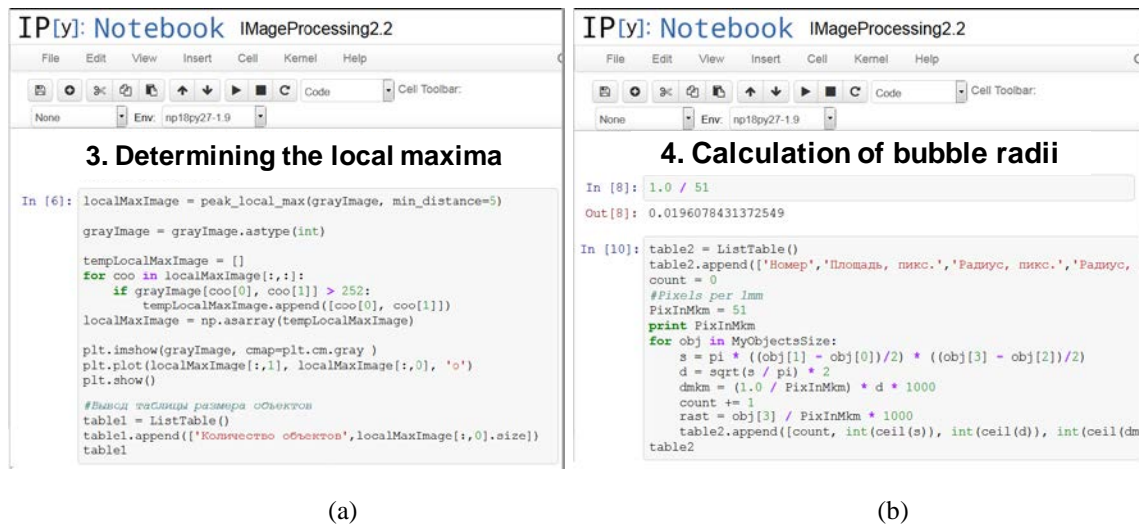
Figure 7. An example of image processing in iPython Notebook software:
step 3: determining the local maxima (a); step 4: calculation the results (b)

(a)   (b)   (c)
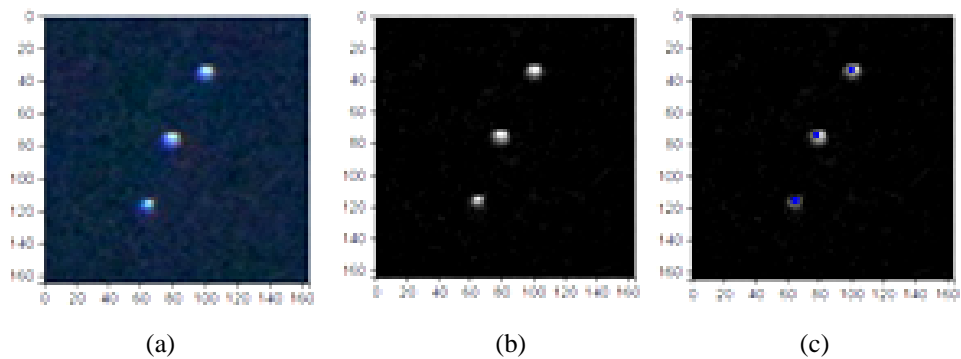
Figure 8. Original image (a), grayscale image (b), image with localized bubbles (c)
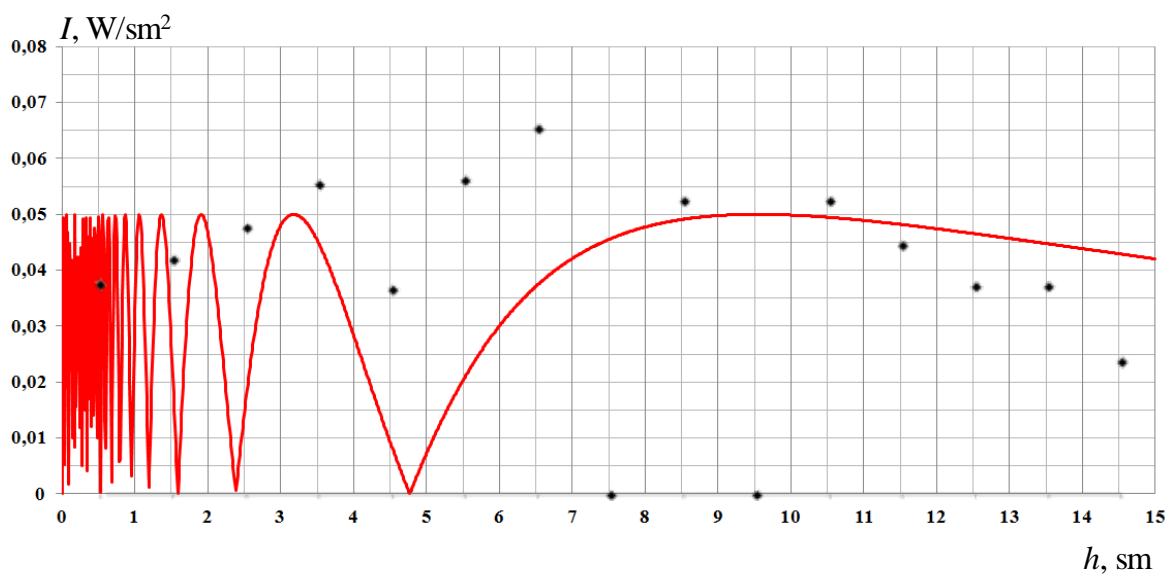
Figure 9. The result of US therapeutic apparatus UST 1.01F intensity evaluation

where r is the radius of a gas bubble in a state of equilibrium; $\delta = \rho_0/\rho$, ρ_0 is the water density, ρ is the bubble density; k is the wave number; $\mu = C/C_0$, C is the sound velocity in a bubble; C_0 is the sound velocity in water.

The developed method, device and software are tested to evaluate the intensity of US therapeutic apparatus UST 1.01F ($f = 880$ kHz) at $I = 0.05$ W/cm^2. The intensity evaluation result is shown in Fig. 9, where each point represents the result of experimental evaluation of US radiation intensity, solid line is a theoretical curve of the intensity distribution in depth. The deviation of experimental results from theoretical ones does not exceed 30 %, which corresponds to intensity tolerances according to the device passport data.

Thus, the paper proposes new approaches to image analysis of equilibrium gas bubbles in a fluid under influence of an acoustic field, and used for evaluation the ultrasonic radiation intensity of medical equipment. The algorithms developed allow to significantly reduce the effect of artifacts caused by unstable behavior of bubbles, geometry deviations, photography distortion, and to improve the bubble geometrical sizes evaluation accuracy. The correctness of image processing results is confirmed by the agreement of theoretical and experimental results of ultrasonic therapeutic equipment radiation intensity evaluation.

REFERENCES

1. L.V. Osipov, Ultrasonic diagnostic instruments: operation, methods and technologies, Moscow: IzoMed, 2011.

2. C.R. Hill, J.C. Bamber, and G.R. ter Haar, Physical Principles of Medical Ultrasonics, John Wiley & Sons, 2004.

3. O.V. Muravieva, O.P. Bogdan, V.N. Milich and S.I. Maslennikov, Russia Patent No. 140996 (27 May 2014).

4. O.V. Korobeynikova, E.P. Kuznetsov and O.P. Bogdan, "The study of Doppler ultrasound artifact "pseudoflow" physical mechanisms," Medical physics, No. 3 (43), pp. 64–70, 2009.

5. A.P. Sarvazyan, O.V. Rudenko and W.L. Nyborg, "Biomedical applications of radiation force of ultrasound: Historical roots and physical basis (Invited Review)," Ultrasound in Medicine and Biol, vol. 36, No. 9, pp. 1379–1394, 2010.

6. R.C. Gonzalez and R.E.Woods, "Digital Image Processing" in. 3rd Ed.: in Rus. Transl., Moscow: Tekhnosfera, p. 1104, 2012.

7. W. Bailer, Writing Image J Plugin, Austria: University of Applied Sciences, 2006.

8. C. Rossant, Learning IPython for Interactive Computing and Data Visualization, Packt Publishing, 2013.

Research and Development of the Encryption Algorithm in Specific Area of Digital Image with Viola and Jones Face Detection Algorithm

R. Bustami [1], I. Klimov [2]

Izhevsk State Technical University, Izhevsk, Russia
E-mail: [1] ridho.bustami@gmail.com, [2] klimov@istu.ru

Abstract. Protecting our information data from third party such as data confidentiality is one aim of cryptography system. Therefore in this paper showed the technique of encryption algorithm for digital image, which encrypted specific area such as face. Simulation describes the technique of detecting, cropping, rearranging, encrypting and decrypting on detected face in image with Viola and Jones algorithm. Using two symmetric block cryptography algorithm: Data Encryption Standard and GOST 28147-89, and also image encryption based on chaotic system. Then simulation is showed in graphic user interface in Matlab.

Keywords: cryptography system, digital image, Viola and Jones algorithm, symmetric block, Data Encryption Standard, GOST 28147-89, chaotic system

INTRODUCTION

Taking photos with mobile phone and storing in the cloud system are nowadays become a common trends. Cloud system is a common used because of increasing on Internet speed and operation system mobile phone like android or I-phone. In the future, data don't need to be saved in personal drive, data automatically will be saved or processed in the cloud system.

Selfie is becoming popular trend that people take their selves photos with own mobile phone. Beside of that, the mobile phone camera also is being developed, especially for increasing pixel to make images better and sharper and also still has good quality if seen in the another media, like personal computer even for printing.

Recently famous actress have got a problem with their selfie photos, when they think I-cloud which created by Apple.inc has secure system, they saved their photos in the I-cloud which connect automatically with their mobile phone. And after third party cracked the apple system, and shared famous actress photos which contains some personal privacy. After the photos leaked, they could do nothing with that, just some kind law of punishment they could do that, but they couldn't bring back their photos.

Actually, if our mobile phone get lost or stolen, if not prepared about that happen, our data can't be secured. Indeed, mobile phone has password protecting, but it's not enough because unresponsive people still can access our data via memory card. It can't be ignored, and also have to be awarded with our data.

METHOD OF CRYPTOGRAPHY

So here introduces a method protecting our digital photo especially taken by selfie. Based on oxford dictionary selfie means "A photograph that one has taken of oneself, typically one taken with a smartphone or webcam and shared via social media". But actually sometimes photos not to be shared via social media because some reason of privacy that users don't want to share to public.

A method that presented is encrypting only in important part of image. In selfie photos, usually the important area or part is at face or faces. In each face will be detected automatically and directly encrypted. Based on this idea, the time processing for encrypting and decrypting image will be reduced and also make privacy in image better.

One of the method for face detection is Viola-Jones algorithm. The Viola–Jones object detection framework is the first object detection framework to provide competitive object detection rates in real-time proposed in 2001 by Paul Viola and Michael Jones [1]. Algorithm for encryption that used is Data Encryption Standard DES [2, 4], GOST 28147-89 [3–4], Logistic Map-One time pad.

EXPERIMENT OF ALGORITHMS

In experiment, divided into 4 general step, First step is detecting Face with Viola–Jones object detection algorithm. Before this step digital image has to convert to value of pixel. The input is digital image which has inside at least one face. Face will be detected by Viola and Jones algorithm. Coordinates of pixel (x, y) and also length of detected part will be saved in database.

Second step is preparing selected image to encryption block if uses DES & GOST. If DES or GOST is used, value of pixel need to convert to binary data with length 64 bit and also preparing key 64 bit for DES and 256 bit for GOST. If Logistic Map-One time pad is used, the value data don't to needed convert to bit because algorithm working in decimal values.
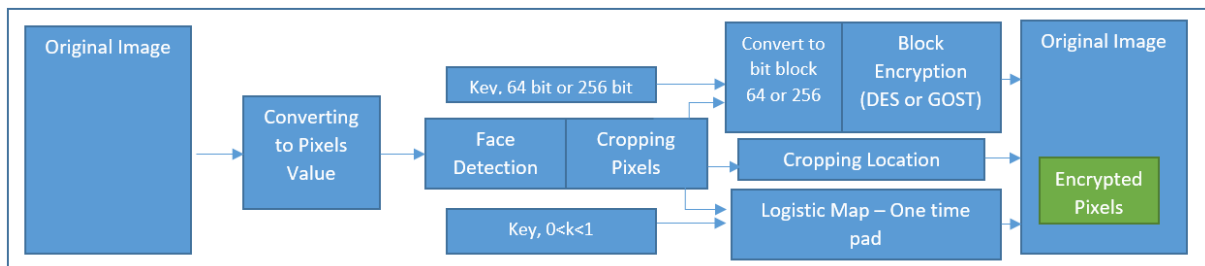
Figure 1. Schema encryption in specific area with face detection algorithm
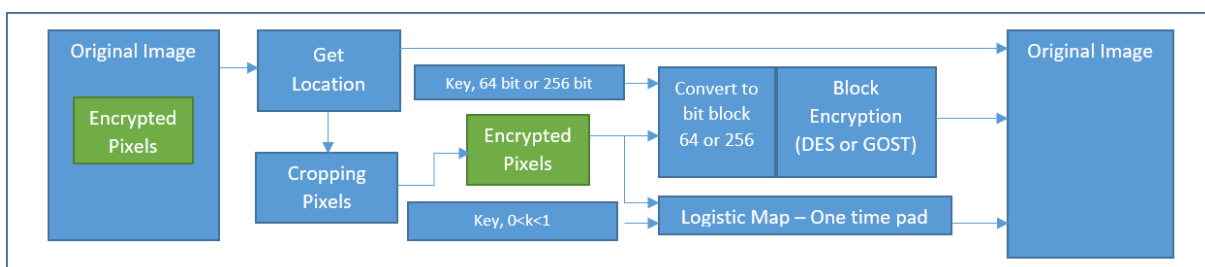
Figure 2. Schema decryption in specific area with face detection algorithm

Third Step is encryption and decryption process. Working with encryption and description is depended on cryptography algorithm that we used (DES, GOST or Logistic Map – One Time pad). In this step every algorithm works dependently each other.

Final Step is collecting from image and rearranging into image. In this step after encryption or decryption process, the pixel which already encrypted or decrypted need to be collected and rearranged into main image. Coordinates of pixel and length will be obtained from database.

SIMULATION

In this simulation, we use Matlab 2012 programming language for this design. Beside of that, created graphical user interface which make easier for people who use this simulation. At the first step just uploaded photos which one face or more is available. After that the program directly detect and encrypt. In decrypting process, actually beside the key for decrypting the system need to know information which place that already encrypted. Decrypted area will be replaced again like in encryption process.
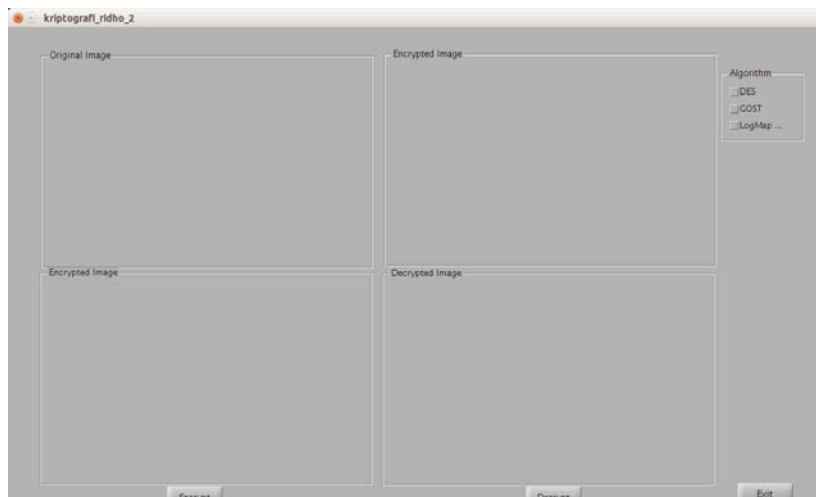
Figure 3. Main page of simulation on Matlab using graphics user interface
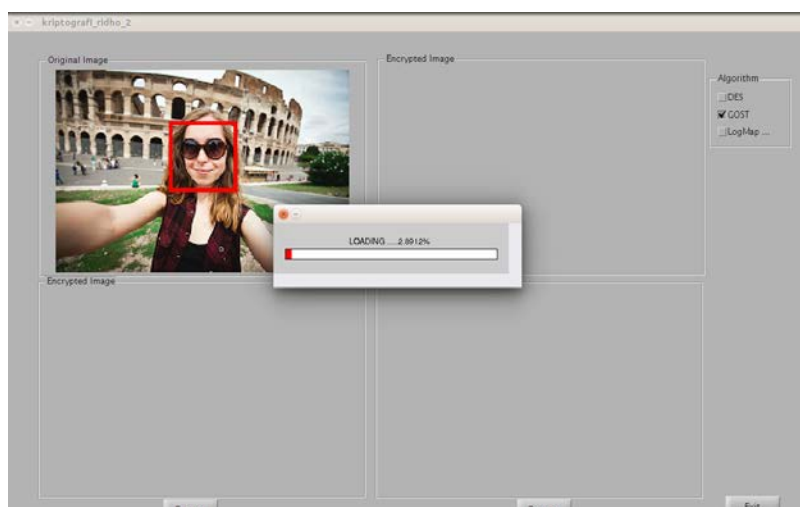
Figure 4. First step, detecting face with Viola and Jones algorithm and encrypting process
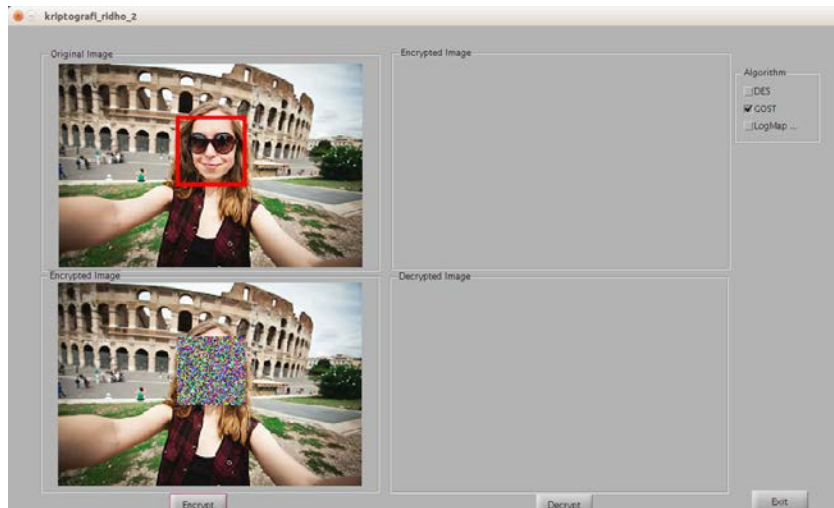
Figure 5. Rearranging pixel into original image and showed the result of encrypted image
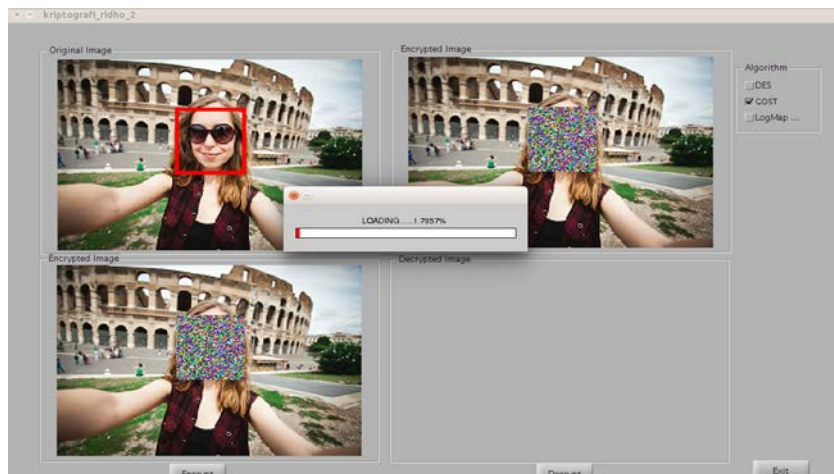
Figure 6. Uploading coordinates and encrypted image for input of decryption process.

Figure 7. Result of decrypting process and rearranging of pixels

Graphics user interface of simulation is run in Matlab 2012 with Linux operating system and hardware specification Intel Core i3-2356M 1.40 GHz, installed RAM 3.87GB. Image with format .bmp (33x73 Pixel, 24 bit depth) has been tested, encrypted and decrypted

successfully with algorithm DES, GOST and logistic map – one time pad, calculated average time processing of encryption which showed at table 1.

Table 1. Comparison time processing between DES, GOST and logistic map — one time pad.

Algorithm	DES	GOST	Logistic map – One time pad
Processing speed (Pixel/second)	4.8150	5.5313	85702
Encryption time processing (second)	124.7029	183.2866	0.098226
Decryption time processing (second) (33x73 Pixel, 24 bit depth)	244.5134	371.2706	0.0865

CONCLUSION

Finally this simulation showed Viola and Jones Algorithm was suitable and also is working for detecting face on selfie photo. In other way, face detection make shorter of step for encrypting face in digital image. This method can be used well on block cipher algorithm or in cryptography based on chaos. Both of them (GOST and DES) still have relatively worst time processing (half an hour) for encrypting digital image. For implementing on mobile phone is recommended using logistic map – one time pad because has relatively better in time processing.

REFERENCES

1. Viola, Paul and Michael J. Jones, "Rapid Object Detection using a Boosted Cascade of Simple Features," Proceedings of the 2001 IEEE Computer Society Conference on Computer Vision and Pattern Recognition, vol. 1, pp.511–518, 2001.

2. Federal Information Processing Standards Publication 46-3. Digital Encryption Standard (DES), U.S. Department of Commerence, National Institute of Standards and Technology, 1999.

3. GOST 28147–89. (1989). Cryptographic Protection for Data Processing Systems.

4. Bruce Schneier, Applied Cryptography, Second Edition, New York: Wiley, 1996.

Modeling of Short-Pulse Laser Radiation in Terms of Photon Wave Function in Coordinate Representation

A. Davydov [1], T. Zlydneva [2]

[1] Dept. of Applied and Theoretical Physics of Physical-Mathematical Faculty,
Nosov Magnitogorsk State Technical University, Magnitogorsk, Russia
E-mail: ap-dav@yandex.ru
[2] Dept. of Applied Mathematics and Informatics of Physical-Mathematical Faculty,
Nosov Magnitogorsk State Technical University, Magnitogorsk, Russia
E-mail: tapazl@yandex.ru

Abstract. On the base of the photon's wave function (wave packet) in Schrödinger coordinate representation developed in previous papers the modeling of the propagation in space and in time of a wave packet of the photon corresponding to a separate laser impulse of radiation of femtosecond diapason is carried out. The development is proceeded from single-particle approach with the usage of the basis eigenfunctions of energy, momentum and helicity operators in continuous momentum spectrum case. The wave packet is constructed in the form of superposition of these eigenfunctions as the integral over the all momentum space. In the case of Gaussian momentum distribution the character of an extension of a form of this wave packet is established. The essence of wave-particle duality of light and microparticles is specified. The hypothesis is formulated, however, that the photon is a quasi-particle corresponding to the propagation of spin wave in physical vacuum. It is claimed that this question is related to the structure of the leptons and other particles on the Planck distances.

INTRODUCTION

Since publication of work [1] it is considered (see also [2–8]) that the wave function of a photon cannot be constructed in configuration space although in momentum representation it is applied in many aspects. The reason of it consists in the zero mass of "rest" of a photon. Nevertheless, for a photon it is also possible to construct wave function ("a wave packet") if it is intended for the indication of density of probability not of localization of a photon, for example in the spirit of electron in atom, but of its detection in space. In modern experiments (transfer of optical signals on quantum communication channels, "quantum teleportation", "paradoxes" with single photons, etc.) there is a need for association of photons with the localized carriers of elementary units of information. Therefore creation of wave function of a photon in coordinate representation becomes again topical "at the new level of knowledge". Then, knowing the wave function, it is also possible with the quantum-mechanical point of view to come to an explanation of interference, diffraction and polarization of electromagnetic waves. Without doing the full review here, we will refer on [2–14] where anyway this subject is touched, the term "wave function of a photon" is used, but nevertheless wave function of a photon, normalized on unit probability, isn't given in coordinate representation. Apparently,

the first works in which the idea of a possible "localization" of a photon described by a probability density, defined by the normalized per unit of the wave function, have been proposed are [15–18]. Further development of the theory and justification of building of coordinate single-particle wave function of the photon was performed in [19–25] and others.

The purpose of this article is the modeling of the propagation in space and in time of a wave packet of the photon corresponding to a separate laser impulse of radiation of femtosecond diapason. This wave packet is the photon wave function in the coordinate representation.

PHOTON WAVE FUNCTION IN COORDINATE REPRESENTATION

We give here some details of the construction and interpretation of the photon wave function in coordinate representation accordantly to [22, 25].

The construction of the photon wave function in coordinate representation is based on the synthesis of classical electrodynamics and quantum mechanics taking into account the correspondence principle. Maxwell's equations in the Majorana form [26], for the vectors $\xi = \mathbf{E} + i\mathbf{H}$ and $\eta = \mathbf{E} - i\mathbf{H}$, made up of the electric $(\mathbf{E})$ and magnetic $(\mathbf{H})$ fields intensities (in Gaussian System), are taken as the initial:

$$i\hbar \frac{\partial \xi}{\partial t} = c(\hat{\mathbf{s}}\hat{\mathbf{p}})\xi, \quad i\hbar \frac{\partial \eta}{\partial t} = -c(\hat{\mathbf{s}}\hat{\mathbf{p}})\eta, \quad (\hat{\mathbf{p}}\xi) = 0, \quad (\hat{\mathbf{p}}\eta) = 0, \tag{1}$$

where $\hat{\mathbf{p}} = -i\hbar\hat{\nabla}$ is the operator of the momentum of the particle; c is the velocity of light in vacuum; $\hat{\mathbf{s}}$ is the operator of the photon spin in vector representation:

$$\hat{\mathbf{s}} = \mathbf{e}_x \hat{s}_x + \mathbf{e}_y \hat{s}_y + \mathbf{e}_z \hat{s}_z =$$
$$= \mathbf{e}_x \begin{pmatrix} 0 & 0 & 0 \\ 0 & 0 & -i \\ 0 & i & 0 \end{pmatrix} + \mathbf{e}_y \begin{pmatrix} 0 & 0 & i \\ 0 & 0 & 0 \\ -i & 0 & 0 \end{pmatrix} + \mathbf{e}_z \begin{pmatrix} 0 & -i & 0 \\ i & 0 & 0 \\ 0 & 0 & 0 \end{pmatrix} = i \begin{pmatrix} 0 & -\mathbf{e}_z & \mathbf{e}_y \\ \mathbf{e}_z & 0 & -\mathbf{e}_x \\ -\mathbf{e}_y & \mathbf{e}_x & 0 \end{pmatrix}. \tag{2}$$

The vectors ξ and η in a matrix form have an appearance:

$$\xi = \begin{pmatrix} E_x + i H_x \\ E_y + i H_y \\ E_z + i H_z \end{pmatrix}, \quad \eta = \begin{pmatrix} E_x - i H_x \\ E_y - i H_y \\ E_z - i H_z \end{pmatrix}, \tag{3}$$

and should be considered as independent [7]. For a bivector $\Phi_{bv} = \begin{pmatrix} \xi \\ \eta \end{pmatrix}$ it is necessary to solve the equation which is the generalization of Dirac equation for a massless particle with spin $s = 1$ in the "standard" or "bivector" representations. In the latter case it has the form:

$$i\hbar \frac{\partial \Phi_{bv}}{\partial t} = \hat{H}_{bv} \Phi_{bv} \quad \text{or} \quad i\hbar \frac{\partial}{\partial t} \begin{pmatrix} \xi \\ \eta \end{pmatrix} = \frac{c}{s} \begin{pmatrix} (\hat{\mathbf{s}}\hat{\mathbf{p}}) & 0 \\ 0 & -(\hat{\mathbf{s}}\hat{\mathbf{p}}) \end{pmatrix} \begin{pmatrix} \xi \\ \eta \end{pmatrix}. \tag{4}$$

Thus together with the solution of the equation (4) *the task is formulated to find the eigenfunctions* Φ_{bv} *and eigenvalues of the mutually commuting operators of the complete set:*

$$\left\{ \hat{E} = i\hbar \, \partial/\partial t; \quad \hat{H}_{bv} = c(\hat{\boldsymbol{\alpha}}_{bv} \hat{\mathbf{p}}); \quad \hat{\mathbf{p}} = -i\hbar\hat{\nabla}; \quad \hat{\Lambda} \right\}, \tag{5}$$

where the matrix $\hat{\alpha}_{bv}$, operators of the helicity $\hat{\Lambda}$ and of the spin $\hat{S}$ of a photon in bivector representation equal:

$$\hat{\alpha}_{bv} = \begin{pmatrix} \hat{s} & 0 \\ 0 & -\hat{s} \end{pmatrix}, \quad \hat{\Lambda} = \frac{(\hat{S}\hat{p})}{sp} = \frac{(\hat{S}\hat{p})}{p} = \frac{1}{p}\begin{pmatrix} (\hat{s}\hat{p}) & 0 \\ 0 & (\hat{s}\hat{p}) \end{pmatrix}, , \quad \hat{S} = \begin{pmatrix} \hat{s} & 0 \\ 0 & \hat{s} \end{pmatrix}. \tag{6}$$

The solution of this task consists in the following [22, 25]:

1) To states of a photon with *positive* energy $E^{(+)}(k) = \hbar kc = +pc$ (which consistent with the special theory of relativity [27]) the orthonormal bivectors, answering to a helicity $\lambda = \pm 1$, are:

$$\Phi^{(+)}_{bv;\mathbf{k},+1}(\mathbf{r},t) = \begin{pmatrix} \xi^{(+)}_{\mathbf{k},+1}(\mathbf{r},t) \\ 0 \end{pmatrix} = \frac{(Oe)\,\mathbf{e}_{+1}(\mathbf{k})}{(2\pi)^{3/2}} e^{i(\mathbf{kr}-kct)} \begin{pmatrix} 1 \\ 0 \end{pmatrix}, \tag{7}$$

$$\Phi^{(+)}_{bv;\mathbf{k},-1}(\mathbf{r},t) = \begin{pmatrix} 0 \\ \eta^{(+)}_{\mathbf{k},-1}(\mathbf{r},t) \end{pmatrix} = \frac{(Oe)\,\mathbf{e}_{-1}(\mathbf{k})}{(2\pi)^{3/2}} e^{i(\mathbf{kr}-kct)} \begin{pmatrix} 0 \\ 1 \end{pmatrix}, \tag{8}$$

respectively, where (Oe) is unit of measure (Oersted) of values ξ and η.

2) To states of a photon with negative energy $E^{(-)}(k) = -\hbar kc = -pc$ (which theoretically possible) the orthonormal bivectors, answering to the helicity $\lambda = \mp 1$, are:

$$\Phi^{(-)}_{bv;\mathbf{k},-1}(\mathbf{r},t) = \begin{pmatrix} \xi^{(-)}_{\mathbf{k},-1}(\mathbf{r},t) \\ 0 \end{pmatrix} = \frac{(Oe)\,\mathbf{e}_{-1}(\mathbf{k})}{(2\pi)^{3/2}} e^{i(\mathbf{kr}+kct)} \begin{pmatrix} 1 \\ 0 \end{pmatrix}, \tag{9}$$

$$\Phi^{(-)}_{bv;\mathbf{k},+1}(\mathbf{r},t) = \begin{pmatrix} 0 \\ \eta^{(-)}_{\mathbf{k},+1}(\mathbf{r},t) \end{pmatrix} = \frac{(Oe)\,\mathbf{e}_{+1}(\mathbf{k})}{(2\pi)^{3/2}} e^{i(\mathbf{kr}+kct)} \begin{pmatrix} 0 \\ 1 \end{pmatrix}, \tag{10}$$

respectively, where the complex polarization vectors $\mathbf{e}_\lambda(\mathbf{k}) = [\mathbf{e}_I(\mathbf{k}) + i\lambda\,\mathbf{e}_{II}(\mathbf{k})]/\sqrt{2}$, and $\mathbf{e}_I$, $\mathbf{e}_{II}$ are the real mutually orthogonal unit vectors forming a right-handed triad with a vector $\mathbf{n} = \mathbf{k}/k$ for a given $\mathbf{k} = \mathbf{p}/\hbar$:

$$|\mathbf{e}_I| = |\mathbf{e}_{II}| = 1, \quad (\mathbf{e}_I\,\mathbf{n}) = (\mathbf{e}_{II}\,\mathbf{n}) = (\mathbf{e}_I\,\mathbf{e}_{II}) = 0, \quad \mathbf{e}_{II} = [\mathbf{n}\times\mathbf{e}_I], \tag{11}$$

$$\mathbf{n} = [\mathbf{e}_I \times \mathbf{e}_{II}] = i\lambda[\mathbf{e}_\lambda \times \mathbf{e}_\lambda^*] = \lambda \mathbf{e}_\lambda^+(\mathbf{k})\hat{s}\mathbf{e}_\lambda(\mathbf{k}), \tag{12}$$

that gives the orthonormality for $\mathbf{e}_\lambda$ and useful relations *if* vector $\mathbf{e}_I$ *does not its change at change of sign of vector* $\mathbf{n}$, namely:

$$(\mathbf{e}_{\lambda'}^*\,\mathbf{e}_\lambda) = \delta_{\lambda'\lambda}, \quad \mathbf{e}_{\lambda'}^+\mathbf{e}_\lambda = \delta_{\lambda'\lambda}, \quad \mathbf{e}_\lambda(\mathbf{n}) = \mathbf{e}_{-\lambda}(-\mathbf{n}), \quad [\mathbf{e}_\lambda(\mathbf{k})]^* = \mathbf{e}_{-\lambda}(\mathbf{k}) = \mathbf{e}_\lambda(-\mathbf{k}). \tag{13}$$

Owing to (13) the orthonormality relations take place for bivectors (7)–(10):

$$\int d^3\mathbf{r}\left[\Phi^{(\pm)}_{bv;\,\mathbf{k}',\,\lambda'}(\mathbf{r},t)\right]^+ \Phi^{(\pm)}_{bv;\,\mathbf{k},\,\lambda}(\mathbf{r},t) = (Oe)^2 \delta_{\lambda'\lambda}\delta(\mathbf{k}'-\mathbf{k}), \tag{14}$$

$$\int d^3\mathbf{r}\left[\Phi^{(\pm)}_{bv;\,\mathbf{k}',\,\lambda'}(\mathbf{r},t)\right]^+ \Phi^{(\mp)}_{bv;\,\mathbf{k},\,\lambda}(\mathbf{r},t) = 0. \tag{15}$$

Then it is postulated that the photon states with the positive and negative energy, and given by **E** *and* **H** *are the superposition of bivectors of monochromatic plane waves* (7)–(10):

$$\Phi_{bv}^{(\pm)}(\mathbf{r},t) \equiv \Phi_{bv;\pm1}^{(\pm)}(\mathbf{r},t) + \Phi_{bv;\mp1}^{(\pm)}(\mathbf{r},t) \equiv$$

$$\equiv \int B(\mathbf{k},\pm1)\Phi_{bv;\mathbf{k},\pm1}^{(\pm)}(\mathbf{r},t)\,d^3\mathbf{k} + \int \left[B(-\mathbf{k},\mp1)\right]^* \Phi_{bv;\mathbf{k},\mp1}^{(\pm)}(\mathbf{r},t)\,d^3\mathbf{k}. \tag{16}$$

Using specified bivectors, satisfying the necessary conditions of orthonormality and completeness, it is possible to write the spatial density distribution of energy of the photon in the state (16) and the wave function $\Psi^{(\pm)}(\mathbf{r},t)$ of this state, normalized per unit probability:

$$\rho_E^{(\pm)}(\mathbf{r},t) \equiv \frac{1}{8\pi}\left[\Phi_{bv}^{(\pm)}(\mathbf{r},t)\right]^+ \Phi_{bv}^{(\pm)}(\mathbf{r},t) = \frac{1}{8\pi}\sum_\lambda \left[\Phi_{bv;\lambda}^{(\pm)}(\mathbf{r},t)\right]^+ \Phi_{bv;\lambda}^{(\pm)}(\mathbf{r},t) =$$

$$= \frac{1}{8\pi}\left\{\left[\xi_{\pm1}^{(\pm)}(\mathbf{r},t)\right]^+ \xi_{\pm1}^{(\pm)}(\mathbf{r},t) + \left[\eta_{\mp1}^{(\pm)}(\mathbf{r},t)\right]^+ \eta_{\mp1}^{(\pm)}(\mathbf{r},t)\right\} \equiv \frac{1}{8\pi}\left\{\left|\xi_{\pm1}^{(\pm)}(\mathbf{r},t)\right|^2 + \left|\eta_{\mp1}^{(\pm)}(\mathbf{r},t)\right|^2\right\} \equiv$$

$$= \frac{1}{8\pi}\left\{\left[\mathbf{E}_{\xi,\pm1}^{(\pm)}(\mathbf{r},t)\right]^2 + \left[\mathbf{H}_{\xi,\pm1}^{(\pm)}(\mathbf{r},t)\right]^2 + \left[\mathbf{E}_{\eta,\mp1}^{(\pm)}(\mathbf{r},t)\right]^2 + \left[\mathbf{H}_{\eta,\mp1}^{(\pm)}(\mathbf{r},t)\right]^2\right\}, \tag{17}$$

$$\Psi^{(\pm)}(\mathbf{r},t) = \int b(\mathbf{k},\pm1)\Psi_{\mathbf{k},\pm1}^{(\pm)}(\mathbf{r},t)\,d^3\mathbf{k} + \int \left[b(-\mathbf{k},\pm1)\right]^* \Psi_{\mathbf{k},\mp1}^{(\pm)}(\mathbf{r},t)\,d^3\mathbf{k}, \tag{18}$$

where

$$b(\mathbf{k},\lambda) = \frac{(Oe)}{\sqrt{8\pi\hbar kc}}B(\mathbf{k},\lambda), \qquad \Psi_{\mathbf{k},\lambda}^{(\pm)}(\mathbf{r},t) = \frac{1}{(Oe)}\Phi_{bv;\mathbf{k},\lambda}^{(\pm)}(\mathbf{r},t). \tag{19}$$

Thus the $\Psi^{(\pm)}(\mathbf{r},t)$ and dimensionless functions $\Psi_{\mathbf{k},\lambda}^{(\pm)}(\mathbf{r},t)$ satisfy the normalization

$$\int d^3\mathbf{r}\left[\Psi_{\mathbf{k},\lambda}^{(\pm)}(\mathbf{r},t)\right]^+ \Psi_{\mathbf{k}',\lambda'}^{(\pm)}(\mathbf{r},t) = \delta_{\lambda'\lambda}\delta(\mathbf{k}'-\mathbf{k}), \tag{20}$$

$$\int d^3\mathbf{r}\left[\Psi^{(\pm)}(\mathbf{r},t)\right]^+ \Psi^{(\pm)}(\mathbf{r},t) = \int d^3\mathbf{r}\,\rho_P^{(\pm)}(\mathbf{r},t) = 1. \tag{21}$$

The photon wave function $\Psi^{(\pm)}(\mathbf{r},t)$ in the state of the wave packet (18) with both positive and negative energy, satisfies the Schrodinger equation of the form (4), from which the continuity equation follows for density of probability $\rho_P^{(\pm)}(\mathbf{r},t)$ and of stream density $\mathbf{j}_P^{(\pm)}(\mathbf{r},t)$ of probability to find the photon in the vicinity of the point $\mathbf{r}$ in a timepoint t:

$$\frac{\partial \rho_P^{(\pm)}(\mathbf{r},t)}{\partial t} + \text{div}\,\mathbf{j}_P^{(\pm)}(\mathbf{r},t) = 0, \tag{22}$$

where

$$\rho_P^{(\pm)}(\mathbf{r},t) = \left[\Psi^{(\pm)}(\mathbf{r},t)\right]^+ \Psi^{(\pm)}(\mathbf{r},t), \quad \mathbf{j}_P^{(\pm)}(\mathbf{r},t) = c\left[\Psi^{(\pm)}(\mathbf{r},t)\right]^+ \hat{\alpha}_{bv}\Psi^{(\pm)}(\mathbf{r},t). \tag{23}$$

The wave function in the momentum representation corresponds to the wave function (18), namely:

$$\Psi^{(\pm)}(\mathbf{k},t) \equiv \left\langle \mathbf{k} \middle| \Psi^{(\pm)} \right\rangle \equiv \frac{1}{(2\pi)^{3/2}} \int e^{-i\mathbf{k}\mathbf{r}} \, \Psi^{(\pm)}(\mathbf{r},t) \, d^3\mathbf{r} =$$

$$= e^{\mp ikct} \left\{ b(\mathbf{k},\pm1) \, e_{\pm1}(\mathbf{k}) \begin{pmatrix} 1 \\ 0 \end{pmatrix} + \left[b(-\mathbf{k},\mp1) \right]^* e_{\mp1}(\mathbf{k}) \begin{pmatrix} 0 \\ 1 \end{pmatrix} \right\}. \quad (24)$$

If coefficients $b(\mathbf{k},\lambda)$ are known, then using wave functions (18), (24) it is possible to calculate all characteristics of a free photon. For example, average value of energy of a photon is defined as:

$$\overline{E^{(\pm)}} \equiv \left\langle \Psi^{(\pm)} \middle| \hat{E} \, \Psi^{(\pm)} \right\rangle = \left\langle \sum_{\lambda'} \Psi_{\lambda'}^{(\pm)} \middle| \hat{E} \sum_{\lambda} \Psi_{\lambda}^{(\pm)} \right\rangle =$$

$$= \int (\pm \hbar k c) \left\{ \left| b(\mathbf{k},\pm1) \right|^2 + \left| b(-\mathbf{k},\mp1) \right|^2 \right\} d^3\mathbf{k} = \int E^{(\pm)}(k) \, \rho_P^{(\pm)}(\mathbf{k}) \, d^3\mathbf{k}. \quad (25)$$

This formula gives the value coinciding with the one defined in classical electrodynamics, and also the formulas (17). This fact expresses the correspondence principle causing the introduction of the wave function of the photon in a condition of a wave packet (18).

EVOLUTION IN SPACE AND TIME OF PHOTON WAVE PACKET CORRESPONDING TO A SINGLE FEMTOSECOND LASER PULSE

On the basis of the above stated general method of construction of wave function of a free photon in coordinate representation in [28] the most important wave packet in scientific and methodical aspects with Gaussian momentum distribution is considered.

In order to more fully reveal the physical content and functionality of the wave packet (18) we will choose the coefficients of this packet having the simplest, "Gaussian" form:

$$b(\mathbf{k},\pm1) = \left[b(-\mathbf{k},\mp1) \right]^* = \sqrt{\frac{\alpha_1\alpha_2\alpha_3}{2\pi\sqrt{\pi}}} \exp\left[-\frac{1}{2}\left(\alpha_1^2 k_x^2 + \alpha_2^2 k_y^2 + \alpha_3^2 (k_z \mp k_0)^2 \right) - i\mathbf{k}\mathbf{r}_0 \right], (26)$$

where parameters $\mathbf{k}_0 = (0, 0, k_0)$, $\mathbf{r}_0 = (x_0, y_0, z_0)$, α_1, α_2, α_3 characterize average values and dispersions of the corresponding physical quantities in the state of a photon (18) and satisfy the normalization condition (21).

Parameterization (26) answers to the state of a photon with a zero average helicity as the values $\lambda = \pm 1$ are presented in (26) with equal probability. All characteristics of this wave packet can be broken into two categories: 1) momentum-energy, expressed only through the parameters appearing in (26), and 2) space-time, for calculation of which it is required to set still polarization vectors $\mathbf{e}_\lambda(\mathbf{k})$. According to statements of quantum mechanics, values of these two categories of characteristics answer to the corresponding uncertainty relations. New here, compared to the quantum mechanics of particles with mass, is the fact that the values of characteristics of the second category essentially can depend on "choice" of vectors $\mathbf{e}_\lambda(\mathbf{k})$.

Momentum-energy characteristics

Applying (18), (26) and quantum mechanical formula of calculation of average value of physical quantity F operator of which is equal $\hat{F}$:

$$\overline{F^{(\pm)}} \equiv \left\langle \Psi^{(\pm)} \middle| \hat{F} \, \Psi^{(\pm)} \right\rangle = \left\langle \sum_{\lambda'} \Psi_{\lambda'}^{(\pm)} \middle| \hat{F} \sum_{\lambda} \Psi_{\lambda}^{(\pm)} \right\rangle, \tag{27}$$

where $\Psi_{\lambda}^{(\pm)}$ at the values $\lambda = \pm 1$ are defined by corresponding terms of the formula (18), we find at once average values of projections of momentum and their squares:

$$\overline{p_x^{(\pm)}} = \overline{p_y^{(\pm)}} = 0, \quad \overline{p_z^{(\pm)}} = \pm \hbar k_0, \tag{28}$$

$$\overline{\left(p_x^{(\pm)}\right)^2} = \frac{\hbar^2}{2\alpha_1^2}, \quad \overline{\left(p_y^{(\pm)}\right)^2} = \frac{\hbar^2}{2\alpha_2^2}, \quad \overline{\left(p_z^{(\pm)}\right)^2} = \frac{\hbar^2}{2\alpha_3^2} + \hbar^2 k_0^2, \tag{29}$$

from where it follows that the average vector of a momentum of the photon in a state of positive energy is directed along the axis z, and with negative is opposite to it:

$$\overline{\mathbf{p}^{(\pm)}} = \pm \hbar \mathbf{k}_0 \equiv \pm \hbar k_0 \mathbf{e}_z. \tag{30}$$

Dispersions of projections of a momentum on the axes are defined by $\alpha_1, \alpha_2, \alpha_3$:

$$D_{p_x} \equiv \overline{\left(p_x^{(\pm)}\right)^2} - \left(\overline{p_x^{(\pm)}}\right)^2 = \frac{\hbar^2}{2\alpha_1^2}, \quad D_{p_y} = \frac{\hbar^2}{2\alpha_2^2}, \quad D_{p_z} = \frac{\hbar^2}{2\alpha_3^2}. \tag{31}$$

Then uncertainty of photon momentum projections an in state (18) are reduced to formulas:

$$\Delta p_x \equiv \sqrt{D_{p_x}} = \frac{\hbar}{\alpha_1 \sqrt{2}}, \quad \Delta p_y = \frac{\hbar}{\alpha_2 \sqrt{2}}, \quad \Delta p_z = \frac{\hbar}{\alpha_3 \sqrt{2}}, \tag{32}$$

where the presence $\sqrt{2}$ is connected with such choice which gives, according to (24) the simplest form of the momentum distribution in the state (18), namely Gaussian form:

$$\rho_P^{(\pm)}(\mathbf{k}) = \left| b(\mathbf{k}, \pm 1) \right|^2 + \left| b(-\mathbf{k}, \mp 1) \right|^2 = \frac{\alpha_1 \alpha_2 \alpha_3}{\pi \sqrt{\pi}} \exp\left[-\alpha_1^2 k_x^2 - \alpha_2^2 k_y^2 - \alpha_3^2 (k_z \mp k_0)^2 \right] \tag{33}$$

Below we present the appropriate formulas in the case when $\alpha_1 = \alpha_2 = \alpha_3$.

Applying the formula (25), (33), we find the average energy of the photon in state (18), respectively with positive and negative spectrum of its energy:

$$\overline{E^{(\pm)}} = \pm \hbar k_0 c \left[\left(1 + \frac{1}{2\alpha_1^2 k_0^2} \right) \operatorname{erf}(\alpha_1 k_0) + \frac{\exp(-\alpha_1^2 k_0^2)}{\alpha_1 k_0 \sqrt{\pi}} \right], \tag{34}$$

and also, similarly, the mean square of energy of the photon in the state (18):

$$\overline{\left(E^{(\pm)}\right)^2} = c^2 \hbar^2 k_0^2 \left(1 + \frac{3}{2\alpha_1^2 k_0^2} \right). \tag{35}$$

Using (34) and (35), it is possible to calculate dispersion and uncertainty of energy of a photon in state (18) with momentum distribution (33), according to the general definition:

$$D_E = \overline{\left(E^{(\pm)}\right)^2} - \left(\overline{E^{(\pm)}}\right)^2, \quad \Delta E = \sqrt{D_E}. \tag{36}$$

Space-time characteristics

Requirements (11)–(13) are satisfied, e.g., for the following vectors [22, 25]:

$$e_I(\mathbf{k}) = \begin{pmatrix} 1-(1-\cos\theta)\cos^2\varphi \\ -(1-\cos\theta)\sin\varphi\cos\varphi \\ -\sin\theta\cos\varphi \end{pmatrix}, \quad e_{II}(\mathbf{k}) = \begin{pmatrix} -(1-\cos\theta)\sin\varphi\cos\varphi \\ \cos\theta+(1-\cos\theta)\cos^2\varphi \\ -\sin\theta\sin\varphi \end{pmatrix}, \text{ at } 0 \le \theta \le \frac{\pi}{2}, \tag{37}$$

$$e_I(\mathbf{k}) = \begin{pmatrix} 1-(1+\cos\theta)\cos^2\varphi \\ -(1+\cos\theta)\sin\varphi\cos\varphi \\ \sin\theta\cos\varphi \end{pmatrix}, \quad e_{II}(\mathbf{k}) = \begin{pmatrix} (1+\cos\theta)\sin\varphi\cos\varphi \\ \cos\theta-(1+\cos\theta)\cos^2\varphi \\ -\sin\theta\sin\varphi \end{pmatrix}, \text{ at } \frac{\pi}{2} < \theta \le \pi, \tag{38}$$

where the Cartesian components of the corresponding vectors in the usual configuration space are specified, expressed in terms of the spherical coordinates of vector $\mathbf{k}$ in momentum space. Taking into account formulas (37), (38) it is also conveniently to carry out the calculation of space-time characteristics in momentum representation, using the formula (24).

In particular for average values of coordinates and their squares of a point of detection of the photon in state (18) we obtain the following expressions:

$$\overline{x^{(\pm)}} = x_0, \qquad \overline{y^{(\pm)}} = y_0, \qquad \overline{z^{(\pm)}} = z_0 \pm ct\,\overline{n_z^{(\pm)}}, \tag{39}$$

$$\overline{\left(x^{(\pm)}\right)^2} = x_0^2 + \frac{\alpha_1^2}{2} + A_1^{(2)} + c^2t^2\,\overline{\left(n_x^{(\pm)}\right)^2}, \quad \overline{\left(y^{(\pm)}\right)^2} = y_0^2 + \frac{\alpha_1^2}{2} + A_2^{(2)} + c^2t^2\,\overline{\left(n_y^{(\pm)}\right)^2}, \tag{40}$$

$$\overline{\left(z^{(\pm)}\right)^2} = z_0^2 + \frac{\alpha_1^2}{2} + A_3^{(2)} + c^2t^2\,\overline{\left(n_z^{(\pm)}\right)^2} \pm 2ct\,\overline{n_z^{(\pm)}}\,z_0, \tag{41}$$

where:

$$\overline{n_z^{(\pm)}} = \left[\left(1-\frac{1}{2\alpha_1^2 k_0^2}\right)\mathrm{erf}(\alpha_1 k_0) - \frac{\exp(-\alpha_1^2 k_0^2)}{\alpha_1 k_0 \sqrt{\pi}}\right], \tag{42}$$

$$\overline{\left(n_x^{(\pm)}\right)^2} = \overline{\left(n_y^{(\pm)}\right)^2} = \frac{1}{2}\left[1-\overline{\left(n_z^{(\pm)}\right)^2}\right] = \frac{1}{2\alpha_1^2 k_0^2}\left[1-\frac{\sqrt{\pi}}{2\alpha_1 k_0}\mathrm{erfi}(\alpha_1 k_0)\exp(-\alpha_1^2 k_0^2)\right], \tag{43}$$

$$A_1^{(2)} = A_2^{(2)} = -\frac{1}{2}A_3^{(2)} + \Delta A_{13}^{(2)}, \quad \Delta A_{13}^{(2)} \equiv 2\alpha_1^2\exp\left(-\alpha_1^2 k_0^2\right)\int_0^1 \frac{\exp\left(\alpha_1^2 k_0^2 u^2\right)}{1+u}\,du, \tag{44}$$

$$A_3^{(2)} = \frac{1}{2k_0^2}\left[\frac{1+2\alpha_1^2 k_0^2}{2\alpha_1 k_0}\mathrm{erfi}(\alpha_1 k_0)\exp\left(-\alpha_1^2 k_0^2\right)\sqrt{\pi} - 1\right]. \tag{45}$$

From (39)–(45) it follows that the dispersions D_x, D_y, D_z of coordinates of a point of detection of the photon which is in the state (18) parameterized by means of (26) are equal:

$$D_x = D_y = \frac{\alpha_1^2}{2} + A_1^{(2)} + c^2 t^2 \overline{\left(n_x^{(\pm)}\right)^2} = \frac{\alpha_1^2}{2} + A_1^{(2)} + c^2 t^2 D_{n_x}, \qquad (46)$$

$$D_z = \frac{\alpha_3^2}{2} + A_3^{(2)} + c^2 t^2 \left\{ \overline{\left(n_z^{(\pm)}\right)^2} - \left(\overline{n_z^{(\pm)}}\right)^2 \right\} = \frac{\alpha_3^2}{2} + A_3^{(2)} + c^2 t^2 D_{n_z}. \qquad (47)$$

According to (46) the dispersions D_x and D_y are the same for the considered wave packet which is symmetric relatively of the z axis.

Analysis of modeling results

As seen from (46), the rate of expansion of the wave packet is the same in each plane xy, in accordance with the fact that the wave packet (18) with the parameterization (26) remains symmetric relatively of the z axis. As characteristics of speed of this expansion it is possible to use periods τ_x, τ_y, τ_z during which initial dispersions (at $t = 0$) are doubled along the directions x, y, z. From (46)–(47) we find:

$$\tau_x = \frac{\Delta x(t=0)}{c\,\Delta n_x} = \tau_y = \frac{\Delta y(t=0)}{c\,\Delta n_y}, \qquad \tau_z = \frac{\Delta z(t=0)}{c\,\Delta n_z}. \qquad (48)$$

Since even in a simple form of distribution (26) it is not possible, analytically to obtain an expression for the probability density in configuration space, we carry out the analysis of the evolution of the considered wave packet by means of calculation of the intensity of electric field, using the initial formula (3), (18), (19). Not equal to zero in this case is only a projection of intensity E_x, which characterizes a certain way, the spatial probability density. At $\alpha_1 = \alpha_1 = \alpha_3$ the spatial "form" of a wave packet in the initial time is "spherical". We will give results of numerical calculation for the packet corresponding to the duration of 80 fs radiation with the central wavelength of 10 microns. On an axis of symmetry of a packet, the density of probability of photon detection in the vicinity of the center of the packet moves practically with velocity of light in vacuum. The farther from the axis, the lower the velocity of probability density is in the direction of the average velocity (along) of wave packet.

Thus, there is a transformation of the original shape of the wave packet in a certain "conical" shape (see. Fig. 1 and 2).

Speed of this transformation is the more, the less initial "radius" of a wave packet (18), according to the general representations of quantum mechanics. Fig. 1 and 2 show the distributions of the most significant projection of the intensity of electric field E_x computed respectively in two different moments of time: $t = \tau_z$ and $t = 2\tau_z$, where τ_z is the time of expansion of the packet (48) along an z axis.

THE MAIN FORMULA OF WAVE-PARTICLE DUALITY AND NATURE OF PHOTON

In our opinion the constructed photon quantum mechanics substantially removes a problem of wave-particle duality of quantum "particles". Main "formula" of wave-particle duality of light and microparticles can be formulated as follows [29]:

1. Photons and microparticles at interaction behave as a corpuscle, transferring and transmitting (to other particles) in a certain quantity as dynamic characteristics (energy, momentum, angular momentum), and "internal" (mass, electric charge, spin, etc.). In particular, such transfer is carried out at hit of a photon or microparticle in quite dot detector

(or a point on the screen) with coordinate **r** at time point t. The fact of hit of "all particle entirely" in the dot detector is characteristic for a corpuscle, but not for some real wave.

2. However, photons and microparticles propagate in space by "wave rules", that is their distribution in space is described by wave function. In particular, density of probability of detection in space of the nonrelativistic particle with a nonzero mass is postulated by a formula $\rho(\mathbf{r},t) = |\Psi(\mathbf{r},t)|^2$, and a photon by (23). This probability density also causes the hit of a photon and microparticle in the dot detector. A characteristic interferential picture on the screen corresponds to distribution of $\rho(\mathbf{r},t)$ along the screen.
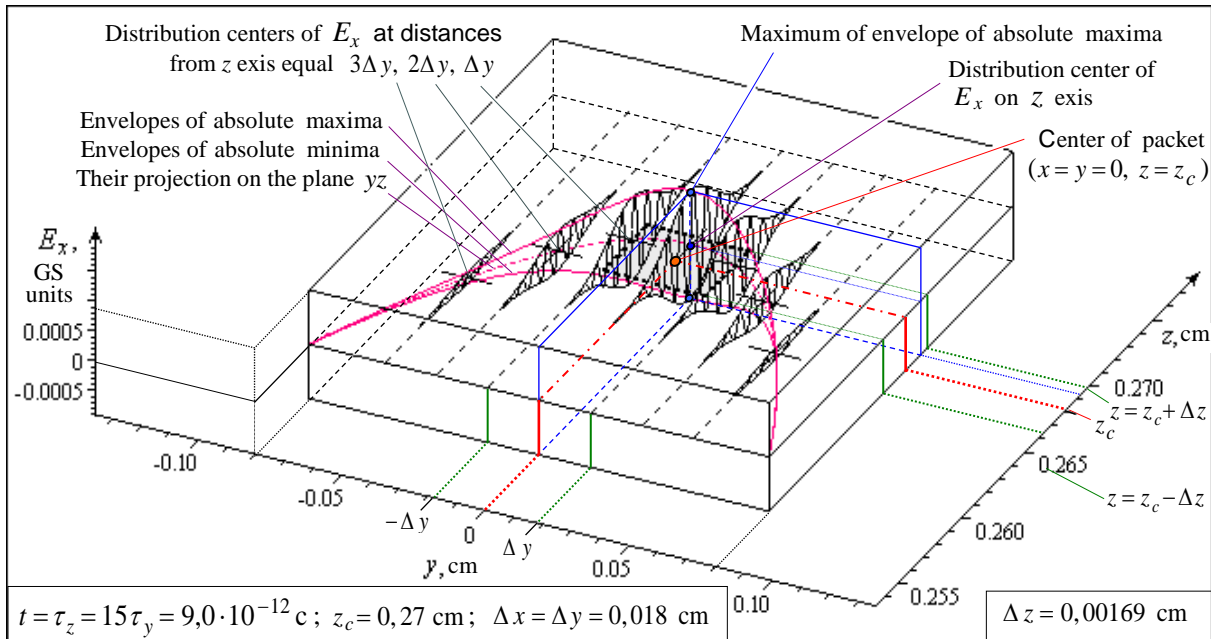
Figure 1. Distribution of electric field intensity E_x at time moment $t = \tau_z$
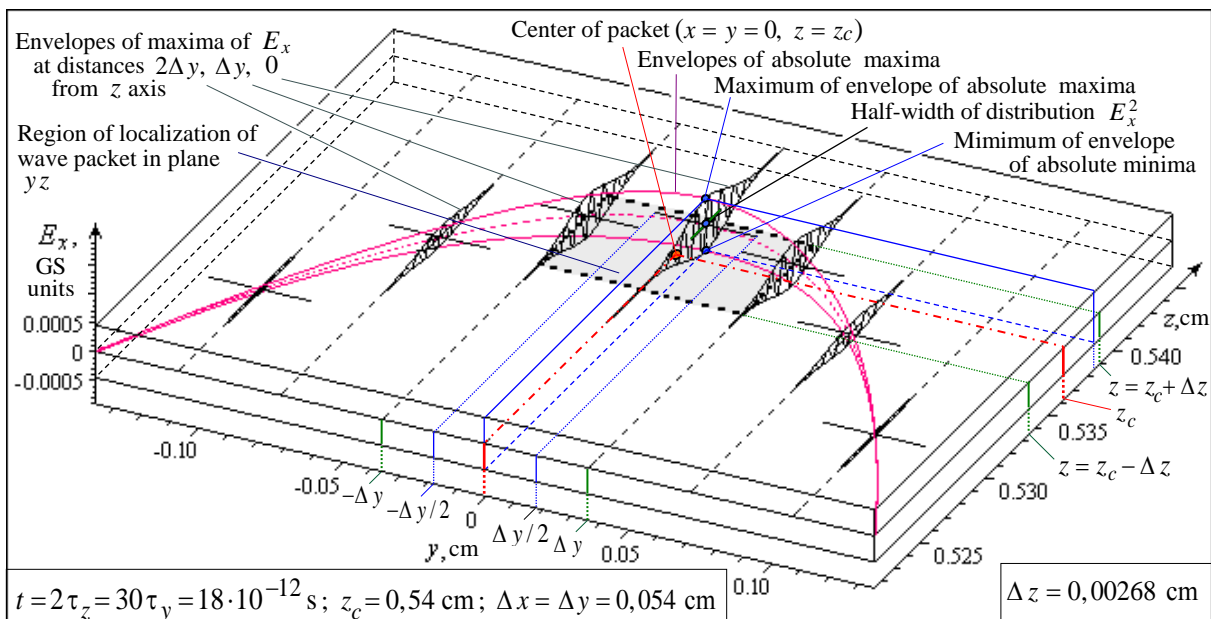
Figure 2. Distribution of electric field intensity E_x at time moment $t = 2\tau_z$

Nevertheless, electromagnetic radiation even in the case of waves small lengths and obviously expressed "corpuscular properties", is *impossible* to consider as a stream of the

certain "created", "dot" particles, similar to the massive particles. In our view, the photon is a quasi-particle, and light is a result of the propagation of a spin wave in physical vacuum, the structure and nature of which have to be considered at the Planck distance [25, 30]. This question is closely related to the structure of the leptons and other fundamental particles on the same distances. According to [31–33] the center of an electron is extreme maximon, that is the quantum nonsingular object creating round itself an extreme Kerr-Newman metric. It has spin $s = 1/2$ and approximately Planck mass, charge and radius. For most observed phenomena involving photons it is possible to give the following interpretation of their propagation in vacuum. In the photon propagation the middle-ordered (in time and space) alternate spins flip occurs of virtual vacuum extreme maximons, which creates the effect of the spin wave, and in "macroscopic scale" produce manifestation the corpuscular-wave properties of photons. However due to the vector dominance also exhibited by the photons, their propagation in vacuum can be associated also with other, more complex virtual processes.

CONCLUSION

The results of our modeling of photon wave packet propagation allow to illustrate the possibility of a single-photon approach to the description of electromagnetic phenomena. In particular, it appears that those aspects of interference and diffraction such as the interference pattern of Young's double-slit experiment, which were described in the language of classical electrodynamics, obviously can be described in the language of quantum mechanics without the involvement of the apparatus of second quantization of the electromagnetic field. This significantly expands the scope of "ordinary" quantum mechanics and considerably reduces the problem of wave-particle duality in the present level of our knowledge.

REFERENCES

1. L. Landau and R. Peierls, "Quantenelectrodynamik im Konfigurationsraum," Zeit. F. Phys, vol. 62, pp. 188–198, 1930.

2. H.A. Kramers, Quantum Mechanics, Amsterdam: North- Holland, 1958 (original ed. 1937).

3. T.D. Newton and E.P Wigner, "Localized states for elementary particles", Reviews of Modern Physics, vol. 21, pp. 400–406, 1949.

4. D. Bohm, Quantum Theory, Constable, London, 1954.

5. E.A. Power, Introductory Quantum Electrodynamics, Longmans, London, 1964.

6. V.B. Berestetskii, E.M. Lifshitz, and L.P. Pitaevskii, Quantum electrodynamics, 2nd ed., NY: Pergamon Press Ltd., 1982.

7. A.I. Ahiezer and V.B. Beresteckij, Kvantovaja jelectrodynamika, M.: Nauka, 1981.

8. V.G. Levich, Ju.A. Vdovin, and V.A. Mjamlin, Kurs teoreticheskoj fiziki, vol. II, M.: Nauka, 1971.

9. R.Y. Chiao, P.G. Kwiat, and A.M. Steinberg, "Quantum non-locality in two-photon experiments at Berkeley," Quantum and Semiclassical Optics: Journal of the European Optical Society, Part B, vol. 7, No. 3, pp. 259–278, 1995.

10. M.O. Scully and M.S. Zubairy, Quantum Optics. Cambridge Univ. Press, 1997, Chs. 1 and 21.

11. V.I. Fushhich and A.G. Nikitin, "O novyh i staryh simmetrijah uravnenij Maksvella i Diraka," W.I. Fushchych. Scientific Works, vol. 2, Kyiv: Editor Vyacheslav Boyko, pp. 233–278, 2000.

12. A.K. Zvezdin, "Kvantovaja mehanika plenennyh fotonov, opticheskie microrezonatory, volnovody, fotonnye kristally," Priroda, No 10, pp. 12–23, 2004.

13. E.E. Zanimonskij and Ju.P. Stepanovskij, "Precessija spina fotonov i geometricheskie fazy", Visnik HNU, Iss. 13, No. 914, Serija Fizika, pp. 36–39, 2010.

14. A.T. Gavrilin, "About the probability amplitude of photon locations," Bulletin of the Lobachevsky Nizhny Novgorod University, No. 6 (1), pp. 70–74, 2011.

15. I. Bialynicki-Birula, "On the Wave Function of the Photon," Acta Phys. Pol. A, vol. 86, pp. 97–116, 1994.

16. M. Mandel and E. Wolf, Optical coherence and quantum optics, Cambridge University Press, 1995.

17. J.E. Sipe "Photon wave functions," Physical Review A, vol. 52, pp. 1875–1883, 1995.

18. A.P. Davydov, "Quantum mechanics photons", in Abstracts of XXXIII scientific conference of teachers MSPI "Science and the school"", (Magnitogorsk, 1995), pp. 206–207.

19. I. Bialynicki-Birula, "The Photon Wave Function," in Coherence and Quantum Optics VII, edited by J.H. Eberly, L. Mandel, and E. Wolf (Plenum Press, New York, 1996), pp. 313–323.

20. I. Bialynicki-Birula, "Photon Wave Function", in Progress in Optics, edited by E. Wolf (North-Holland, Elsevier, Amsterdam, 1996), vol. XXXVI, pp. 248–294.

21. M. Hawton, "Photon wave functions in a localized coordinate space basis," Phys. Rev. A, vol. 59, pp. 3223–3227.

22. A.P. Davydov, Photon wave function in the coordinate representation," Herald MaGU, Vol. 5, pp. 235–243, 2004.

23. J. Cugnon, "The Photon Wave Function," Open Journal of Microphysics, vol. 1, No. 3, pp. 41–52, 2011.

24. P. Saari, "Photon localization revisited," in Quantum Optics and Laser Experiments, edited by S. Lyagushyn, InTech, Open Access Publisher, Croatia, 2012, pp. 49–66.

25. A.P. Davydov, "Quantum mechanics of the photon wave function in the coordinate representation," Electromagnetic waves and electronic system, vol. 20, No. 5, pp. 43–61, 2015.

26. R. Mignani, E. Recami, and M. Baido, "About a Diraclike equation for the photon, according to Ettore Majorana," Left. Nuovo Cimento, vol.11, No. 12, pp. 568–572, 1974.

27. A.P. Davydov, "Construction of spetsial'noy otnositel'nosti theory (SRT) from the symmetry of space and time without the postulates of SRT," Electromagnetic waves and electronic system, vol. 8, No. 1, pp. 49–58, 2003.

28. A.P. Davydov, "Simulation of three-dimensional space in the photon wave packet," in Actual problems of modern science, technology and education: Materials of 73 the international scientific-technical conference vol. 3, pp. 133–137, 2015.

29. A.P. Davydov, A course of lectures on quantum mechanics. The mathematical apparatus of quantum mechanics, Magnitogorsk: Izd-vo Magnitogorsk State Technical University named G.I. Nosov, 2014.

30. A.P. Davydov, "Photon as a quasi-particle with excitation of spin waves in physical vacuum at Planck distances", in abstracts of XLIV intrahigh science teachers conference MaSU "Modern problems of science and education", (Magnitogorsk, 2006), p. 174.

31. A.P. Davydov, "New quantum objects Astroparticle Physics – besingulyarnye elementary black holes - as a consequence of the KJeD i OTO," in collection of scientific papers "The fundamental applied research", (Magnitogorsk, 1997), pp. 22–41.

32. A.P. Davydov, "Features besingulyarnyh quantum black holes with the Planck parameters and metrics of extreme physics and cosmology," Electromagnetic waves and electronic system, vol. 3, No. 2, pp. 67–78, 1998.

33. A.P. Davydov, "Extreme maximons structure of fundamental particles, KJeD, OTO and RTG A.A. Logunova," Electromagnetic waves and electronic system, vol. 6, No. 5, pp. 4–13, 2001.

Method of Performance Evaluation of Tasks in E-Learning Systems

V. Emelianov [1], M. Emelianova [2]

Dept. Communication Networks and Telecommunication Systems,
Kalashnikov Izhevsk State Technical University, Izhevsk, Russia
E-mail: [1] em.vl@mail.ru, [2] mariya.m.pavlova@mail.ru

Abstract. In this paper the method of performance the evaluation of students' self-made works in distance learning systems is carried out. The aim of methodology is to encourage students to make quality work in time. To do this, it is assumed the final assessment will depend not only on the quality of work, but also on the spent time for work, the duration of the visit of the resource. The paper presents a visualization of the results of this technique.

INTRODUCTION

Currently, information technologies are being actively implemented in the educational process of high education, in order to ensure continuous and easy access to all the necessary materials. There is a large number of local and global electronic resources created to educate students. The mosts of local systems are based on Moodle, eFront, WebTutor. Examples of global systems are networking academies (eg, Cisco, Huawei, Microsoft, Intel, etc.) and universities (for example, "National Open University "INTUIT" in Russia).

At present time elearnig is very popular. Usually state encourages and points to create accessible knowledge base and remote schools and universities, for example, according to Federal Target Programme for Development of Education for 2011–2015 years in Russia. As well, at the request of many universities, teachers create personal electronic cabinets on which they place materials of disciplines. Moreover, the content of these resources is fairly unique, designed for a special course. Online lectures (webinars) are gaining popularity, checking assignments in electronic form and the use of automated tools to assess knowledge saves working time of teacher [1, 2].

On the other hand, when there are many distractions in extracurricular activities of students, arises an important task to stimulate the student to work by himself, not only in university, but also at home, for example like in papers [3, 4]. Also in view of the fact that the relationship between the modern university with students is gradually transformed into the market where the school acts as a seller of knowledge, and the student in the role of the buyer, self-discipline of students is reduced. With all the possibilities for the use of electronic knowledge base for his training, the student simply doesn't make it. To stimulate students to perform homework in a timely manner, within the specified time, to have less time for various

dishonest manipulation with the task, the most rational approach is performance the evaluation with accounting factors (time and quality of work). When task is issued for learners the best students usually perform and pass it before the others. After some time percentage of self-performed tasks decreases (which is especially important if similar task were issued).

EVALUATION OF A STUDENT'S HOMEWORK

Evaluation of a student's homework S that depends from the time t can be represented by the equation (1):

$$S = \begin{cases} f_1(t), if \ t < t_1 \\ f_2(t), if \ t_1 < t < t_2 \\ ... \\ f_T(t), if \ t_T > t > t_{T-1} \\ 0, if \ t > t_T \end{cases} \tag{1}$$

where T – the number of time intervals for grading; t_1, t_2, t_T – limits of time intervals.

Number of different parameters can affect on a final grades. Depending on the requirements of the teacher it can be, for example, the quality of the performed task, completeness of the topic, the accuracy of formalization, etc. As a result, each evaluation parameter $f(t)$ can be represented, for example, as a linear function (2):

$$f(t) = k_1 \cdot x_1 + ... + k_n \cdot x_n \tag{2}$$

where n – the number of parameters considered in the evaluation; x_1, x_2, x_n – score for each parameter; k_1, k_2, k_n – normalized weighted coefficients for the parameters of evaluation (can be individually selected by teacher).

VISUALIZATION OF PRESENTED METHOD

For visualization of presented evaluation method can be created three-dimensional models [5], which shows the dependence of final grade from two parameters: time and quality.
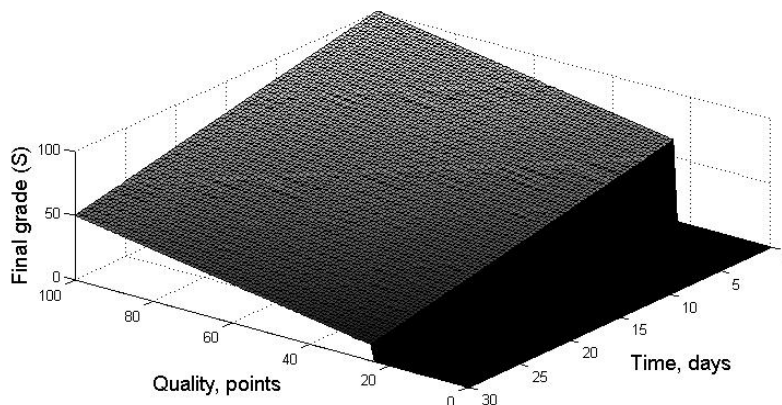
Figure 1. The linear dependence of the final grade from time of performance and quality

Figure 1 shows an example of the visualization of linear dependence of the final grade S (on a 100-point scale) from the given time for task t (in days) and the quality of the performed work (on a scale for 100 points) using two time slots ($S = 0$ for $t > t_T = 30$ days).

The graph shows the evaluation of all possible options, but it is logical that the grade lower than "satisfactory" level (chosen by teacher), does not have a positive value. Usually even if the work is done after the maximum time interval ($t > t_T$) the teacher must determine the maximum value that can earn the homework, and the student will receive either this mark or work will be considered not done. It is reasonable to assume that it is not necessary to evaluate the performance positively, if the quality of performance is low, so in the example in Figure 1 task will be graded only if the level of quality is above 25 points.

If in use of a hundred point scale for final evaluation, it makes sense to specify an equation in which the grade will tend to zero. In the case of the expiration of a long period of time it can be meaningless to put grade, but the work still requires verification, but with graduation – pass / fail. Usually student must make homework before being admitted for exam.

If the relationship is non-linear, but exponential, the final grade can decrease faster with increasing duration of the assignment:

$$f(t) = A \cdot (p_1^{x_1} \cdot ... \cdot p_n^{x_n}) \tag{3}$$

where A – the maximum value of the final grade that depends on the evaluation scale; p_1, p_n – foundation degree, selected by teacher ($p_1, ..., p_n < 1$).

Visualization example of the final grade for this case is shown in Figure 2.
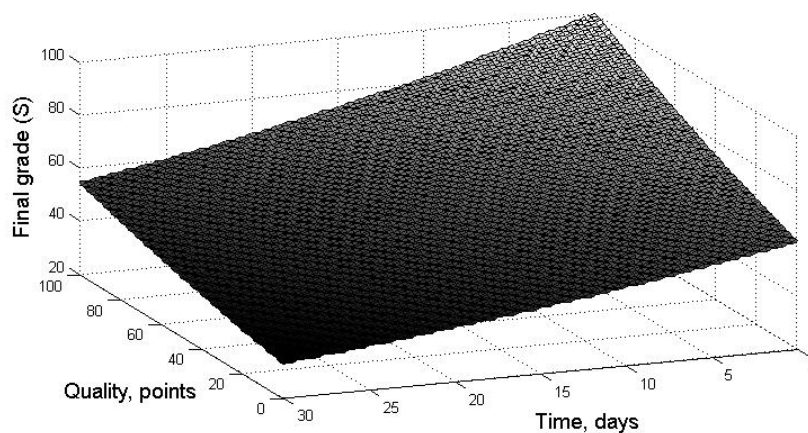
Figure 2. The exponential dependence of the final grade from time of performance and quality

To stimulate students to self-study and review the materials a similar approach can be applied, that tracks time of students attending of course material. Fact of viewing the contents $S_a(t)$ of an electronic resource can be used as a small addition to the final grade S, if it is formed as the sum of the scores for several tests, exercises and attendance (S_1, S_2).

$$S = S_1 + S_2 + ... + S_a(t) \tag{4}$$

where $S_a(t)$ – grade for viewing the materials.

$S_a(t)$ can be defined as the sum of scores for all views of materials. Fact of viewing the contents of an electronic resource needs to be used primarily for the analysis of educational outcomes. And it shows the reason why the student has not learned (or learned) material.

CONCLUSION

The above time tracking mechanisms may be incorporated into the shell of e-learning websites. In the simplest case method of evaluating homework can be implemented using a table editor (Microsoft Excel, Libre Office Calc) using macros or formulas. To use this technique teacher needs to have interaction with the system only once at the beginning. To establish evaluation the parameter values required such as boundary timeslots (t_1, t_2, ..., t_T), the weighting coefficients for the evaluation parameters (k_1, k_2, ..., k_n). Further, when checking the homework it's required to evaluate quality of done task and the system will calculate the final result.

When using the proposed method, consider the following recommendations:

✓ students should be warned in advance about the dependence of the final grade for the assignment from time of its implementation;

✓ algorithms that implement the procedure should be embedded in the e-learning system in such a way as not to complicate the work of the teacher, have the ability to set the initial values of the default settings and ability to transport parameters between different classes and groups;

✓ on the personal page of the student's e-learning system must be created a function that shows the time what has passed since the issuance of the task, and it will serve as a clear, direct incentives to do the work on time.

REFERENCES

1. I. Simonics, "Changing of multimedia elements in eLearning development," Emerging eLearning Technologies and Applications (ICETA), pp. 345–349, 2013.

2. B. Khatri, P. Chouskey, and M. Singh, "Comparative Analysis Study of E-learning and Traditional Learning in Technical Institution," Communication Systems and Network Technologies (CSNT), pp. 770–773, 2013.

3. V.Emelyanov, and A. Obukhov, "Video conferencing system as an effective tool for teaching information and communication technologies," in Collection of Materials II Russian scientific and technical conference of students, graduate students and young scientists, Izhevsk: Publishing House of the Izhevsk State Technical University, 2012, pp. 180–184.

4. V. Emelyanov, M.M. Pavlova, and I.A. Kajsina, "Security issues using payment bank cards," in Collected papers of the international scientific-practical conference "Science and Modernity", Ufa: "Scientific Publishing Center "Aeterna", 2015, pp. 16–19.

5. N.F. Nasyrov, "Visualization of learning results as way of improving quality of technical training," T-Comm – Telecommunications and Transport, No. 5, pp. 72–74, 2014.

Non-Linear Programming in the Synthesis of Regulators

T.A. Emelyanova [1], A.V. Voronin [2], V.I. Goncharov [3]

Department of Integrated Computer Control Systems, Tomsk Polytechnic University, Tomsk, Russia
E-mail: [1] 3ene4ka@sibmail.com, [2] voroninav@tpu.ru, [3] gvi@tpu.ru

Abstract. The article deals with the synthesis of regulators. There are presented the opportunity of using the non-linear programming in the synthesis the control systems by real interpolation method.

Keywords: regulator, control object, transfer function, real interpolation method, non-linear programming

INTRODUCTION

The modern control objects have very complex structure. In this connection regulators also increases complexity. At the same time, it is known that satisfactory quality of regulation can be obtained using relatively simple controls often. In addition, the simple controls are more preferable then complex. Since they are easier to understand and configuration, and it is less demanding of computing resources. Although some of these problems of complex regulators is gradually reduced in transition to digital implementation, the problem of creating regulators of reduced order is still relevant, and attracts the attention of researchers.

Many approaches to the construction of regulators can be divided into two groups. In the first case, the regulator was projected with a simplified structure. Initially its order is below the order of the control object. For example, there are all methods of PID-regulators synthesis. Sometimes, this process is known as setting regulator.

In the second case, full regulator is calculated, then its order is reduced to a predetermined or minimum possible without significant loss of basic properties of a closed-loop system.

For the second approach detailed model and a good formalization of the control object need. Thus, the system is configured in such a way has more control accuracy. And it is possible to arbitrarily set the desired requirements for the synthesized system. In the first approach there is no such possibility in principle.

Thus, the problem of the synthesis of the regulator minimum order is current in the theory of control for complex systems.

The paper presents a method for the synthesis regulators, including minimum order, based on the real interpolation method and nonlinear programming.

The real interpolation method for synthesis the control systems

The real interpolation method (RIM) [1, 2] refers to a group of operator methods. From the classical approach it different views of direct integral transformation. The method uses a real transformation, that is the transition from the original function $f(t)$ to the image-function $F(\delta)$, that has real variable δ.

The formula for the real image $F(\delta)$ it follows directly from the formula of the Laplace transform. There the complex variable s replaced by real variables δ:

$$F(\delta) = \int_0^\infty f(t) \cdot e^{-\delta t} dt, \ \delta \in [0, \infty). \tag{1}$$

Thus the function $f(t)$ has the natural limitations. It must be continuous, equal to zero for all values of t in the interval $(-\infty; 0]$. And it must be integral absolutely:

$$\int_0^\infty |f(t)|^2 dt < \infty.$$

The image-function of the $f(t)$ can be obtained in an analytical form of a simple replacement the relevant formula Laplace complex variable s to a real variable δ or as a graph $F(\delta)$ and a set of samples $F(\delta_i)$, which are called numerical characteristics. Thus numerical characteristic takes full information about the original model. With regard to the synthesis of the regulator using the model in the form of numerical characteristics makes it easy to realize the computing aspects of this procedure.

Solution of the problem synthesis of the regulator be the RIM is based on an approximate equality of the numerical characteristics of the synthesized the regulator $W_{reg}(\delta)$ and dividing the numerical characteristics of the desired model $W_{des}(\delta)$ to the numerical characteristics of the control object $W_{OU}(\delta)$:

$$\{W_{reg}(\delta_i)\} = \{W_{des}(\delta_i) / W_{OU}(\delta_i)\}, \ i = 1, n, \tag{2}$$

where n – the number of points of the numerical characteristics, which are called interpolation nodes [1].

The key role in the process of synthesis played of the approximate numerical characteristics. The quality of this procedure can influence choice of interpolation nodes and the principle of approximation. And also the introduction of restrictions on the coefficients $W_{reg}(s)$ impact on it.

Normally, the number of interpolation nodes n is chosen so that it was possible to form a square a system of algebraic equations and solve it relatively the unknown control parameters [1]. It is useful to use a much larger number of points, focusing not on the exact solution of algebraic equations, and approximate solution.

Absence of restrictions on the coefficients $W_{reg}(s)$ is result in unstable or non-robust closed-loop system. It is known that the maximum robustness of the system is achieved by using the minimum-phase regulators. It is important for unstable objects especially.

All noted problems can be solved using the procedure of nonlinear programming in the Matlab.

Statement and solution synthesis problem based the RIM as a nonlinear programming problem

Nonlinear programming problem in the program FMINCON of the Optimization Toolbox Matlab section posed as a problem of finding the minimum of the nonlinear problem:

$$\min_x f(x)$$

with restrictions:

$$c(x) < 0;$$

$$ceq(x) = 0;$$

on condition that:

$$A\,x \le b,$$

$$Aeg \cdot x = beg,$$

$$lb \le x \le ub,$$

where x – vector of unknowns; b – vector of put limits on inequality, beg – vector point constraints of equality, lb, ub – vectors of restrictions above and below, A – matrix inequality constraints; Aeg – constraint matrix equations, $c(x)$ and $ceq(\mathrm{x})$ – the function of non-linear constraints.

Let the numerical characteristic of the dividing the numerical characteristics of the desired model to the control object is given in the form n samples p_i in interpolation nodes δ_i. The regulator is calculated as:

$$W_{reg}(s) = \frac{b_2 s^2 + b_1 s + b_0}{a_2 s^2 + a_1 s + 1}. \tag{3}$$

The problem of synthesis the regulator can be formulated as a nonlinear programming problem. It is required to minimize the functional $f(x) = e^T \cdot He$ under conditions:

$$b_2 \delta_1^2 + b_1 \delta_1 + b_0 - p_1 \delta_1^2 a_2 - p_1 \delta_1 a_1 + e_1 = p_1,$$

$$\ldots$$

$$b_2 \delta_n^2 + b_1 \delta_n + b_0 - p_n \delta_n^2 a_2 - p_n \delta_n a_1 + e_n = p_n,$$

$$b_2 \ge 0,$$

$$b_1 \ge 0,$$

$$b_0 \ge 0,$$

$$a_2 \ge 0,$$

$$a_1 \ge 0.$$

Vector e is the discrepancy of the approximate solution of a system of linear equations in the interpolation nodes. The vector of unknown x include the regulator parameters b_2, b_1, b_0, a_2, a_1 and the components of the vector of discrepancies e.

The restrictions are imposed only on parameters b_2, b_1, b_0, a_2, a_1.

Apply the proposed approach for the control system with object of type:

$$W_{OU}(s) = \frac{15}{s^2 + s + 15}.$$

In [4] the synthesis of the compensation regulator of the second order was considered. It provides in a closed system, the specified quality and accuracy of static. Design a regulator minimal order using nonlinear programming.

The result of solving the problem non-linear programming using the program FMINCON obtained regulator in type:

$$W_{reg}(s) = \frac{0.02s + 0.265}{0.06s + 1}.$$

Graph of transient processes is shown in Fig. 2. It shows that the obtained regulator has provided parameters of quality, close to the required quality.
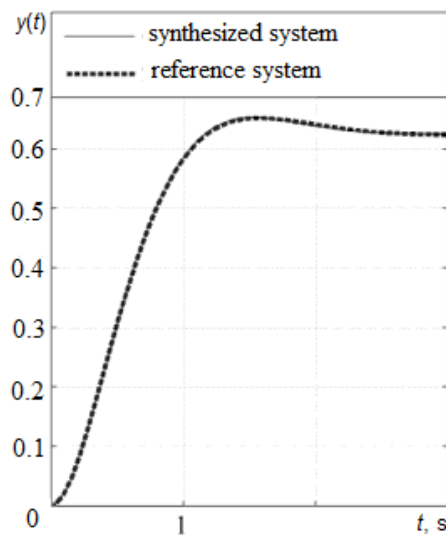
Figure 2. The transient processes in the synthesized and the reference systems for minimal-phase control object

The analysis shows that the special benefit from approximations and restrictions on signs of the coefficients of synthesized regulator in the case of the minimum-phase objects of the second order do not have. However, the situation changes drastically during the transition to non-minimal-phase objects.

Consider the non-minimal-phase object of the second order of the form:

$$W_{OU}(s) = \frac{-s + 15}{s^2 + s + 15}.$$

It has one zero in the right-half of the s-plane.

The structure of the regulator and view the desired transfer function remained the same.

The result of solving the problem non-linear programming using the program FMINCON obtained regulator in type:

$$W_{reg}(s) = \frac{0.0148s + 0.4270}{0.001s + 1}.$$

Graph of transient processes is shown in Fig. 3.
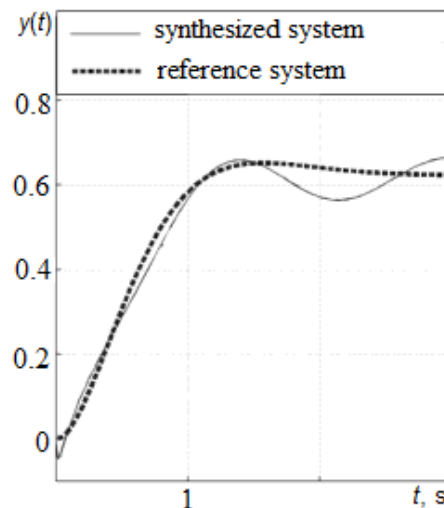
Figure 3. The transient processes in the synthesized and the reference systems
for non-minimal-phase control object

Figure 3 shows that the obtained regulator provided stability in a closed-loop system with non-minimal-phase control object without compensation, but the quality of the transition process is not fully compliant. The transition process is a great time setting.

In the case of unconstrained optimization for synthesis regulator system is not stable because right pole of control object is compensated right zero of regulator.

CONCLUSION

In the present paper we investigated the possibility of using real interpolation method combined with nonlinear programming tools for solving the problem of synthesis of regulator. There is a possibility of the synthesis regulator, which provides the stability of the closed-loop control system for minimum-phase, and for non-minimal-phase control object.

REFERENCES

1. V. Goncharov, I. Aleksandrov, and V. Rudnicki., Real Interpolation Method for Automatic Control Problems Solution, Saarbrucken: LAP Lambert Academic Publishing, 2014.

2. I.A. Orurke, New methods for the synthesis of linear and certain nonlinear dynamical systems, Moscow: Nauka, 1965.

3. Y.L. Ketkov, A.Y. Ketkov, M.M. Schultz, MATLAB 7: programming, numerical methods, St. Petersburg: BHV-Petersburg, 2005.

4. A.V. Voronin, T.A. Shchelkanova, "The use of quadratic programming in the synthesis of regulators the real interpolation method," Bulletin of the Tomsk Polytechnic University, vol. 321, No. 5, pp. 150–154, 2012.

Estimation QoS Parameters in Mobile Communication Networks

A. Gaysin [1], A. Nadeev [2]

Radioelectronics and Telecommunications System Department, Kazan National Research Technical University
named after A.N. Tupolev, Kazan, Russian Federation
E-mail: [1] akgaysin@kai.ru, [2] afnadeev@kai.ru

Abstract. The article presents the results on evaluation of quality of service parameters in mobile networks. This methodology is based on measuring the energy parameters of the radio interface and assessment congestion of channel resources. We present probabilistic relationships that take into account the multiple classes of subscribers traffic. It can be used in constructing model of mobile cell and assessment of current load.

Keywords: QoS, WCDMA, probabilistic model of a queuing system

INTRODUCTION

Current mobile technologies are characterized by an increasing level and diversity of traffic. Creating a unified system of quality of service (QoS) parameters and methods of their measurement is the most important task. The purpose of current investigation is to develop the measurement and analysis method of QoS parameters in WCDMA networks. This development is also required for the Communication Commission (CC) to control the QoS parameters. This should allow performing measurements at a minimum of time and money, and getting reliable results of QoS-parameters without direct connection to the equipment of service provider (SP). Existing methods of measurement do not allow this.

There are three main definitions of QoS in mobile networks:

1. QoS in terms of customer services – standard metrics that can be assessed by end users. These include: coverage, accessibility (GoS) and the sound quality, video streaming, data transmission services.

2. Evaluation of QoS from experts position – measurements needed to assess the network performance and to deliver the results to planning and optimization departments of SP. Usually, this is an internal audit, conducted by SP. These measurements require a specific set of tools and methods (protocol analyzers, drive tests, etc.).

3. Evaluation of QoS from the perspective of CC includes firstly, QoS-parameters control, provided by the operator to the end-user, according to regulatory indicators and secondly, the regulation of the communications market.

The aim of the present work is the development method of QoS-parameters control in WCDMA networks. It should include monitoring the energy parameters of the radio interface and evaluation of channel resource distribution for an end-user. To account for the

characteristics of the radio interface presented method is specified for WCDMA technology. The possibilities of modern measurement systems, which are built on the basis of software defined radio (SDR), allow to measure not only the energy and time parameters of the radio interface, but also to analyze the signaling traffic of protocols used in radio access networks. The proposed method consists of two parts. The first part is a coverage analysis in a given measurement area, an estimation of the interference situation and the possible bandwidth of the radio channel. The second part evaluated degree of channel resources occupation based on analysis of subscriber's activity. For this we should decode control channel messages. This data determines the state of the system based on the intensity of requests for channel resource allocation. We present here the process of base station (BS) channel resource distribution in the form of a queuing system analytical model. A recursive Kaufman-Roberts method is used to simplify the computational complexity of the model.

1. METHODS OF EVALUATING QOS PARAMETERS IN THE MOBILE COMMUNICATION NETWORK

The general perception of the QoS for the subscriber represents some total score, which is affected by many components of communication network. Fig. 1 shows the elements of the GSM / UMTS network, involved in a typical connection. This approach is reflected in the ETSI and 3GPP specification [1–5]. For the CC it is important to have a possibility to measure QoS parameters remotely. In mobile networks this is provided only in Radio Access Network(RAN).
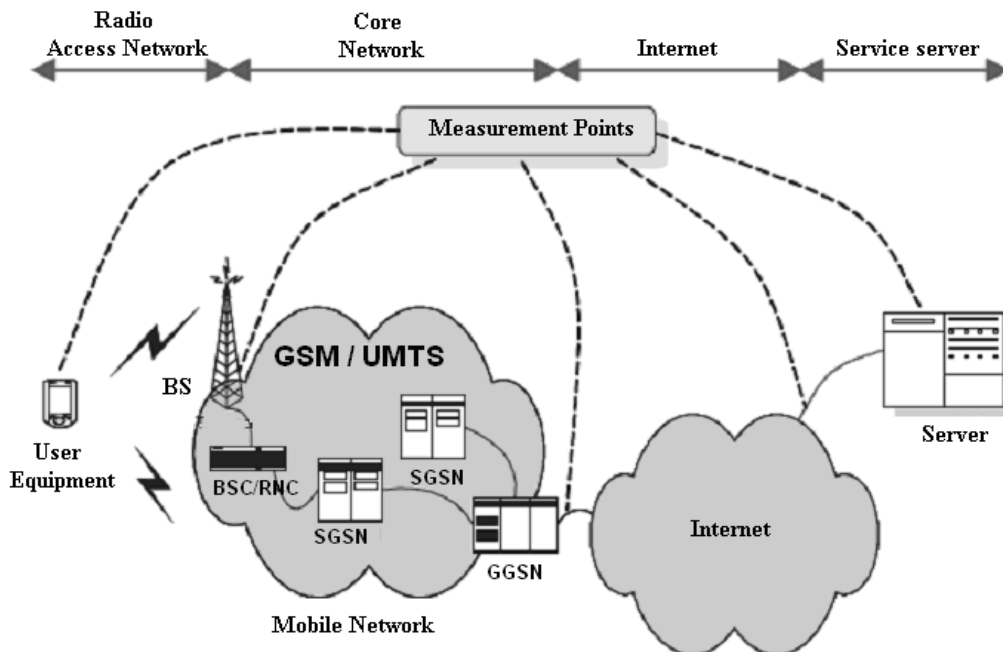
Figure 1. Heterogeneous network with multipoint measurement of QoS parameters

We assume that the strongest limiting factor on the integral QoS level is the channel capacity of the RAN. It determines the spectral efficiency of the system (bit / s / Hz) and has a huge impact on the efficiency of frequency resources occupation allocated in the network. Obviously, this value cannot be measured accurately due to the noise and interference in communication channels. This means that for different S/N ratios in the channel different extent of redundancy will be used, this in turn, reduces the available data rate of the user data stream. This S/N ratio may be too low and thus unacceptable, for the following reasons:

- abnormal loss of the radio channel;
- increased level of interference signals.

The next factor to be considered is the distribution of subscribers in the service area. Well-known models only considered the equilibrium state of the system and the assumption of statistical homogeneity of calls [5]. This approach is acceptable during the planning of the network and modeling algorithms of call admission control (CAC). But it did not take into account the actual behavior of users based on their social activity. Dismatch of the frequency plan for the current distribution of subscribers leads to deterioration of the expected QoS-parameters. In section 2 we describe a proposed measurement method.

2. CONTROL OF THE ENERGY PARAMETERS OF THE RADIO INTERFACE

In [6] an expression for the signal / noise ratio in the WCDMA / UMTS is described. In the downlink the lower limit of the signal / noise ratio is given by:

$$\beta_j \geq \gamma_j = \frac{P_j^{BS}}{\sigma^2 q_j + \dfrac{I(r_j)}{N} + \dfrac{1-\varepsilon}{N} \sum_{i=1}^{K} P_i^{B}}, \tag{1}$$

where P_j^{BS} – radiated signal strength of BS for j-th mobile station; P_i^{B} – the signal emitted by the base station for user i; σ^2 – is the power of the background Gaussian noise, N – is the spreading factor; ε – is the orthogonality factor; q_j is the path loss between mobile j and the base station, r_j – is the distance between mobile j and the base station; $I(r_j)$ – is the upper bound of the other-cell interference at mobile j, based on a log-normal approximation of this interference.
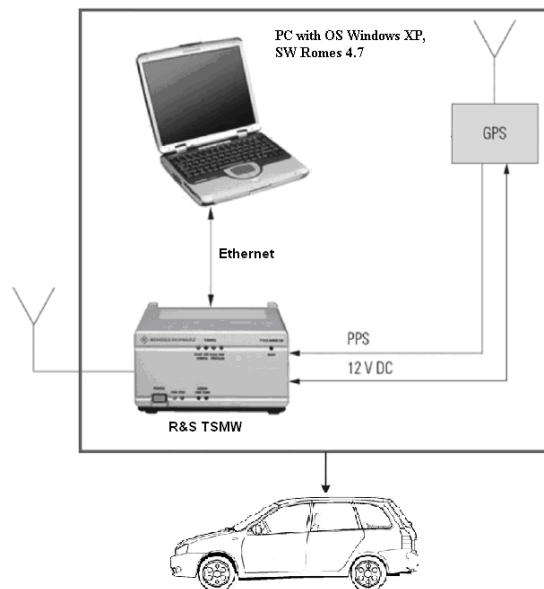
Figure 2. A block scheme of measurement equipment

Some parameters of the formula (1) can be measured directly at radio interface and used to evaluate coverage quality. For this measurement we use commercially available measurement system, which consists of Radio Network Analyzer TSMW (Rohde & Schwarz) and Romes software. To measure the power and timing of a communication channel we used "UMTS PN Scanner Driver" mode. This feature allows us to estimate the multipath

components using correlation properties of pseudo-random sequences. Fig. 2 shows how devices are connected during the measurements.

Communication between TSMW and ROMES SW platform is based on a standardized FireWire interface. Additionally, external GPS receiver provides the PPS (pulse per second) source of synchronization, for the geo-reference data. The complete measurement apparatus is installed in a mobile vehicle (medium size van about 1.5 meters high) and connected to an omnidirectional ½ wavelength dipole antenna (with a gain of 2 dBi) on the roof.

The first part of the proposed method is to evaluate the network coverage quality and includes the following steps:

1. determination of coverage area;
2. evaluation of the interference;
3. evaluation of the possible bandwidth of a radio channel.

To solve the first problem we measure the power levels of the following signals:

- RSCP – the received signal code power of a common pilot channel (CPICH);
- RSSI – received signal level. The total wideband power in a channel measured in the correlation section pilot channel (CPICH).

In the second step we control interference situation. For WCDMA systems main characteristics quality of the air interface is E_c/N_0 (ratio of energy consumed to transmit one chip code sequence to the noise spectral density). This parameter unlike RSCP varies depending on the pay-load. For weakly loaded cells this value is around 0 dB. During high subscriber activity it decreases down to −15 dB. The denial of service occurs if this value is exceeded based on the CAC algorithm [6]. In the Table 1 we present classes of coverage depending on the E_c/N_0 and RSCP.

Table 1. Classes of coverage in WCDMA

dB / dBm	$E_c/N_0 \geq -8$	$-8 > E_c/N_0 \geq -10$	$-10 > E_c/N_0 \geq -15$	$E_c/N_0 < -15$
RSCP ≥ −80	Class 1	Class 2	Class 3	Class 4
−84 ≤ RSCP < −80	Class 1	Class 2	Class 3	Class 4
−94 ≤ RSCP < −84	Class 2	Class 2	Class 3	Class 4
−105 ≤ RSCP < −94	Class 3	Class 3	Class 3	Class 4
RSCP < −105	Class 4	Class 4	Class 4	Class 4

TSMW Radio Network Analyzer allows you to measure the following parameters:

- ISCP – Power signal interference code. It characterizes the level of interference from the neighbor BS;
- E_c/I_o – ratio CPICH power to total spectral noise power and interference;
- SIR – Signal to noise ratio of the channel CPICH (SIR = RSCP / ISCP · SF_{CPICH}, where $SF_{CPICH} = 256$ – spreading factor for the CPICH).

3. ESTIMATION OF CHANNEL RESOURCES UTILIZATION

In this part of the measurements is estimated degree of utilization of channel resources based on analysis of subscriber activity. For these purposes are decoding message signal control channels, and based on the intensity of requests for allocation of channel resources determine the state of the system. The following assumptions are made for the system under consideration:

- The network serves n independent classes of Poisson traffic streams with arrival rates $\lambda_1, \lambda_2, \ldots, \lambda_n$.

- Each call is assigned a single or multiple channels (BBUs) depending on the parameters of the particular service class. The conversion from power-interference based capacity into channel-based capacity, as also explained in the previous section. A channel unit is chosen to be a data rate of 12.2 kbit/s, corresponding to the highest speech rate in UMTS.

- Service class k is characterized by its data rate of $d_k = m_k \times 12.2$ kbit/s, $k = 1, 2, \ldots, n$, and m_k is a positive integer. We choose the BBU so that each services class' demand is an integer multiple of the BBU.

- The service time for calls of a particular service class is exponentially distributed.

- A call holds the requested resources for a period of time, called mean holding time (or service time) τ_k. The resources are released with a service rate $\mu_k = 1 / \tau_k$.

- The mean traffic offered to the system for service class k is $\rho_k = \lambda_k / \mu_k$, which is the mean number of connections.

- Calls of different service classes get different resource allocation (user transmission rate and service time), which depend on the total number of already occupied channels. This means, that a new call of service k can be admitted into the system with a transmission rate that differs from the initially requested one. We call this call admission strategy Transmission Rate Reduction Policy (TRRP).

We, thus, have a Multiservice Loss Model (MLM), and the objective is to determine the call blocking probability and average user transmission rate for each service class in the system. The above mentioned model can be described by a multi-dimensional Markovian process of type $u(t) = \{i_1(t), i_2(t), \ldots, i_n(t)\}$, where each dimension represents one traffic class and $i_k(t)$ is the number of currently active users of service class k. The state-transition-rate diagram of a two-dimensional Markov chain is shown in Figure 3.
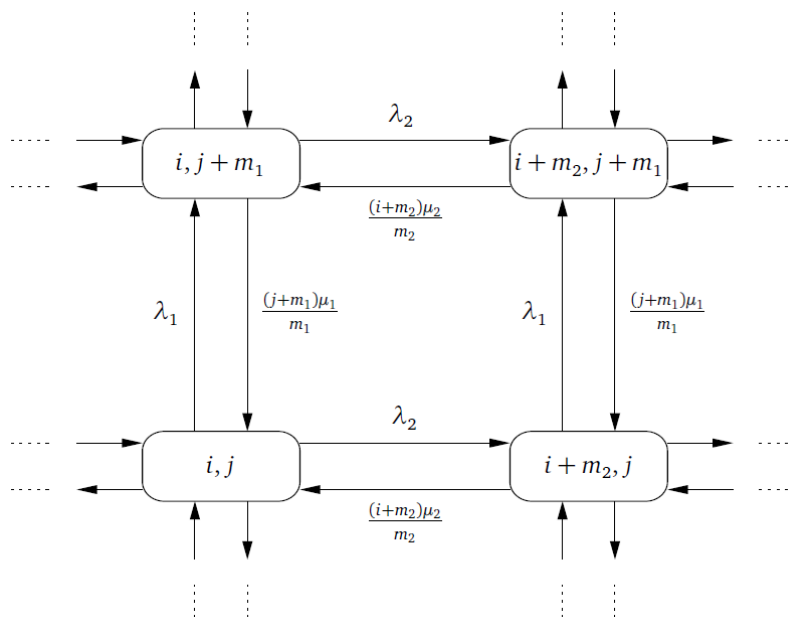
Figure 3. A fragment of a Markov chain for a two service system

The theory, which deals with Multiservice Loss Models states that there exists a unique stationary distribution for the stochastic process $u(t)$, thus $P(i_1, i_2, \ldots, i_n)$ is the steady-state probability, where $\{i_1, i_2, \ldots, i_n\}$ belongs to the state space S defined as follows:

$$S = \left\{ i_1, i_2, ..., i_n \left| \sum_{k=1}^{n} m_k i_k \leq N \right. \right\}, \tag{2}$$

where $0 \leq i_k \leq N$, and m_k denotes the number of channels for service-class k, requires to establish one connection, $m_j \geq 1$; both are integer. The values of $P(i_1, i_2, ..., i_n)$ can be shown to be composed of a product of the state probabilities of the traffic streams of each service class in isolation, i.e., before truncation (it is known that the traffic streams are independent before truncation) and thus, given by the product form solution:

$$P(i_1, i_2, ..., i_n) = \prod_{k=1}^{n} P(i_k). \tag{3}$$

However, calculating the blocking probabilities by using the above equations is numerically intractable and not suitable for multi-dimensional scenarios in large-scale networks, since the size of the transition matrix will grow exponentially with the number of service classes. In fact, the blocking probability for an arriving call does not only depend on the number of users in the network but also on the resources they occupy. Consequently, it is sufficient to determine the steady state distribution of the resource occupancy. We aggregate a multi-dimensional service process with different multi-rate traffic streams by a two-dimensional Markov chain, since the product form solution allows for this. Furthermore, we adopt the Kaufman-Roberts recursion, based on recurrence determination of the channel occupancy distribution $P(r)$, where $P(r)$ is the probability of r busy BBUs:

$$P(r) = \frac{1}{r} \sum_{k=1}^{n} \rho_k m_k P(r - m_k), \tag{4}$$

where $P(r) = 0$ for $r < 0$.

In order to extend our algorithm to support dynamic user transmission rates, we incorporate TRRP into the model by using a modified analytical approach for estimating the blocking probability in Asynchronous Transfer Mode (ATM) networks proposed in [7]. In this threshold model for blocking avoidance, new calls of certain service classes can get service with requests different to the initial resource and service time requests, which are state dependent. After some modifications to (4) and the addition of the expression from [7] we get:

$$P(r) = \frac{1}{r} \sum_{k=1}^{n} \rho_k m_k \delta_k(r) P(r - m_k) + \frac{1}{r} \sum_{k=1}^{n} \sum_{i=1}^{S_k} \rho_{k_i} m_{k_i} \delta_{k_i}(r) P(r - m_k) \tag{5}$$

for $r = 1, ..., N$, where $\delta_k(r) = 1$ and $\delta_{kl}(r) = 0$, when $1 \leq r \leq N$ (for service classes without rate reduction policy), or $r \leq J_{kl} + m_k$ (for service classes that have the possibility to be admitted with reduced transmission); s is the number of possible variations of the transmission rate, and J_{kl} is the adjusted threshold. The algorithm enables a performance assessment for each individual service class.

For calculating the total blocking probability for a service class while taking TRRP into account we modify the limits of the summations in the following expression:

$$B_{k_S} = 1 - \sum_{r=0}^{N-m_{k_S}} P(r). \tag{6}$$

This is the probability of a call of service class k to be blocked with its lowest possible transmission rate. In the next section we discuss the extensions to the multi-cell case.

Thus, using the functionality of modern measurement systems to decode control channel signaling flows, we can obtain the intensity data for subscriber traffic. Restore original parameters of this model, then possible to estimate the degree of utilization of channel resources BS and blocking probability of user calls.

CONCLUSION

This paper presents a method for evaluation of QoS-parameters in WCDMA mobile networks. This method is based on the measurements of the power parameters of the radio interface and on the assessment of payload of channel resources. We derive QoS parameters considering the class of calls. These analytical models can be used in constructing model cell and assessment of its current payload. User traffic intensity can be estimated based on the decoding of signaling message flow associated with the channel resource allocation request.

REFERENCES

1. ETSI TS 102 250-1. Speech Processing, Transmission and Quality Aspects (STQ); QoS aspects for popular services in GSM and 3G networks; Part 1: Identification of Quality of Service criteria.

2. 3GPP TS 23.107. 3rd Generation Partnership Project;. Technical Specification Group Services and System Aspects; Quality of Service (QoS) concept and architecture (Release 10).

3. 3GPP TS 23.401. 3rd Generation Partnership Project;. Technical Specification Group Services and System Aspects; General Packet Radio Service (GPRS) enhancements for Evolved Universal Terrestrial Radio Access Network (Release 10).

4. 3GPP TS 23.203. 3rd Generation Partnership Project;. Technical Specification Group Services and System Aspects; Policy and charging control architecture (Release 10).

5. S.-E. Elayoubi, T. Chahed and G. H´ebuterne, "On the Capacity of multi-cell UMTS," in proceedings of IEEE GLOBECOM 2003, San Fransisco, 2003, pp. 487–491.

6. A.K. Gaysin, A.F. Nadeev, and S.S. Sedov, "Model of Call Admission Control in the WCDMA/UMTS," Vestnik KGTU named after A.N. Tupolev, No. 2, pp. 123–128, 2012.

7. I. Moscholios, M. Logothetis, and G. Kokkinakis, "Connection-dependent threshold model. Performance Evaluation," Elsevier Publisher, No. 48, pp. 177–200, 2002.

Computer Simulation of Uncoordinated Dynamic Channel Access Method in Cognitive Radio Network for Radio Terminal Device

A. Grebeshkov, A. Zuev

Chair of Automatic Telecommunications, Povolzhskiy State University of Telecommunications and Informatics, Samara, Russia
E-mail: grebeshkov-ay@psuti.ru, zoomer499@mail.ru

Abstract. An implementation of the cognitive radio networks raises an issue of the medium access control (MAC) protocol researching, in particular MAC protocol impacts on the access delay to radio channels. In this paper uncoordinated access method is studied where the event of spectrum and channel accessing is random and determined by probabilistic value from 0.1 to 0.99 named as channel availability. The subject of research was impact of channel availability on the access delay with simulation on the base ns2 program simulator with CRNC patch.

Keywords: cognitive radio, radio terminal device, software-defined radio, dynamic spectrum access, media access control protocol, simulator ns2

INTRODUCTION

Cognitive radio (CR) is a new wireless communication concept, that can help to use all available radio resources at a local area more efficiently [1–3]. Cognitive radio has a clear ability to be concerning as self-configurable and self-planning platform including set of different software and hardware.

Cognitive radio is based on the radio spectrum access technology with dynamic spectrum access, DSA. Generally, DSA technology explores an opportunistic spectrum access. It means that available spectrum segments are used in an intelligent manner with help of advanced spectrum analysis and probing for unoccupied radio frequencies. For this purpose advanced methods like as machine learning, game theory are accepted. CR and DSA forms a new paradigm for radio spectrum and radio channel access and a great challenge for traditional use of fixed and non-distributed spectrum and radio channel using. Traditional wireless and cellular systems (2G, 3G, 4G, WiFi, WiMax) was designed on the base of centralized principle of spectrum using with a licensed spectrum and predefined terminal construction features. But this approach was appropriable just for centralized spectrum control.

Now this scheme has a drawback in term of flexibility and adaptability which are the important point of advantage of cognitive radio. There are two types of users sharing a common spectrum under DSA rules:

- Primary (licensed) users who have absolutely priority in spectrum utilization within the defined frequency bands.

- Secondary users who must access the spectrum in a temporary manner with DSA technologies.

There is a situation on practice when the part of frequency band previously licensed for primary user, is not being utilized by this kind of user for a short period of time. In traditional wireless systems there are no technologies that can help to use these random chance for data transmission through unexpected "white spaces" [4]. Cognitive radio technologies with software defined radios (SDR) [5] are more adaptable than traditional radio terminals. This new type of radio communication terminal device on the base of SDR can work under continuously changing radio environment and support conflict-free coexisting with other wireless devices that use lots of physical protocols, datalink – media access control layer protocols and network layer protocols.

STANDARDIZATION ASPECTS OF COGNITIVE RADIO

These days cognitive radio technologies, equipment developments and productions are the matter of innovations because DSA access with combination with an intellectual control and transmission technologies bring new paradigm of the spectrum access. The problem is that these new CR devices would be able to avoid co-channel interference in wireless communications. For that reason a great standardization working activity regular take place in the cognitive radio technologies and SDR. These efforts are implemented by the Institute of Electrical and Electronics Engineers (IEEE), International Telecommunication Union (ITU), European Telecommunications Standards Institute (ETSI) and European Computer Manufacturers Association (ECMA) [6].

One of the first standard consider cognitive radio principles, technologies and DSA was IEEE 802.22, initiated in 2004. This standard has been designed for data transmission devices in the wireless regional area network (WRAN) where radio terminal uses white spaces in the TV frequency spectrum. Because the importance of CR researching area is great, in 2004 was initiated some standardization project called IEEE P1900. These projects became a part of IEEE Standards Coordinating Committee 41 (IEEE SCC41) in 2006 and finally IEEE SCC41 was renamed as IEEE Dynamic Spectrum Access Networks Standards Committee (DySPAN-SC). In the focus of this committee is development of the research ideas into commonly used standards of CR. Next, ECMA-392 standards was finally published in 2012 with information concerning physical layer and media access control layer for cognitive network and personal devices/terminals functioning and operating in digital TV frequency based.

The efforts of the ETSI Reconfigurable Radio Systems Technical Committee are concentrated on the software-defined radio (SDR) architecture, function and use case standards. This couple of ETSI CR and SDR standards addressing the regional conditions and requirements of the European regulators in telecommunications and TV white spaces (TVWS) standards adapted to the digital TV signal characteristics in European Union.

In 2012 the cognitive radio systems was defined by ITU-R Communication Sector (ITU-R) as a radio system employing advanced technology that provides the telecommunication system the clear facilities to obtain knowledge of its radio environment with help of sensing and probing technologies and equipment, to adjust operational parameters and characteristics including PHY, MAC and network protocols attributes.

RESEARCH ISSUE IN CR PHYSICAL AND DATA LINK LAYERS

On the base of discussed standards there are three base parts in the cognitive cycle of DSA decision making [7]:

1. Analysis of the radio environment and search of free frequencies, which is performed in the receiver of by radio communication terminal CR device.

2. Dynamic spectrum access management, transmit power control, both of which are performed in the transmitter by radio communication terminal CR device.

3. Global feedback, enabling the transmitter to act in context of information about the radio environment feedback to it by the receiver.

Furthermore, it's need to add a stage of cognitive management information transfer with media access control protocol. MAC protocol used data had collected at the stage 1, 2 and stage 3.

On the base of receiver information and with help of its own information, including MAC layer, cognitive radio system can learn from the obtained results and probing. The knowledge used by the CR/SDR includes parameters of operational radio environment, information of geographic area and wireless networks at this area, internal and external state of radio communication devices like as base stations and user terminals, existing policies of spectrum access, usage segment of spectrum and users' needs, quality of service and preferable network and terminal demands.

There are a lot of methods for obtaining knowledge, for example getting information from special programmable component of SDR with spectrum sensing, from geo location data base (GLDB) with information about white spaces, and with access to a cognitive pilot channel (CPC) [8, 9].

To avoid interference and to aim the opportunistic spectrum access the couple of information to making decision about DSA has to include received signal power, load of desired channel, signal to interference and noise ratio (SINR).

For spectrum access a special coordinating devices are used. These devices can collect and provide useful information like as available frequency bands, radio access technologies (RAT) in association with base stations, access points and user terminals, restriction to the transmission power values. The coordination of base stations' and radio terminals' positions and positions of another telecommunication systems can be obtained using global position system (GPS) or wireless systems coordinating and positioning features.

Next in this paper the subject of research will be case with uncoordinated access as a more common point in CR system. The idea is that the estimation of the access delay [10] for uncoordinated manner of access will be an upper estimation of access delay when secondary users have to wait for a time to get access to the spectrum and radio channel resource.

Since early 2000s a numerous different platforms and prototypes of radio communication terminal with supporting of cognitive radio have been designing. A common view of main functional block for the physical and data layer of radio communication terminal with supporting of cognitive radio is on the Figure 1 (inspired by [1, p. 69]).
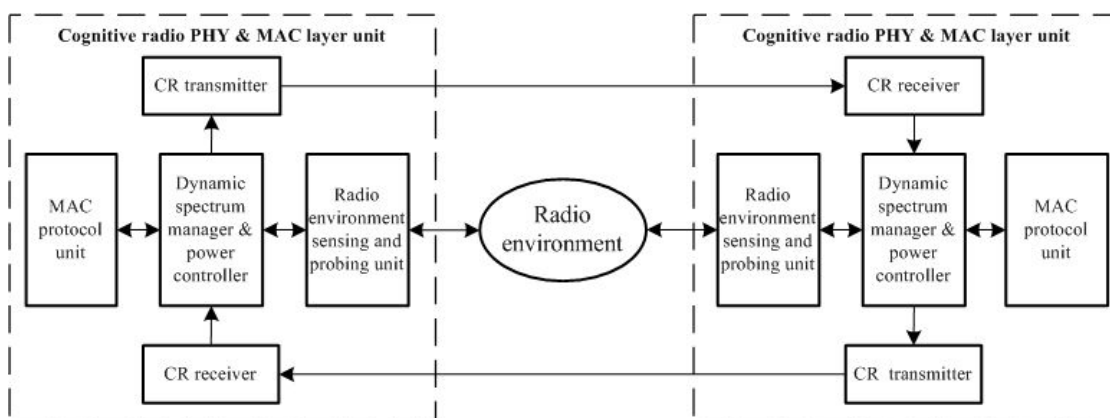
Figure 1. Functional block scheme of radio terminal device with supporting of cognitive radio features

Cognitive radio transceivers have the features that support changing their transmitter parameters in wide values range. These parameters are the type of modulation, transmission power, operating spectrum and communication technology. This device regards as software defined radio that can sense a wide spectrum range, probing and identify temporary unused spectrum segments and use these unoccupied frequency bands for data transmission or receiver.

The subject of further research with computer modelling will be a MAC protocol unit [11, 12]. Before describing a process of simulation, it is necessary to make some preliminary commentaries.

In the cognitive networks, the list of available channels is a variable parameter. Therefore, the issue of best acceptable channels selection is discovered. This problem solution in term of open system interconnection (OSI) model is at the data-link level where is a control access protocol that grants an access to the transmission medium. As it said above, it is a medium access control protocol with specificity in the context of cognitive network and DSA.

MAC protocol operation bases on received data from the physical layer. This data used to solve the problem of recognition of temporary unoccupied radio frequencies. The next step is decision making process about which of the unoccupied channels could be using, how to get access to this selected channel. However, information from data link layer help to find the optimal direction / transmission path, indicating a list of available channels for the network layer. In return, the network layer can transfer to the link layer an information about which channel has an appropriable quality of service (QoS) for the data transferring session initiation. As a result, the MAC protocol unit at the Fig. 1 for uncoordinated spectrum access has support following main functions:

- The control and prevention of interference in the primary users of radio frequency spectrum.
- Prevention of conflicts of access to the channel for the secondary users.
- Realization of the selection process and finding the best in the predefined criteria, unoccupied radio channel.

The MAC protocol performance research is discussed in [11] with a summary that to the MAC protocol for CR network some special features are added. In this circumstance in this paper the network simulator ns2 is used. The computer model of uncoordinated access method to the cognitive network based on the Cognitive Radio Cognitive Network (CRCN) patch for network simulator ns2 on the base of Linux Ubuntu 10.04 operating system [13, 14].

CRNC SETTINGS FOR UNCOORDINATED ACCESS METHOD SIMULATION

The CRCN patch has the input data as the amount of radio terminal devices with SDR features and the overall number of radio channels. The main modelling scenario provides a description of queues and channels for each SDR scenario with help of the TSL program library. Finally, the network simulator ns2 with CRCN patch has the following functionality for simulation cognitive MAC protocol unit:

1. The description of multi-channel data transmission medium.
2. The interface description for radio channel selecting.
3. A possibility to change and choice transmission power value.
4. Interference information.
5. Information about the motion or position of radio terminal devices.

The CRCN patch provides a needful opportunities to describe the collisions on the MAC layer. Before start of modelling process user has to add description of multichannel transmission medium layer structure in the form of program code component (see in Fig. 2).

```
Component 1. Select the number of interfaces and channels of distribution zone to
TCL script

set val(ni)                    2;# number SDR

set val(channum)   2;# channels available for SDR

Component 2: New facilities in the channel specified in the first component.

for {set i 0} {$i<[expr $val(ni)*$val(channum)]} {incr i} {
                        set chan_($i)[new $val(chan)]}

}

Component 3: Setting the SDR and the channel

$ns_node-config -ifNum $val(ni) -channel $chan_(0)

$ns_node-config -ChannelNum $val(channum)

Component 4: Communication objects in an array of channel

for {set i 0} {$i<[expr $val(ni)*$val(channum)]} {incr i} {
                        $ns_add-channel $i $chan_($i)

}
```

Figure 2. A fragment of the CRCN code with different number of channels

In fact, the choice of unoccupied channel depends on the MAC layer cognitive radio features or depends on the algorithm with exploration of the public key DSA (digital signature algorithm).

Next, in the program code to the "sendDown" procedure the function "WirelessPhy" be added. This function includes the description of the frame transmission process when the frame transmits to the physical layer.

However, to avoid access conflicts or to reduce interference between adjacent nodes the special channel index is used in CRNC. This channel index obtained from the MAC layer or from DSA algorithm.

For example, the index "channelindex" determines the packet header, which carries data for cognitive routing (see in Fig. 3).

```
Module WirelessPhy: The interface for selecting channel MAC

void WirelessPhy::sendDown(Packet*p)

{

        ...

        //Send the packet

        //channel_>recv(p,this);

        //send packet over the channel specified by channel index.

        multichannel [hdr_cmn::access(p)>channelindex_]>rexv(p,this);

        ...

}
```

Figure 3. A fragment of the CRCN code to select the MAC-level channel

An addition there is recommendation to use mechanism for the prevention of collisions that used as a part of ns2 features.

In this paper, we are considering the model of "hello" packets transition and the routing of these messages at the same time on several radio interfaces of radio terminal with aim to establish communication session. This simulation uses described functionality of the CRNC patch. A particular channel can be assigned by means of simulator to specific interface radio terminal device with SDR features. The assignation may be carried out by MAC level or can

be transmitted from the network level. The graphical user interface (GUI) allows to define process and data that necessary to CRCN. At the network layer the routing protocol named as "ad hoc on-demand distance vector" (AODV) is used by procedure of routing simulation.

The test carried out on multi-channel static network structure. The aim of test is verification of network operability with procedure network layer sends available channel data to the data link layer. In the routing procedure, the algorithm AODV making decisions on the use of the assigned channel. Since management of multi-channel structure is performed by simulator for MAC protocol layer only, the test includes two stages. In the first stage, each node sends a packet to the upper OSI layer and provides with information about the unoccupied channel(s). In the second stage, the node will use the already selected channel to transmit and receive data. Simulation parameters shown at the Table 1.

Table 1. Simulation CRNC parameters

Description	Value
Simulation tool	NS-2 (with CRNC patch)
Network area	100 m × 100 m
Number of nodes	10, 20
Number of channels	2, 5, 10
Channel availability (availability)	0.01 to 0.99
Simulation time	50 s

It is need to say, that evaluating the probability of channel availability was described in [15]. In [16] a special monitoring network was proposed for channel availability classification. In [17] the results of statistical modelling of channel availability were shown.

The three options of multichannel structure performed for simulation. At the first option there were 2 channels, at the second option there were 5 channels and in the end there were a 10 channels. An overall number of nodes was 10 in the first experiment and was 20 in the second experiment.

ANALYSIS OF COMPUTER SIMULATION RESULTS

For comparative analysis, all network nodes provided results, but the simulation results do not provide accurate values because modeled by a random processes. In order to estimate probability p of event, where event was a channel occupation, the probing simulation was done with result in 14 success attempts of channel occupy during 50 tests, since probing $p = 0.28$. The accuracy evaluation (closeness in estimation) in all simulation experiments was set to $\varepsilon < 0.01$. With the 95 % confidence interval for the 30 points used for plot composition, the number of tests in the one statistical experiment was determined as 9939, round to 10000. During simulation process was realized three experiments with 10000 tests in one experiment for 10 and 20 nodes respectively.

The nodes placed static in random order. These nodes selected randomly as senders or receivers data. The queue service time of each network described by the exponential distribution. The node selection is randomly. In addition, necessary to note that availability defined as the probability that a channel is available for the secondary user as result of sensing and probing process. The data rate was in interval from 0.3 Kbit/sec to 0.5 Kbit/sec as for low-rate sensor [18]. On the Fig. 4 and the Fig. 5 the number of the channels sets as "C".
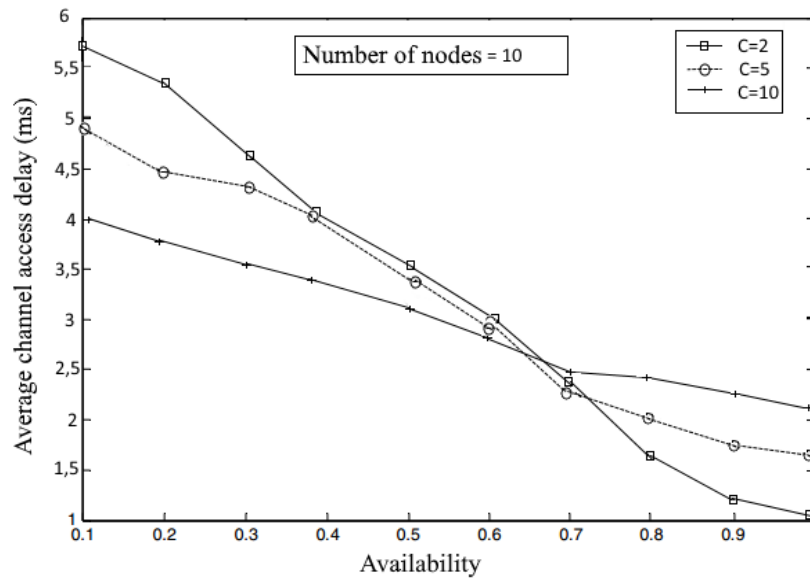
Figure 4. The channel access delay by using 10 nodes
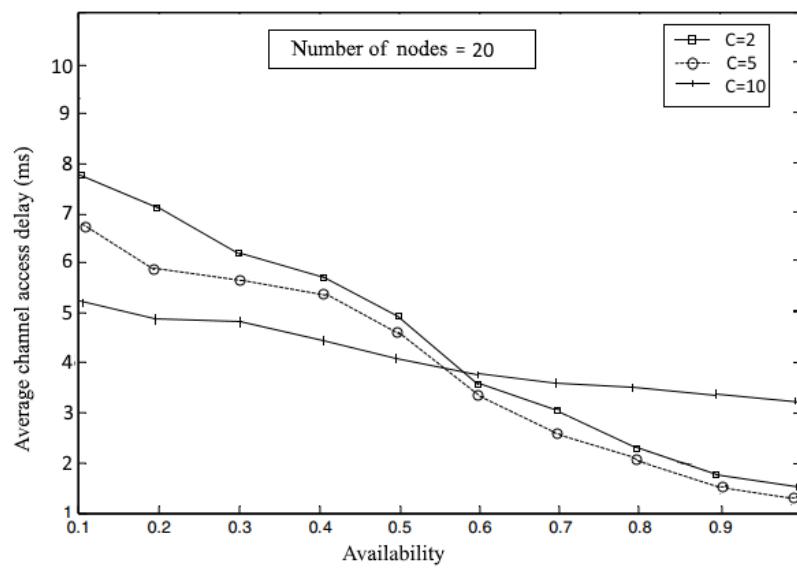
Figure 5. The channel access delay by using 20 nodes

Simulation is carried out with a different number of channels (C = 2, 5, 10), nodes get access to the channel at the same time, this procedure leads to access delay and collisions in the simulated network.

When availability value is observed from 0.1 to 0.6, there is high-delay access scheme, but when the availability is increasing the number of collisions is reduced. The matter of the observation is visible crossing point of lines on the plot in Fig. 4 and Fig. 5. On the plot's right side from the crossing point (for availability value from 0.65 to 0.99) is not too much changing of the channel access delay (delay changing from 2.5 ms to 1 ms) as in interval of availability value from 0.1 to 0.6 (delay changing from approximately 5.7 ms to 2.5 ms). Moreover, on the Fig. 4, as example, after graphs crossing, the scheme with C = 2 channels is a bit more better than scheme with C = 5 and 10 channels in context of channel access delay. Since in real network there is a possibility with specific value of availability emerging to decrease number of accessible channels without greater increasing of average channel access

86

delay. This result could be used in radio devices tune-up and for network design, planning and analysis.

On the Fig. 5 the simulation result shows the visible crossing point of graphs and there is no big differences between graph for C = 5 and C = 2 in channel access delay context. There is no big advantage of scheme with C = 2 on the Fig. 5 like on the Fig.4, but the number nodes on the Fig.5 is double number of nodes on the Fig. 4.

It is need to remark there are some rises and falls in the plot at the Fig. 4 and Fig. 5 because the process of channel selecting is a random and the channel availability is random value too.

The results of simulation show there is a threshold value availability for static ad-hoc network in context of average channel access delay. If the value availability will be bigger than threshold value (approximately 0.6…0.65 in Fig. 4 and Fig. 5) then network with smaller number of channels looks better than network with bigger number of channels as an effect of cognitive network features.

In the future DSA with cognitive radio principles and software configurable radio-terminals create a wide range opportunities for reconfigurable radio networks in military, social works, medicine, radio access technology new generation including cognitive wireless sensor networks.

CONCLUSION

In the future DSA method with cognitive radio principles and software configurable radio-terminals create a wide range opportunities for research and applications in military, social works, medicine, radio access technology new generation. The great aim of these technologies is to improve the spectrum efficiency using for radio terminal devices with SDR features.

The actual issue is the research of future parameters estimation of the cognitive radio networks, like as access delay for secondary users. The results of computer simulation for uncoordinated access method shows that access delay value depends of availability of radio channels. There is a possibility to decrease number of accessible channels without dramatically average channel access delay changing at the network with low-rate nodes. For the further studying, the problem of the access delay for coordinated access method and network with high-rate nodes will be important.

REFERENCES

1. K.R. Rao, Z.S. Bojkovic, B.M. Bakmaz "Cognitive radio networks," in Wireless multimedia communication systems. Design, Analysis and Implementation. CRS Press. Taylor & Francisc Group, NW, 2014, pp. 65–109.

2. R.C. Qiu, Z. Hu, H. Li, M.C. Wicks. Cognitive radio communications and networking. Principle and practice, UK: Wiley, John Wiley and Sons Ltd., 2012.

3. Y. Zhang, J. Zheng. Cognitive radio networks: architectures, protocols, and standards, USA: CRC Press, Taylor & Francis Group, 2010.

4. ETSI TS 103 145. (2015). Reconfigurable radio systems (RRS); System architecture and high level procedures for coordinated and uncoordinated use of TV white spaces: technical specification.

5. H. Tuttlebee, Software defined radio: origins, drivers and international perspectives, Published by John Wiley & Sons, 2002.

6. S. Filin, H. Harada, H. Murakami, K. Ishizu, "International standardization of cognitive radio systems," IEEE Communications Magazine, vol. 49, No. 3, pp. 82–89, March 2011.

7. S. Haykin, "Cognitive Dynamic Systems: Radar, Control, and Radio," in Proceedings of the IEEE vol. 100, No. 7, pp. 2095–2103, July 2012.

8. ETSI TR 102 684. (2012). Reconfigurable radio systems (RRS); Feasibility study on control channels for cognitive radio systems: technical report.

9. ETSI TS 103 143. (2015). Reconfigurable radio systems (RRS); System architecture for information exchange between different Geo-location Databases (GLDBs) enabling the operation of White Spaces Devices (WSDs), technical specification.

10. Report ITU-R SM.2256. Spectrum occupancy measurement and evaluation. SM series. Spectrum management, ITU electronic publication, Geneva, 2012.

11. A. De Domenico, S.E. Calvanese, "A survey on MAC strategies for cognitive radio networks," IEEE Comm. surveys & tutorials, vol. 14, iss. 1, pp. 21–44, 2012.

12. U. Shahid Khan, T. Maqsood, "CRN survey and a simple sequential MAC protocols for CRN learning," in Proceedings of the Second international conference on advances in cognitive radio, COCORA 2012 edited by P. Dini (Concordia university, Canada), 2012, pp. 22–27.

13. P. Lee, G. Wey, "NS2 model for cognitive radio networks routing," in Proceedings of the First International Symposium on Computer Network and Multimedia Technology, CNMT 2009 edited by J. Wu and Z. Wey (Wuhan, China), 2009, pp. 1–4.

14. M. Bhrugubanda, "A Survey on simulators for cognitive radio network," International journal of computer science and information technologies IJCSIT, vol. 5(3), pp. 4760–4761, 2014.

15. R. Kaniezhil, C. Chandrasekar, "Evaluating the probability of channel availability for spectrum sharing using cognitive radio," International journal of engineering research and applications (IJERA), vol. 2, iss. 4, pp. 2186–2197, 2012.

16. B. Canberk, S. Oktug, "A channel availability classification for cognitive radio networks using a monitoring network," in Proceedings of the 17th IEEE Symposium on Computers and Communications, ISCC'2102, 2012, pp. 690–695.

17. A. Amich, "Efficient spectrum utilization using statistical modelling of channel availability," Ph.D. thesis, University of Surrey, 2014.

18. F. Tsvetanov, I. Georgieva, S. Radeva, D. Radev "Modelling of low-rate sensor network access," in Proceedings of papers 21st Telecommunications forum, TELFOR 2013, 2013, pp. 78–81.

Forming the Panoramic SPM-Images Scans during Nanoparticles Dispersity

P.V. Gulyaev [1], E.Yu. Shelkovnikov [2], A.V. Tyurikov [3], A.I. Korshunov [4]

[1-3] Laboratory of informational and measuring systems, Institute of Mechanics UB RAS, Izhevsk, Russia
E-mail: [1] lucac@inbox.ru, [2] evshelk@mail.ru, [3] alex.tyurikov@mail.ru
[4] Kalashnikov Izhevsk State Technical University, Izhevsk, Russia
E-mail: [4] kai@istu.ru

Abstract. The basic principles of particles detectors application, overlapped SPM-images binding programs, positioning devices and sensors for nanoparticles in the scanning probe microscopy research are described.

Keywords: scanning tunneling microscopy, coordinate binding, characteristic point of the image, basis function, image shift and angle of rotation

INTRODUCTION

In present days searching of an optimal trajectory of sample movement for creation of panoramic images of its surface is an important problem of dispersity control of nanoparticles by methods of the scanning probe microscopy (SPM). The optimum trajectory has to provide:

– the coordinate binding of all images received with scanning probe microscope (SPM-images) to each other;

– minimum duration of control process.

Selection of the nanoparticles sizes has to be the result of sample movement. The less images are required for receiving selection, the quicker dispersion control process is.

FORMULATION

A series of the overlapping SPM-images at scanning probe microscopy can be received in the traditional «snake» sequence used for panoramic pictures developing. During developing of panoramic pictures the value of overlapping Δx and Δy doesn't change. During the dispersity control of nanoparticles Δx and Δy can change depending on different factors [1, 2] (quantity of particles in the pictures for examples, Figure 1). For the automation of Δx and Δy calculation procedure it is necessary to formalize the following procedures.

1. Detecting of special (control) points on the SPM-image i.e. the centers of the particles; calculation of their sizes and coordinates, selection filling; selection filtration for removal of the duplicating sizes of the particles located in a zone of scans overlapping [3, 4].

2. Shifting of the sample or the scanning area in sight of the microscope, implementation of the subsequent scan; definition of mutual orientation of the overlapped scans (shift, turn),

definition of position of special points in single coordinate system. Couples of similar special points are used for a coordinate binding of the overlapped SPM-images. The values of shift and turn of a set of the similar pairs form shift and turn histograms. This procedure formalization is described in [4].

3. Definition of the peripheral area containing enough special points. It is the planned overlapping area. For the SPM-images of high quality 2–3 pairs of special points in an overlapping zone are sufficient.
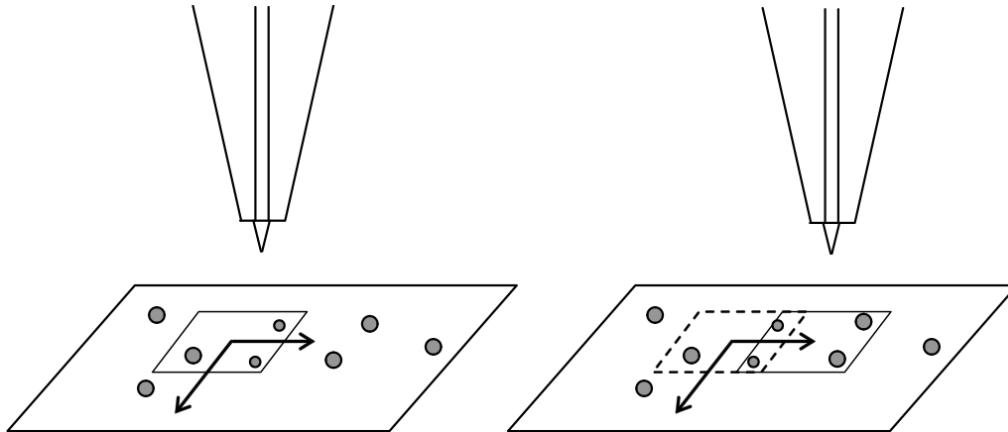
Figure 1. Scanning by the overlapping images and a coordinate binding of a probe and particles to a single coordinate system

OVERLAPPING AREA FORMATION

Consider the definition of optimal overlapping area and the features of a coordinate binding of the overlapped SPM-images.

If the particles concentration on a surface is small or the particles are localized within a certain area the duration of control process can be significant. For reduction of its duration it is necessary to reduce overlapping zones depending on a quantity of the found particles.

The size of overlapping depends on the following factors.

1. The more particles or other special points are on the periphery of the image, the less the overlapping area is:

1.1. the detectors of the special points based on the analysis of surface curvature are sensitive to noise therefore the size of overlapping is increased at their application;

1.2. detectors of special points based on the correlation analysis of the image and reference images of special points do not demand the overlapping zone increasing since they can carry out a coordinate binding of the SPM-images without presence of the particles.

2. Use of movements sensors or other means of the images overlapping estimation complication gives the possibility to reduce the overlapping size.

The overlapping area at the periphery of the image has to contain enough pairs of points for the subsequent coordinate binding of the overlapped images. The minimum quantity of pairs is two. Special points coordinates define the position of the overlapping zone and the planned shift of the subsequent scan. This shift will be used for results specification of the coordinate binding algorithm.

If the scanner control voltages are used for overlapping of the SPM-images, difference between real and planned overlappings will be approximately 5–10 % owing to temperature drift of the structure.

If for obtaining the overlapping images the stepper drive is used, the real and planned overlappings can differ for tens percent. In this case it is necessary:

1. to increase the minimum value of the overlapping coefficient;

2. to use movement sensors indications of which are used for filtration of coordinate binding results.

At shift histograms there is a set of false local maxima. At small quantity of the special points in the overlapping area, the amplitudes of true and false peaks are equal. In this case the estimation of the overlapping size or sensors indication allows to filter false extrema of the shift histogram.

Other types of the coordinate binding inaccuracies are:

1. at significant density of the particles there are histogram maxima with shift close to zero;

2. noises distort shape of the particles and their centers coordinates therefore there can be some small local maxima instead of one big in the shift histogram.

The shift estimation eliminates the first type of errors and limits an error of coordinate binding by means of a true histogram maximum positioning area localization.

THE SAMPLE NANOSCALE MOVEMENTS FORMATION

Originally scanning is carried out with constant Δx and Δy overlapping coefficients until the quantity of the nanoparticles is insignificant. Thus the coordinate binding is carried out by method of statistical differentiation with use of reference images (Figure 2) [4]. Processing of the SPM-image with using a detector gives the average radius of roughnesses which is used for scaling of the SPM-image of the special point.
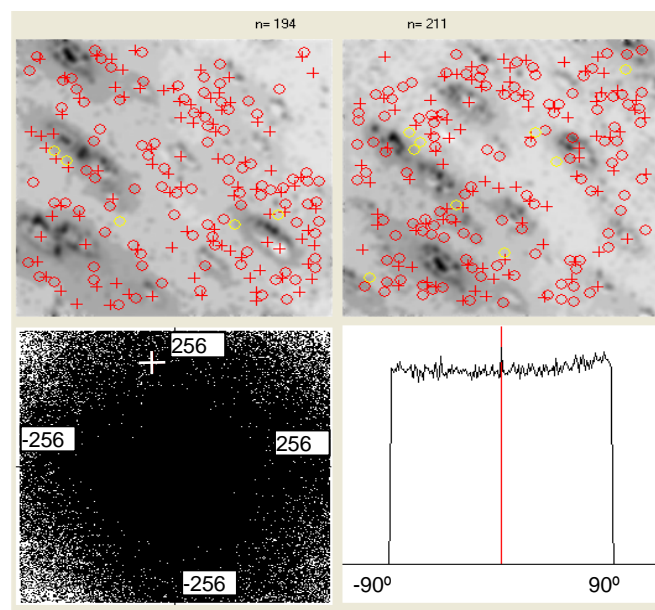
Figure 2. SPM-images **c**oordinate binding results with the reference image (two overlapping images of 256×256 pixels are above, the special points are marked by crosses and circles; two-dimensional shift histogram of 512×512 pixels with the maximum marked by a cross and the turn histogram are below)

If the detector shows enough quantity of nanoparticles in the SPM-image, the "tracing" trajectory of the sample shift can be established (Figure 3). The coordinates and the size of particles are established by means of the detectors of particles depending on the curvature of a surface. Thus coordinates are sorted by increase. The minimum values of overlapping Δx, Δy is established at the level of 2 rcp, where rcp is the average radius of the particles determined by the detector. Then values Δx, Δy serially increase until enough quantity of nanoparticles are at the area of overlapping.
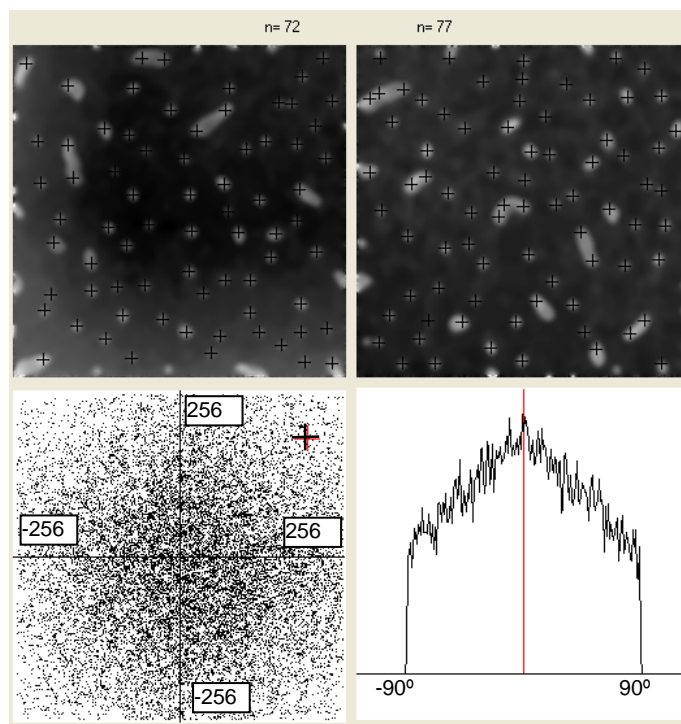
Figure 3. Results of a coordinate binding of SPM-images with the analysis of a surface curvature
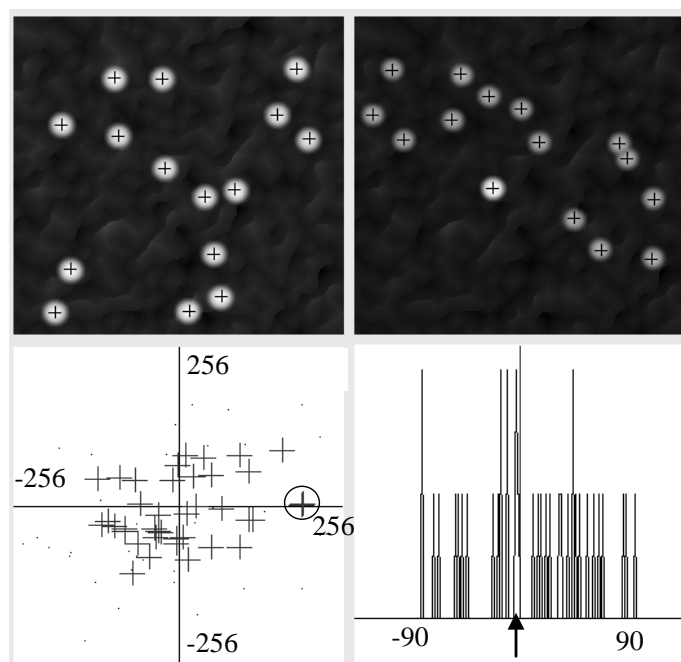
Figure 4. Use Δx and Δy values for the choice of a true SPM-images shift

In the subsequent calculation of orientation parameters of these SPM-images, using the values Δx and Δy as shift estimation is obligatory owing to the presence of the set of "false" extrema at the shift histogram.

The case when values Δx and Δy allow to choose the true estimate from a set of estimations of the shift of the SPM-images is presented in Figure 4.

Using the Drives of the Coordinate Nanoscale Movements of the Sample

For coordinate nanoscale moving of the sample at *XY* plane the step drives of positioning can be used. Thus the established overlapping values of Δx and Δy are used for determination of the operating signals amplitude. As it was mentioned, the size of a positioning error can be significant [5]. In this case the estimations of Δx and Δy can be inexact and their application will lead to an error of a coordinate binding of the SPM-images. This problem is solved by use of drives with the integrated movement sensors [6] considering functioning features of the drive of nanoscale coordinate movements.

Conclusions and Results

Thus, optimum scans sequence formation demands complex use of nanoparticles detectors, programs of mutual shift calculation of the overlapped SPM-images and the sample positioning drive control. Detectors are used to define the planned overlapping area the estimation of which is used for the nanoscale movements drive control and calculation of the mutual shift of the overlapped SPM-images. The sensors of movements integrated into the drive can be used for specification of an estimation of the real overlapping area if an error of drives positioning is significant.

References

1. D.W. Pohl, R. Moller, "Tracking" tunneling microscopy," Rev. Sci. Instrum., vol. 59, No. 6, p. 840, 1988.

2. R.V. Lapshin. Russia Federation Patent No. 2181212. Way of a scanning microscope – nanolithographer probe movement in the field of a rough X-Y positioner. Publ. 10.04.2002.

3. P.V. Gulyaev, E.U. Shelkovnikov, A.V. Tarasov and others, "Features of the surface curvature detectors use for nanoparticle dimensions analysis," Chemical Physics and Mezoskopy, vol. 15, No. 1, pp. 138–143, 2013.

4. Y.K. Shelkovnikov, M.R. Gafarov, P.V. Gulyaev and others, "Building SPM images of the surface with the multiframe mode of scanning tunneling microscope," Chemical Physics and Mezoskopy, vol. 10, No. 4, pp. 514–520, 2008.

5. P.V. Gulyaev, Yu.K. Shelkovnikov, A.V. Tyurikov, N.I. Osipov, "High-accuracy inertial rotation-linear piezoelectric drive," Russian Electrical Engineering, vol. 81, No. 10, pp. 521–524, 2010.

6. V.A. Bykov, "New developments in NT-MDT microscope line," SPM-2004, Proceedings, Nizhni Novgorod, May 2–6, 2004, p. 73.

Exploiting Intelligent Systems in Aircraft Pitch Control

I.N. Ibrahim [1], M.A. Al Akkad [2]

Dept. Mechatronics and Robotics, ISTU, Izhevsk, Russia
E-mail: [1] ibrncfe@gmail.com, [2] aimanakkad@yandex.ru

Abstract. This paper aims to develop a model for controlling the aircraft pitch angle during its longitudinal motion. The developed model is a time variant nonlinear mathematical model that reflects all the parameters that affect the aircraft dynamics, by describing its motion, space range, and dynamic model of its turbo engine. Several experiments were made on a simulation model of the aircraft to define the problems that may face the autopilot, and the results showed that there is a close relation between the model parameters and the inertia, and between the non-linearity and changing with time that describes the models equations that required simplifying and approximating the model. The developed model is characterized by its precision in describing the aircraft motion and by offering real dynamics compared to other proposed models of similar cases, as it does not rely on rounding operations that allow putting precise evaluation of several pitch controllers. This research tries to find the best performance solution for the autopilot when taking into consideration the time response and the changes within the dynamical model.

Keywords: PID controller, Fuzzy logic controller, Steady-state error, Pitch angle

1. INTRODUCTION

Many researches concerning the problems of stability and control of aircrafts was appeared, started by flight experiments on physical models [1, 2] which recently reached using the computer for making simulations which mathematically describe the dynamic and physical characteristics of the aircraft.

A mathematical model was developed in the year 2000 aiming at developing a method that automatically controls the landing of the aircraft [3], this model started as a non-linear model then changed to a linear model that made the control mechanism linear. Then, a mathematical model [4] which accurately describes the aircraft motion was developed, but with constraints on the range of the aircraft motion and flight conditions of the pilot, and when linearizing this model, it became unable to describe the dynamics of the aircraft. In 2011, some researchers suggested a mathematical model [5] that describes the aircraft motion in 3D space of DOF, which was a linear model that simplified the design of the required controllers. The feature that was common among most of the research was its low quality in describing the dynamics and motion of the aircraft due to its dependence on mathematical approximation operations and the linearizing procedures of the systems in order to simplify the study. In this study, the developed model is a mathematical model that describes the motion of a jet-engine small-sized aircraft using LabVIEW language and without any approximation operations, trying to achieve an actual study that shows the effects of controllers on the aircraft, aiming to study the response and stability enhancement. This paper

gives details about the stages of the modeling method. Starting from the formulation of the differential equations that describes the aircraft motion, until the development of the mathematical model describing the jet engine, and the model that describes the environment around the aircraft taking into consideration the input data such as the components that control the wings, thrust force, measured output data, and the aerodynamic data. In 3D space, two types of aircraft motion are distinguished: longitudinal motion and lateral-directional motion. This simplifies the controllers design process. Motion is controlled by the elevators, the ailerons, and the rudder. Here focusing will be on the longitudinal motion and study the control response of the pitch angle by controlling the elevators.

The objective of this research is to improve the control system stability of the pitch angle of an aircraft model during its longitudinal motion, depending on a non-linear time variant mathematical model. The resulting model in this study is characterized by the accuracy in describing the aircraft motion, and in giving real dynamics. Because it does not dependent on approximation operations or linearizing procedures, allowing to reach a precise evaluation of many controller types as traditional and fuzzy controllers which are used to reach the best response.

In the first part of this paper, modeling the control system and defining its technical specifications were discussed. Then aircraft control methods and its motion coordinates in space were presented. In the second part, the controllers design and their effect on the system's performance and response. Three models of PID controllers were used like the general PID controller, the anti-windup PID controller, and the Washout PID controller, and fuzzy control system; taking into consideration that during the study of response, three points were focused on the steady-state error, the time response, and the vibrations.

2. MODELING OF THE SYSTEM

Designing a control system of a jet aircraft requires building a mathematical model that comprehensively describes the aircraft motion, and how it responds to the commands and the external conditions. Creating this model requires modeling the following aspects of the aircraft: the aircraft motion, the engine, the natural environment around the aircraft, and the aerodynamic model.

2.1. Aircraft Motion Modeling

The aircraft moves in 3D space and its motion changes non-linearly by time, the thing that complicates the analyzer mission in finding a fixed mathematical model which describes the aircraft motion. For putting a time invariable mathematical model, the analyzers usually make approximation operations. In this research, the differential equations which describe the actual aircraft motion within the simulation environment are programmed as a method of modeling the motion and the actual response of the aircraft without making any approximation. There are many external factors that affect the aircraft model: weather factors and disturbances, aircraft weight, basic control parameters, jet thrust force, aerodynamic parameters, and the physical characteristics of the aircraft. Depending on Newton Second Law of motion [6], the equations that describe the aircraft motion can be deduced. These equations offer a comprehensive description of the aircraft motion taking into consideration that the coordinates' frame of the aircraft-body is the reference frame. These equations are divided into four groups, which describe the aircraft velocity and moment relative to the coordinate's axis, the aircraft location, and its aerial orientation [11]:
- Force Equations:

$$\dot{U} = RV - QV - \frac{F_x^G}{m} + \frac{F_x^A}{m} + \frac{F_x^T}{m}$$

$$\dot{V} = -RU + PW + \frac{F_y^G}{m} + \frac{F_y^A}{m} + \frac{F_y^T}{m}$$

$$\dot{W} = QU - PV + \frac{F_z^G}{m} + \frac{F_z^A}{m} + \frac{F_z^T}{m}$$

- Kinematics Equations:

$$\dot{\phi} = P + Q \sin\phi + \tan\theta + R \cos\phi \tan\theta$$

$$\dot{\theta} = Q \cos\phi - R \sin\phi$$

$$\dot{\psi} = Q \sin\phi \sec\theta + R \cos\phi \sec\theta$$

- Moment Equations:

$$\Gamma \dot{P} = I_{xz}\left(I_x - I_y + I_z\right)PQ - \left[I_z\left(I_z - I_y\right) + I_{xz}^2\right]QR + I_z M_x + I_{xz} M_z$$

$$I_y \dot{Q} = \left(I_z - I_x\right)PR - I_{xz}\left(P^2 - R^2\right) + M_y$$

$$\Gamma \dot{R} = \left[\left(I_x - I_y\right)I_x + I_{xz}^2\right]PQ - I_{xz}\left(I_x - I_y + I_z\right)QR + I_{xz} M_x + I_x M_z$$

$$\Gamma = I_x I_z - I_{xz}^2$$

- Navigation Equations:

$$\dot{p}_N = Uc\theta c\psi + V\left(s\phi s\theta c\psi - c\phi s\psi\right) + W\left(s\phi s\psi + c\phi s\theta c\psi\right)$$

$$\dot{p}_E = Uc\theta c\psi + V\left(c\phi c\psi + s\phi s\theta s\psi\right) + W\left(c\phi s\theta s\psi - s\phi c\psi\right)$$

$$\dot{h} = Us\theta - Vs\phi c\theta - Wc\phi c\theta$$

where (U, V, W) are components of velocity along x, y, z body axes, (P, Q, R) are Roll, Pitch and Yaw rates about body axes, m is the total mass, (θ, φ, ψ) are Pitch, Roll and Yaw angles about body axes, I_X, I_Y, I_Z are the moments of inertia about x, y, z body axes, M_x^T, M_y^T, M_z^T are moments produced by the propulsive forces about the body axes, M_x^A, M_y^A, M_z^A are moments produced by the aerodynamic forces about the body axes, M_x, M_y, M_z are the resultant of moments about the body axes, and (p_n, p_E, h) are the geographical coordinates.

2.2. Equations of Motion

The aircraft is influenced by force and moment components; the forces affecting the center of gravity are divided into three main forces: the gravity force (F^G), the jet thrust force (F^T), and the aerodynamic force (F^A), while the moment components, which affect the aircraft, are only the aerodynamic moments (M^A). If we suppose that the aircraft engine is allocated at axis x of the aircraft-body frame, then the components are defined as follows [11]:

- gravitational forces: $\begin{pmatrix} F_x^G \\ F_y^G \\ F_z^G \end{pmatrix} = -mg \begin{pmatrix} sin\theta \\ cos\theta sin\phi \\ cos\theta cos\phi \end{pmatrix}$,

- aerodynamic forces: $\begin{pmatrix} F_x^A \\ F_y^A \\ F_z^A \end{pmatrix} = \overline{q}S \begin{pmatrix} C_{x,t} \\ C_{y,t} \\ C_{z,t} \end{pmatrix}$,

- propulsive forces: $\begin{pmatrix} F_x^T \\ F_y^T \\ F_z^T \end{pmatrix} = \begin{pmatrix} Th \\ 0 \\ 0 \end{pmatrix}$,

- total forces: $\begin{pmatrix} F_x \\ F_y \\ F_z \end{pmatrix} = \overline{q}S \begin{pmatrix} F_x^G + F_x^A + F_x^T \\ F_y^G + F_y^A + F_y^T \\ F_z^G + F_z^A + F_z^T \end{pmatrix}$,

- aerodynamic moments: $\begin{pmatrix} M_x^A \\ M_y^A \\ M_z^A \end{pmatrix} = \begin{pmatrix} bC_{l,t} \\ \overline{c}C_{m,t} \\ bC_{n,t} \end{pmatrix}$,

where g is the gravity constant, $\overline{q}$ is the dynamic pressure, S is the Wing area, Th is the thrust force, b is the wing span, c is the mean aerodynamic chord of the wing, $(C_{x,t}, C_{y,t}, C_{z,t})$ are the total force coefficients in x, y, z body axes, $(C_{l,t}, C_{m,t}, C_{n,t})$ are the total rolling, pitching and yawing-moment coefficients. In case, there is a wind, the equations that describe the aerodynamic motion of the aircraft are modified where the real air speed (V_T), and the aerodynamic angles of the aircraft axis α, and β relative to the wind coordinate frame (W_C):

- airspeed: $V_T = \sqrt{U^2 + V^2 + W^2}$;

- attack angle: $\alpha = tan^{-1}(\dfrac{W}{U})$;

- sideslip angle: $\beta = sin^{-1}(\dfrac{V}{V_T})$.

The aerodynamic parameters can be obtained by experimenting on prototypes of the aircraft in an air tunnel, and as a result, data covering a wide range of air attack and sideslip of aircraft can be obtained and grouped in 50 tables. Taking into consideration the practical values of these angles in actual tests, these tables are reduced to 20 tables [6, 7].

2.3. Engine Modeling

The jet aircraft is driven by a combustion turbine engine that discharges hot air, modeling this engine depends on its power, throttle level, and some measurements offered by the aircraft indicators such as, altitude, and atmosphere pressure, etc.
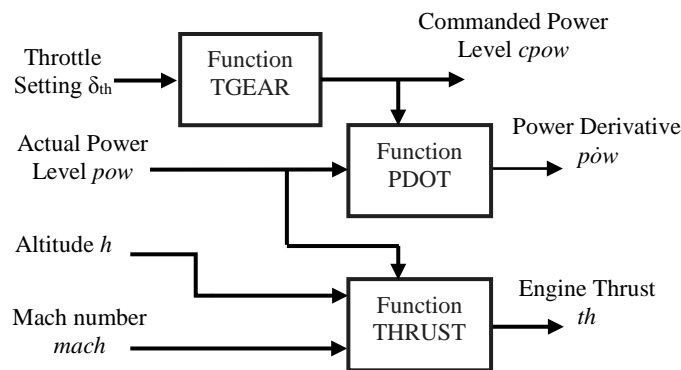
Figure 1. Block diagram of the aircraft engine model

Figure 1 illustrates the block-diagram of the aircraft engine model [7] showing the main operations that take place in the engine: PDOT, TGEAR, THRUST, in addition to the required data to make these operations such as the throttle value δ_{th}, and the current altitude value h of the aircraft, and airspeed in (*mach*) and engine power value *pow*. The thrust operation calculates the thrust depending on the current power values of the engine, and the velocity and altitude of the aircraft. Data is given in three tables; each table takes into consideration one state of the working states of the engine (military, idle, or maximum) [6, 8].

2.4. Modeling the International Standard Atmosphere

Modeling the International Standard Atmosphere requires the study of several layers of the atmosphere starting at the sea level until the Stratosphere. Air in the surrounding environment is characterized by a set of properties of which some have a direct influence on the aerodynamic powers affecting the flying objects such as, weight, mass, and pressure, and some other properties have indirect influence such as the degree of temperature. Decreasing air density leads to decreasing the thrust and altitude force of the aircraft in spite of keeping the same control values. Therefore, it will be useful to study the natural atmosphere and put a dynamic model of the aircraft adaptive with the natural atmospheric changes. Modeling of the International Standard Atmosphere starts by calculating the natural atmosphere parameters, which are variable. The airspace can be divided into several layers due to the altitude from the sea level as shown in Figure 2.
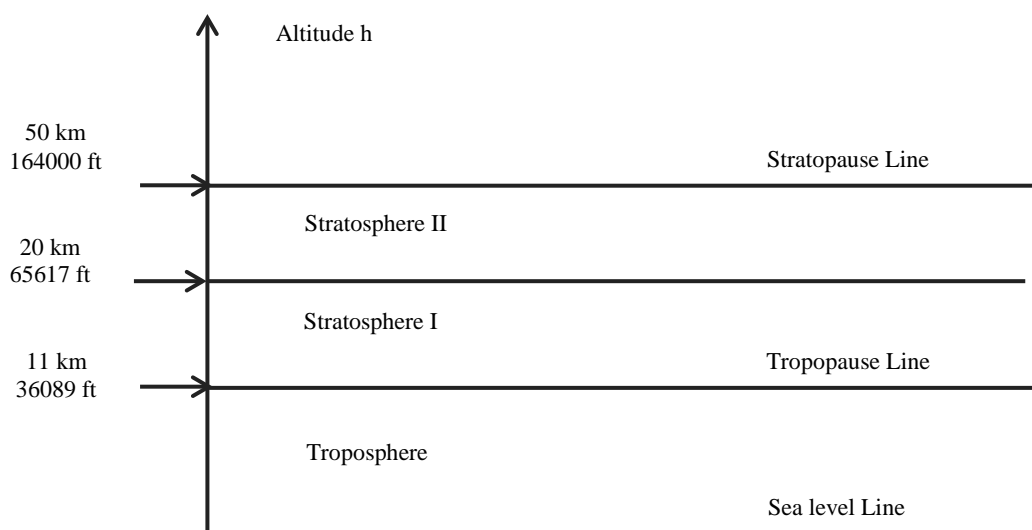
Figure 2. Layers of atmosphere

Then the standard atmosphere parameters can be calculated using the following equations, where ρ is the atmospheric density, T is the atmospheric temperature and P is the atmospheric pressure.

$$at\,Sea\,Level \begin{cases} p_s = 101.325\ \dfrac{N}{m^3}\ ,\ 2116.7\ \dfrac{lbf}{ft^2} \\[2mm] \rho_s = 1.225\ \dfrac{kg}{m^3}\ , 0.002378\ \dfrac{slug}{ft^2} \\[2mm] T_s = 15\ ^0C\ ,\quad 518\ ^0R \end{cases}$$

$$at\,Tropopause\,Level \begin{cases} T_{tr} = 389.99 \quad (^0R) \\ p_{tr} = 472.68 \quad (\frac{lbf}{ft^2}) \\ \rho_{tr} = 7.0613E-4 \quad (\frac{slug}{ft^2}) \end{cases}$$

$$in\,Troposphere \begin{cases} T = T_s - Lh = 518.69 - (3.5662E-3) \times h\,(^0R) \\ p = (1.1376E-11) \times T^{5.256} \left(\frac{lbf}{ft^2}\right) \\ \rho = \frac{p}{RT} = (6.6277E-15) \times T^{4.256} \left(\frac{slug}{ft^2}\right) \end{cases}$$

$$in\,Stratosphere \begin{cases} T = 389.99\,(^0R) \\ p = p_{tr} \cdot e^{\frac{g}{RT_{tr}}(h_{tr}-h)} \\ \rho = \frac{p}{RT} = (1.4939E-6) \times P \left(\frac{slug}{ft^2}\right) = 2678.4\,e^{-(4.8063E-5)h} \end{cases}$$

3. DESCRIPTION OF AIRCRAFT MOTION AND METHODS OF MOTION CONTROL

Table 1 shows the technical properties that describe the aircraft model as a non-linear time variant model, for making experiments build the controllers and after that verify its performance. The used aerodynamic data were obtained by experiments made in the air tunnel on F16 aircraft by the American Space Agency [6, 8]. We will depends in this research on ready components for designing the aircraft and on the traditional and fuzzy control libraries for controllers design within LabVIEW software from National Instruments company.

The aircraft motion is controlled by the following components: the elevator, the rudder, the aileron, and the throttle; the throttle controls the jet power force while the other parts generate the aerodynamic forces that direct the aircraft motion as lift, rotation and sliding-slip. Figure 3 shows these parts and the generated motions [3]. Afterwards, The Derived Dynamic System of the Aircraft Model is shown in Figure 4 that contains the differential equation of motion, the engine model, the aerodynamic model and the ISA model. These models require two inputs: control variables and state variables.

Table 1. The technical properties of the aircraft model

Inertia Moments	$I_z = 63100$ slug.ft^2	$I_y = 55814$ slug.ft^2		$I_x = 9496$ slug.ft^2
	$I_{xz} = 982$ slug.ft^2		$I_{yz} = I_{xy} = 0$ slug.ft^2	
Mass and Geometric Properties	$c = 11.32$ ft	$b = 30$ ft	$S = 300$ ft^2	Weight 20500 lbs
Actuators	Aileron limit $\delta_\xi = \pm21.5$		Elevator limit $\delta_\eta = \pm25$	Rudder limit $\delta_\zeta = \pm30$
Rate limit	$r = 120°/s$		$p = 80°/s$	$q = 60°/s$

4. THE RESULTS OF CONTROLLERS DESIGN

The variables that describe the dynamic model of the aircraft are strongly correlated together; this is associated with inertia, non-linearity and asymmetry of the controlled aircraft input and output. While designing the fuzzy controller, some problems appeared related to error signals normalization of velocity and others, which is generally solved by approximation methods on the dynamic models in order to cancel the close coupling between these variables, or to largely minimize it so that it can be neglected, and therefore make disconnection between the equations. For example, the control process of lifting the aircraft is described as a longitudinal motion by the equations in [4], where we notice the relation of the aircraft state variables with the elevators variable η:

$$\begin{cases} \dfrac{u(s)}{\eta(s)} = \dfrac{f_u(s)}{\Delta(s)} \\[2mm] \dfrac{\omega(s)}{\eta(s)} = \dfrac{f_{\omega(s)}}{\Delta(s)} \\[2mm] \dfrac{q(s)}{\eta(s)} = \dfrac{f_q(s)}{\Delta(s)} \\[2mm] \dfrac{\theta(s)}{\eta(s)} = \dfrac{f_\theta(s)}{\Delta(s)} \\[2mm] \dfrac{\alpha(s)}{\eta(s)} = \dfrac{f_\alpha(s)}{\Delta(s)} \\[2mm] \dfrac{\gamma(s)}{\eta(s)} = \dfrac{f_\gamma(s)}{\Delta(s)} \end{cases}$$
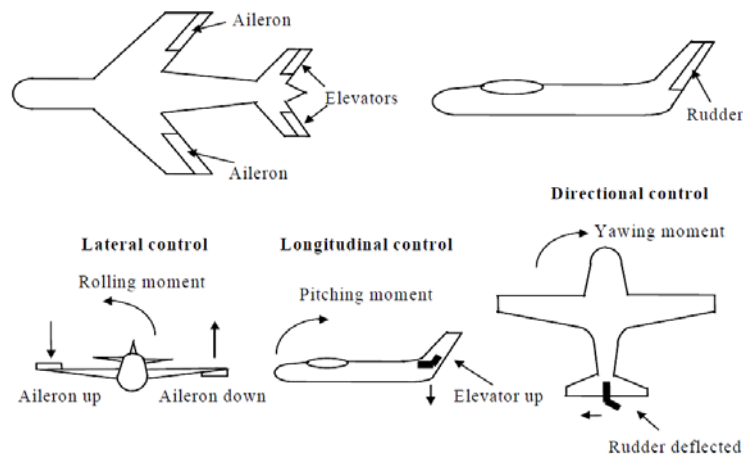
Figure 3. Deflection Actuators and motion generated

Sometimes, approximation operations and separation of the variables are used to get independent equations within definite assumptions like the equations in [5]:

$$\frac{\theta(S)}{\eta(S)} = \frac{11.7304S + 22.578}{S^3 + 4.9676S^2 + 12.941S}$$

In this research, we evaluate the control systems' performance by monitoring the aircraft behavior and motion without putting any constraints on the variables that generate the separation operations in the motion equations. While the changes that may happen on the variables that describe the aircraft motion will be studied when controlling a single variable of

the system's input variables, noting that any change in one of the input variables is accompanied with slight or large changes in the output variables due to the changing input variable, as in Figure 5.
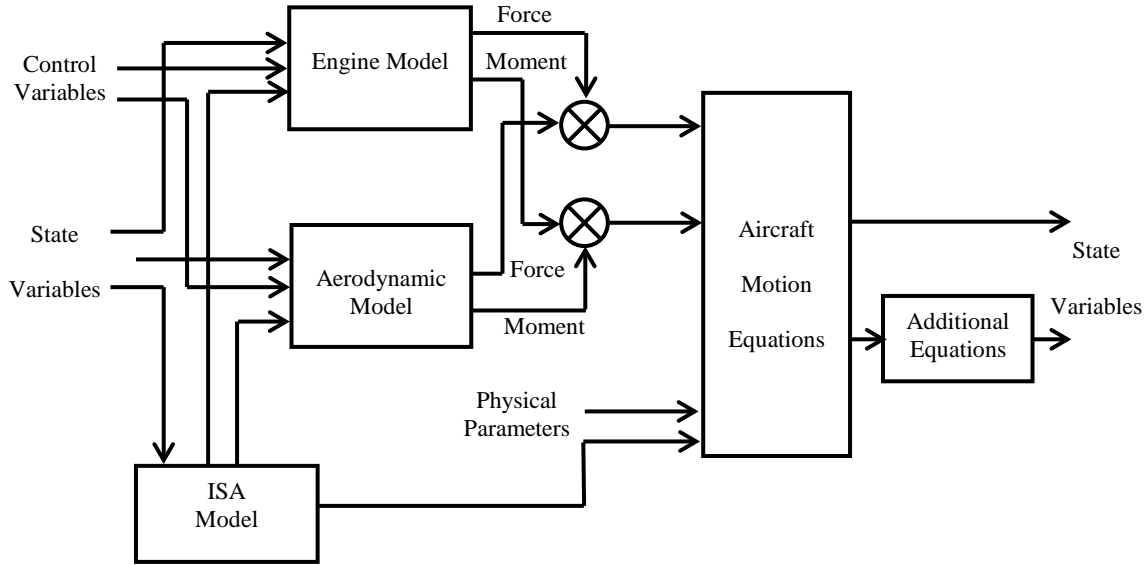
Figure 4. Block diagram of Plant Dynamic model
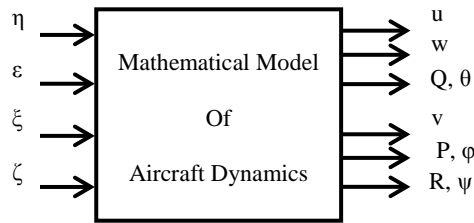
Figure 5. The mathematical model of the aircraft motions

First, we clarify several different types of PID controllers with pointing out the differences between them, the used fuzzy controllers and their description, and result comparison between controllers; according to the physical properties of aircraft set in the Table 1. Experiments and measurements were made on the previously described aircraft within the flight conditions shown in the Table 2.

4.1. Proportion, Integrated, and Differential (PID) Controller Design

A close-loop control mechanism used in industrial control systems, and considered a standard control structure in the conventional control theory. The linear relation of the mathematical model between the controller input and output is described by the following equations [9]:

$$u(t) = K_p e(t) + K_i \int e(t)dt + K_d \frac{de(t)}{dt}$$

$$u(t) = K_p [e(t) + \frac{1}{T_i} \int e(t)dt + T_d \frac{de(t)}{dt}]$$

The controller requires defining the values of PID gain parameters in order to get the best performance of the controller. Changing these Parameters will cause changes in the system response compared to the required response. The parameters will be defined using Ziegler-

Nichols algorithm [10]. In this research, three different types of PID controllers are explained depending on the obtained results in order to get rid of vibrations, steady-state errors, and to minimize the response time.

Table 2. Primary flight conditions for the controllers experiments

U component of velocity along x body axis	243.84 m/s
V component of velocity along y body axis	0
W component of velocity along z body axis	0
p roll rate about x body axis	0
q pitch rate about y body axis	0
r yaw rate about z body axis	0
Altitude	3.048 km
Airspeed Control	Constant

4.1.1. General PID Controller
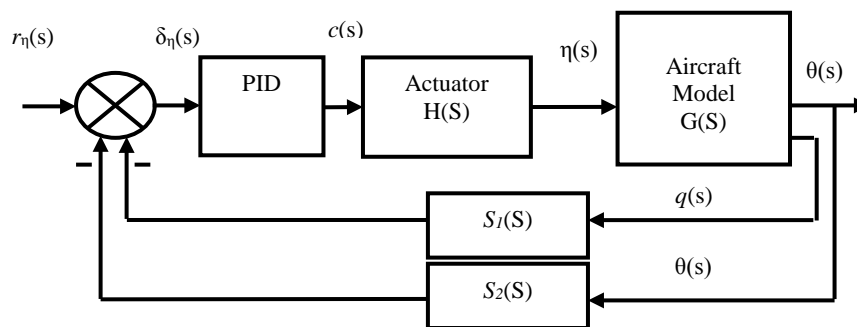
Figure 6. Block diagram of a general PID Controller: $S_1(S) = \dfrac{1}{1+2S}$, $S_2(S) = \dfrac{1}{1+6S}$

Figure 6 shows using a general PID controller to control the aircraft pitch angle θ. The required value r_η of the angel is defined, the error is calculated depending on the current angel, and then the control signal C is given to the actuator of the elevators, which in turn will move with an angle of η, which is responsible for moving the aircraft. The pitch rate q of the aircraft motion through axis y is included to maintain the motion within the limit of velocity and acceleration of the aircraft motion in order to avoid the risks resulting from sudden movements and to reduce vibrations. Figure 7 shows the control results, and Figure 8 shows the differences when including velocity rate in the control process.
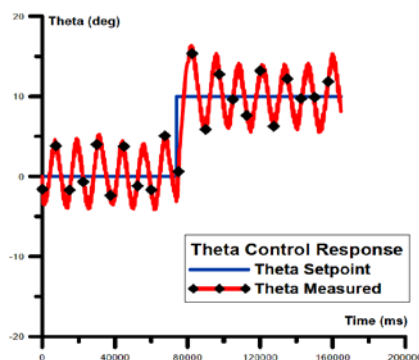
Figure 7. Time response of the aircraft model general PID controller
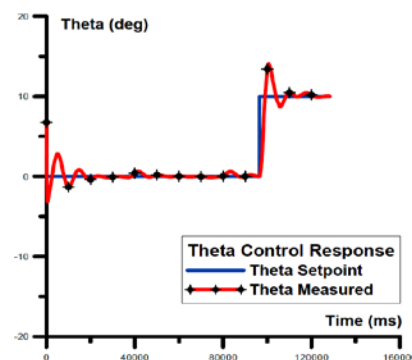
Figure 8. Time response of the general PID controller after including the pitch rate

4.1.2. PID-Anti Windup Controller

Block diagram in Figure 9 shows PID-Anti Windup Controller [9]. This controller work is based on getting rid of the error when exceeding the elevators operation limit of the aircraft, which generally leads to breaking down the closed feedback loop and transfers system operation as if it is in an open loop. The integrator existence in the controller leads to error integration and the immersion of large values making the aircraft in an unstable state and out of control.

Figure 9. Block diagram PID-Anti Windup Controller

Figure 10. PID-Anti Windup Controller time response of the aircraft model

Figure 10 shows the result of control, and we notice regularity in the output vibrations within fixed limits that are coming from the aircraft aerodynamic model.

Figure 11. PID-Washout controller diagram

103

Figure 12. PID-Washout Controller time response of the Aircraft model

The final controller offers a very slight steady-state error, and it is acceptable. This controller is characterized by a quick response to the set points, but it suffers from the problem of the existence of vibrations in the cases when moving from a set point to another as shown in Figure 12; these vibrations are damped after 30 seconds.

4.2. The Fuzzy Controller

It is considered one of the important control systems among the smart control systems, and it is defined as a hybrid model between artificial intelligence and control theory due to its dependence on emulating the human thinking way in the control decision-making methods. The adopted fuzzy controller in this research is Mamdani model based on the extraction of membership functions of input and output together. Mamdani model allows to describing the human experience more obviously than other fuzzy systems such as Sugeno or Tsukamoto, so that it is considered the closest to the human behavior. The fuzzy controller is considered more flexible where controlling its behavior can be made using the rules without the need to using theories and changing the numbers in order to get slight error compared to PID control. Three fuzzy controllers were suggested to achieve optimal control of the aircraft pitch angle within the longitudinal control space. Three different control methods exist for these controllers to achieve the best performance. Several problems appeared related to the aircraft system when using the fuzzy control, as this system's variables are asymmetric 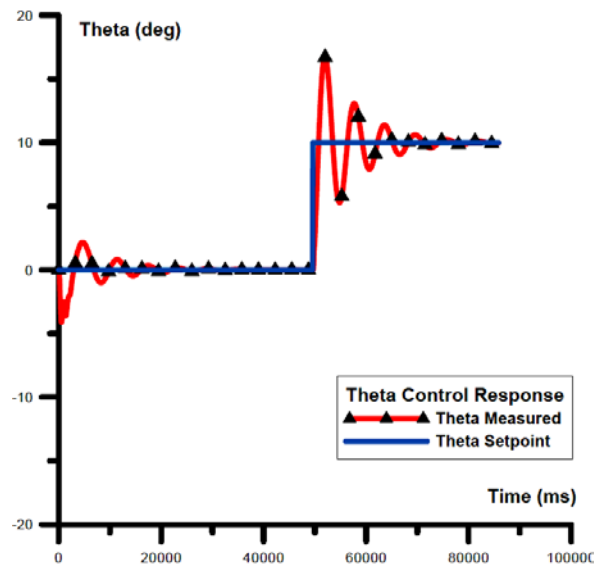and have a wide range. One of these problems is the use of normalization in the fuzzy control. The normalization process cancels the accuracy, and the variations will be from the tens and hundreds order (e.g., the change from 10.01 to 10.03 degrees by mistake means a large decrease in velocity and lead to the existence of a steady-state error permanently in the velocity state of the aircraft). Also a change in the pitch error of the aircraft around axis *y* from 5.00 to 5.05 degrees (i.e., declining of the aircraft and hence generating a steady-state error in the aircraft pitch and occurring of vibrations in the range −0.7 to +0.8 degrees which lead to disturbances of the aircraft altitude). These variations are considered acceptable by some aircraft's control systems. The fuzzy logic systems face the problem of dissymmetry in the variables where the aircraft moves around axis y in angles range between +15 to −80 degrees. These characteristics of the system's control and status variables put a burden on the controller designer in designing non-arbitrarily the best affiliation functions to reach a controller that contains the least possible value of vibrations, small steady-state error, and

high response time. These issues of the used fuzzy logic controllers and the obtained solutions to solve these issues will be discussed. The idea of damping the vibrations is merged in the fuzzy logic controllers, and will be discussed in the last PID controller in which a high-pass filter is used.

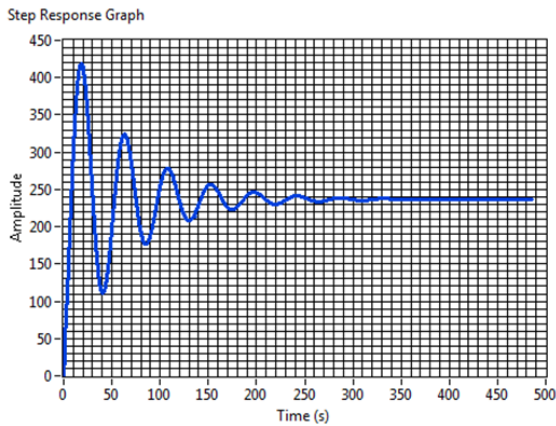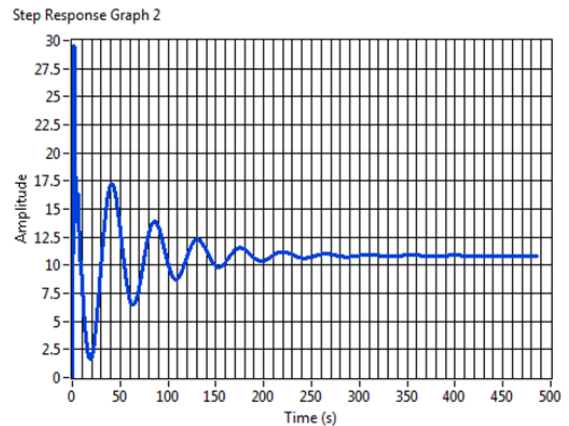**Figure 13.** Velocity response along x to 1° step elevator input

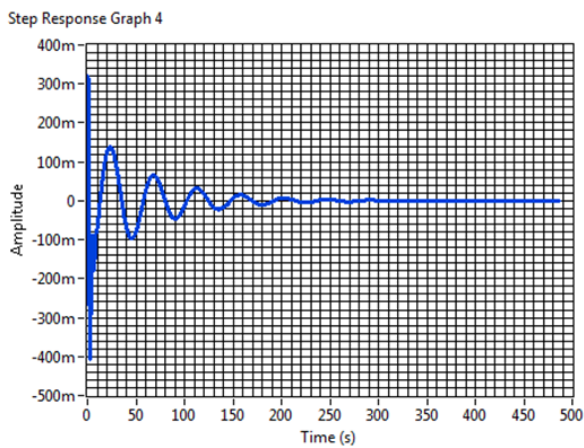**Figure 14.** Yaw angle response to 1° step elevator input

Figure 15. Pitch rate response to 1° step elevator input

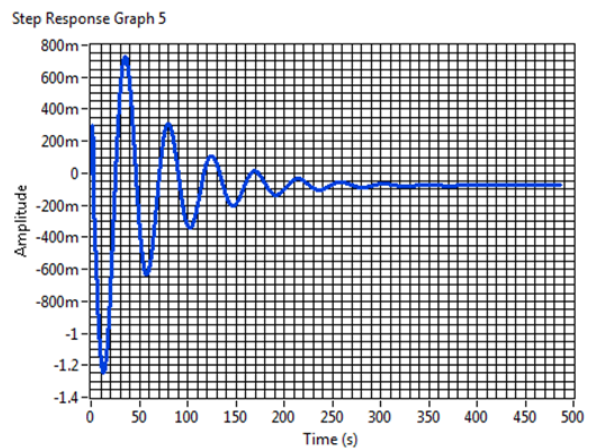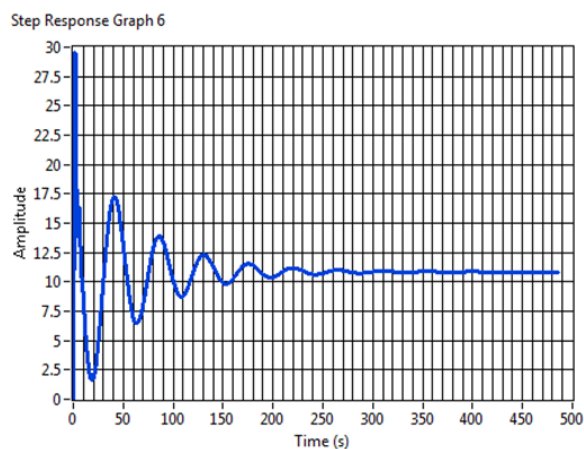**Figure 16.** Pitch angle response to step 1° elevator input

Figure 17. Attack angle response to 1° step elevator input
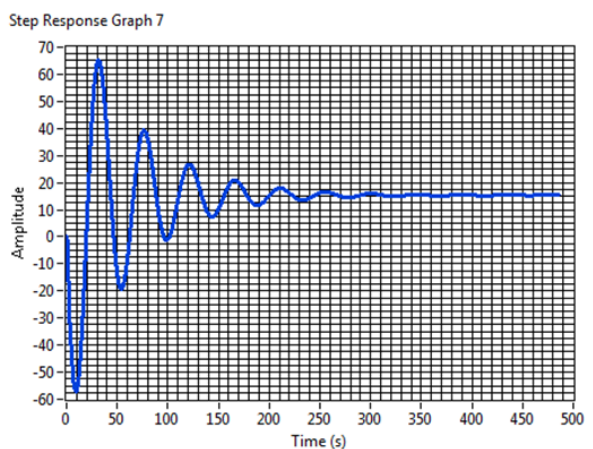
Figure 18. Aircraft flight angle response to 1° step elevator input

4.2.1. Studying the System's Response without a Controller to Facilitate Defining the Rules

This research explains the system's response to those variations within the longitudinal motion, and this is when controlling the elevators by an angle η that leads to raising and lowering the aircraft within flight motion of angle θ. The response curves are shown in Figures 13–18 help in having a clear vision about the variations that occur on the aircraft state variables and the negative and positive effects that should be considered when altering the climb and landing pitch angle. When a change of one degree occurs, vibrations occur on all the aircraft variables that damp and vanish after 250 msec. In addition, changes in the variables amplitude and direction occur. We can notice the amplitude of these vibrations and their disparity for finding the suitable affiliation function and its location, finding the suitable rule that damps and restrict this vibration, and does not allow its repetition when designing the fuzzy logic controller.

4.2.2. Designing the Fuzzy Controller

Figure 19 shows the block diagram of a simple fuzzy logic controller of the type single-input/single-output controller (SISO), which has a single input variable called *angle error*, and a single-output variable called *elevator angle*. Many experiments and measurements were carried out on this system at the assumed flight conditions by building several fuzzy logic controllers to solve the mentioned problems that differ from each other by the rules and the membership function. The reached accuracy of the system is a steady-state error $E = -0.08342$, in the fuzzy logic controller under investigation, in addition to canceling the vibrations or reducing them largely.

The input and output membership functions were designed due to Figure 20 as required for solving the steady-state error problem. It is clear from the response result in Figure 21, that an acceptable steady-state error of $E = -0.08342$ can be obtained. Table 3 shows main rules, and Figure 22 shows control signal of elevators.

Figure 23 shows a comparison between the three studied controller types: General PID, Washout PID, and Fuzzy PID. The comparison was made at the following conditions: altitude from sea level is 10000 foot, and airspeed 1200 foot/s. We conclude from the figure that the fuzzy controller offers minimum possible vibrations, and better response speed compared with other controllers.
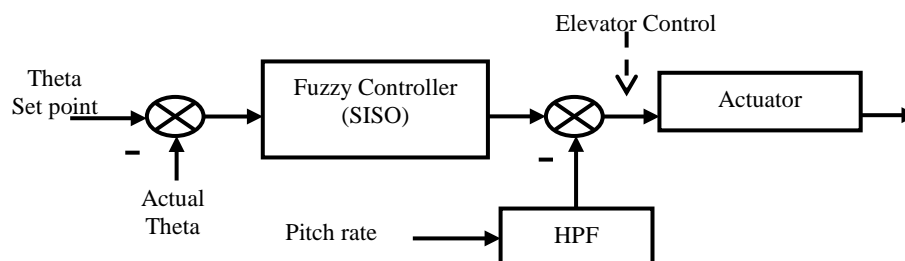
Figure 19. Block diagram of Control System
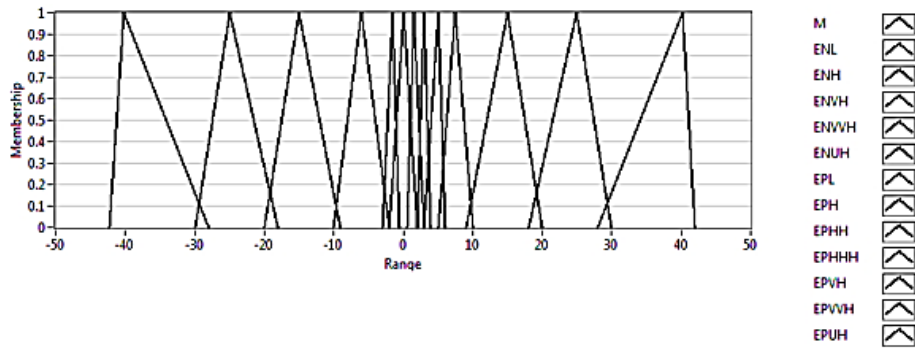
(a)
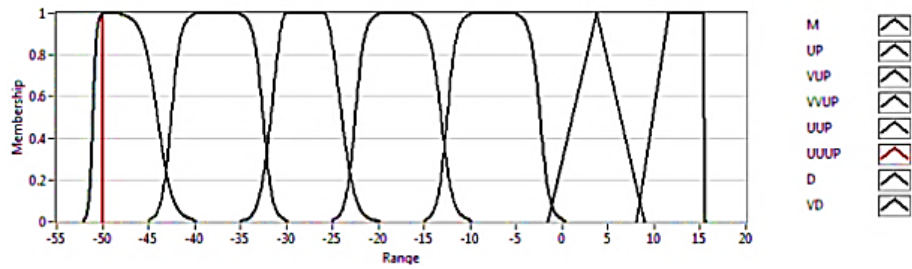
(b)

Figure 20. Input (a) and output (b) membership functions
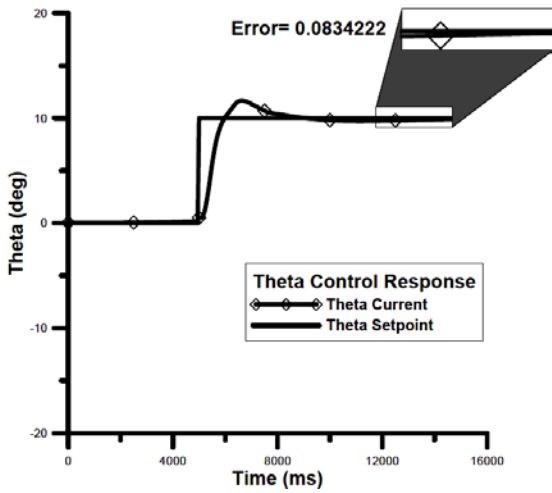
Figure 21. Time response of fuzzy Controller at Aircraft model
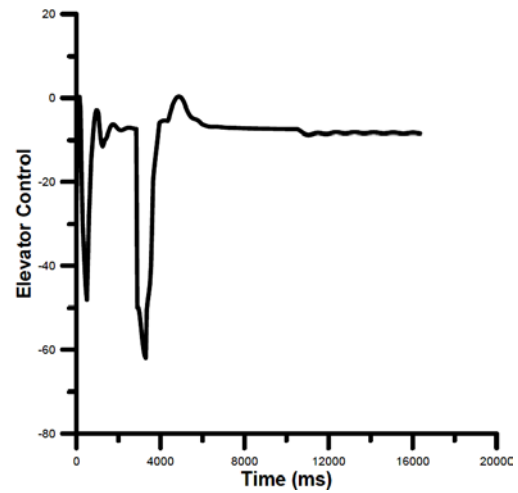
Figure 22. Elevator control signal at aircraft model

Table 3. Rules of fuzzy controller

ELEVATOR	THETA_ERROR	Rule No.	ELEVATOR	THETA_ERROR	Rule No.
VD	ENUH	1	VVUP	EPH	8
VD	ENVVH	2	VVUP	EPHH	9
VD	ENVH	3	UUUP	EPHHH	10
D	ENH	4	UUUP	EPVH	11
D	ENL	5	UUUP	EPVVH	12
M	M	6	UUUP	EPUH	13
UP	EPL	7			

The result of this research was implemented in LabVIEW platform using Runge-Kutta 2 method with fixed step 0.05 (sec) and summarized in that a better response of fuzzy controllers can be obtained by decreasing the vibrations and noise to the minimum compared with the traditional PID controllers as shown in Figure 23. Table 4 shows the result of the comparison.
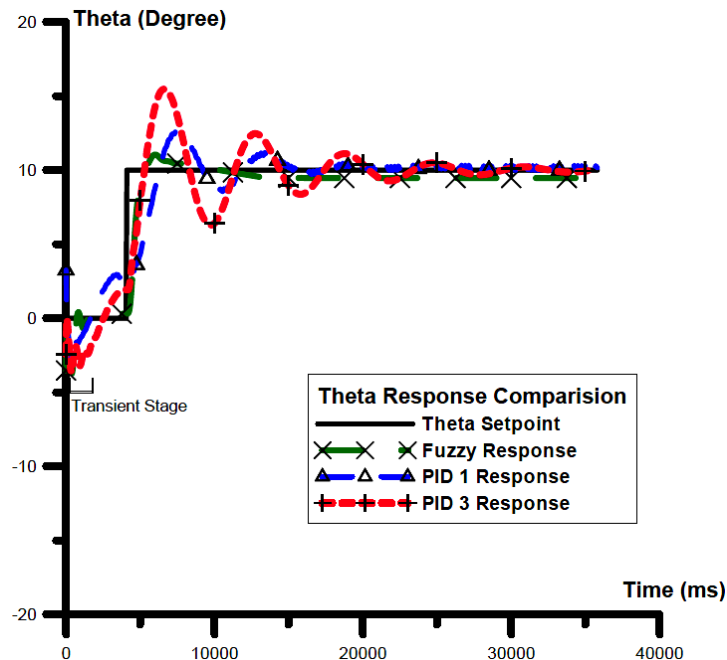
Figure 23. Comparing the plant response of three types of controllers

Table 4. Comparison values between controllers

Controller Used	Response Time (ms)	Steady-State Error (deg)
Generic PID	10900	0.17618
PID-Washout	18700	−0.0297136
Fuzzy Controller	3150	0.0834222

5. CONCLUSION

The aircraft is exposed to disturbances and noise because of many factors such as surrounding environment that negatively affects the system's response and leads to vibrations and steady-state error. Therefore, the stage of longitudinal control of the aircraft requires a controller that preserves the value of the actual pitch angle at the required values. Many control models were conducted to evaluate and compare the system's response at three important points: cancelling of vibrations, minimizing steady-state error, and reducing response time. The result of this research was implemented in LabVIEW platform using Runge-Kutta 2 method with fixed step 0.05 (sec) and summarized in that a better response of fuzzy controllers can be obtained by decreasing the vibrations and noise to the minimum compared with the traditional PID controllers. The fuzzy controllers offer more flexibility than the traditional PID controllers through the ability it offers for changing the rules and the membership functions in order to get wider range of control, and the ability to understand sophisticated systems that are difficult to describe by mathematical relations, thus, it is considered the closest to the human thinking style.

REFERENCES

1. F.W. Lanchester, Aerodonetics, Constable and Co. Ltd, London, 2nd ed., 1910.

2. G.H. Bryan, Stability in Aviation, Macmillan and Co, London, 1911.

3. D. Seto, E. Ferreira, T.F. Marz, "Case study: development of a baseline controller for automatic landing of an F-16 aircraft using linear matrix inequalities (LMIs)," NASA Technical Paper CMU/SEI-99-TR-020, 2000.

4. M.V. Cook, Flight Dynamics Principles, Elsevier, Publisher: Butterworth-Heinemann, ed. 2, 2007.

5. N. Wahid, N. Hassan, M.F. Rahmat and S. Mansor, "Application of intelligent controller in feedback control loop for aircraft pitch control," Australian Journal of Basic and Applied Sciences, No. 5 (12), pp. 1065–1074, 2011.

6. L.S. Brian and L.L. Frank, Aircraft Control and Simulation, Publisher: John Wiley and Sons INC., 2nd ed., 2003.

7. A.F. Cabernet, "Controllers for systems with bounded actuators: modeling and control of an F-16 aircraft," Master Degree Thesis, University of California, Irvine, 2007.

8. L.T. Nguyen, M.E. Ogburn, W.P. Gillert, and et al., "Simulator study of stall/post-stall characteristics of a fighter airplane with relaxed longitudinal static stability," NASA Technical Paper 1538, 1979.

9. K.J. Astrom, R.M. Murray, Feedback Systems, Publisher: Princeton University Press, 2nd ed., 2014.

10. F. Haugen, "Ziegler-Nichols' open-loop method," URL: http://home.hit.no/~hansha/documents/control/theory/zn_open_loop_method.pdf, 2010.

11. H. Farah, "The fuzzy logic control of aircraft," Master Degree Thesis, Carleton University, Ottawa, 1999.

A System of Graphical Searching for Electrical Circuits and Parts of Instruments

D.R. Kasimov [1], A.V. Kuchuganov [2]

Department of Automated Data Processing and Control Systems,
Kalashnikov Izhevsk State Technical University, Izhevsk, Russia
E-mail: [1] kasden@mail.ru, [2] Aleks_KAV@udm.ru

Abstract. We propose a system for content-based retrieval of instrumental graphical documentation on the base of matching graphic patterns of a query image and archival images. Analogous systems are analyzed. Experiments on searching for electrical circuits as well as devices' parts are presented, which show high efficiency of the system.

Keywords: search, recognition, matching, scheme, drawing, part, instrument

INTRODUCTION

When designing new instruments, engineers often rely on existing components and solutions in order to reduce new product development time and to avoid repeated designing.

At an instrument-making enterprise, technical information is usually accumulated in a centralized enterprise archive. In addition, a lot of useful documents can be found at employees' workplaces. A significant proportion of key instrumental documentation is represented in the form of vector and raster schemes, drawings and sketches of devices and their components.

An engineer can manually browse only a small fraction of the total number of available graphic documents, which are estimated in tens or even hundreds of thousands. Automated searching by keywords, text descriptions or ciphers created according to some coding system often has big losses in recall and precision since in such searching a very limited part of a graphic document's content is considered.

A more efficient way of retrieving relevant graphical information is provided by systems of searching by a sample image, which are based on matching graphic objects and evaluating their similarity. In the search process, an image given by a user as a query is compared with all images in a database. Images that are most similar (from the system's point of view) to the query image are placed into results.

We developed the system *GrSearch*, which searches for technical drawings and schemes by a sample image (sketch). The system differs from its analogues by a more advanced search dialog and variety of search types [1].

In this paper we describe the developed system and provide results of its approbation on real instrumental engineering drawings and schemes.

SURVEY OF ANALOGUES

In the experimental system *ShapeLab* of Purdue University [2] two methods of matching parts' drawings are implemented. In the first method images are represented as spherical harmonics; their matching is based on a fast transform. In the second statistical method a drawing is represented as a 2D shape histogram, i.e. as a distribution of distances between pairs of randomly sampled points; the Minkowsky distance is used for measuring similarity between two such histograms.

The commercial system *CADFind* [3] represents a part's drawing by a so-called GT (Group Technology) code, which describes geometry of the part as well as text information related to it (material, process technology, etc.). Comparison of GT codes is performed with help of fuzzy logic.

A system of researchers Wang and Jiang [4] represents drawing images in the form of hierarchical topological graphs and performs their matching on the base of the nested assignment algorithm and the EMD distance (Earth mover's distance).

Existing systems of searching for drawings by a sample image have the following shortcomings:

- methods that are implemented in one systems are operable only on part drawings, and methods that are used in other systems haven't been experimentally verified for applicability for electrical circuits and installation diagrams;
- don't allow to customize queries;
- don't fix elements of similarity and dissimilarity (give only mathematical estimation of similarity of objects).

THE DEVELOPED SYSTEM

In the system *GrSearch* a graph model of description of a drawing image is used, which includes four level of abstraction: graph of singular points and segments; graph of contours; graph of 3D objects; graph of heterogeneous components. Graph nodes describe an image's components, and graph edges represent spatial relations between them in qualitative concepts on the base of linguistic variables [5].

Matching of drawing images is based on applying the beam graph [6]. It allows comparing drawing images of different scales and orientations, performing searching for entries of one graphic object in another one, identify elements of similarity and dissimilarity, considering special requirements that can be attached to particular components of a query image.

An extended model of a search dialog is implemented, which includes several types of searching, the possibility to specify general and specific requirements to search results, visualization of elements of similarity and dissimilarity. It enables a user to implement a flexible search strategy and to refine search needs.

The system also supports searching for scanned raster drawings. Raster images are first vectorized. The feature of our approach to automatic vectorization of drawings is performing ternary segmentation of an image, fuzzy synthesis of a skeleton on the base of two variants, multistep approximation and refinement [7]. As for any other vectorizer, image resolution and the quality of a paper carrier are of great importance. Conducted preliminary experiments have shown that our vectorizer copes with drawings of not very good quality better than commercial analogues (GTX Raster R2V, VPstudio, Scan2CAD, Vextractor).

EXPERIMENT ON SEARCHING FOR ELECTRICAL SCHEMES

We have conducted experiments on searching for electrical schemes of various devices. The search system indexed 20 schemes created in the CAD system KOMPAS-3D. Fragments from these schemes as well as sketches made in KOMPAS-3D were used as queries. The search was carried out on the base of graphs of singular points and segments.

Fig. 1 shows an example of search results. At the top of the figure a query fragment and its graph representation are presented. Since the relay and the incandescent lamp may have connections of different length in required schemes, we specified the clarifying requirement "Length = Any" for the corresponding edges of the graph. At the bottom of Fig. 1 the schemes that have been retrieved by the system are presented. All these schemes have the given fragment. The entries have been automatically circled in red by the system.

Search speed depends on the size of a query fragment; in this experiment the search lasted at least 1 s and a maximum of 6 s.
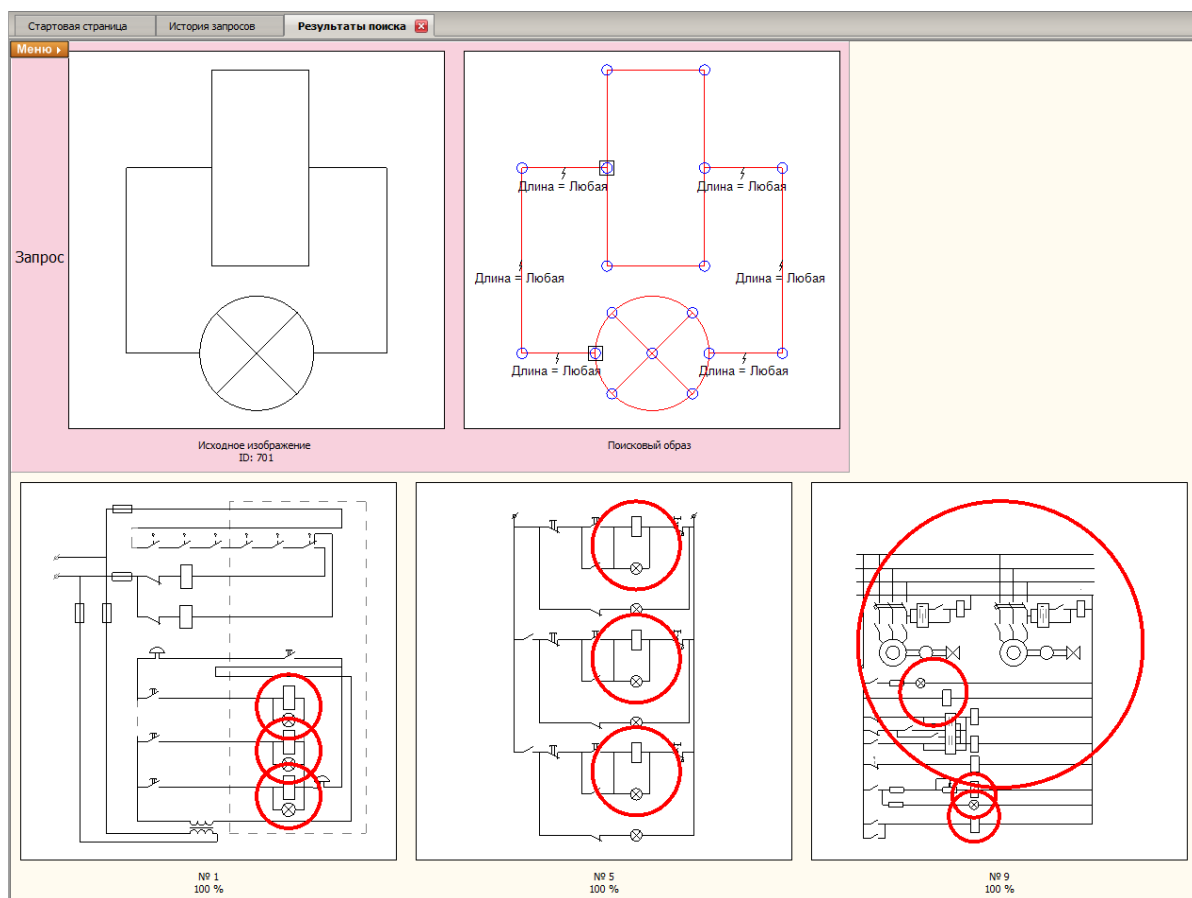
Figure 1. Example of results of searching for electrical circuits containing the given fragment

EXPERIMENT ON SEARCHING FOR PARTS OF INSTRUMENTS

An experiment on searching for instrument drawings has also been conducted. 117 drawings in the DXF format of the Mitutoyo corporation [8], which produces high-precision measuring instruments, have been added to the searchable database. The search was carried out on the base of graphs of contours.

Fig. 2 provides an example of search results. The query is the image of the working end of a measuring rod. The retrieval contains drawings of linear gauges and digital dial indicators.

Searching for instrument drawings was faster (1–3 s) than searching for electrical schemes since graphs of drawings have a smaller number of nodes and edges.
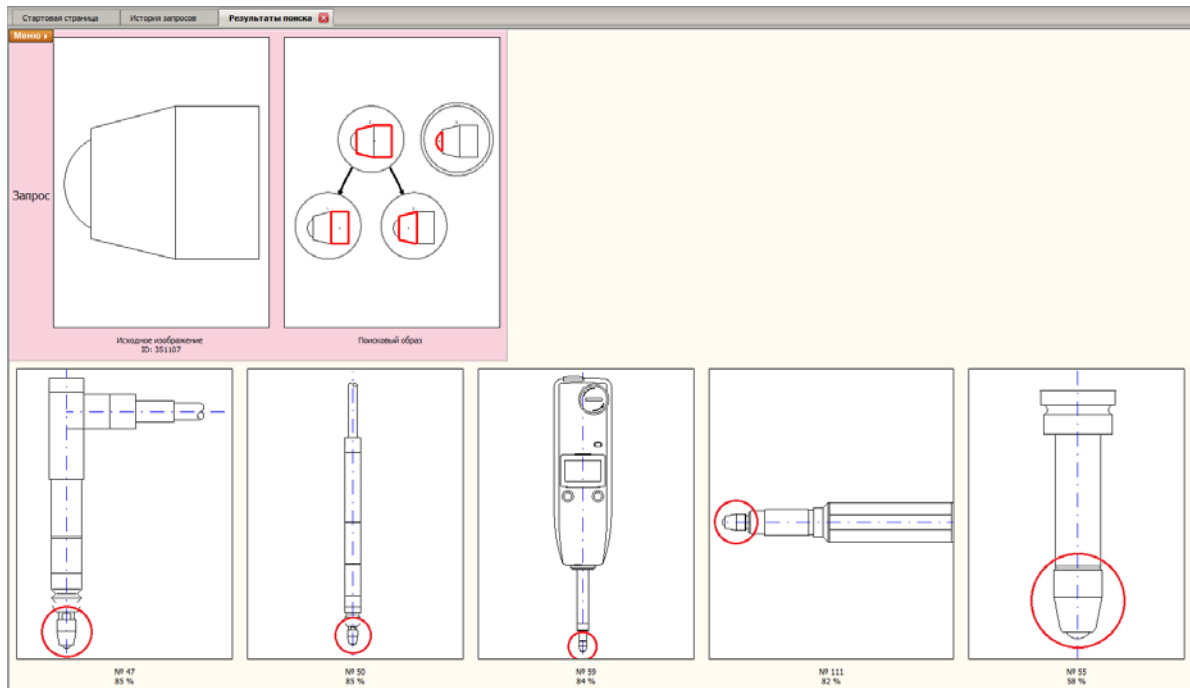
Figure 2. Example of results of searching for measuring instruments having a measuring rod with the given end

EVALUATING THE RETRIEVAL RECALL

A popular way of assessing the search quality is determining the recall parameter. Retrieval recall is the ratio R/T, where R is the number of retrieved relevant documents, and T is the total number of relevant documents in the database [9].

We have assessed the recall of searching for part drawings. Test database contained 2500 CAD drawings. We have performed 10 queries in our system.

Recall charts of searching for analogues that are highly relevant to queries are presented in Fig. 3.
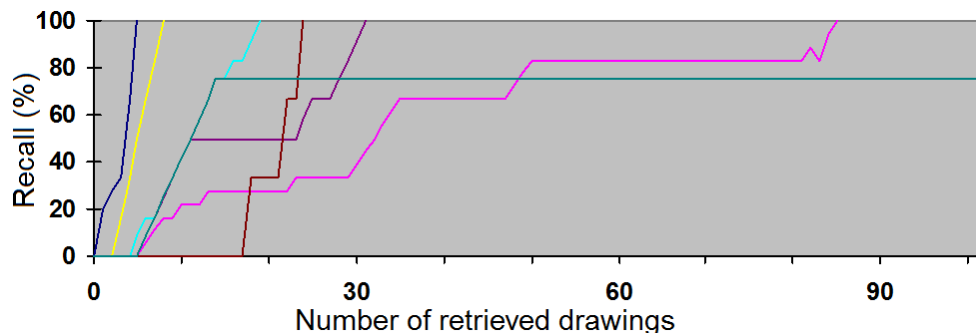
Figure 3. Retrieval recall charts for analogues that are highly relevant to queries

Fig. 4 shows recall charts of searching for analogues that are medium relevant to queries. It is natural that the recall level is a bit less for parts that are vaguely similar to queries.

The average recall is 72 %. In our opinion, this value is a good enough since parts that are very different in shape can be considered as relevant in some engineering tasks (see Fig. 5).

The minimum search time was 5 s, and the maximum was 40 s.
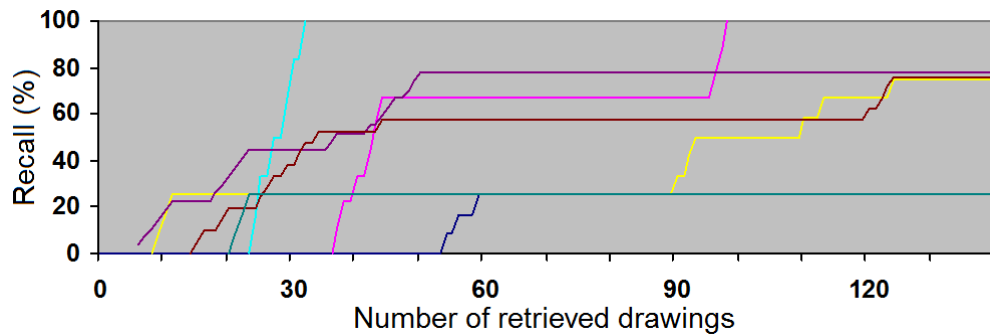
Figure 4. Retrieval recall charts for analogues that are medium relevant to queries

Figure 5. Examples of parts that are relevant to each other but have significant differences in shape

CONCLUSION

Existing ways of searching for drawings don't completely meet designers' needs in terms of relevance, the range of tasks, controllability and transparency.

Our methods and software tools of searching for drawings and electrical schemes by a sample image (sketch) allow a user to effectively retrieve useful information from archives of technical documentation.

The proposed system provides several types of the search, allows a user to clarify a query by means of customizing a search pattern, and visualizes matched elements in search results. A user can implement flexible search strategies.

The effect of applying the system is reducing the time and costs of designing new products.

REFERENCES

1. D.R. Kasimov, A.V. Kuchuganov, V.N. Kuchuganov, "Individual strategies in the tasks of graphical retrieval of technical drawings," Journal of Visual Languages and Computing, Vol. 28, pp. 134–146, 2015.

2. J. Pu, K. Ramani, "On visual similarity based 2D drawing retrieval," Computer-Aided Design, vol. 38, iss. 3, pp. 249–259, 2006.

3. D. Love, J. Barton, "Aspects of design retrieval performance using automatic GT coding of 2D engineering drawings," IDDME 2004 Proceedings, 2004.

4. P. Wang, S. Jiang, "An engineering drawing retrieval method based on nested assignment algorithm," Journal of Computational Information Systems, vol. 9, iss. 2, pp. 713–720, 2013.

5. L.A. Zadeh, "The concept of a linguistic variable and its application to approximate reasoning," Journal of Information Science, vol. 8, No. 3, pp. 189–281, 1975.

6. A.V. Kuchuganov, D.R. Kasimov, "Multilevel cognitive analysis in graphical retrieval of drawings," Pattern Recognition and Image Analysis, vol. 23, No. 4, pp. 518–523, 2013.

7. A.V. Kuchuganov, D.R. Kasimov, "Soft Computing in the Task of Vectorizing Archive Drawings," Proceedings of International Conference on Artificial Intelligence and Systems IS&IT'15, vol. 1, pp. 266–271, 2015.

8. Mitutoyo Deutschland CAD-Zeichnungen, URL: http://mitutoyo.de/de_de/downloads/cad-zeichnungen/.

9. C. Manning, R. Prabhakar, H. Schütze. Introduction to Information Retrieval, New York: Cambridge University Press, 2008.

The Analysis of Efficiency of Space-Diversity Reception

A. Kopysov, I. Klimov, Yu. Zagidullin

Radioengineering Department, Kalashnikov Izhevsk State Technical University, Izhevsk, Russian Federation
E-mail: kan_kan@istu.ru

Abstract. Space-diversity reception on two or three antennas is considered. Coherent and incoherent methods of signal addition in diversity branches are offered. Simulation results for DPSK and DQPSK signal reception in Rayleigh-Rice fading channel are represented.

Keywords: space-diversity reception, HF channel, Rayleigh fading, correlation, coherent and incoherent addition

INTRODUCTION

The space-diversity reception is an effective way to increase noise immunity in fading radio channels [1, 2, 4–10]. There are different types of diversity, but space diversity is the only method, which doesn't lead to division of transmitted power on diversity branches.

However, the analysis of efficiency of space-diversity reception shows that there are questions connected with degree of compliance between initial prerequisites and results of efficiency calculation for the real channel. First, the fading law changes over a wide range in real communication channel [3, 10, 11]. Second, the condition of statistical independence cannot be satisfied for this type of reception that affects the diversity reception. Besides, calculation of diversity reception efficiency is carried out for a case of optimum coherent addition of diversity branches. Practical realization of coherent addition is connected with difficulty of determine of diversity branch parameters that are coefficient of transfer, phase of a signal and spectral density of additive interference [1, 2]. Therefore efficiency analysis of processing methods of space-diversity reception, which ensure the desirable noise immunity, is the task of interest.

Incoherent addition of diversity branches is the simplest variant of realization. However efficiency estimation of this variant is connected with considerable mathematical difficulties due to fast fading and correlation of fading in branches. This is related to frequently used signals such as time-and-frequency signals and DPSK signals [5]. The only possibility to get objective estimate of real efficiency of space-diversity reception is to simulate the diversity branch reception with incoherent addition of branches [6, 7, 9].

SIMULATION

Random process distributed under the generalized Rayleigh-Rice law with the correlated quadrature components was chosen as a model of fading. Correlated quadrature components set transfer coefficients for time diversity branches with the average fading period which is significantly exceeded symbol duration. This model allows to vary fading intensity in necessary limits. Also it allows to create necessary correlation level of fading in diversity branches. Modeling conditions of reception were set by three parameters: mean square of transfer coefficient (mean value of SNR in diversity branch); fading parameter β^2, which defines fluctuation intensity (or dispersion) of transfer coefficient; correlation coefficient of fading in branches R, which defines paired correlation in diversity branches.
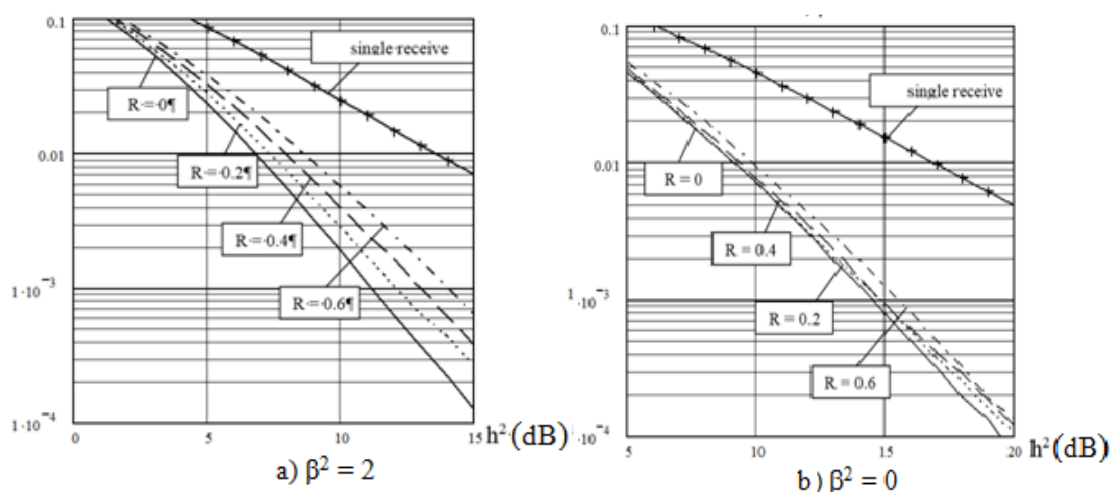
Figure 1. Bit error rate (BER) in case of incoherent DPSK signal reception using two diversity branches
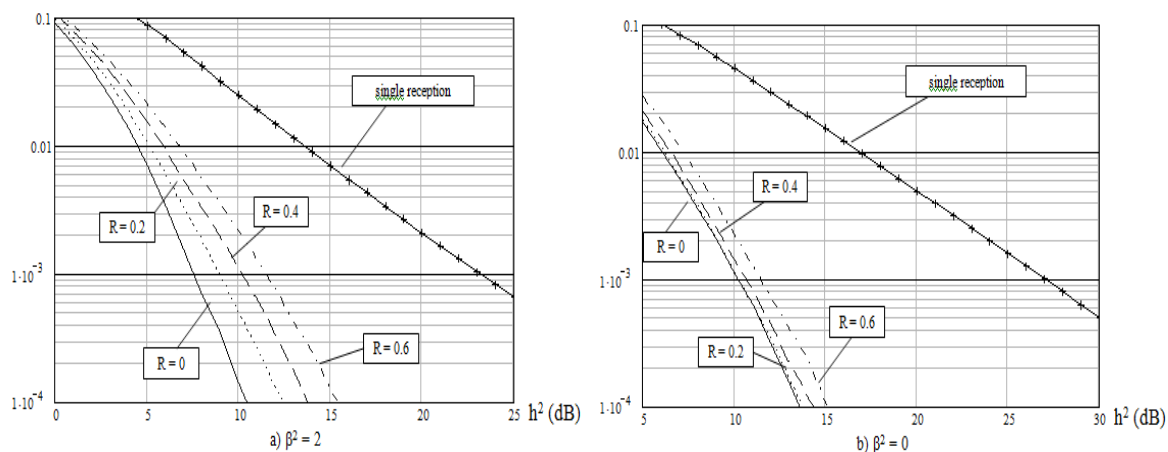
Figure 2. Bit error rate in case of incoherent DPSK signal reception using three diversity branches

Modeling results of incoherent addition in diversity branches of DPSK and DQPSK signals are presented in Figures 1–4 as a dependence of bit error rate versus mean SNR value. Simulation has been carried out for the most typical values of fading parameters for HF channel and for following values of fading correlation coefficients $R = 0$; 0.2; 0.4 and 0.6. The dependences of bit error rate of single, incoherent reception under the same conditions are presented for comparison. According to the results we can draw following conclusion: first, incoherent addition provides rather high efficiency in spite of its nonoptimality (equilibrium addition without taking current SNR into account was realized). Considerable gain in

comparison with single incoherent reception is received. Secondly, gain is increased with increase of requirement for reception quality, number of diversity branches and fading intensity [6, 8, 9]. Thirdly, the growth of fading correlation in diversity branches leads to degradation of diversity reception. However diversity reception provides considerable gain even at $R = 0.6$. Extent of correlation influence in diversity branches is decreased with reduction of parameter β^2.
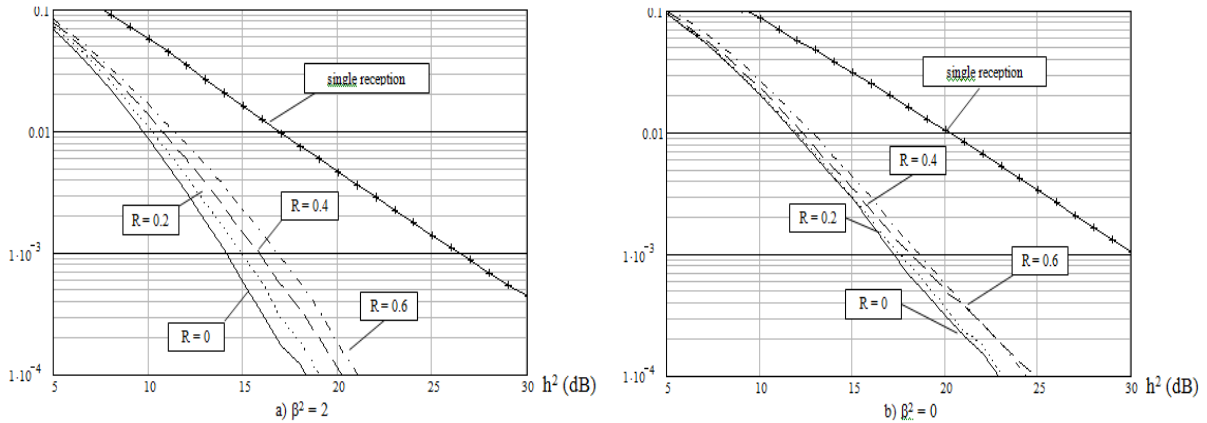
Figure 3. Bit error rate in case of incoherent DQPSK signal reception using two diversity branches
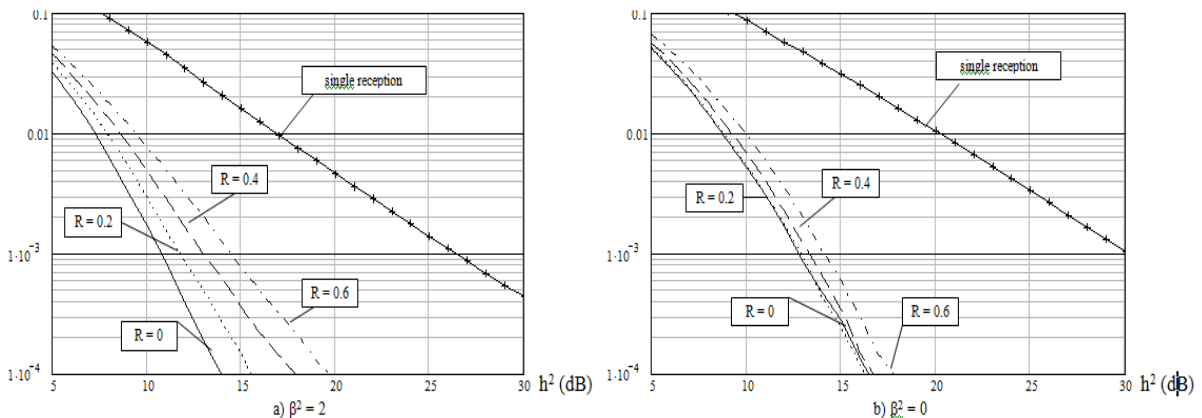
Figure 4. Bit error rate in case of incoherent DQPSK signal reception using three diversity branches

Gain values versus SNR at incoherent addition of diversity are presented in Table 1. Those values correspond to Figures 1–4 for three values of BER. Incoherent addition of two diversity branches provides gain of at least 9 dB in case of fading intensity $\beta^2 < 2$, correlation $R < 0.6$, BER $= 10^{-3}$. Incoherent addition of three diversity branches provides gain of at least 12 dB. At BER $= 10^{-3}$ degradation of diversity reception due to correlation does not exceed 3.3 dB for $\beta^2 = 2$ and 1.2 dB for $\beta^2 = 0$ (Rayleigh fading).

If the base of space diversity is comparable to radio wave length, the mutual delay in diversity branches is much less than duration of package. Therefore, when addition is realized there is no need to solve a problem of mutual synchronization in branches. That fact simplifies process of addition and allows realizing the timing using total signal, providing thereby significant improvement of synchronization quality.

Since mutual delays of signals in diversity branches are negligible and phase difference is changed rather slowly, we can get high quality estimation of phase differences without tracking phases of signals in each diversity branch. High quality estimation of phase differences allows executing coherent addition of branches with the subsequent incoherent

reception of information from a total signal. The estimation of a constant phase difference of two complex sequences (each sequence represents response to DPSK signal sample) can be calculated as following:

$$\Delta\varphi(X,Y) = \arg\left\{\sum_{i=1}^{n_0} x_i \hat{y}_i\right\} = \arg\left\{\begin{bmatrix} x_1 & x_2 & \cdots & x_{n_0} \end{bmatrix} \begin{bmatrix} \hat{y}_1 \\ \hat{y}_2 \\ \vdots \\ \hat{y}_{n_0} \end{bmatrix}\right\}. \tag{1}$$

Table 1. Gain in SNR in comparison with single reception

Modulation type	Number of branches	Fading β^2	Correlation R	Bit error rate		
				10^{-2}	10^{-3}	10^{-4}
DPSK	2	2	0	6.7	12.1	17.5
			0.6	5	9.1	14
		0	0	7.6	12.1	16.7
			0.6	6.9	11.6	16.5
	3	2	0	9.1	15.5	22.3
			0.6	6.6	12.1	18.3
		0	0	10.6	16.6	23
			0.6	9.6	15.5	21.5
DQPSK	2	2	0	7.1	12.4	18.1
			0.6	5.3	9.2	14
		0	0	8.2	12.8	17.5
			0.6	7.3	11.7	16.2
	3	2	0	9.5	15.7	22.5
			0.6	7.3	12.1	17.8
		0	0	11.2	17	23.1
			0.6	10.1	15.7	21.5

The simulation results of phase shift estimation in fading branches are presented in Figure 5. The figure depicts the dependence of error dispersion of mean SNR for two values of sequence length n_0. The analysis of results shows that estimation of error dispersion should be equal to 10^{-3} radian^2 to achieve high quality of coherent addition. Therefore, correct selection of parameter n_0 ensures necessary estimation quality in given SNR range, which correspond to current transfer quality index.

Transfer quality estimation of DPSK signal was taken to determine the importance of transfer coefficient calculation in case of coherent addition with equal weight. The dependence of BER from mean SNR for reception of DPSK signal and $n_0 = 512$ is presented in Figures 6 and 7. The reception is coherent (i.e. phase shift and transfer coefficient are known) and fading in branches is independent ($R = 0$). Comparison of simulation results and theory calculation shows that there is a negligible degradation if the weight is not taken into account. The degradation is maximum for Rayleigh fading, but it is less than 1.2 dB for BER = 10^{-2}–10^{-4}. The losses do not exceed 0.7 dB at $\beta^2 = 2$ and three branch reception. Comparison of dependences in Figures 1, 2, 6 and 7 shows that coherent addition with equal weight provides for miserable gain. It is about 0.8 dB better than incoherent addition gain. Correlation influence is similar for both coherent and incoherent addition. The influence is strong if transfer coefficient has regular component and one is weak Rayleigh fading channel ($\beta^2 = 0$).
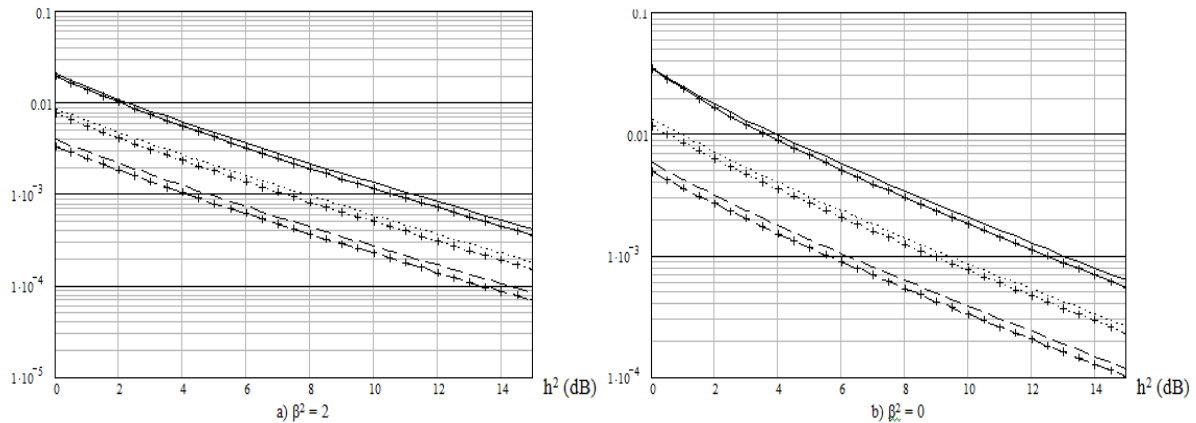
Line type			Marker	
$n_0 = 128$	$n_0 = 256$	$n_0 = 512$	$R = 0$	$R = 0.6$
————	··············	— — — — —	–	+

Figure 5. Dispersion of estimation error of mutual phase shift in diversity branches
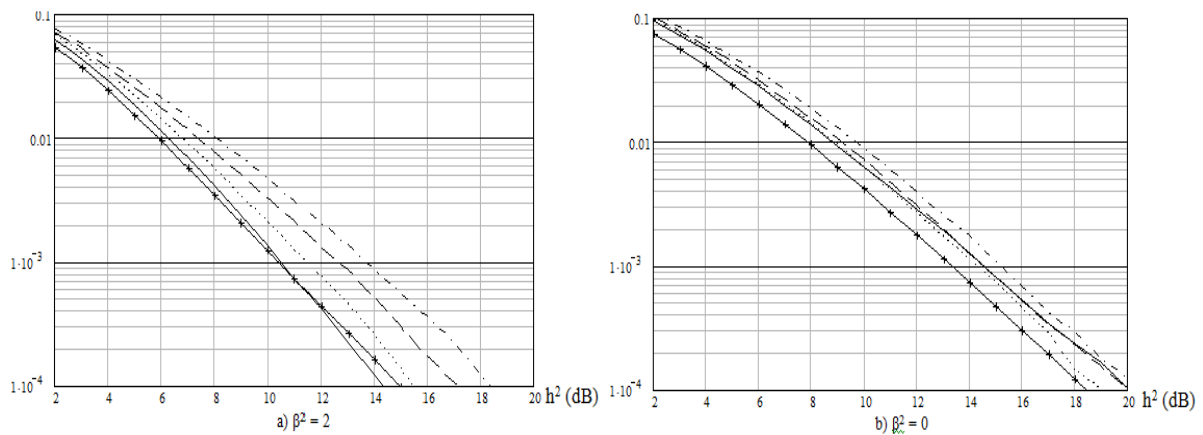
Simulation of addition with equal weight				Optimal
$R = 0$	$R = 0.2$	$R = 0.4$	$R = 0.6$	
————	··············	— — — — —·	–·–·–·–··	—+—+—+—

Figure 6. Bit error rate in case of coherent DQPSK signal reception using two diversity branches
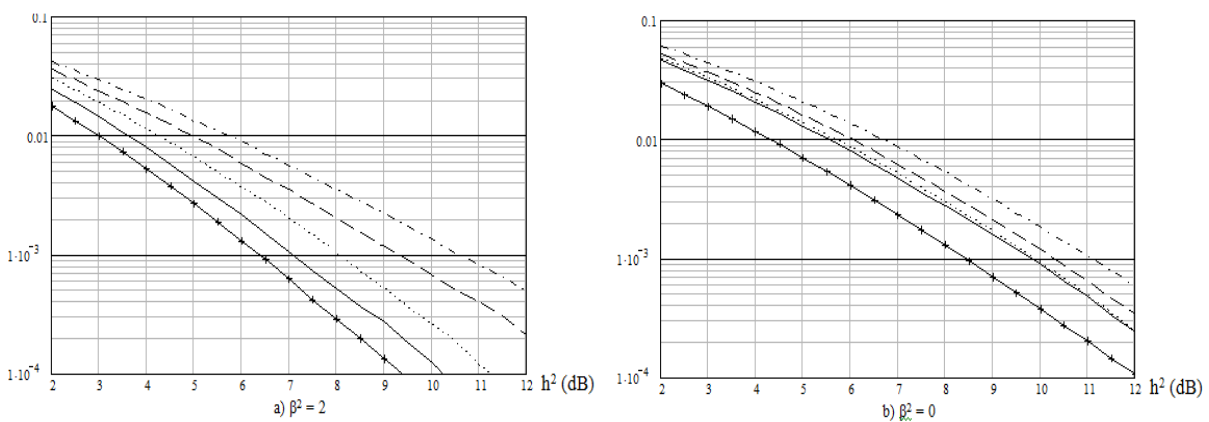
Simulation of addition with equal weight				Optimal
$R = 0$	$R = 0.2$	$R = 0.4$	$R = 0.6$	
————	··············	— — — — —·	–·–·–·–··	—+—+—+—

Figure 7. Bit error rate in case of coherent DQPSK signal reception using three diversity branches

CONCLUSION

According to the results of research we draw the following main conclusions:

1. Space-diversity reception allows to increase reception quality significantly. Efficiency of space-diversity reception directly depends on requirement to reception efficiency. So, SNR gain that correspond to BER = 10^{-3} is about 10 dB for two branch reception. SNR gain that correspond to BER = 10^{-4} is not less than 14 dB.

2. Fading correlation in diversity branches reduces efficiency of space-diversity reception. However this influence is negligible at Rayleigh fading channel. Fading correlation reduces efficiency of space-diversity reception considerably if transfer coefficient component is regular and huge. So, the losses caused by correlation influence on efficiency of space-diversity reception are about 3–4 dB at $R = 0.6$ and $\beta^2 = 0$ and satisfactory SNR (it is typical for HF channel). Therefore it is necessary to collect the information about real fading correlation level at reception on spaced antennas and find the ways to ensure not significant values of correlation.

3. Efficiency of incoherent addition of DPSK signals slightly concedes to coherent addition efficiency. Since realization of incoherent addition is easier than coherent addition, it allows to include more diversity branches. Besides, incoherent addition can be executed before timing is established. And efficiency of timing can be increased since we process overall signal. Therefore incoherent addition is more preferable in terms of efficiency/costs ratio.

4. Incoherent addition is less sensitive than coherent to differences in frequency shift in branches. In this case phase incursion has a weak influence to reception quality. And it is enough to synchronize only clock frequencies of synchronization. As a result relatively high space diversity can be used to get negligible fading correlation. If difference of phase incursion is significant, synchronization with the leading generator should be foreseen. Phase incursion is caused by reference generator instability in line channel and by duration of package.

REFERENCES

1. L.M. Fink, Communication Theory of Discrete Message, Moscow: Soviet Radio, 1970.

2. A.A. Sinkarev, and A.I. Falko, Optimal Reception of Discrete Message, Moscow: Sviaz, 1978.

3. E.A. Khmelnitsky, Realistic Noise Immunity Estimation of Signal Reception in HF channel, Moscow: Sviaz, 1975.

4. V.F. Komarovich, and V.N. Sosunov, Random Radio Frequency Interference and Reliability of HF Communication, Moscow: Sviaz, 1977.

5. A.N. Kopysov, I.Z. Klimov, and M.V. Tyulkin, "The article about time-frequency signal research in multipath channel," Bulletin of the Izhevsk State Technical University, No. 4, pp. 125–127, 2009.

6. A.N. Kopysov, I.Z. Klimov, and M.V. Tyulkin, "Diversed reception algorithm research for HF time-frequency signals," Intelegent Systems in Manifacuring, No. 2, pp. 9–16, 2010.

7. Andrey Kopysov, Igor Klimov; Yuri Zagidullin, Vitaliy Muravev, and Olga Muraveva, "The use of polarization characteristic of ionosphere for data communications," Mechanical Engineering, Automation and Control Systems (MEACS), (2014 International Conference), 2014, pp.1–4.

8. A.N. Kopysov, I.Z. Klimov, V.A. Moshonkin, and A.A. Bogdanov, "Polarization patterns of high frequency channel for digital measuring complex," in Proceedings of the 16th International Conference "Digial Siglal Processing – DSPA-2014", (Moscow, Russia, March 2014), 2014, pp. 618–622.

9. I.Z. Klimov, A.N. Kopysov, V.A. Moshonkin, and A.S. Baturin, "Fidelity growth of information transmission using polarization patterns of high frequency channel," in Proceedings of the Second International Scientific-Technical Conference "Radio Engineering, Electronics & Communication – RE&C-2013", (Omsk, Russia, October, 2013), 2013, pp. 110–114.

10. I.Z. Klimov, A.N. Kopysov, and A.M.Chuvashov, "The comparative estimation of different kinds of wideband communication system developments," in Proceedings of the First International Scientific-Technical Conference "Radio Engineering, Electronics & Communication – RE&C-2011", (Omsk, Russia, October, 2013), 2013, pp. 57–66.

11. I.Z. Klimov, A.N. Kopysov, and A.M.Chuvashov, "Wide band radio channel multiplexing for telemeter information transmission," Issue of Electromechanics, vol.119, No. 6, pp. 57–61, 2010.

Method and Apparatus for Measuring of the Heat Flow Density in Soil

V.A. Kulikov [1], K.A. Nikitin [2], S.G. Seletkov [3], Y.K. Shelkovnikov [4]

[1–3] Department of Computer Engineering, Kalashnikov Izhevsk State Technical University, Izhevsk, Russia
E-mail: [1] kulik00@istu.ru, [2] nikitin.a.kirill@gmail.com, [3] s.g.seletkov@mail.ru
[4] Laboratory measuring systems, IM UrDRAS, Izhevsk, Russia
E-mail: [4] evshelk@mail.ru

Abstract. Temperature gradient and the thermal conductivity of the soil is measured by the three-phase thermo-converter. Density of the heat flux is calculated by the Fourier's law. The design of the sensor circuit and the measuring device are presented. The ability to measure of the heat flux density in the soil caused by the dissipation of heat from the heating duct, confirmed experimentally.

Keywords: Temperature, thermal conductivity, heating, heat flow density in the soil

INTRODUCTION

In most cases, heating of buildings and structures in Russia is carried out by supplying hot water conduits recessed into the soil (h eat pipelines) from thermal energy centers. The effectiveness of this method of heating depends largely on the condition and quality of thermal insulation of heating pipes. Currently, assessment of heat pipelines is carried out during the energy audit using thermal imaging units [1]. The devices mentioned make measurements of the surface temperature of the soil, which depends largely on the air temperature which surrounds the device and introduces a significant readings random error.

The paper proposes a method and a device allowing to measure the heat flux density in the soil, and excluding the impact of air above the track in the heat readings.

METHOD FOR MEASURING DENSITY OF HEAT FLOW IN SOIL

Measuring the heat flux density is based on Fourier's law. [2]

To perform the calculation temperature of soil is determined in its two points located on one vertical above the thermal route (Fig. 1). Then the heat flux density is calculated by the formula:

$$q = \lambda \frac{\Delta T}{l}. \tag{1}$$

The formula (1) denotes: ΔT – difference of temperatures at two points of measurement; l – distance between the temperature measuring points; λ – coefficient of thermal conductivity of the soil.
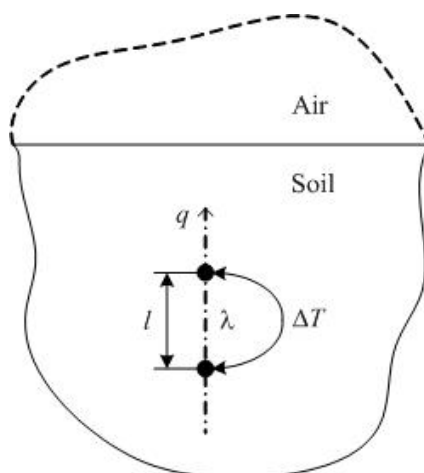
Figure 1. The circuit of measuring of heat flow density

Dynamic method of linear heater [3, 4] is selected for the measurement of the thermal conductivity coefficient of the soil (the "hot wire" method [5, 6]). The thermal conductivity coefficient λ is determined by the formula:

$$\lambda = \frac{P}{4\pi L \Delta T_{\lambda}}(\mathrm{Ln}(\tau_2) - \mathrm{Ln}(\tau_1)). \tag{2}$$

The formula (2) indicated: P, L – the power and the length of the heater; ΔT_{λ} – change of the heater temperature in the interval between time points: τ_1, τ_2. Registration of the soil temperature values τ_1 and τ_2 is performed on the linear portion of the function of temperature versus time measurements (Figure 2).
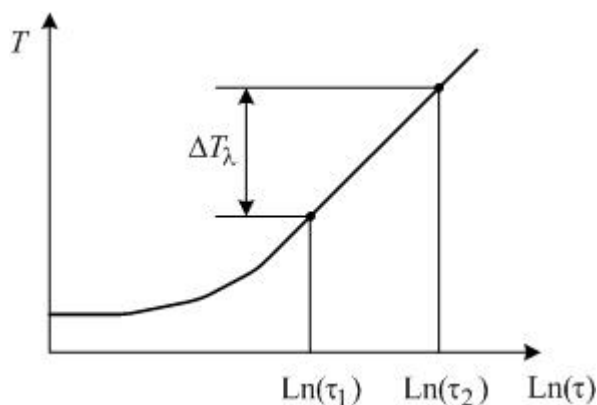
Figure 2. Determining the value ΔT_{λ}

To eliminate the influence of the edge effect a certain relation between the size of the length L and the diameter D of the heater must be fulfilled [7]:

$$\frac{L}{D} \geq 30. \tag{3}$$

THE SENSOR CONSTRUCTION

To measure the temperature ΔT and the thermal conductivity coefficient λ there used three-phase thermal resistance inverter (RTC) constructed as a cylinder (Fig. 3) [8]. It contains three coils: 1, 2, 3 of copper microwire, arranged in a single layer coil to coil on the inner wall of the protective tube 4. Coils 1 and 3 are RTC sensors for measuring temperature differences ΔT and localized along the length of the sensor. The coil 2 is used for measuring the thermal conductivity λ and is simultaneously the heater and sensor element for measuring the RTC temperature difference ΔT_{λ}.
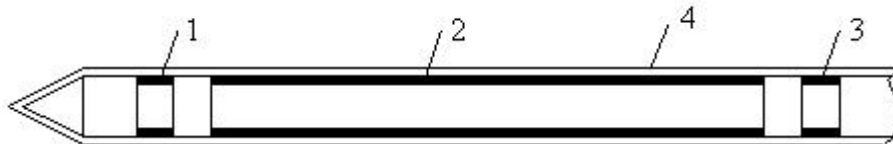
Figure 3. The construction of the heat flow density measuring sensor

Location of coils on the inner surface of the tube provides a low thermal resistance between them and the soil in the direction of the sensor radius. This ensures the total time of the measurement of the heat flux in the soil no more than two minutes.

THE DEVICE DIAGRAM

The authors have developed a device to work with the sensor. Its block diagram is shown in Figure 4.

The device contains three measuring channels to provide connection of the sensor coils: 1, 2, 3. Each channel includes a resistance-voltage converter (Converter), a normalizing voltage amplifier (Normalizing amplifier) and a low pass filter (Analog filter). All channels are connected to the ADC (ADC). Digital-to-analog converter (DAC) is used to control the sensor coil current . The measurement process is under control of a controller (MCU), which also calculates the heat flux density value and outputs the results on a LCD-display. The device model is made in the case of portable performance. At the same time a modern element base is used of and microcontroller ARM-architecture is applied.

EXPERIMENTAL RESULTS AND DISCUSSION

Device presetting with a sensor and its tests were carried out under laboratory conditions.

It is found that the scheme of the device on all channels provides a temperature resolution of 0.001 K, which provides measurement of values ΔT and λ with a sufficient accuracy for the task consisting in evaluating the heat losses from the heat carrier.

In the field conditions in April measurement of the heat flux density produced in the soil of heating pipeline at several depths from the surface. Near the surface to a depth of 0.5 m dependence of the results on the daily fluctuations in air temperature is well observed, while it decreased as the deepening probe. Measurements of heat flow density were carrying out at the same depth in the soil for two variants of the state of the heating pipeline. In the first case the heating pipeline contained no damage of thermal protection, and in the second case, the thermal protection was damaged.
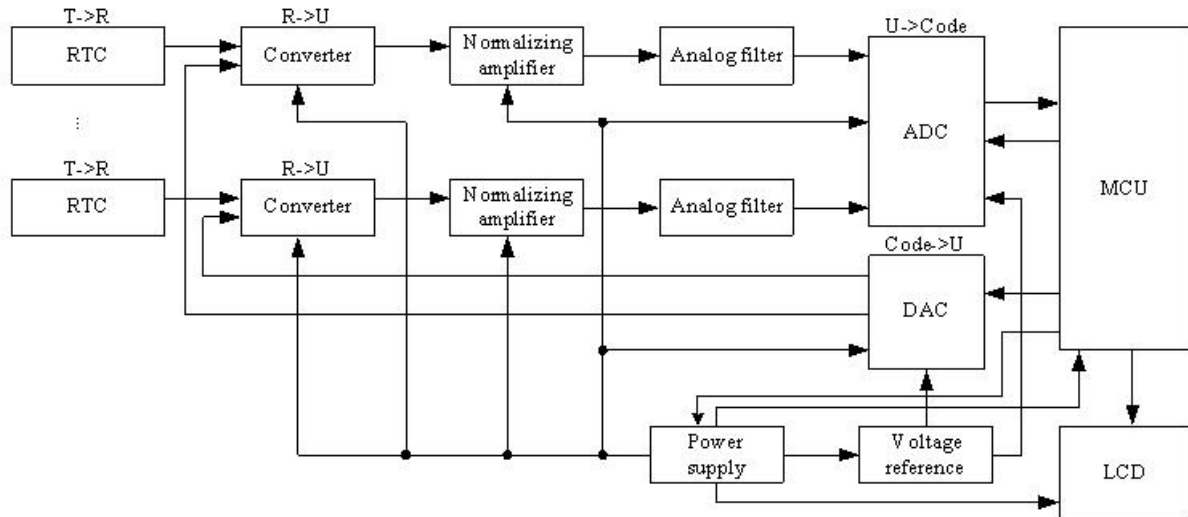
Figure 4. Block diagram for measuring heat flow density

In-situ measurements of soil temperature at different depths using these methods and device have established the value of the heat flow and its losses. If there was no damage to the track, the density value was 9.9 W/m^2, and in the presence of damage – 27.1 W/m^2. Thus, the absolute values of the thermal losses have been defined as well as the values of heat losses, characterizing their increase in case of heating pipeline damage.

There have been several measurements at the site of a heating pipeline with normal thermal insulation along the pipeline. Heat loss values were within 10 % with a probability of 0.95. It was found that the differences in the instrument readings are due to the heterogeneous composition of the soil, the presence of fragments of bricks, pebbles, broken glass. In general, the instrument readings in all cases are not contrary to the theoretical, and observed anomalies had reasonable explanations.

CONCLUSION

The authors have proposed and experimentally tested a modification of gradient method for measuring of the heat flux density in the soil on the basis of multi-zone thermal resistance converter of cylindrical structure. In the proposed execution the method, the technique and device implementing it allow measuring the heat flux density in the range of values corresponding to the heat dissipation of the heating mains, intended for heating buildings. The device allows to effectively identify areas with broken thermal insulation. The prospect of its further development and bringing to the industrial version is confirmed by experts on energy supply of buildings and structures.

REFERENCES

1. A.M Goncharov, "Methods of diagnosis of heating systems used in real-world conditions of existing heating networks of" MTK," in Report of the seminar "Technology, technology and work organization emergency dispatchers heat supply companies", (TGC "Izmailovo", March 14–16, 2007).

2. V.A. Kulikov, V.V. Syaktereva, K.A. Nikitin, "Experimental studies of information-measuring system for measuring the thermal conductivity of soil," Intelligent systems in production, No. 1 (17), pp. 191–196, 2011.

3. V.A. Kulikov, V.V. Syaktereva, "Dynamic measurement of the thermal conductivity of the soil with the use of linear-heater temperature sensor," Bulletin of Izhevsk State Technical University, No. 2 (50), pp. 137–140, 2011

4. B. Merckx, P. Dudoignon, J.P. Garnier, and D. Marchand, "Simplified Transient Hot-Wire Method for effective thermal conductivity measurement in geo materials: microstructure and saturation effect," Advances in Civil Engineering, p. 10, 2012.

5. B. Merckx, P. Dudoignon, J.P. Garnier, S. Martemianov, "Development of effective thermal conductivity measurement in geomaterials by Surface Transient Hot-Wire Method," International Review of Mechanical Engineering, vol. 6, No. 2, pp. 270–276, 2012.

6. J.H. Blackwell, "A transient-flow method for determination of thermal constants of insulating materials in bulk," J. Appl. Phys, vol. 25, pp. 137–144, 1954.

7. A. Kulikov, K.A. Nikitin, V.V. Syaktereva, Russian Patent No. 129635 (27 June 2013).

Monte Carlo Simulation Model for Estimation of Reliability Indexes of Electronic Means

A. Lyubchenko[1], P. Castillo[2], A. Mora[2], P. García-Sánchez[2], E. Kopytov[3]

[1] Institute of Automation, Telecommunication and IT, Omsk State Transport University, Omsk, Russia
E-mail: allyubchenko@gmail.com
[2] Dept. of Computer Architecture and Technology, University of Granada, Granada, Spain
[3] Dept. of Communication and Information Safety, Omsk State Technical University, Omsk, Russia

Abstract. The Monte Carlo method is a well-known technique for solving a verity of stochastic problems. Development of a simulation model based on this method provides flexibility for analyzing investigated processes and estimated parameters. In this paper, the Monte Carlo method was used for construction of a simulation model for the operational process of electronic medium for the purpose of integrated reliability index estimation. Multi-state functioning process considers a set of exploitation factors, such as sudden, gradual, latent and fictitious failures, human factor of service staff and time parameters of preventive maintenance. Implementing simulation experiments with the proposed model allows analyzing the reliability of electronic through popular indexes, coefficient of operation efficiency and availability coefficient, taking into account important factors of the operational process.

Keywords: simulation, Monte Carlo, Semi Markov process, reliability indexes

INTRODUCTION

Modern electronic devices consist of multiple components which are susceptible to aging and deterioration and that could lead to sudden and gradual failures of the whole system or its parts. These circumstances are a reason for system's reliability decreasing. One of the well-known method for reliability rising is preventive maintenance (PM), which main objective is to keep allowable reliability level through operations implemented periodically or deepening on the current system's condition. In both cases maintenance are performed by service staff, which could have different level of professional skills that could exert influence on reliability. Besides, preventive operations are implemented during a time that is not generally a constant; also a variety of diagnostic device could be used for testing and checking of fault state that cause appearance of latent and fictitious failures. All mentioned factors define multiple quantity of states of operation process for analyzed system and as a result it can affect reliability characteristics such as coefficient of operation efficiency (K_{OE}) and availability coefficient (K_A) [1]. Reliability analysis for basic operation process model with two main states, operable and non-operable, is enough well-known and could be easily performed with analytical solution [1]. Realization of analytical model with consideration of abovementioned factors could be implemented using theory of Markov and Semi Markov process [2, 3]. But such approach is not always a convenient analysis way because it is necessary to make routine operations for input of some changes into the model. Simulation technique seems to be more

attractive method for studying of observable system's process and to obtain estimations of reliability characteristics taking into account factors which are inherent in real situations. In this paper, a simulation model based on Embedded Markov chain of Semi Markov process in combination with a Monte Carlo technique is proposed to calculate integrated reliability indexes: coefficient of operation efficiency and availability coefficient. The model gives an opportunity to obtain easily estimations of the reliability indexes depending on the abovementioned factors and to use it for further optimization of PM parameters.

METHODOLOGY

Development of a simulation model is a well-known process and usually consists of the sequence of stages, such as conceptual description of the researched process, its mathematical formalization, development of simulation algorithm and its implementation [4, 5]. These steps are presented in the sections below.

Conceptual Description

Conceptual description of researched process is one of the steps for development of any mathematical model and includes relevant information about its peculiarities [4]. In this paper we use important knowledge in order to provide necessary comprehension.

Functioning process of electronic consists of two stages: normal operation and active ageing. The service staff implements PM at the point of normal operation in order to keep workable condition and required reliability level. PM is performed with periodicity T_{int} and intended to prevent partially sudden failures, but generally gradual failures. This kind of failures is preceded by a misalignment of system's parts in irreversible physicochemical processes of components, in other words due to ageing. Gradual failures of components could amount 30–80 percentages of total quantity of failures. Consequently, accounting of misalignment state of repairable systems is necessary to analyze of its reliability. Time parameters of PM are defined according to branch documentation and usually are presented by the following quantities: testing time (t_t), time for system tuning and configuration (t_a), fault search time (t_s) and emergency repair time (t_r). Systems' parameters control and diagnosis could be implemented by different measurement devices and automated diagnosis apparatuses. Validity of diagnostic devices information could be estimated by probability of erroneous determination of real system state.

The following assumptions were made for development of the conceptual model:

1. The electronic equipment is subjected to misalignments during its exploitation and misalignments' rate and failures of detuned electronics subordinate to exponential law.

2. Misalignment of equipment isn't detected during its exploitation.

3. Failures of diagnostic devices aren't taken into account.

4. Recovery time and duration of maintenance are constants.

5. Repair starts immediately after a failure occurs or it is detected by diagnostic devices.

6. Service staff can make errors during PM which could result to failures.

7. Probability of service staff errors vanishes while the maintenance intervals tend to zero.

Electronic medium could be in the following states during its operational process:

1. Operable state (*S1*).

2. Misalignment state (*S2*).

3. Non-operable state (*S3*).

4. PM of operative system (*S4*).

5. Maintenance of system with misalignment (*S5*).

6. Latent failure (*S6*).

7. Maintenance of system being in latent failure (*S7*).

8. Fictitious failure (*S8*).

Sojourn time of *S1* state has stochastic character and is determined by distribution function and failure rate and misalignment rate of system. System passes to *S2* state if one of its parameters exceeds its assumed value. Non-operable state *S3,* due to an obvious failure, defines system's inability to perform required function in consequence of a failure of its component. The system stay in this state during necessary time to be repaired, which includes testing time t_t, fault search time t_s and emergency repair time t_r.

The system passes to *S4*, *S5* and *S7* states at the schedule date according the maintenance system for testing and adjusting of equipment if the last is necessary. Testing is an operation for confirmation of operable system's state or detection of misalignment or identification of latent failure state and it's characterized by duration of testing time t_t. Adjusting is a set of operations for recovery of normative values of system's parameters. It could be realized replacing components leading to misalignment, as well as tuning parameters during time t_a using, for example, adjusting elements or automated tuning facilities. Testing and tuning are performed only in *S5* state. Maintenance operations are carried out by operating staff, therefore, during testing t_t and adjusting time t_a an error could be made leading to equipment's failure and its transition to *S3* state. Distribution function of probability of operating staff errors $F_p(T_{int})$ is offered to use in order to take into account this factor.

Monitoring electronic medium conditions is usually performed by external and embedded diagnostic devices (DD). Besides, built-in DD implement periodic diagnostic system' modules and fix failures using beeps and/or fault light. External DD are exploited during implementing of PM procedures. The main DD's parameters are I type (α) and II type (β) errors.

Diagnosis error α is a probability to declare the operable device as "out of order". Error β is a probability to declare the inoperable device as "faultless". Diagnostic devices which are used for maintenance have higher grade of accuracy than embedded medium, therefore, $\alpha_1 > \alpha_2$, $\beta_1 > \beta_2$. For the stochastic process under study, the diagnosis errors are supposed not to be equal to zero, consequently, there are states of latent failure and fictitious failure. In *S6* state the system stands until performing of maintenance procedures, and during it operative staff can detect the malfunction. In *S8* state the system passes on when embedded DD makes an error giving a signal about fictions failure. Besides, it's assumed that instantaneous testing is executed during time t_t, after the system proceeded to operable state *S1*.

Thus, if it is possible to obtain statistical data for each state of the process then the coefficient of operation efficiency K_{OE} could be calculated as:

$$K_{OE} = \frac{T_{OS}}{T_{OS} + T_{RS} + T_{MS}}, \tag{1}$$

where T_{OS}, T_{RS} and T_{MS} – mean time of operable, repair and maintenance states, accordingly.

The expression for availability coefficient K_A can be written as:

$$K_A = \frac{T_{OS}}{T_{OS} + T_{RS}}. \tag{2}$$

Generally, next step of the mathematical model development is interpretation of conceptual description with an illustrative graphical model. Graphical interpretation is presented in Fig. 1 by way of a graph with 8 states and transitions between states with accordance to the values of one-step transition probabilities P_{ij}, $i \in [1, 8]$, $j \in [1, 8]$.
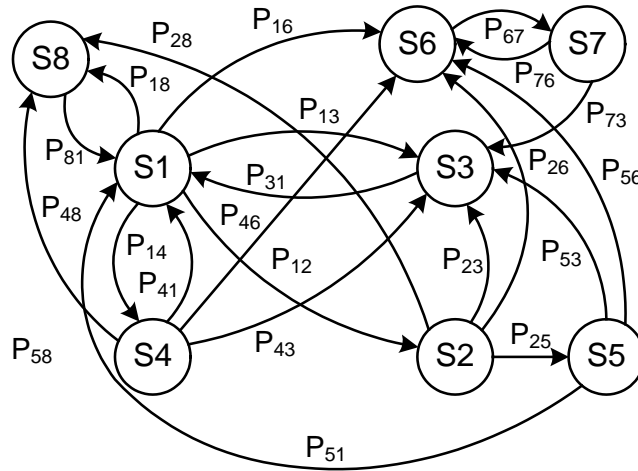
Figure 1. Transition state graph of the functioning process of repairable and maintainable electronic medium

Mathematical Formulation

According to conceptual description and graphical model, the observable operational could be presented as a random sequence of transitions from current state S_i to next state S_j. An example of such transitions in time domain is shown in Fig. 2.
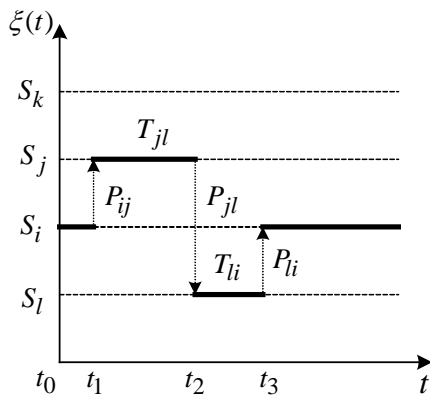
Figure 2. Time dependence of stochastic transitions

Theory of Markov and Semi Markov is used for mathematical formalization of transition sequence $\xi(t)$ [2, 3]. According to the theory this sequence of stochastic transitions could be described by Markov chain with continuous time and discreet state space. Furthermore, Markov property is obligatory to be hold true. This property, inherent in exponential law, however, sojourn time complies with this law only in state *S1* and *S2*. In the rest of states the duration of stay is a constant. Therefore, was suggested to use the model of the model of Embedded Markov chain of Semi Markov process [2, 3]. Application of simulation technique gives opportunity to take into account different character of input parameters without difficult routine operations with analytical formulas' manipulations [4].

The model's set of parameters for the observable process is presented as:

- vector of initial states:

$$P_0 = \left\{ P_1^0, P_2^0, P_3^0, P_4^0, P_5^0, P_6^0, P_7^0, P_8^0 \right\}; \tag{3}$$

- square matrix of transition probabilities:

$$P = \begin{Vmatrix} 0 & (1-F_{13})\times F_{12} & (1-\beta_1)\times F_{13} & (1-\alpha_1)\times \times(1-F_{13})\times(1-F_{12}) & 0 & \beta_1\times F_{13} & 0 & \alpha_1\times \times(1-F_{13})\times \times(1-F_{12}) \\ 0 & 0 & (1-\beta_1)\times F_{23} & 0 & (1-\alpha_1)\times \times(1-F_{23}) & \beta_1\times F_{23} & 0 & \alpha_1(1-F_{23}) \\ 1 & 0 & 0 & 0 & 0 & 0 & 0 & 0 \\ (1-\alpha_2)\times \times(1-F_p) & 0 & (1-\beta_2)\times F_p & 0 & 0 & \beta_2\times F_p & 0 & \alpha_2(1-F_p) \\ (1-\alpha_2)\times \times(1-F_p) & 0 & (1-\beta_2)\times F_p & 0 & 0 & \beta_2\times F_p & 0 & \alpha_2(1-F_p) \\ 0 & 0 & 0 & 0 & 0 & 0 & 1 & 0 \\ 0 & 0 & 1-\beta_2 & 0 & 0 & \beta_2 & 0 & 0 \\ 1 & 0 & 0 & 0 & 0 & 0 & 0 & 0 \end{Vmatrix}, \tag{4}$$

where F_{12} – exponential distribution function of transition probability from *S1* to *S2* with periodicity equals T_{int}; F_{13} – exponential distribution function of transition probability from *S1* to *S3* with periodicity equals T_{int}; F_{23} – exponential distribution function of transition probability from *S2* to *S3* with periodicity equals T_{int}; $F_p(T_{int})$ – distribution function of service staff errors probability.

- vector of density functions:

$$f = \left\{ (\lambda_{13}+\lambda_{12})e^{-(\lambda_{13}+\lambda_{12})T_1}, \lambda_{23}e^{-\lambda_{23}T_2}, t_t+t_s+t_r, t_t, t_t+t_a, T_{int}, t_t, t_t \right\}, \tag{5}$$

where λ_{12}, λ_{13} – rates of misalignments and sudden failures, respectively, hours^{-1}; λ_{23} – rate of sudden failures of misaligned system, hours^{-1}; t_t – testing time, hours; t_a – time for system configuration, hours; t_s – fault search time, hours; t_r – emergency repair time, hours.

Thus, multiple simulations of transition sequences from S_i state to S_j in accordance with abovementioned model provide opportunity to collect statistical data about system's operational process and to estimate values of integrated reliability indexes K_{OE} and K_A.

Simulation Algorithm

The simulation algorithm was developed applying discreet-event approach [5]. According to this method, the process is implemented only in its significant states, and transitions between them are realized by means of specially organized statistical sampling procedure which is based on Monte Carlo method [3, 6]. The technique includes three main steps:

1. Determining the first state of the process described by Semi Markov model according to the initial states' vector (3).

2. Calculating the system's duration of stay in current state using the vector (5) before to pass to another state. In order to perform this operation with specified density function could be used the inverse transforms method [5];

3. Defining the next state S_j according to the square matrix of transition probabilities (4) when the following inequality is correct:

$$\sum_{j=1}^{f-1} P_{ij} < u \le \sum_{j=1}^{f} P_{ij}, i = const, j = \overline{1,8}, \tag{5}$$

where u – uniformly distributed number within the range of 0–1.

After correcting the expression (5), target value of *j*-index equals to variable *f*. By way of the random values generator was used L'Ecuyer algorithm with period of reiteration of pseudorandom numbers about 10^{18} [7]. The flow chart of the algorithm, taking into account the periodicity of preventive procedures as the main parameter of maintenance system are presented in Fig. 3
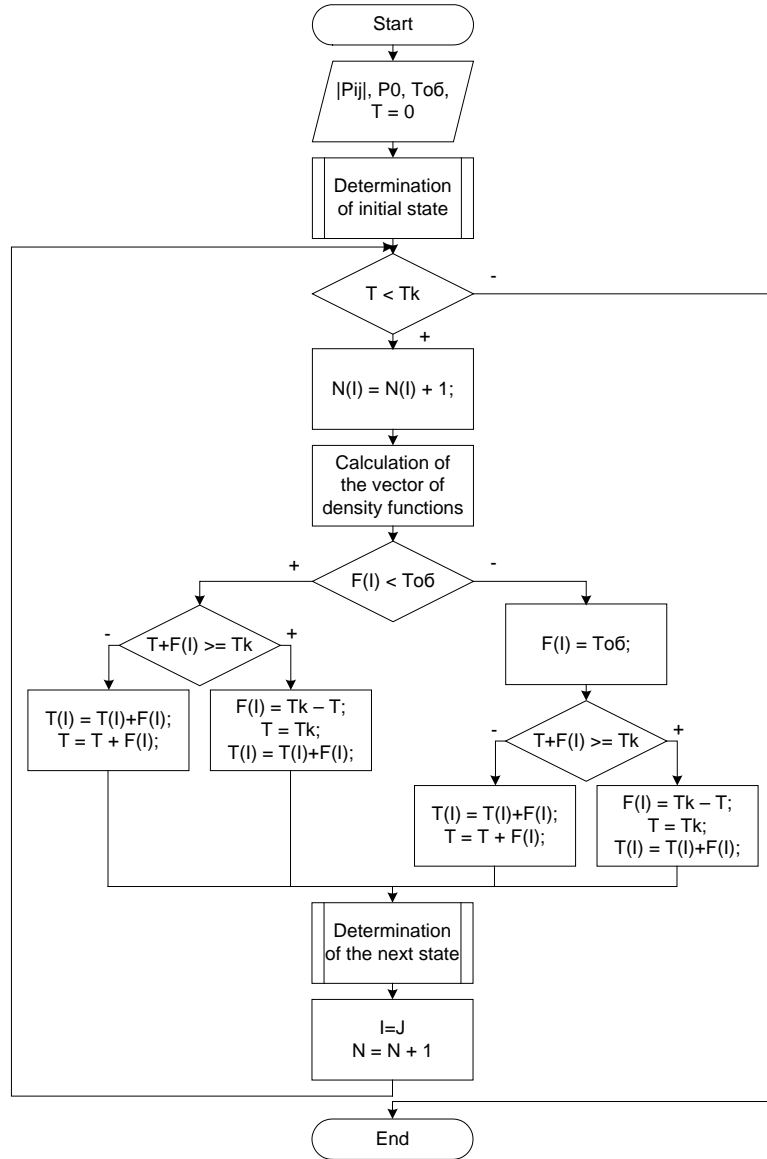
Figure 3. Flow chart of the simulation algorithm

Thus, if we can simulate the investigated process using the described algorithm during time T_k for each value of periodicity of maintenance $T_{int} \in [0, T_k]$ with step ΔT then it is possible to calculate sojourn time for each process's state S_i, $i \in [1, 8]$. On basis of collected statistical data, the estimations of integrated reliability indexes $\overline{K_{OE}}(T_{int})$ and $\overline{K_A}(T_{int})$ are implemented with specified accuracy ε and confidence probability Q:

$$\overline{K_{OE}^m}\left(T_{int}^m\right) = \frac{1}{N_m}\sum_{j=1}^{N_m} \frac{T_1^j\left(T_{int}^m\right) + T_2^j\left(T_{int}^m\right) + T_8^j\left(T_{int}^m\right)}{\sum_{i=1}^{8} T_i^j\left(T_{int}^m\right)}, \, m = \overline{1, M}; \tag{6}$$

$$\overline{K_A^m}\left(T_{int}^m\right) = \frac{1}{N_m}\sum_{j=1}^{N_m}\frac{T_1^j\left(T_{int}^m\right)+T_2^j\left(T_{int}^m\right)+T_8^j\left(T_{int}^m\right)}{\sum\limits_{i=1}^{3}T_i^j\left(T_{int}^m\right)+T_6^j\left(T_{int}^m\right)+T_8^j\left(T_{int}^m\right)}, \ m=\overline{1,M}, \tag{7}$$

where T_i^j – total stay time in S_i for j replication of the model; M – quantity of points for calculation determined as $T_k/\Delta T$; N_m – quantity of replications of simulation model for each estimated point of the dependences $\overline{K_{OE}}\left(T_{int}\right)$ and $\overline{K_A}\left(T_{int}\right)$ as the calculation is performed using different amount of sampling of simulation experiment which is organized by automatic stop principle with achievement of specified accuracy ε [8].

The simulation model, on the basis of the suggested algorithm, was developed in C++ programming language. As a language selection criterion, the effectiveness and usability were considered, and also the possibility to interact with Matlab software was taken into account. Thus, the model was prepared as a mex-function that provides opportunity to perform some functions, for example, statistical data processing, using the library of the Matlab system. However, the model's part demanding a lot of machine time due to applying the Monte Carlo method is realized on C++ language, that significantly reduce the time for implementation of simulation experiments.

SIMULATION EXPERIMENT

As an example the simulation experiment was performed with the following specified parameters: $\lambda_{12} = 50{\cdot}10^{-6}$ hours^{-1}, $\lambda_{13} = 5{\cdot}10^{-6}$ hours^{-1}, $\lambda_{23} = 0.5\lambda_{12}$, $\alpha_1 = 0.01$, $\alpha_2 = 0.005$, $\beta_1 = 0.01$, $\beta_2 = 0.005$, $t_t = 2$ hours, $t_a = 1$ hours, $t_s = 3$ hours, $t_r = 3$ hours, $F_p(T_{int}) = 0$, $T_k = 10^6$ hours and $\Delta T = 600$ hours. The results of the experiment are illustrated in Fig. 4.
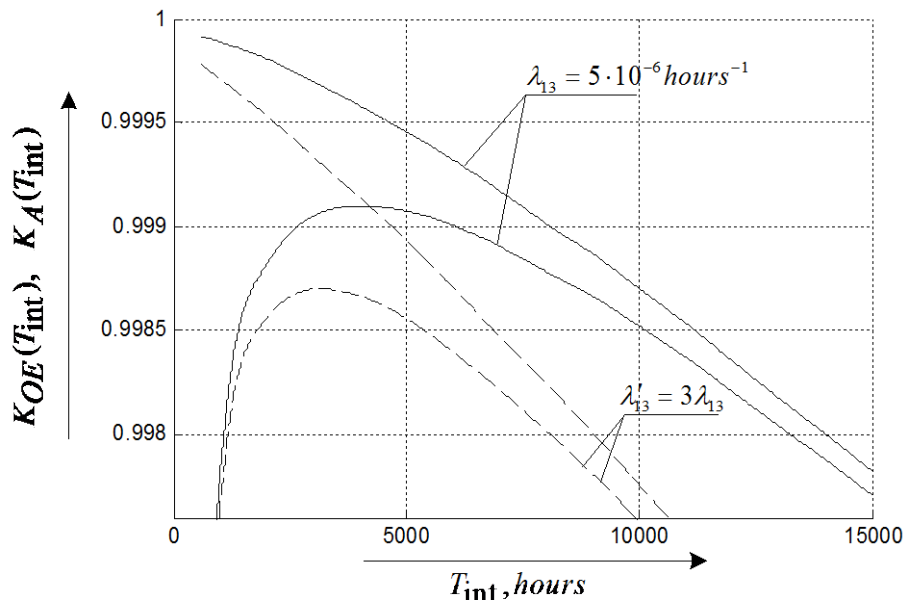
Figure 4. Simulation experiment results

The graphs in Fig. 4 present estimations of the reliability coefficients K_{OE} and K_A obtained with specified accuracy $\varepsilon=1{\cdot}10^{-5}$. The solid lines refer to the model with the abovementioned values of input parameters. The dashed lines characterize the calculations with three times increased failure rate $\lambda'_{13}=15{\cdot}10^{-6}$ hours^{-1}. Thus, performing the simulation experiments with developed model allows to obtain estimations of two popular integrated

reliability indexes, coefficient of operation efficiency (K_{OE}) and availability coefficient (K_A) depending on the values of input parameters. Moreover, the obtained dependencies nature allows speaking about determination of optimal periodicity of PM and the model could be used in optimization procedures.

CONCLUSION

In this paper a simulation model was proposed for analyzing both the operational process of electronic medium and the estimation of the integrated reliability indexes, coefficient of operation efficiency (K_{OE}) and availability coefficient (K_A). Mathematical formalization of the process is performed using an Embedded Markov chain for semi Markov process model. As the proposed process is a stochastic sequence, then the Monte Carlo method was used in order to simulate its behavior.

The graphical interpretation of the model presents a set of states that are conditioned by a group of operational factors considered in the model. It takes into account the following factors: appearance of sudden, gradual, latent and fictitious failures, human factor of service staff and time parameters of PM. Implementation of simulation experiments provides opportunity to analyze reliability of electronic medium through the coefficients K_{OE} and K_A and to investigate the influence of the factors on reliability indexes.

Subsequent research concerning the simulation model will be devoted to determination of its parameters such as the imitation time T_k and step ΔT in order to obtain maximally adequate results and to implementation the model's verification.

REFERENCES

1. A.M. Polovko, S.V. Gurov, Reliability theory. SPb: BHV-Pererburg, 2008.

2. V.S. Barbu, and N. Limnios, "Semi-Markov chains and hidden semi-Markov models toward applications: their use in reliability and DNA analysis," Springer Science & Business Media, vol. 191, 2009.

3. E. Pardoux, "Markov processes and applications: algorithms, networks, genome and finance," Published: John Wiley & Sons, Vol. 796, 2008.

4. A. Sirota, Computational modeling and effectivenes estimation of complex systems, Moskow: Technosfera, 2006.

5. W.D. Kelton, and A.M. Law, Simulation modeling and analysis, McGraw Hill Boston, 2000

6. S. Asmussen, and P.W. Glynn, "Stochastic simulation: Algorithms and analysis," Springer Science & Business Media, vol. 57, 2007.

7. W.H. Press, Numerical recipes 3rd edition: The art of scientific computing, Cambridge university press, 2007.

8. J.A. Sokolowski, and C.M. Banks, Principles of modeling and simulation: A multidisciplinary approach, Published: John Wiley & Sons, 2011.

Elasticity Moduli Estimation Using Different Elastography Methods: A Phantom Based Approach

D.S. Murashova [1], S.A. Murashov [2], O.P. Bogdan [2], O.V. Muravieva [2],
E.P. Kuznetsov [3], S.O. Yugova [2]

[1] OOO "IRZ TEST", OAO "Izhevskiy Radiozavod", Izhevsk, Russian Federation
E-mail: d_kuleshova@gmail.com
[2] "Instruments and Techniques for Measurements, Testing, Diagnostics" Department,
Kalashnikov Izhevsk State Technical University, Izhevsk, Russian Federation
E-mail: sm-ii@yandex.ru
[3] "Internal Diseases" Department, Izhevsk State Medical Academy, Izhevsk, Russian Federation

Abstract. Recently elastography has become a rapidly developing set of non-invasive techniques for estimation of soft tissues mechanical characteristics. The article represents the results of direct comparison of static (strain), vibration (based on mechanically induced vibrations) and shear wave elastography methods. For the first two methods the possibility of quantitative elastic moduli estimation has been proved previously. The results of the study on gelatin phantoms show satisfactory correspondence between all three methods. Besides of that, the results of comparison of static and vibration methods were very good.

Keywords: static, transient, shear wave elastography, elastometry, ultrasonic diagnostics, soft tissues strain, gelatine phantoms, ultrasound

INTRODUCTION

Elastography is a non-invasive ultrasonic visualization technique that allows examination the mechanical properties of soft tissues and organs and overcomes certain limitations of palpation, the technique used for thousands of years in the past and widely used nowadays, such as limited accessibility to internal organs and disease detectability, subjectiveness. The European Federation of Societies for Ultrasound in Medicine and Biology (EFSUMB) attempted to classify elastography methods [1] and proposed recommendations on their clinical use. All elastography methods can be divided in static (or strain) and dynamic ones. In static methods mechanical forces or pressure are considered constant (or changing slowly enough to get a set of images for comparative analysis to get a field of displacements in quasi-static methods). Dynamic methods pre-suppose the exposure of the soft tissue to variable forces like impulses of acoustic waves (focused or not focused at depth) or external pressure applied to the tissue surface.

The elasticity imaging emerged in the late 1980s from static and quasi-static methods, but still these methods are qualified as qualitative and not quantitative [1, 2]. The idea behind the methods is quite simple: being under compression, a softer tissue deforms greater than a stiffer tissue due to the difference of elasticity. In medical diagnostics, the inverse problem is

to be solved: to get elasticity characteristics of the tissue (shear modulus), it is necessary to know displacement and stress data in a zone of interest. While the first can be obtained using conventional ultrasonic scanners (at selected points) or by using equipment realizing the quasi-static method (as B-mode image), the second depends on many factors including pressure of surrounding tissues, pose of patient, tissue and inhomogeneity geometry, pressure under compression by external device or free-hand. However, as noted in [2], model-based approaches could decrease the shear modulus estimation error.

A static model of soft tissue inhomogeneity deformation proposed in [3] allows quantitative evaluation of the shear modulus for round-shaped inhomogeneity located at specified depth in homogeneous isotropic tissue. According to [4], the static method potentially can be up to 10 times more sensitive to small changes in shear modulus than vibration sonoelastography dynamic method.

Vibration elastography is based on applying the dynamic pressure to a soft tissue to induce periodical longitudinal and transversal displacements, which can be detected as vibration speed in specified tissue region by using the Doppler system of conventional ultrasonic scanners. Additional setup is required to create the dynamic pressure. The shear module can be evaluated by measuring the vibration speed in transversal direction and setting the amplitude and frequency of vibrations at zone of interest.

Shear Wave Elastography (SWE) is based on imaging the shear wave velocity [1]. The shear wave is exited by short radiation force impulses focused at various depths (or sweeped over depth fast enough to create a Mach cone of shear wave). No additional devices such as vibration generators or pressure sensors are needed for SWE methods, which allows so-called "free-hand" scanning technique, which is convenient in practice. On the other hand, specially designed acoustic sensors and ultrasonic scanners are needed for SWE option, so there is no compatibility with convenient ultrasonic equipment. Also, the "free-hand" method implies the absence of pressure requirement. Practically, shear vibrations are hard to excite from surface, but due to viscosity and complexity of tissues, focusing ultrasonic excitation techniques allow to produce longitudinal waves propagating in forward direction together with very fast fading shear vibrations propagating with very slow speeds around 3–10 m/s in transverse direction. There are several techniques to detect shear waves based on phased array sensors. Despite the fact that SWE technology is quite complex and obtained images are subjected to artifacts, large local variations and a little depth dependency in measured values, it allows to construct 2D elasticity map of a selected tissue region.

As stated in [5], due to different physical principles and computational algorithms used, static methods are suitable for local diseases, while shear wave methods are better for diffuse diseases.

Because of the widespread application of elastography in the medicine, it is necessary to make a direct comparison of different elastography methods and numeric values of soft tissue mechanical parameters given by them with general aim to increase the accuracy and reliability of elastography methods being developed. In this paper the research is based on comparison the static, vibration and shear wave elastography methods when measuring elasticity moduli of the same gelatin phantoms with inhomogeneities.

METHODS AND EQUIPMENT

To perform the study we created three gelatin phantoms with one cylindrical inhomogeneity in each of them as shown in Fig. 1. The main volume of phantoms was made of water solution with gelatin of 0.1 g/ml concentration to imitate the soft biological tissue. The first inhomogeneity in phantom 1 imitating the stiff tumor consists of 0.3 g/ml gelatin with small amount of talc powder. The second inhomogeneity in phantom 2 contains the same
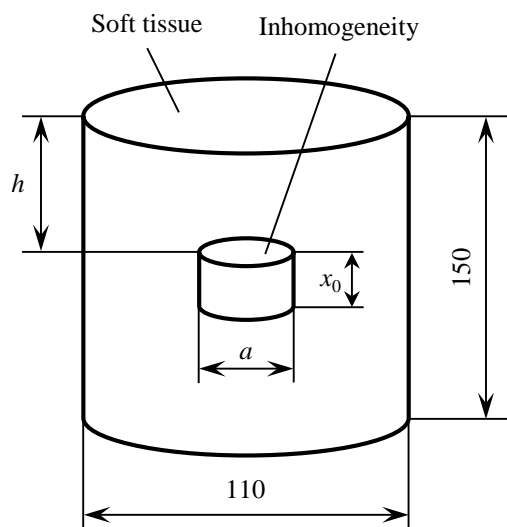
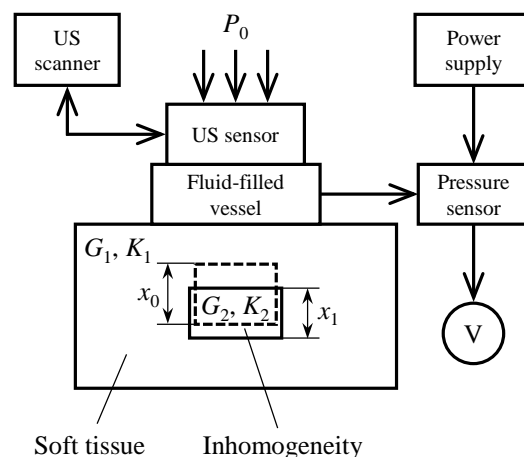**Figure 1.** Scheme of soft tissue with inhomogeneity gelatin phantoms

Figure 2. Functional block-diagram of the experimental setup for the static elastography

amount of gelatin but without talc. The third inhomogeneity in phantom 3 was made of 0.05 g/ml solution of gelatin in water to imitate softer (benign) tumor. Inhomogeneity parameters are presented in Table 1.

Table 1. Parameters of inhomogeneities

No.	Depth h, mm	Height x_0, mm	Diameter a, mm	Mass m, g	Density ρ, kg/m³	Longitudinal waves velocity C_l, m/s
1	75	15	36	16	1048	1503
2	75	14	36	15	1053	1500
3	75	12	36	10	819	1375

For static elastography method, we used physical model of compression with constant pressure P_0 applied to the soft tissue [4] based on linear elasticity theory for isotropic media, according to which all the elastic moduli are connected with the following equations:

$$\nu = \frac{C_l^2 - 2C_t^2}{2C_l^2 - 2C_t^2}, \tag{1}$$

$$E = \frac{C_l^2 \rho (1+\nu)(1-2\nu)}{1-\nu}, \tag{2}$$

$$G = C_t^2 \rho = \frac{E}{2(1+\nu)}, \tag{3}$$

$$K = \frac{E}{3(1-2\nu)}, \tag{4}$$

where ν – Poisson's ratio; C_l and C_t – longitudinal and transverse wave velocities, m/s, correspondingly; E – Young's modulus, Pa; ρ – density, kg/m³; G – shear modulus, Pa; K – bulk elasticity (modulus of dilatation), Pa.

The block diagram of experimental setup is presented in Figure 2. The convenient ultrasonic scanner (in our case, the Edan U50 portable system by Edan Instruments, Inc. with C352UB convex array sensor) works in standard B-mode and provides graphical interface for

distance measurements (assuming $C_l = 1540$ m/s) necessary for longitudinal strain ε_{xx} evaluation. Pressure P_0 is controlled by hand of researcher holding the ultrasonic sensor and is measured by specially designed device consisting of fixed soft silicone vessel filled with water, an infusion system and a pressure sensor with linear characteristic curve. Two measurements, before ($P_0 = 0$) and during compression ($P_0 > 0$), are necessary to evaluate the deformation ε_{xx}.

The inhomogeneity shear modulus G_2 evaluation is based on numerical dependencies [3] of deformation ε_{xx} on pressure P_0 and shear modulus G_2 obtained with the use of finite element method modeling and taking into account geometrical and physical peculiarities of phantoms.
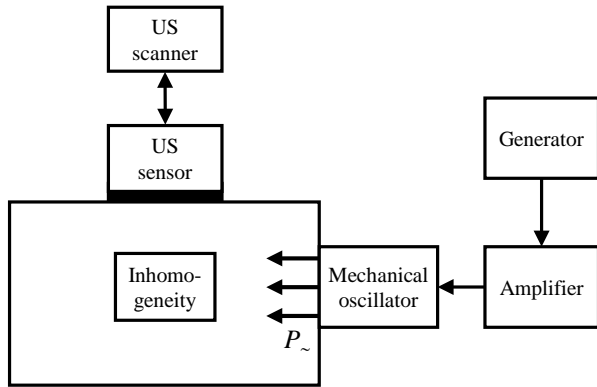

Figure 4. Block diagram for vibration elastography method

The block diagram for vibration elastography method is presented in Fig. 4. Mechanical oscillator supplied by amplified harmonic signal of 60–150 Hz frequency from a function generator creates the variable pressure $P_\sim$ in volume near the inhomogeneity from a lateral phantom wall. Ultrasonic scanner Edan U50 operates in power Doppler mode and displays vibration speed V measured at zone of inhomogeneity as a color map or in spectrogram-like form (vibration speeds versus time) at maximum of the first harmonic. The Young's modulus E was then calculated from the equation [4]:

$$V = 2.13\pi f_{US}\frac{\sigma_{xx}\lambda}{E},$$

where f_{US} – ultrasound frequency, σ_{xx} – mechanical harmonic stress, λ – wavelength.

Shear wave elastography was performed using Aixplorer® ultrasonic system (by SuperSonic Imagine) with convex SC6-1 probe with following technical specifications: 192 elements, spatial resolution 2.9 mm, precision on elasticity displayed ±15 %, elasticity range 0–300 kPa, penetration depth >75 mm. The system measures the shear (transversal) wave propagation velocity C_t in m/s and then converts it to a Young's modulus E, using the approximate equation $E = 3\rho C_t^2$, where the tissue density ρ is assumed to be close to that of water and equal to 1000 kg/m² [6]. The output on-screen Young's modulus values E_{min} (minimum), E_{max} (maximum) and E_{mean} (mean) are computed for selected round shaped area of 2 cm in diameter by corresponding equations:

$$E_{min} = 3000 \cdot (V_{min})^2, \quad E_{max} = 3000 \cdot (V_{max})^2,$$

$$E_{mean} = 3000 \cdot (V^2)_{mean} = \frac{3000 \cdot \sum_{i=1}^{n} V_i^2}{n},$$

where $n \in N$ – amount of values measured inside the area.

RESULTS AND DISCUSSION

Static elastography requires performing the linear dimensions measurement in B-mode. Because it is necessary to do at least two measurements – before and during compression, the

measurement accuracy highly depends on clearness of the region of interest borders. B-mode images of inhomogeneities in gelatin phantoms obtained by Edan U50 ultrasonic scanner are presented in Fig. 5. Borders can be clearly seen although to get an accurate result the probe should not be taken off the surface or revolved about its axis between measurements. The first inhomogeneity looks grey because of the talc powder presence, and its strain ε did not exceed 8.8 % (1.4 mm) under pressure P_0 of 4.2 kPa. Considering model dependencies of strain ε on elastic and geometric parameters of the phantom described in [3], the estimated Young's modulus E value is 60 kPa. The strain of the second inhomogeneity ε under the same pressure is 12.5 % (2.2 mm), and the Young's modulus E is 31 kPa. The third inhomogeneity is softer than surrounding media, its borders are not that contrast, but the strain under the same pressure $P_0 = 4.2$ kPa is larger: $\varepsilon = 28.8$ % (3.2 mm), so the Young's modulus $E = 18$ kPa.
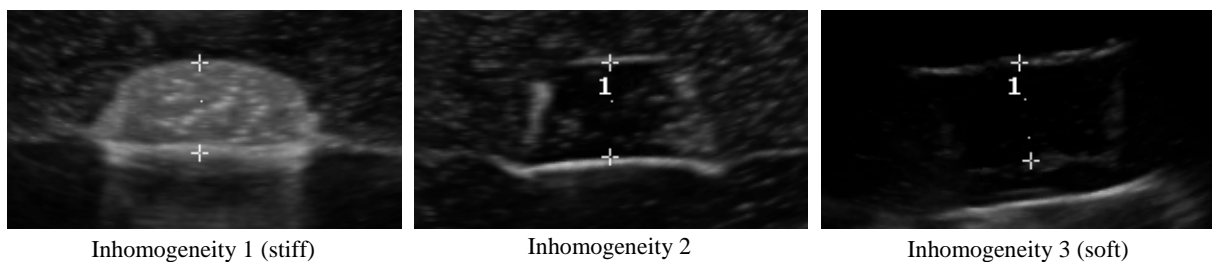

| Inhomogeneity 1 (stiff) | Inhomogeneity 2 | Inhomogeneity 3 (soft) |

Figure 5. Measurements of inhomogeneity height in B-mode (static elastography)

Vibration speed measurement accuracy may vary depending on the Power Doppler mode implementation, scaling to low values under 10 cm/s and pixel resolution in the ultrasonic scanner. An example of vibration elastography measurement on Edan U50 is shown in Fig. 6. Vibration speed spectrogram at frequencies under 20 Hz starts to be discontinuous in the time domain, and under 10 Hz it becomes hard to distinguish the peak value. On the other hand, waves of lower frequencies are able

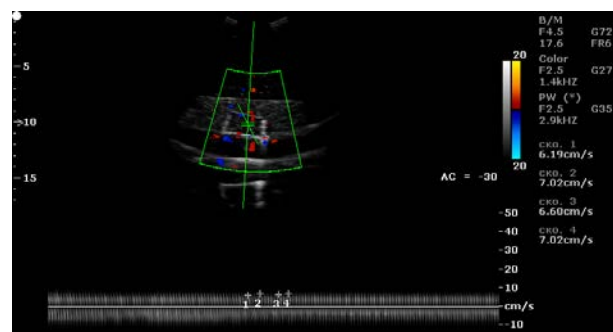**Figure 6.** Vibration speed measurement (vibration elastography)

to propagate deeper. So, the appropriate rate to expose inner organs, tissues or inhomogeneities in gelatin phantoms, as in our case, to sonic vibrations excited from the surface should belong to the range of 10–200 Hz. The resulting values of Young's modulus E for the first, the second and the third inhomogeneities, are 62, 36, 23 kPa, correspondingly.

2D elasticity images of the same inhomogeneities obtained from Aixplorer ultrasonic system, implementing shear wave elastography method, and presented in Fig. 7 shows that stiffness of inhomogeneities varies from hard to soft. Apart from the colormap, the min, mean and max values over the round area are displayed. The first inhomogeneity is clearly mapped red and the mean $E = 84$ kPa. The second inhomogeneity is not very explicit, and the colormap changes a lot during measurements. As a result, the image contains extremely small ($E_{min} = 1$ kPa) and extremely large ($E_{max} = 160$ kPa) values. From Fig. 7, b it can be seen that the border area is more stiff than the central area. The reasons of this may be specific phantom properties or imaging artefacts, which need more study. Nevertheless, the mean Young's modulus value $E = 41$ kPa. The third inhomogeneity in Fig. 7, c looks like it is stiffer than surrounding media, which is wrong (it may be a border effect), and the red spot on the right seems to be an artefact. Inside the circle, the mean Young's module value is equal to reasonable 22 kPa.
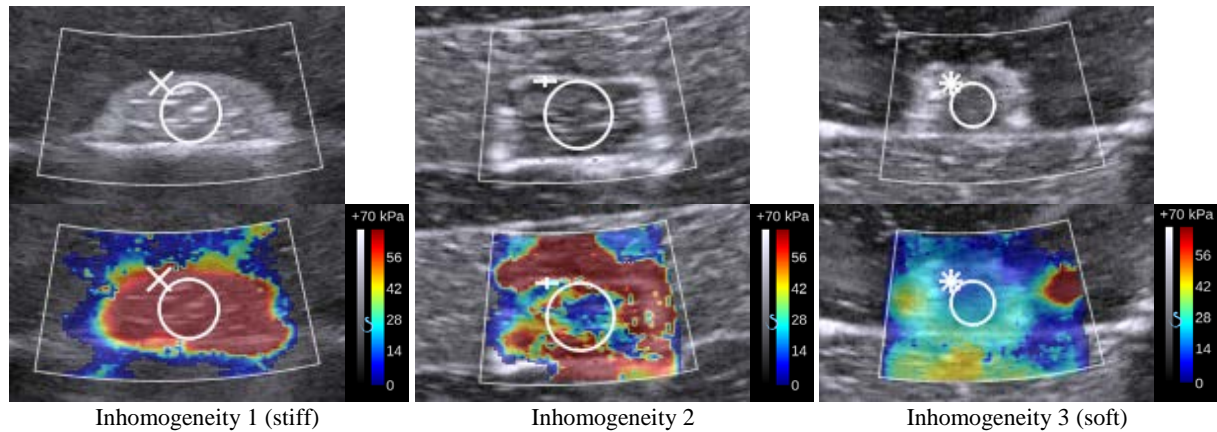
| Inhomogeneity 1 (stiff) | Inhomogeneity 2 | Inhomogeneity 3 (soft) |

Figure 7. B-mode and Young's modulus distribution images (shear wave elastography)

Table 2. Elastic moduli of inhomogeneities in gelatin phantoms estimated using different elastography methods

No.	Young's modulus *E*, kPa					Shear modulus *G*, kPa	
	Shear Wave Elastography (Aixplorer®)			Vibration elastography	Static elastography	Vibration elastography	Static elastography
	Min	Mean	Max				
1	61	84	103	62	60	20	19
2	1	41	160	36	31	12	10
3	15	22	29	23	18	8	6

The results of comparative study are accumulated in the Table 2. We can see satisfactory correspondence between all examined elastography methods and better correspondence between static and vibration methods.

CONCLUSION

Static and vibration elastography methods are applicable for quantitative measurements of elastic moduli in viscoelastic media, for example, gelatin phantoms, soft tissues or rubber-like materials, using conventional ultrasonic scanners. For soft tissues diagnostics more specific model is required considering geometric and elastic properties of the tissue itself and its surroundings (other tissues, blood vessels). Whereas static and vibration methods allows to estimate integral shear moduli values over all of the inhomogeneity depth, the Shear Wave Elastography methods allows to get local elastic moduli values at the region of interest. Large local deviations in measured values of the Young's modulus *E* could be caused by inhomogeneous phantoms structure and imaging artefacts. There is a need in less stiff and more homogeneous phantoms for soft tissues imitation.

REFERENCES

1. J. Bamber et al. "EFSUMB guidelines and recommendations on the clinical use of ultrasound elastography. Part 1: Basic principles and technology," in Ultraschall in Med, 2013, vol. 34, pp. 169–184. – DOI: 10.1055/s-0033-1335205.

2. A.P. Sarvazyan, T.J. Hall, M.W. Urban, M. Fatemi, S.R. Aglyamov, and B.S. Garra, "An overview of elastography – an emerging branch of mediacal imaging", in Curr Med Imaging Rev., 2011, November, vol. 7(4), pp. 255–282.

3. O.V. Muravieva, D.S. Murashova, S.A. Murashov, O.P. Bogdan, "Mathematical modeling of static elastography," in Biomedical Engineering, September 2014, vol. 48, no. 3, pp. 148–152. – DOI: 10.1007/s10527-014-9440-3.

4. O.V. Muravieva, O.P. Bogdan, S.A. Murashov, D.S. Murashova, "Capabilities of elastography methods in ultrasound diagnostics," in Proceedings of 2014 International Conference on Mechanical Engineering, Automation and Control Systems, MEACS 2014, pp. 1–6. – DOI: 10.1109/MEACS.2014.6986937.

5. B.S. Garra "Elastography: history, principles, and technique comparison," in Abdominal Imaging, 2015, vol. 40, pp. 680–697 – DOI: 10.1007/s00261-014-0305-8.

6. M. Kudo, et al. "JSUM ultrasound elastography practice guidelines: liver," in J Med Ultrasonics, 2013, vol. 40, pp. 325–357. – DOI 10.1007/s10396-013-0460-5.

7. C.R. Hill, J.C. Bamber, and G.R. ter Haar, "Physical principles of medical ultrasonics", 2nd ed. Wiley, 2004.

Research of Estimate's Possibility of Thermal Stresses in Rails

V. Muraviev, L. Volkova, A. Platunov, I. Buldakova, K. Ajpalov, A. Budrin, A. Jakimov

Department of Devices and Methods for Measurement, Control, Diagnostics,
Kalashnikov Izhevsk State Technical University, Izhevsk, Russia
E-mail: ludmila396@rambler.ru

Abstract. The article discusses the possibility of assessing the thermal stress in the rail service. To assess stress method is used on the basis of phenomena acoustoelasticity. The results of the control of residual stresses in the rail at the site jointless track.

Keywords: acoustoelasticity, electromagnetic-acoustic conversion, residual stresses, rails

INTRODUCTION

The occurrence of longitudinal compressing stresses and tensile strengths in the rails is explained by thermal action, first of all, that creates high loads, which can become the cause of rail's blowout or its deflection. Rail breakage and changing of rail's shape are the prime causes of train delay and derailing. The consequences of rail's deformation is considerable for safety, reliability and efficiency of rail transportation, especially at service of a high-speed passenger traffic.

Stresses in the rails can be measured by using strain gauges, thereby strain-gauge sensor must be securely fixed with an object surface [1, 2]. Measurements of strains are performed only in the process of their change, so value of zero reading is necessary. The account of temperature influence is also necessary, because resistance of the strain-gauge sensor depends not only from the strains, but also from the temperature.

Making of gauges of internal stresses in rails is important a nondestructive testing stage. Using of portable gauges of stresses in rails will allow railway's service to check jointless track sites of a railway. There aren't practical methods of such gauging of stresses level in rails now. The most suitable method for the solution of this problem is the hypersonic method based on the phenomenon of acoustoelasticity [3, 4]. The operation purpose is the exploration of control's possibility of internal stresses in rails while in service.

MEASUREMENT TECHNIQUE

The basis of rail's stresses measurement technique is the known procedure of control of the stress-strain state in railway sprockets [5].

The acoustoelasticity method is based on the dependence of ultrasonic waves propagation velocity on mechanical stresses in a solid body taking into account coefficients of acoustoelasticity [3, 4]. For ultrasound excitation and receiving the SEMA structurescope (Fig. 1a) equipped with the noncontact electromagnetic-acoustic (EMA) transducer (Fig. 1b) is used [5]. The SEMA structurescope was designed in the «Department of Devices and Methods for Measurement, Control, Diagnostics» of Izhevsk State Technical University (Izhevsk, Russian Federation).
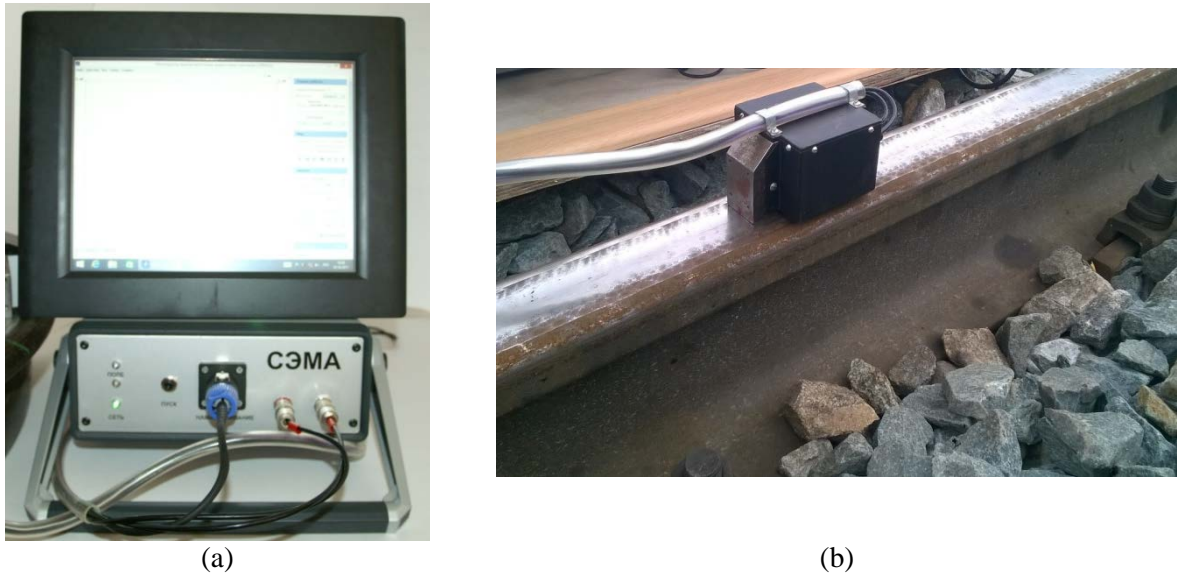

| (a) | (b) |

Figure 1. The experimental equipment: entire view of structurescope SEMA (a), the EMA transducer (b)
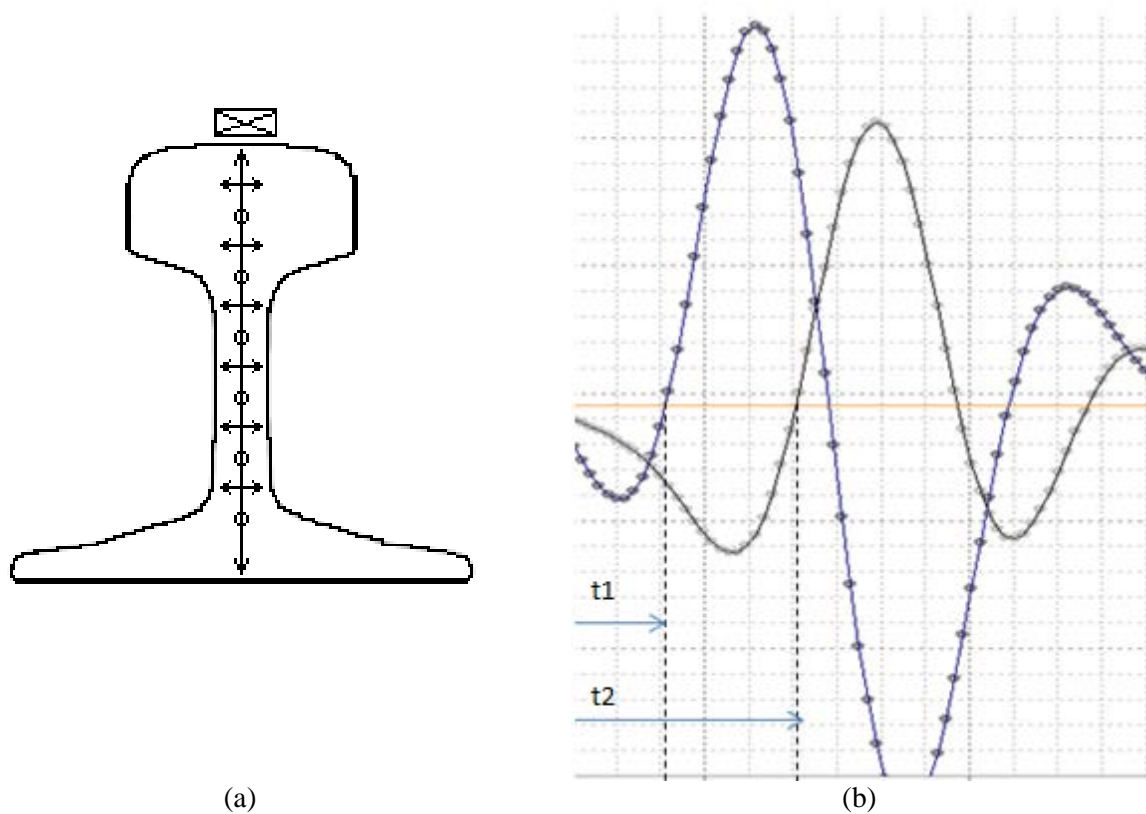

| (a) | (b) |

Figure 2. Plan of the rail scanning (a), the accepted signals (b)

The plan of rail scanning is presented on Fig. 2a. The EMA transducer is installed on a rail head; two pulses of orthogonally polarized transverse waves are excited from a rail head and received after reflection from a rail base by the same EMA transducer. The received signals (Fig. 2b) are then handled by specialized software called "Sensitive" which allows to measure amplitudes and arrival times discrepancy of two received echo-pulses.

The discrepancy in propagation time of the impulse signals, which are polarized lengthwise and perpendicularly rail axes, is proportional to residual stresses value. Values of propagation time of transverse waves t_1 and t_2 in one section of a rail, are used for the calculation of residual stresses σ by the formula [5]:

$$\sigma = D\left(\frac{t_1}{t_2} - 1\right), \tag{1}$$

where D – coefficient of elastic-acoustic linkage for the explored material, spotted experimentally and equal to 145 GPa.

RESEARCH RESULTS

Studies have been conducted on the site of continuous welded rail track Yuski – Ludzy haul of Agryz – Izhevsk section of Gorky Railways. Residual stresses were determined on a region of 400 m in length in several places, at a distance of 50 m from each other in the same locations and at different ambient temperatures and respectively rail: 4 °C, 24 °C and 32 °C. The research results for various temperatures are shown in Fig. 3. The lengthening of the rails occurs during heating, so the temperature rise must increase the compressive stresses in the fixedly secured rail. It is known that the rails fixed to the sleepers twice a year for use in summer and in winter.
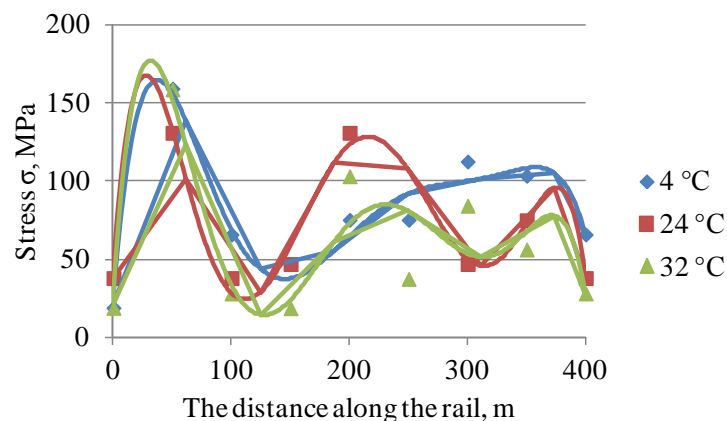
Figure 3. The stress distribution in the rail at different test temperatures

The rails are laid at a temperature of 20 °C (the initial "neutral temperature"), designed for summer operation. The stresses occur from the present temperature and the thermal expansion coefficient of the rail, if the neutral temperature is known, therefore, stress redistribution conditions are predictable. During processing results of research the temperature of 24 °C was selected as the neutral temperature of rail lying. The stress distributions in the rail taking into account the neutral temperature are shown in Fig. 4. Reducing the stress occurs with increase temperature, since the rail expands and undergoes compressive loads, as can be seen from the diagram.
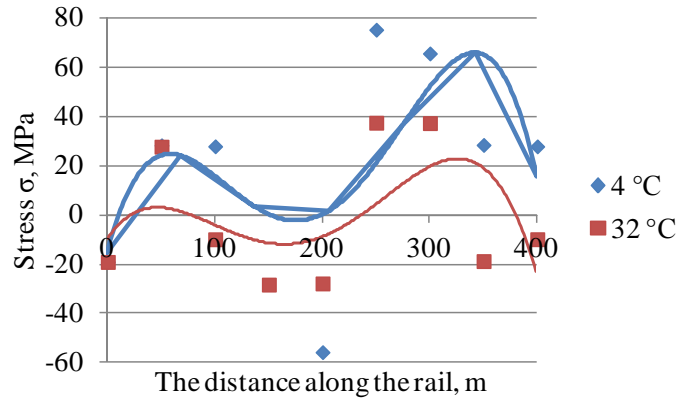
Figure 4. The stress distribution in the rail at different test temperatures compared with stress-free temperature

Unfortunately, the neutral temperature can be changed after laying the rails associated with locomotive traction and braking. Cross-section of a rail bar was selected to investigate the influence of a load moving train on the stress level. Stress at the point was 103 MPa at a distance of 300 mm from the beginning, before the passage of electric train ED9M with 4 cars, after passing train the stress increased to 113 MPa.

A series of measurements was carried out at two points at a distance of 20 cm from each other, to take account of the influence of errors. The results are shown in Table 1.

Table 1. Results of measurement errors

The number measurement	Stresses in the section 1, MPa	Stresses in the section 2, MPa
1	38	28
2	28	28
3	28	19
4	28	19
5	38	28
σ_{avg}	32	24
$\Delta\sigma$	5	5

Changing the stress after the passage of a train is in the range of error and can be not taken into account when evaluating thermal stresses.

CONCLUSION

The tried control technology compression-tensile thermal stress in the rails allows measurements in any section of the rail and provides highly accurate results. However, indefinite stress variation with temperature change of the rail requires additional studies evaluating residual stresses in the rails during the production and accumulation of residual stresses during operation.

REFERENCES

1. C.C.H. Lo, "Nondestructive evaluation of residual stresses in case hardened steels by magnetic anisotropy measurements," in Review Of Progress In Quantitative Nondestructive Evaluation: Vol. 31, AIP Conference Proceedings 820, edited by Donald O. Thompson and Dale E. Chimenti (Burlington, VT, 2012), pp 1445–1452.

2. P.B. Nagy, "Opportunities and Challenges for Nondestructive Residual Stress Assessment," in Quantitative Nondestructive Evaluation, AIP Conference Proceedings 820, edited by Donald O. Thompson and Dale E. Chimenti (Brunswick, Maine (USA), 2006), pp. 22–41.

3. N.E. Nikitina, Acoustoelasticity. Practical experience, N. Novgorod: Talam, 2005.

4. S.A. Becher, A.N. Kurbatov, and L.N. Stepanova, "Using acoustoelasticity effect in the study of the mechanical stresses in the rails," Herald RSTU, No. 2, pp. 104–110, 2013.

5. V.V. Muraviev, L.V. Volkova, E.N. Balobanov, "Estimation of residual stresses in locomotive wheel treads using the acoustoelasticity method," Russian Journal of Nondestructive Testing, vol. 49, No. 7, pp 382–386. July 2013.

Probabilistic and Statistical Characteristics of Signals in Mirror through Transmission Technique on Multiple Reflections for Rod Cross Section Ellipticity Testing

O.V. Muravieva, K.V. Petrov, M.A. Gabbasova

Department "Devices and Methods for Measurement, Control, Diagnostics",
Kalashnikov Izhevsk State Technical University, Izhevsk, Russia
E-mail: pmkk@istu.ru

Abstract. This article suggests an approach to validation of new informative parameters in mirror through transmission electromagnetic-acoustic technique on multiple reflections for cylindrical object ellipticity testing, based on probabilistic and statistical analysis of multiple reflection series. The results of data array analysis obtained in the process of multiple reflection oscillogram modeling are presented. Behavior of probability density distribution, dispersion, root-mean-square deviation and asymmetry, depending on ellipticity value, is shown. Their applicability as informative parameters is introduced.

Keywords: ellipticity, rod, multiple mirror through transmission technique, probabilistic and statistical analysis

INTRODUCTION

The need for cross section shape testing arises in the process of circular section rod production. Defects of cross section shape deviation from roundness called cross section ovality (ellipticity) appear due to equipment deterioration or other factors. During rod manufacturing cross section ellipticity is detected by general-purpose measuring tools such as a caliper rule, a micrometer, a roundness measuring tool. One of promising problem-solving methods in non-destructive testing, material property characterization and thickness gauging of bar steel rolled stock is application of mirror through transmission technique using an encircling electromagnetic-acoustic (EMA) transducer [1–4]. In this case ultrasound impulse multiple reflection series of shear waves axially polarized in all radial directions over the cross section of the rod is formed. The model of acoustic wave propagation in mirror through transmission technique for cross section ellipticity testing is introduced in the paper [5]. In the case of rod cross section deviation from roundness, envelope of multiple reflections series is modulated. It is shown that envelope period and time shift of main reflection echo-impulses for an elliptical rod in comparison with a circular section rod can be used as informative parameters. This article suggests an approach to validation of new informative parameters in mirror through transmission technique for cylindrical object ellipticity testing, based on probabilistic and statistical analysis of multiple reflection series.

APPROACHES USED

The results of modeling of ultrasound wave multiple reflections in elliptical cross section rod obtained as the result of superposition of waves radiated by encircling coils EMA transducer radiating elements and received by encircling coils EMA transducer receiving elements on opposite surface with regard to ultrasound beam path in elliptical rod cross section in accordance with ray acoustic theory are used as input data for this research. Examples of modeled multiple reflection series in the rod with different ellipticity rates are represented in Fig. 1. Ellipticity Δ is defined as a half of difference between the highest d_1 and the least d_2 values of diameters in orthogonally related directions.
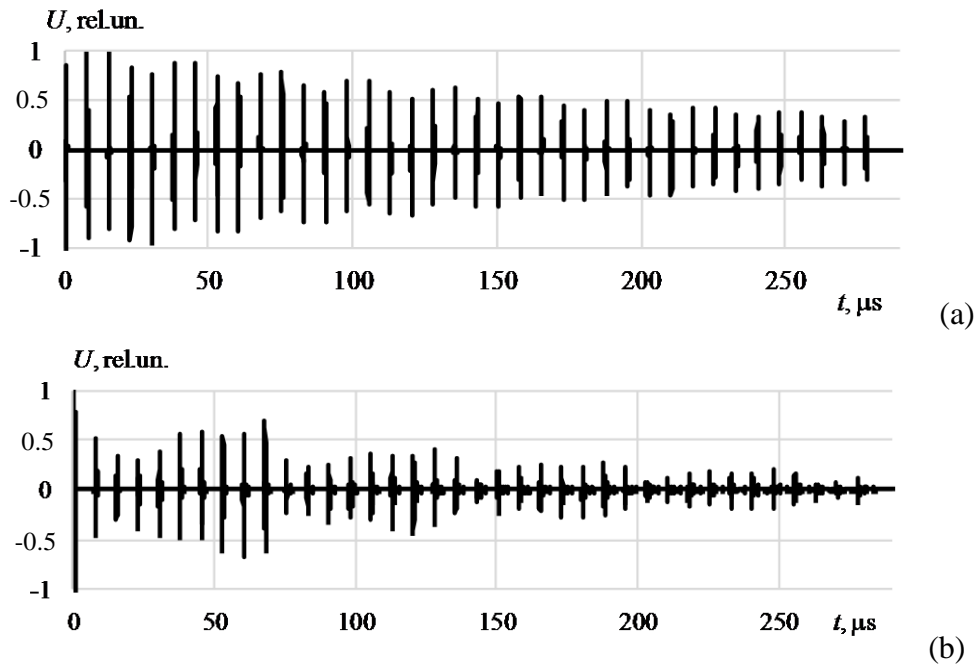
Figure 1. Oscillograms of multiple reflections with ellipticity $\Delta = 0$ mm (a) and $\Delta = 0.25$ mm (b) for the rod with diameter $d = 24$ mm

Such probabilistic characteristics as probability density distribution $P(x)$, dispersion Dx, root-mean-square deviation σ_x, asymmetry S_x and excess E_x were investigated to study the applicability of probabilistic characteristics as informative parameters for oscillograms represented in the form of sample sequence $\{x_n, n = 0, \ldots, N–1\}$. These parameters are defined by following formulas [6]:

$$P(x) = \frac{1}{N \cdot h} \cdot \sum_{n=0}^{N-1} \left(-\frac{x_m - x_n}{2h^2} \right)^2, \tag{1}$$

$$D_x = \frac{1}{N-1} \cdot \sum_{n=0}^{N-1} (x_n - m_x)^2, \tag{2}$$

$$\sigma_x = \sqrt{D_x}, \tag{3}$$

$$S_x = \frac{1}{N \cdot \sigma_x^3} \cdot \sum_{n=0}^{N-1} (x_n - m_x)^3, \tag{4}$$

$$E_x = \frac{1}{N \cdot \sigma_x^4} \cdot \sum_{n=0}^{N-1} (x_n - m_x)^4 - 3, \tag{5}$$

where N – amount of data in array x_n; $h = \sigma N^{-1/5}$; σ – root-mean-square deviation of the process; $m = 1, \dots, M$, M – number of points in estimated probability density function.

RESULTS AND DISCUSSION

The obtained probability density distribution $P(x_m)$ is represented in Fig. 2. Different patterns of probability density are observed due to different ellipticity rates: the higher ellipticity rate, the sharper distribution peak.
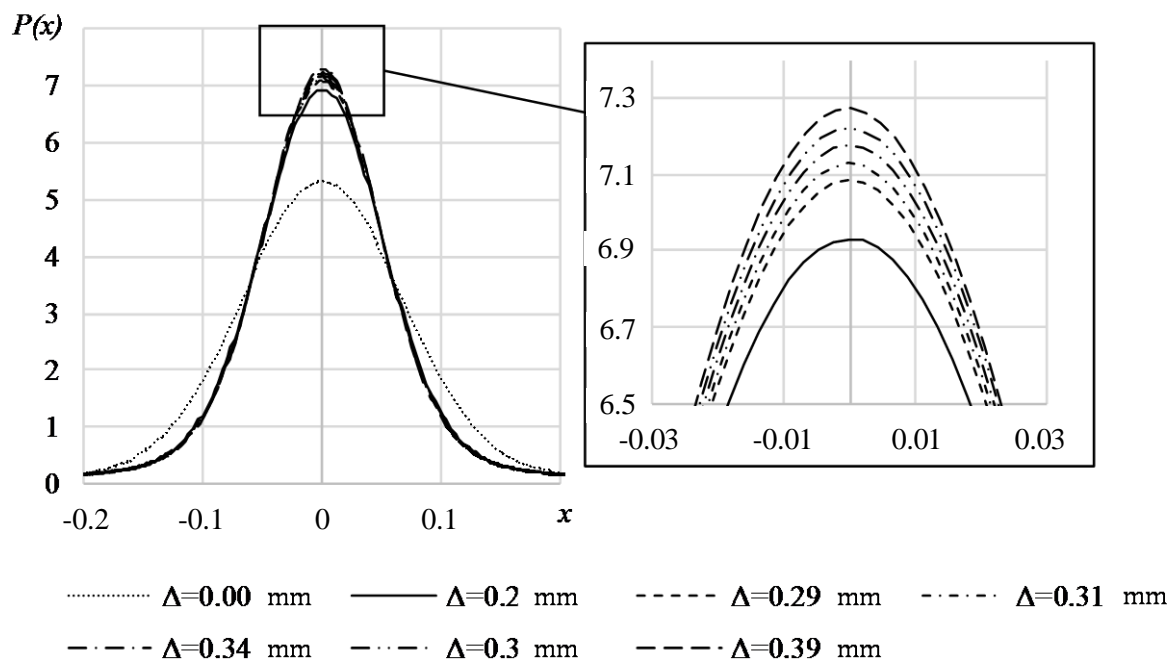

Figure 2. Probability density distribution $P(x)$ with different ellipticity rates Δ
for the rod with diameter $d = 17$ mm

Probabilistic and statistical analysis of the given oscillograms was made in special-purpose software suite WinPOS Professinal, which is intended for post experimental measurement data processing by means of standard mathematical and statistical algorithms, study of dynamic and slowly changing processes, graphical representation and documenting of the data [7].

The dependence of oscillogram probabilistic characteristics on ellipticity Δ for the rod with diameter $d = 24$ mm is represented in Fig. 3. It is obvious that all presented probabilistic characteristics have evident non-linear dependences on ellipticity. Ellipticity increase causes decrease of such characteristics as dispersion and root-mean-square deviation. In particular, ellipticity $\Delta = 0.5$ mm causes decrease of parameter "dispersion" D_x by 60 % and parameter «root-mean-square deviation» σ_x by 37 %. Excess and asymmetry, on the contrary, increase with increase of cross section ellipticity. Thus, ellipticity $\Delta = 0.5$ mm for the rod with diameter $d = 24$ mm causes increase of parameter "asymmetry" S_x by 46 % and parameter "excess" E_x by 108 %.
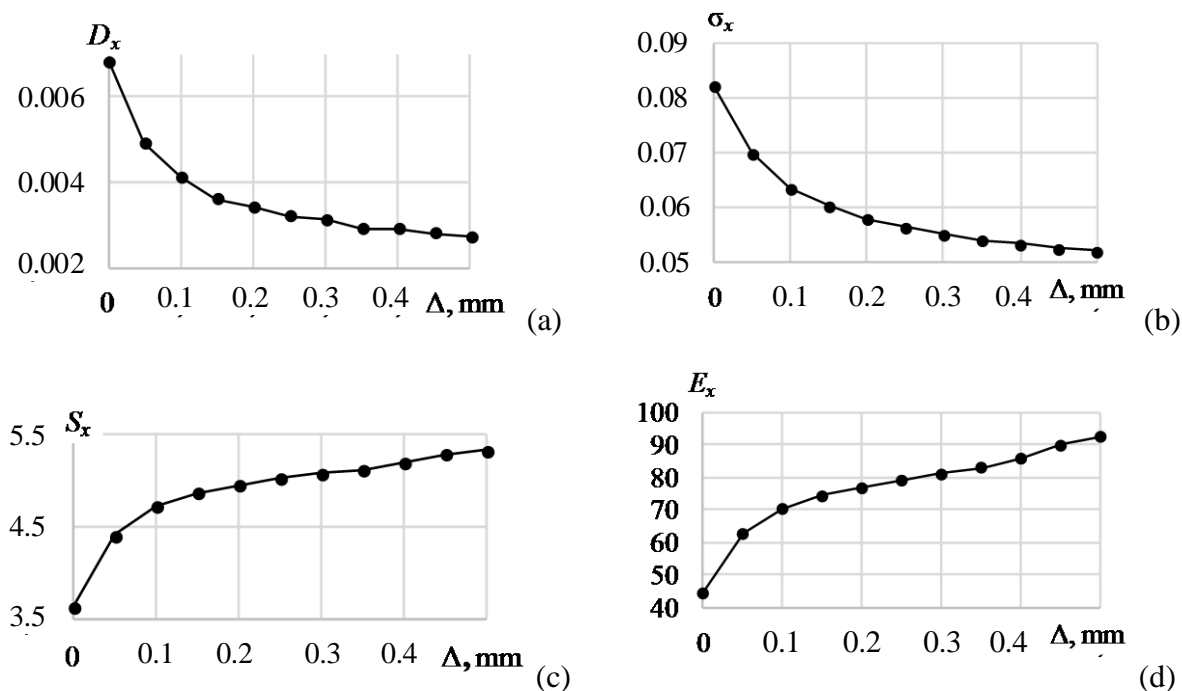
Figure 3. Dependences of dispersion D_x (a), asymmetry S_x (b), root-mean-square deviation σ_x (c), excess E_x (d) on ellipticity Δ for the rod with diameter $d = 24$ mm

CONCLUSION

In sum, developed approach allows to validate informative characteristics of signal in multiple mirror through transmission technique for cylindrical object ellipticity testing and to formulate rejection criterion for ellipticity testing of cylindrical objects with any diameters using probabilistic and statistical analysis.

REFERENCES

1. S.Ya. Molokanov, V.S. Volkov, A.A. Chernikov, V.N. Artyushov, A.M. Kashin, "Ultrasound monitoring of a rolled bar in the Volna-7 automated system," in Steel in Transl., 2010, vol. 40, No. 4, pp. 357–362.

2. M. Hirao and H. Ogi "EMATS for science and industry: noncontacting ultrasonic measurements," Boston: Kluwer Academic Publishers, 2003.

3. A.V. Mikhailov, Y.L. Gobov, Y.G. Smorodinskii, S.V. Shcherbinin, "An Electromagnetic–Acoustic Transducer With Pulsed Biasing," Russian Journal of Nondestructive testing, vol. 51, No.8, pp. 467–475, 2015.

4. V.V. Muraviev, O.V. Muravieva, E.N. Kokorina, "Quality control of heat treatment of 60C2A steel bars using the electromagnetic–acoustic method," Russian Journal of Nondestructive testing, vol. 49, No.1, pp. 15–25, 2013.

5. O.V. Muravieva, K.V. Petrov, M.Iu. Sokov, M.A. Gabbasova, "The simulation and study of interaction of the acoustic waves radiated by an encircling electromagnetic-acoustic transducer with the rod ellipticity," Russian Journal of Nondestructive Testing, vol. 51, No. 7, pp. 400–406, 2015.

6. M.N. Stepnov, Statisticheskie metody obrabotki rezul'tatov mekhanicheskikh ispytanii. Spravochnik, Moscow: Mashinostroenie, 1985.

7. WinPOS Signal Processing Package, User's Guide, edition 3.2, RPE «Mera», Mitichshi, 2014.

Influence of the Viscoelastic Media Properties on the Lowest Lamb Wave Mode Propagation in Pipe

Y.V. Myshkin [1,2], O.V. Muravieva [2]

[1] Physical Technical Institute Ural Branch of Russian Academic Scientists, Izhevsk, Russian Federation
E-mail: mubm@yandex.ru
[2] Department of measurement, control, diagnostics instruments and techniques,
Kalashnikov Izhevsk State Technical University, Izhevsk, Russian Federation

Abstract. The results of comparative experimental research in influence on torsional $T(0,1)$, symmetrical and antisymmetrical Lamb waves attenuation in pipe under the loading conditions on viscoelastic media such as internal fluid (water, glue) and external loose media are presented in this article. The technique and the experimental installation allowing to generate and receive different kinds of Lamb waves with special-purpose electromagnetic-acoustic oscillators and piezoelectric receivers are introduced. The obtained results can be taken into account when equipment and waveguide techniques for pipeline testing being developed with the use of torsional, symmetrical and antisymmetrical waves to estimate sensitivity of methods and distance of extended object scanning.

Keywords: viscoelastic medium, symmetric wave, antisymmetric wave, torsional wave attenuation, long-range guided wave testing, pipe

INTRODUCTION

Long-range guided wave acoustic testing technique based on the use of normal Lamb waves becomes more common in instant testing of pipelines due to an opportunity of normal wave propagation for long distances in pipes covered with insulation and laid under ground or water. It is stated [1–10], that a range of pipe scanning distances can be changed from 1 to 200 meters depending on the used wave mode, a type of transported substance, a type of insulation, operating conditions of pipelines (underwater, ground-surface, underground) and their typical sizes.

The results of experimental research in influence of pipe loading conditions on attenuation of zero-order symmetrical and antisymmetrical Lamb waves and torsional waves are presented in the article.

APPROACHES USED

The guided wave testing technique installation which includes a probe pulse generator, a sync pulse generator, an amplifier, a registration unit (digital oscillograph RIGOL) was used for experimental research. Electromagnetic-acoustic transducers (EMAT) operating on electrodynamic mechanism were used as oscillators. Reception was performed with the use of

piezoelectric transducer based on shearing piezoceramics labeled as NFI50. Generation and reception of both horizontal polarized (torsional) waves and zero-order symmetrical and antisymmetrical Lamb wave modes is possible depending on locations of oscillators and receivers about a pipe axis (Figure 1).
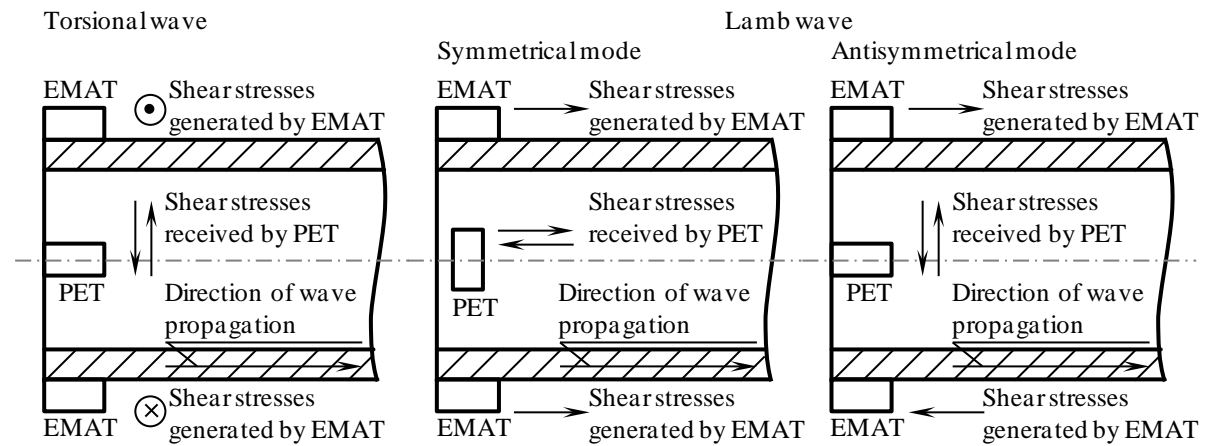

Figure 1. A scheme of different type wave excitation and transducer locations around the pipe end: EMAT – electromagnetic acoustic transducer, PET – piezoelectric transducer
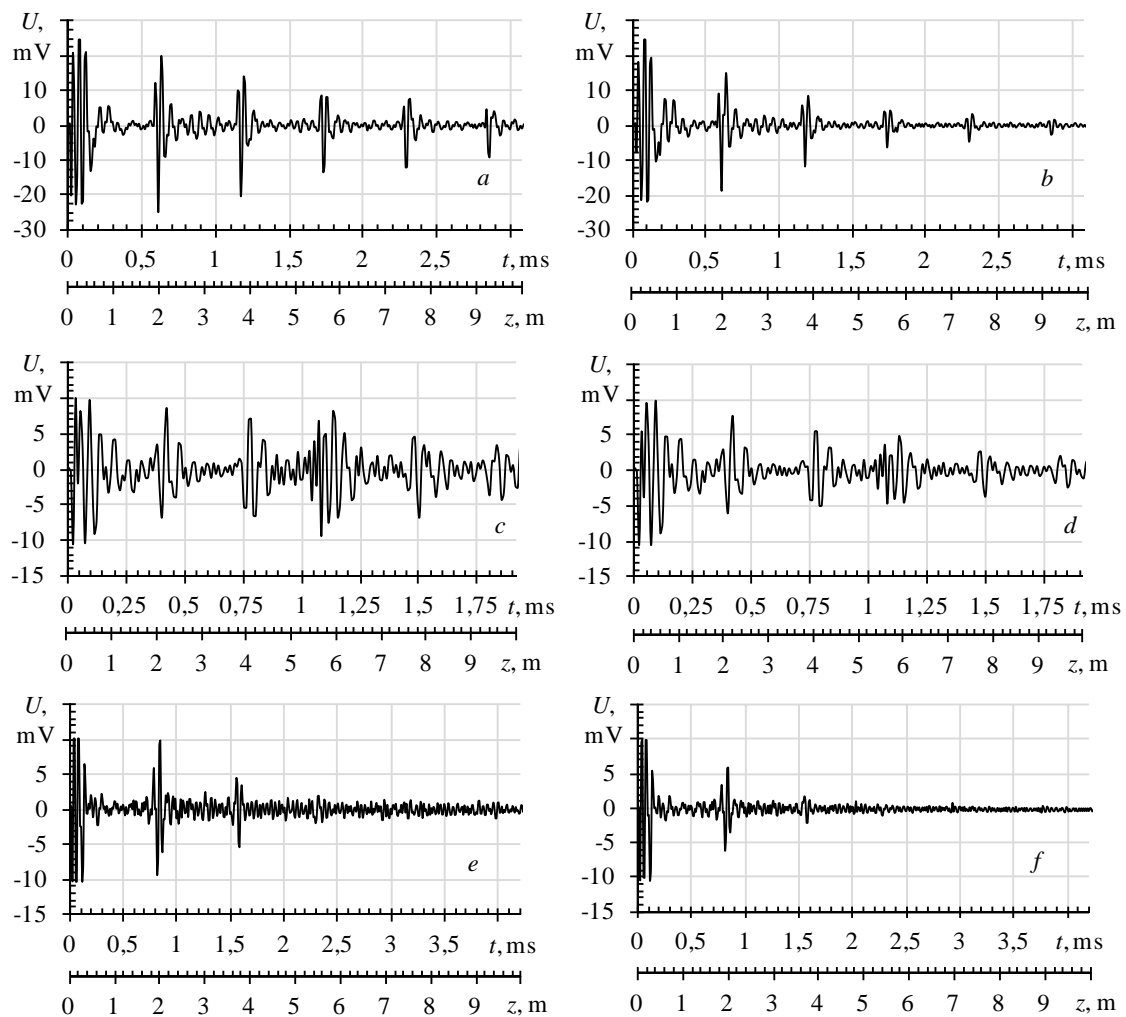

Figure 2. Pulse echo ultrasound torsional, symmetrical, antisymmetrical wave images for unloaded pipe (*a*, *c*, *e* respectively) and pipe buried in sand (*b*, *d*, *f* respectively)

Experiments were carried out for steel pipe with diameter 33.7 mm, wall thickness $h = 4.2$ mm and length $l = 100$ mm under operating frequency 30 kHz. The pipe was located in plastic container and loaded on contact external and internal media. Air, water and dextrin (oil simulation) were used as internal media, and damp sand, arid ground and clay were used as external media. The result of echo-pulse series registration of torsional, symmetrical and antisymmetrical waves repeatedly reflected from free pipe edges and the same waves under loading conditions on damp sand is represented in Figure 2.

RESULTS AND DISCUSSION

The propagation velocities of symmetrical, antisymmetrical and torsional waves are defined by the following formula:

$$C = \frac{nl}{\Delta t}, \tag{1}$$

where C is a velocity of certain type Lamb wave, n is a number of analyzed reflections, Δt is time between probe impulse and the nth impulse of certain type Lamb wave.
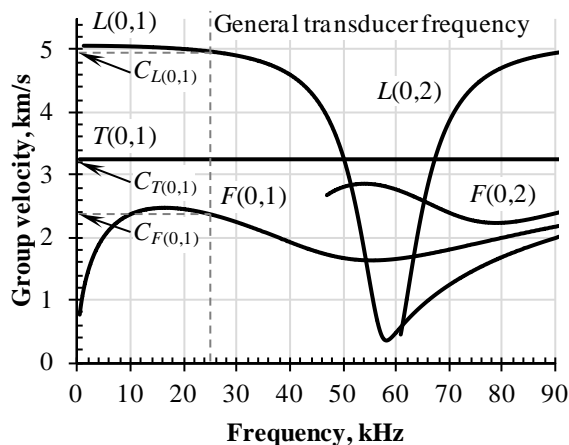
Figure 3. Dispersion curves for pipe: diameter 32 mm, wall thickness 4.2

Velocities calculated according to the obtained oscillograms are $C_{L(0,1)} = 5225$ m/s for Lamb wave symmetrical mode $L(0,1)$, $C_{F(0,1)} = 2375$ m/s for Lamb wave antisymmetrical mode $F(0,1)$, $C_{T(0,1)} = 3250$ m/s for torsional mode $T(0,1)$. It's worth mentioning, that the given values are in agreement with the values calculated by Lamb wave dispersion curves, built in special-purpose software (Figure 3).

Figure 2 shows that values of attenuation are different by distance of different Lamb waves, even for unloaded pipe, that is caused by influence of dispersion. The attenuation has the lowest

Figure 4. Generalized dependences of pulse echo symmetrical (*a*) and antisymmetrical (*b*) wave attenuation in dB for pipe loading on ground, sand or clay compared to unloaded pipe

value for torsional waves $T(0,1)$ where dispersion is absent (Figure 3) and attenuation is caused by internal viscous losses and scattering from surface inhomogeneity; the highest value of attenuation is observed for the mode $F(0,1)$ with the highest value of dispersion. Reradiation of vertical, horizontal (in the cases of modes $L(0,1)$ and $F(0,1)$) and angular (in the case of mode $T(0,1)$) displacement components in surrounding media influence more on attenuation for the pipe loaded on contact media.

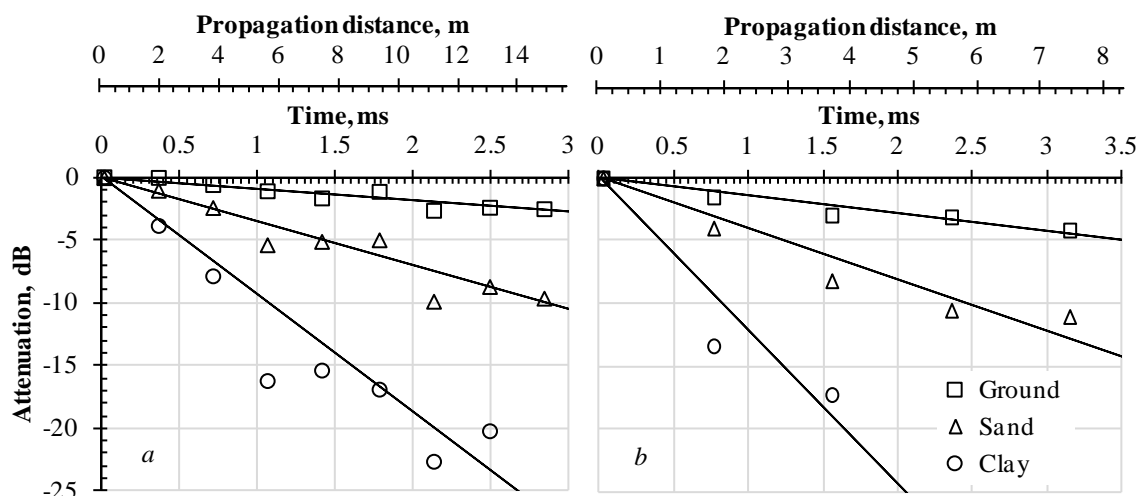Generalized dependences of echo-pulse amplitude attenuation for the modes $F(0,1)$ and $L(0,1)$ in dB compared to unloaded pipe (level of 0 dB) by the distance for different contact media are represented as an example in Figure 4. It follows from the given dependences, that in the case of pipe loading on ground echo-impulse amplitude attenuation compared to unloaded pipe is the lowest for the mode $T(0,1)$ and it is equal to 2 dB at the distance of 10 m for this mode, 2 dB at the distance of 10 m for the mode $L(0,1)$, 6 dB at the distance of 10 m for the mode $F(0,1)$. The pipe loading on clay causes more essential wave attenuation: 30 dB at the distance of 10 m for the mode $T(0,1)$, 18 dB at the distance of 10 m for the mode $L(0,1)$, approximately

Figure 5. Signal/noise level dependences on the pipe end reflections for different types of wave propagation in pipe loaded on air, dextrin and water (for torsional wave)

50 dB at the distance of 10 m for the mode $F(0,1)$. It should be noted, that in the cases of loading on water and dextrin both from external and internal sides of pipe, essential echo-impulse amplitude variation for the mode $T(0,1)$ isn't observed that is caused by the absence of torsional wave reradiation effect in fluid media due to impossibility of shear displacement generation in latter waves. Whereas, influence of these media is enough essential for the mode $F(0,1)$.

Obstructive waves, which are basically acoustic noise restricting the sensitivity to defects, can appear together with the main Lamb wave modes during generation (reception). It is essential, that in the case of the mode $T(0,1)$ the level of acoustic noise, caused by radiation of obstructive mode oscillation (symmetrical and antisymmetrical), decreases essentially under loading on fluid media (by 1.3 times under loading on water, by 1.8 times under loading on dextrin) compared to unloaded pipe, that is caused by absence of torsional wave reradiation effect in fluid media due to impossibility of shear displacement generation in latter waves.

The obtained results can be taken into account when equipment and waveguide techniques for pipeline testing are being developed with the use of torsional, symmetrical and antisymmetrical waves to estimate sensitivity of methods and scanning range.
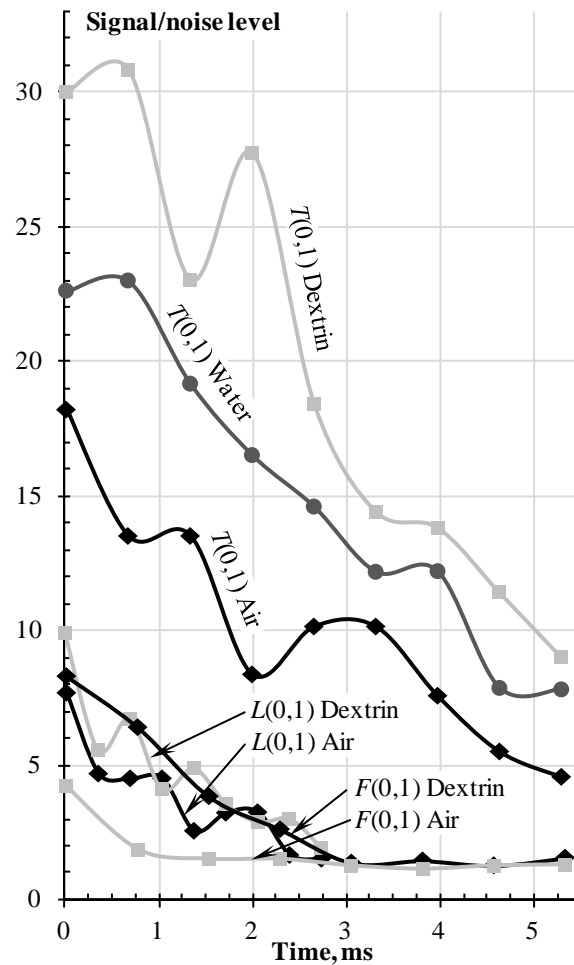
ACKNOWLEDGMENTS

REFERENCES

1. E. Leinov, M.J.S. Lowe, P. Cawley, "Investigation of guided wave propagation and attenuation in pipe buried in sand," Journal of Sound and Vibration, vol. 347, pp. 96–114, 2015.

2. D.N. Alleyne, T. Vogt, P. Cawley, "The choice of torsional or longitudinal excitation in guided wave pipe inspection", Insight, vol. 51, pp. 373–377, 2009.

3. O.V. Muravieva, V.A. Strizhak, D.V. Zlobin, S.A. Murashov, A.V. Pryahin, "Tehnologiya akusticheskogo volnovodnogo kontrolya nasosno-kompressornyh trub," [A guided wave testing technology of pump-compressored pipes], In the nondestructive world, vol. 4 (66), pp. 55–60, 2014.

4. O.V. Muravieva, S.V. Lenkov, S.A. Murashov, "Torsional waves excited by electromagnetic acoustic transducers at the guided wave testing of pipelines," Acoustical Physics, vol. 62, No. 1, 2016, in press.

5. M. Ces, D. Royer, C. Prada, "Characterization of mechanical properties of a hollow cylinder with zero group velocity Lamb modes," The Journal of the Acoustical Society of America, vol. 132 (1), pp. 180–185, 2015.

6. J. Mu, J.L. Rose, "Guided wave propagation and mode differentiation in hollow cylinders with viscoelastic coatings," The Journal of the Acoustical Society of America, vol. 124 (2), pp. 866–874, 2008.

7. J.N. Barshinger, J.L. Rose, "Guided wave propagation in an elastic hollow cylinder coated with a viscoelastic material," IEEE Transactions on Ultrasonics, Ferroelectrics, and Frequency control, vol. 51 (11), pp. 1547–1556, 2004.

8. J. Hua, J. Mu, J.L. Rose, "Guided wave propagation in single and double layer hollow cylinders embedded in infinite media," The Journal of the Acoustical Society of America, vol. 129 (2), pp. 691–700, 2011.

9. R. Kirby, Z. Zlatev, P. Mudge. "On the scattering of longitudinal elastic waves from axisymmetric defects in coated pipes", Journal of Sound and Vibration, vol. 332, pp. 5040–5058, 2013.

10. F. Simonetti, P. Cawley. "A guided wave technique for the characterization of highly attenuative viscoelastic materials", The Journal of the Acoustical Society of America, vol. 114 (1), pp. 158–165, 2003.

Interpolation Information-Measuring System on the Basis of Television Scanistor

Y.K. Shelkovnikov [1], A.I. Korshunov [2], S.G. Seletkov [3], V.A. Kulikov [4]

[1] Laboratory of information-measuring systems, Institute of Mechanics UB RAS, Izhevsk, Russia
E-mail: evshelk@mail.ru
[2] Kalashnikov Izhevsk State Technical University, Izhevsk, Russia
E-mail: kai@istu.ru
[3] Department of Higher Mathematics, Kalashnikov Izhevsk State Technical University, Izhevsk, Russia
E-mail: s.g.seletkov@mail.ru
[4] Department of Computer Engineering, Kalashnikov Izhevsk State Technical University, Izhevsk, Russia
E-mail: kulik00@istu.ru

Abstract. The purpose of the paper is to discuss the issues of improving the accuracy of determining the coordinates of the middle of the light zone of the TV scanistor. The expediency of applying two methods of comparison to this purpose was shown, particularly when the dimensions of the light zone may vary during the measurement. Interpolation information and measuring system with the proposed interpolation method of measuring the time interval was described.

Keywords: TV scanistor, information and measuring system, video signal, measurement accuracy, time interval, interpolation method

INTRODUCTION

A television semiconductor p-n-p structure of scanistor (solid scanistor, discrete multiscan) is a non-vacuum analogue of a television transmitter tube and can be used as a sensor for automatic control of the space-time state of the object [1–3]. Scanistor structures are used in various fields of science and technology for measurement of angular and linear movement, velocity, acceleration, size and relative position of objects [4–7]. It was established that the most appropriate method of scanistor utilization is to use them as the coordinate-sensitive photodetectors for measuring sizes and positions of various light zones. In this case, a coordinate resolution equals to several units or fraction of a micron (i.e., 2 orders of magnitude higher than their television resolution and almost an order of magnitude higher than the actual resolution of the coordinates (size) light zones have and photodiode structures) [8, 9]. The broad functionality of TV scanistor structures, simplicity of design, manufacturing technology and the scheme of formation and allocation of the video signal allow to create simple and reliable scanistor information-measuring systems (SIMS) for instrumentation, process control systems in the field of aerospace, chemical and physical studies, etc. [10]. It was noted that increase of measurement accuracy of coordinates of light streams with the help of SIMS is a relevant task.

BLOCK DIAGRAM OF THE INTERPOLATION SIMS

Figure 1 shows a block diagram of a high-precision interpolation SIMS for coordinate measuring of the middle of the light zones of the scanistor, where TS – television scanistor; FD – frequency divider; CPS – clock pulse source; VC – videosignal converter; SAW – sawtooth-voltage generator; VS – bias voltage source; T_1–T_4 – RS-triggers; DA_1, DA_2 – differentiating amplifiers; LA – limiting amplifier; Sh – shaper of the signals; AND_1–AND_5 – AND gates; OR_1-OR_3 – OR gates; PC_1-PC_5 – pulse counters; TAC_1–TAC_3 – time-to-amplitude converters; ADC_1-ADC_3 – analog-to-digital converters; MCU – microcontroller unit; LCD – liquid-crystal display.

FORMATION OF THE VIDEO SIGNAL IN THE INTERPOLATION SIMS

Scanistor (TS) is a narrow strip of silicon of p-n-p structure and three ohmic contacts, two of which (E_1, E_2) are located on the edges of the emitter region. The strip itself is a photosensitive layer, and simultaneously a voltage divider bias source (see Figure 1). The third contact (K) serves as the contact to the equipotential collector region.

There are such high metrological characteristics of the scanistor due to the fact that the scanning is carried out with the analog method equipotential zero line, which is created and moves along the photodiode structure using the sawtooth generator and emitter bias source (fission) layer. In the output of VC there is forming of a video signal that reflects the light distribution of relief F along the photosensitive surface of the scanistor. Timing diagrams are shown in Figure 2, they explain the work of the interpolation SIMS. A video signal of trapezoidal shape is being formed in the output of VC block during the differentiation of the current of the scanistor (Figure 2c) then is differentiated twice by a DA_1 (Figure 2d) and DA_2 (Figure 2e) to highlight coordinates x_1, x_2 of the edges of the light zone, then the video signal enters through the limiting amplifier LA (Figure 2f) into the shaper of the signals Sh, which generates at its first output video pulse of the beginning of the zone (Figure 2g), and at its second output – video pulse of the end of the zone (Figure 2h). At its third output the shaper generates a video strob, leading and trailing edges of which coincide in time with the video pulses of the start and the end of the zone of scanistor respectively.

OPERATION OF THE INTERPOLATION SIMS

Measurement of the time coordinate t_x of the middle of the video strobe, corresponding to coordinate x in the middle of the light zone scanistor, carried out consecutively in two stages. At the first stage trigger T_1 forms the measuring impulse of the duration t_{x1}, the gate AND_1 is filled by counting pulses from CPS with the repetition period t_{cp} (Figure 2i).

At the second stage he elapsed time $(t_{x2} - t_{x1}) / 2$ is measured, which equals to half the length of the video strobe that is formed by the shaper Sh, this video strobe is filled with counting pulses from the output of the frequency divider FD with the repetition period $2t_{cp}$ (Figure 2j). The time coordinate t_x is determined in the output of gate OR_1 as the sum N (Figure 2k) of the number of pulses n_1, which are proportional to the interval t_{x1}, and the number of pulses n_2, which are proportional to the interval $(t_{x2} - t_{x1}) / 2$. The sum is calculated by the counter PC_1 and recorded by the microprocessor MCU.
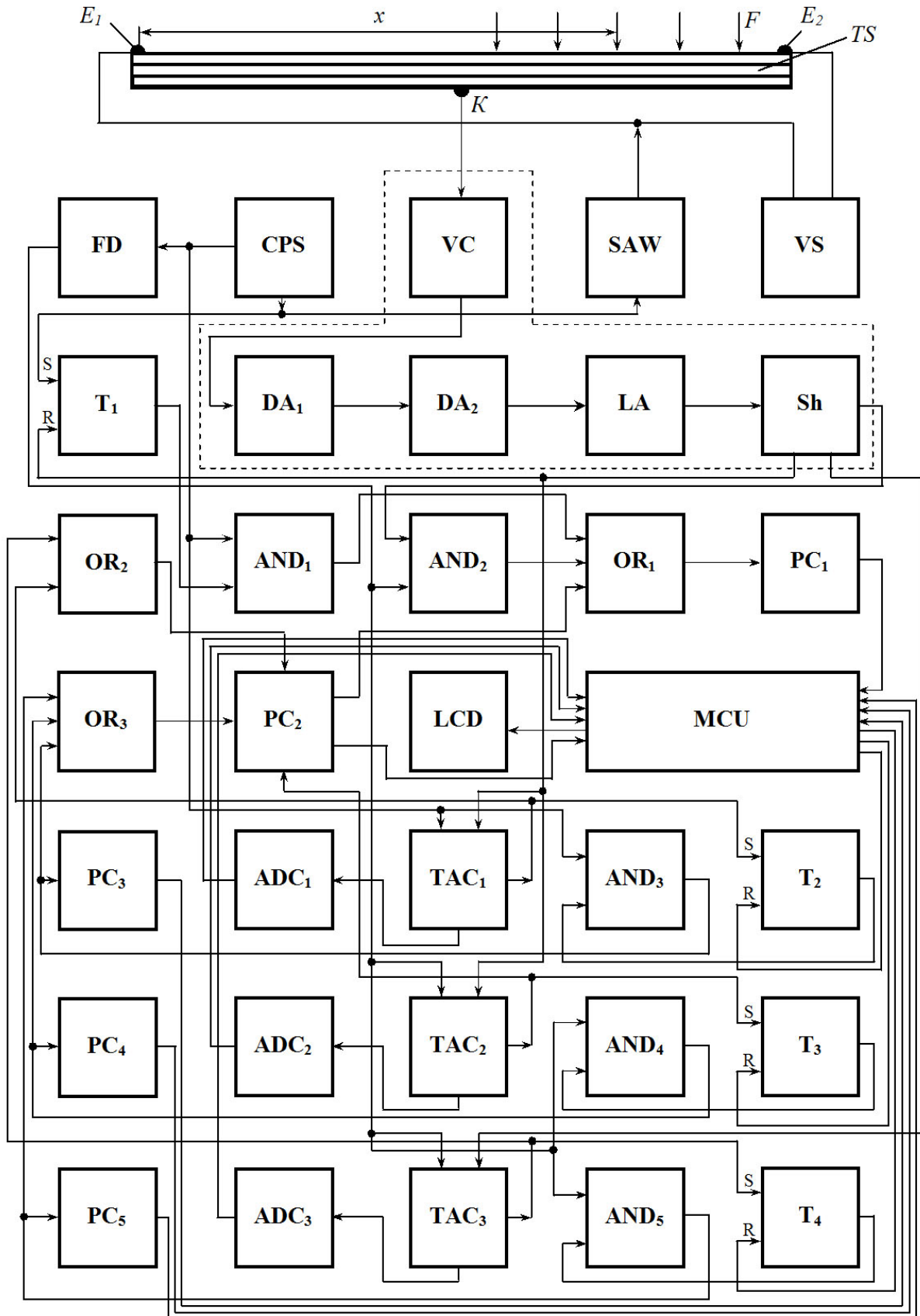
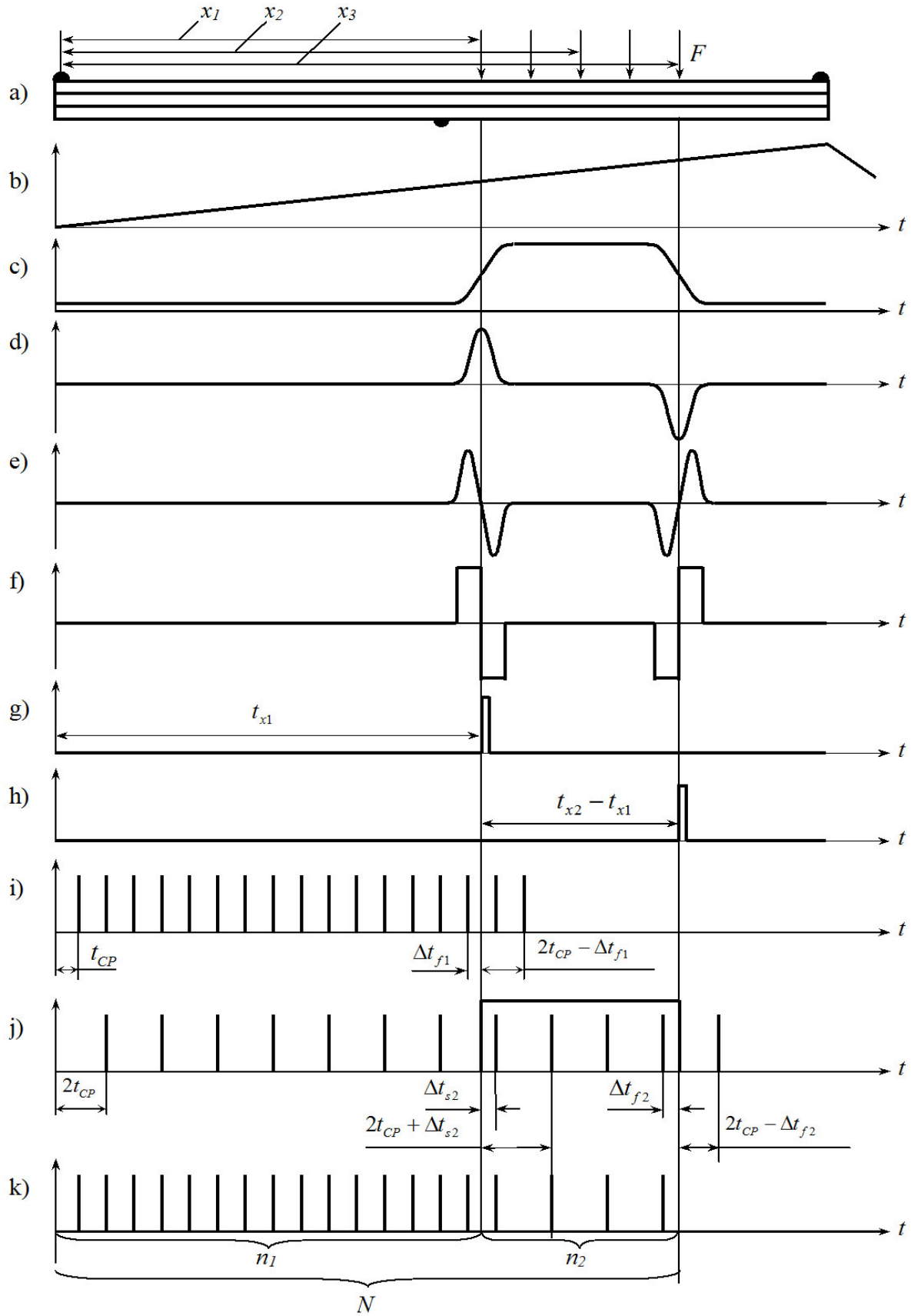**Figure 1.** Block diagram of precision interpolation SIMS

Figure 2. Timing diagrams explaining the operation of the interpolation SIMS

In this SIMS compare error δ_{comp} is appeared from the neglect of the time interval Δt_{f1} (Figure 2i) during the quantization of the interval t_{x1} by counting pulses with a repetition period t_{cp}, and from the neglect of time intervals Δt_{s2}, Δt_{f2} (Figure 2j) during the quantization of the interval $(t_{x2} - t_{x1})$ by counting pulses with a period $2t_{cp}$:

$$\delta_{comp} = \Delta t_{f1} + \Delta t_{s2} + \Delta t_{f2} \tag{1}$$

The most rational way of accounting Δt_{f1}, Δt_{s2}, Δt_{f2} is to use segments of the interpolation method of measuring of time intervals. This method allows to combine the advantages of the digital and the analog hardware implementations successfully. In the considered SIMS a version of the proposed interpolation meter [11] is implemented. Number of disadvantages inherent in the known devices have been eliminating. In this embodiment, time intervals $(2t_{cp} + \Delta t_s)$, $(2t_{cp} - \Delta t_f)$ are subjected to analog conversion, instead of the segments $0 \div \Delta t_s$, $0 \div \Delta t_f$ as in the known meters, that is way the relative variation range of the converted interval does not exceed 50 % of the maximum value of the interval t_{cp}, which improves linear characteristics of interpolating blocks.

Consider the formation of the error δ_{comp} in measuring the interval $t_x = t_{x1} + (t_{x2} - t_{x1}) / 2$ (Figure 2, i–k):

$$\begin{aligned}
t_x &= (t_{cp} \cdot n_1 + 2t_{cp} \cdot n_2) + \delta_{comp} = (t_{cp} \cdot n_1 + \Delta t_{f1}) + [2t_{cp} \cdot (n_2 - 1) + \Delta t_{s2} + \Delta t_{f2}] = \\
&= (t_{cp} \cdot n_1 + 2t_{cp} \cdot n_2) - (2t_{cp} - \Delta t_{f1}) + (2t_{cp} + \Delta t_{s2}) - (2t_{cp} - \Delta t_{f2});
\end{aligned} \tag{2}$$

or

$$\delta_{comp} = -(2t_{cp} - \Delta t_{f1}) + (2t_{cp} + \Delta t_{s2}) - (2t_{cp} - \Delta t_{f2}). \tag{3}$$

To estimate the error of the comparison δ_{comp} SIMS (Figure 1) has extra equipments: time-to-amplitude converters TAC_1–TAC_3, analog-to-digital converters ADC_1–ADC_3, down counter PC_2, counters PC_3–PC_5, gates AND_3–AND_5, gates OR_2, OR_3, triggers T_2–T_4. The first term of the expression (3) is formed by blocks SIMS as follows. Time-to-amplitude converter TAC_1 is started by the video pulse (Figure 2g) of the beginning of the zone, the end of the conversion cycle is formed at the second counting pulse nearby the video pulse with a repetition period t_{cp} (Figure 2i). At TAC_1 the time slice $(2t_{cp} - \Delta t_{f1})$ is transformed into an amplitude proportional to the length of the segment. For this transformation a condenser with a linear drive charge capacity with a constant current can be used during the duration of this interval. Then the amplitude formed by the analog-digital converter is converted into a code which enters from the output of ADC_1 to the input of MCU for comparing the codes. End of conversion cycle signal on TAC_1 starts trigger T_2, the output voltage of which is supplied one of two inputs of the gate AND_3 and permits passage of countable pulses with the period t_{cp} to the input of counter PC_3 and simultaneously through the gate OR_3 to the information input of down counter PC_2, which is set to subtraction serving mode (to acquire the minus sign before the first term) on its control input through the gate OR_2 with output pulse of end of the conversion cycle TAC_1. Once the code of the counter PC_3 is equal to the code, which is available at the output of ADC_1, MCU generates a signal which sets trigger T_2 in its initial state, as a result the further counting pulses advancing to the counter PC_2, PC_3 stops.

The second and the third terms of the expression (3) are formed by units of the SIMS in a similar manner, wherein for forming the second term conversion cycle TAC_2 is redefined by the video pulse of the beginning of the zone, and the end of the cycle – by the second neighboring pulse after the counting pulse with the repetition period $2t_{cp}$; to form the third term of conversion cycle TAC_3 is redefined by the video pulse of the end of the zone and the first neighboring pulse after it with the repetition period $2t_{cp}$ (Figure 2j).

The total number of M output pulse of down counter PC_2, is proportional to the sum of unaccounted time segments Δt_{f1}, Δt_{s2}, Δt_{f2}, defines the figure in the junior (secondary) discharge of the LCD and, as a consequence – increase in the accuracy of interpolating the SIMS. Since the value of the total time period may exceed counting pulses repetition period t_{cp} – for transmission transfer pulses from the counter PC_2 to PC_1 serves gate OR_1.

CONCLUSION

Thus, the work of precision interpolation system based on the principle of using two methods of comparison for measuring the time position in the middle of the light zone scanistor. First, to measure the time interval from the start of the survey of scanistor to a time coordinate of the start of the light zone as the first measure applies counting pulses repetition period. Then, doubled counting pulses repetition period during is used to measure the time interval corresponding to half the width of the light zone. The principle implemented in the SIMS, two-coordinate measuring midpoints of both broad and narrow light bands is universal, that is especially important when the dimensions of these zones may vary during the measurement. In the proposed interpolation SIMS the compare error of neglect of fixed time periods. The error is formed during the quantization of the time intervals with counting pulses. To this purpose, the proposed interpolation method of measuring time intervals is used.

REFERENCES

1. B.G. Podlaskin, E.G. Guk, "Position-Sensitive photodetector-multiscan," Measurement Techniques, pp. 31–34, Aug. 2008.

2. Y.K. Shelkovnikov, Y.I. Evseev, Russia Patent No. 974122 (15 November1982).

3. A.M. Lipanov, Y.K. Shelkovnikov, N.I. Osipov, S.R. Kiznertsev, Russia Patent No. 2348900 (10 March 2009).

4. A.M. Lipanov, Y.K. Shelkovnikov, N.I. Osipov, A.V. Aliev, "Noise-free scanistor meter for the angular movements of the objects," Intelligent Systems in Manufacturing (journal), No. 2, pp. 106–112, 2012.

5. Y.K. Shelkovnikov, "Precision Information and Measuring System Based on Television Scanistor," Intelligent Systems in Manufacturing (journal), No. 1, pp. 244–249.

6. Y.K. Shelkovnikov, "Improving the Stability and Linearity of a Coordinate Characteristic of Scanistor Information and Measuring Systems," Intelligent Systems in Manufacturing (journal), No. 1, pp. 251–255, 2011.

7. A.M. Lipanov, Y.K Shelkovnikov., N.I. Osipov, "Usage of discrete-one-piece structure of multiscanner in electrooptical measuring device,"Sensors & Systems, No. 2, pp. 46–49, 2003.

8. A.M. Lipanov, Y.K. Shelkovnikov, N.I. Osipov, "The analysis of multiscanner with amplitude-modulated light rays," Sensors & Systems, No. 10, pp. 12–16, 2003.

9. Y.K. Shelkovnikov, "Extraction of signal from multiscanner with modulation of deploys voltage," Polzunovsky vestnik, No. 2, pp. 107–112.

10. A.M. Lipanov, Y.K. Shelkovnikov, Theoretical science and technique of TV scanistor structures manufacturing, Yekaterinburg: Ural division of RAN, 2005.

11. V.A. Potekhin, Y.K. Shelkovnikov, Russia Patent No. 1302236 (22 Mach 1987).

Effect of Circuit Resistance and Inductance on Surge Current Testing of Tantalum Capacitors with Different Capacitance

B.I. Sibgatullin

Kalashnikov Izhevsk State Technical University, Izhevsk, Russia
E-mail: bullatts@gmail.com

Abstract. Since tantalum capacitors are used in low-impedance circuits, where they are exposed to surge current impact, it is important to have the special technique to evaluate the performance of tantalum capacitors in such conditions. For these purposes surge current testing according to ESA/SCC Generic Specification №3012 and MIL-PRF-55365 standards is used. But even slight variations of testing parameters in allowable range can significantly change testing conditions. This article is devoted to analysis of the relationship between surge current testing circuit parameters and surge current conditions during testing of tantalum capacitors with different capacitance. The influence of circuit resistance on amplitude of current spike and overvoltage at different capacitor values and circuit inductance is evaluated.

Keywords: tantalum capacitor, surge current testing, surge current failure, transients, breakdown, overvoltage

INTRODUCTION

Tantalum capacitors are widely used as filters, bypass capacitors, coupled capacitors and so on. They have much better characteristics in comparison with their analogs. For example, they have solid electrolyte, which increases reliability against electrolytic aluminum capacitors, and they have larger values of capacitance and rated voltage with the same size, which is the strongest trait of tantalum capacitors and outweighs some disadvantages of this capacitors. Because of their properties, tantalum capacitors are used in military and aerospace applications. That's why requirements of reliability of tantalum capacitors are very high. The worst mode of failure of tantalum capacitor is the short-circuit failure. If current through broken capacitor is not restricted, capacitor may ignite due to exothermic reaction of Tantalum with Oxygen and damage surrounding equipment. Such type of failures is often observed in low-impedance circuits.

The main hypothesis of a relatively high failure rate of tantalum capacitors in low-impedance applications is that self-healing mechanisms in unlimited current conditions don't occur [1]. From the other hand, in low-impedance circuits, tantalum capacitors are exposed to high surge currents impact, which can lead to so-called surge current or turn-on failures. And, according to the results in [1], surge current breakdown voltages are significantly lower than breakdown voltages in steady-state conditions, or scintillation breakdown voltages. It can be

assumed, that the fast rise of voltage on the capacitor, *dV/dt*, is the major reason of surge current failure. As a consequence of the fast rise of voltage, capacitor is exposed to impact of high surge current spike, *i = CdV/dt*. Unfortunately, there is still not theory, which can clearly explain a mechanism of surge current failure, and different hypothesis was suggested by different researchers [2].

For evaluating the capability of tantalum capacitors to withstand high surge current impact, a specific method, called surge current testing (SCT), is used. This method is regulated by ESA/SCC Generic Specification №3012 and MIL-PRF-55365 standards. During this testing, capacitors are exposed to a certain number of charge-discharge cycles from the power supply with very low impedance. To simulate such power supply a battery of aluminum electrolyte capacitors are used. But, surge current failure events are still observed among the tested capacitors. This may be due to that the present SCT method doesn't simulate the worst surge current conditions and needs to be improved.

As shown in [3], circuit inductance and resistance has a significant effect on transients during SCT and surge current conditions in different testing equipment can be different. In this case reliable and reproducible evaluation of performance of tantalum capacitors in surge current conditions can't be obtained. The problem is complicated by the fact that tantalum capacitors have the wide range of rated capacitance – from 0.1 µF to 2500 µF. The main goal of this work is to evaluate the influence of circuit inductance and resistance on the surge current conditions at different capacitance of tested capacitors.
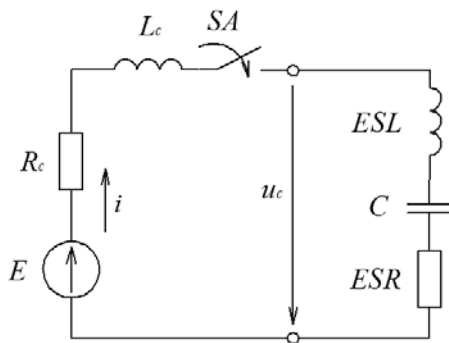
DISCUSSION OF MODEL

Figure 1. RLC equivalent circuit of tantalum capacitor

As shown in [3], the RCL model of transients during SCT gives a reasonable agreement with the experimental data (Fig. 1). But it is well-known that equivalent series resistance (ESR) and capacitance C of the tantalum capacitor depend on frequency. Thus, for accurate calculations it will be better to use the RC-Ladder equivalent circuit of tantalum capacitor (Fig. 2). In [4] was shown that in the most of cases, difference between results of calculation of transients by using RCL and RC-Ladder model is negligible. So, to simplify the calculations, in this work RCL model is chosen.
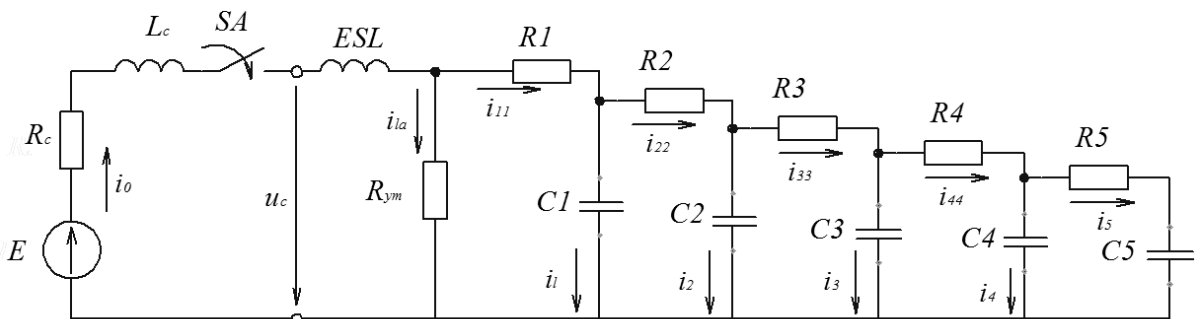

Figure 2. *RC*-Ladder equivalent circuit of tantalum capacitor

Transients during charging of capacitor according to Fig. 1 can be described by system of differential equations:

$$
\begin{cases}
(L_c + ESL)\dfrac{d^2u(t)}{dt^2} + C(R_c + ESR)\dfrac{du(t)}{dt} + u(t) = E, \\[2mm]
i(t) = C\dfrac{du(t)}{dt}.
\end{cases}
\tag{1}
$$

Initial conditions for system (1) are follows:

$$
\begin{aligned}
u(0) &= 0, \\
\frac{du(0)}{dt} &= 0.
\end{aligned}
\tag{2}
$$

For all calculations it was be assumed, that ESR = 0.1 Ohm and equivalent series inductance ESL = 10 nH.

CALCULATION AND DISCUSSION

According to [3], total external inductance of circuit used for surge current testing, L_c, may vary from ~150 nH to ~1500 nH. According to MIL-PRF-55365 the version of December, 2012, the maximum allowable total external direct current resistance of the test circuit is equal to 1 Ohm. Hence, for calculations in this work, circuit resistance R_c was varying from 0.1 Ohm to 1 Ohm, circuit inductance was varying from 100 nH to 1500 nH. The range of rated capacitance was chosen from 1 µF to 1000 µF. Since that current through the capacitor is directly proportional to the rate of voltage rise on the capacitor, for analyzing the influence of circuit inductance and resistance on transients, it would be enough to analyze only current's changings with this parameters. All conclusions for current dependencies will be similar for the rate of voltage rise dependencies. The exception is the overvoltage on the capacitor, which may develop at underdamped conditions of transients. The value of overvoltage should be analyzed separately.
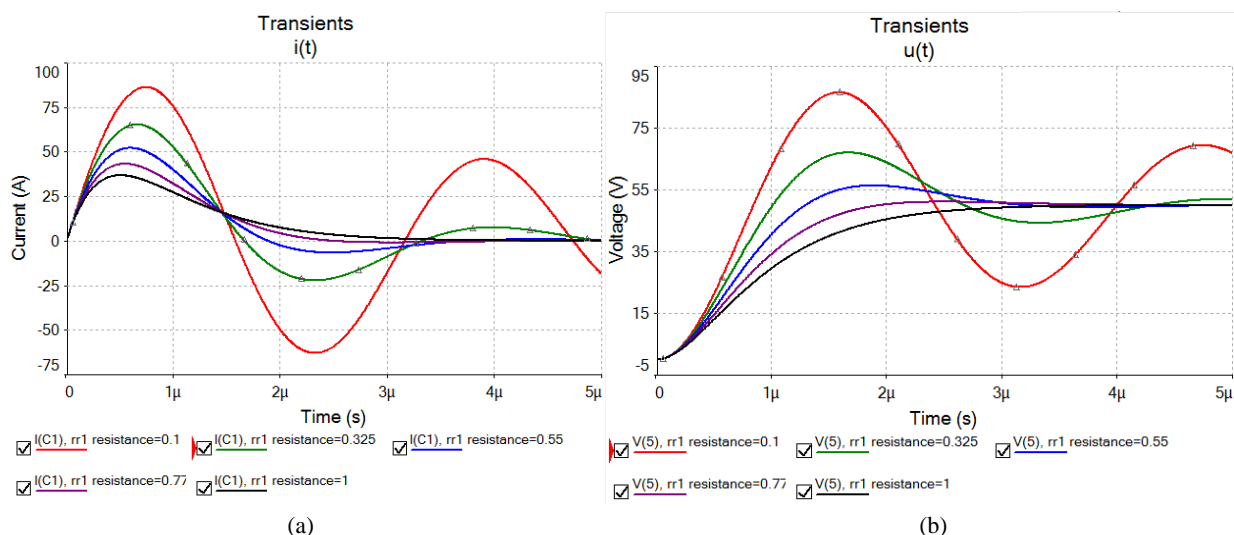
Figure 3. Current through capacitor (a) and voltage across the dielectric (b) during surge current testing of 1 µF 50 V Capacitor with different resistance of the circuit at L_c = 250 nH

The example of calculation of transients for 1 µF 50 V capacitor with different resistance of external circuit is shown on Fig. 3. Calculation was made for external inductance L_c = 250 nH. The range of external resistance is from 0.1 Ohm to 1 Ohm. As it can be seen, changing of external resistance in allowable range per MIL-PRF-55365 lead to significant

varying of amplitude of current spike, duration of current spike and the rate of voltage rise across the dielectric. For example, with increasing external resistance of the circuit from 0.1 Ohm to 1 Ohm, the amplitude of current spike decreases from 86.3 A to 36.8 A. Note that although the time to maximum increases along with increasing resistance, the rate of current rise decreases. Since that the cathode of tantalum capacitor, manganese dioxide MnO_2, has a semi-conductor properties, it can be assumed that tantalum capacitors are sensitive to the rate of current rise di/dt. The character of transients changes from the underdamped to the overdamped conditions while the external resistance decreases. At underdamped conditions capacitor may suffer from overvoltage up to $2 \cdot V_0$. In this example overvoltage across capacitor was $1.73V_0$ at $R_c = 0.1$ Ohm. Hence, all this variations significantly change the surge current testing conditions.

It is reasonable to assume that influence of circuit resistance will be different at different circuit inductance and capacitance of tested capacitors. To analyze this influence, dependencies between the amplitude of current spike I_m and circuit resistance R_c at different circuit inductances L_c was calculated. Results of calculations are shown on Fig. 4.

It is seen, that the effect of circuit resistance decreases while the circuit inductance increases and capacitance decreases. For example, increasing of circuit resistance from 0.1 Ohm to 0.5 Ohm for 1 µF capacitor at circuit inductance $L_c = 100$ nH leads to decreasing the amplitude of current spike from 126 A to 70 A. The same changing of circuit resistance at $L_c = 1500$ nH leads to decreasing the amplitude of current spike from 38 A to 30 A. For 47 µF capacitor this changes leads to decreasing I_m from 190 A to 50 A at $L_c = 100$ nH and from 96 A to 30 A at $L_c = 1500$ nH. It can also be seen that almost all curves have the inflection point at $R_c \sim 0.4$ Ohm, after which the slope of relationship $I_m(R)$ decreases. At the low capacitance this effect is less strongly expressed. It may be due to that transients become underdamped and current exhibit oscillations. It is seen that at circuit inductance $L_c = 1500$ nH and capacitance $C = 1$ µF relationship $I_m(R)$ is almost linear.

Note that all curves can be approximated by the power law $I_m = I_1 R^{-\beta}$, where I_1 is the amplitude of current spike at circuit resistance $R_c = 1$ Ohm and β depends on circuit inductance and vary from 0.2 to 0.95. The same dependencies were obtained by Reed and Paulsen in [5] between the breakdown voltage and circuit resistance. The value of β in their research was ~ 0.2. The similar results were obtained by Teverovsky in [3] for dependencies between overvoltage across the dielectric and circuit resistance for 1 µF and 15 µF capacitors. But overvoltage may appear only at relatively low capacitance. For 220 µF and 330 µF capacitors overvoltage almost never observed in practice, because it is need to have the circuit inductance $L_c \sim 20$ µH. From the other hand, difference between β in present work and β of Reed and Paulsen is too significantly to claim that breakdown voltage depend only on circuit resistance. Many researchers hold hypothesis that the rate of voltage rise has a significant influence on probability of surge current failure. It can also be mentioned here that the rate of current rise through capacitor also is of value.

The effect of circuit inductance increases while the circuit resistance and capacitance decreases. Increasing of circuit inductance from 100 nH to 1500 nH at $C = 1$ µF and $R_c = 0.1$ Ohm leads to decreasing the amplitude of current spike from 126 A to 38 A. The same changing of circuit inductance at $R_c = 1$ Ohm leads to decreasing the amplitude of current spike from 42 A to 24 A. For higher capacitance the influence of circuit inductance on I_m at $R_c > 0.4$ Ohm tends to zero and can be neglected in most cases. But for $R_c < 0.4$ Ohm this effect is still significant. Along with decreasing of I_m the pulse width increases, but the rate of current rise di/dt and the rate of voltage rise decrease. The influence of circuit inductance on the pulse width and the rate of voltage rise is significant at small resistance and capacitance. Whereas the effect of circuit inductance on the rate of current rise di/dt is observed at all range of capacitance from 1 µF to 1000 µF. It can be assumed that the fast rise of current can lead to local overheating of the MnO_2 cathode and local breakdowns. In this case variations of

circuit inductance even in relatively narrow range between 150 nH and 1500 nH for big capacitance can change the surge current condition and probability of failure.
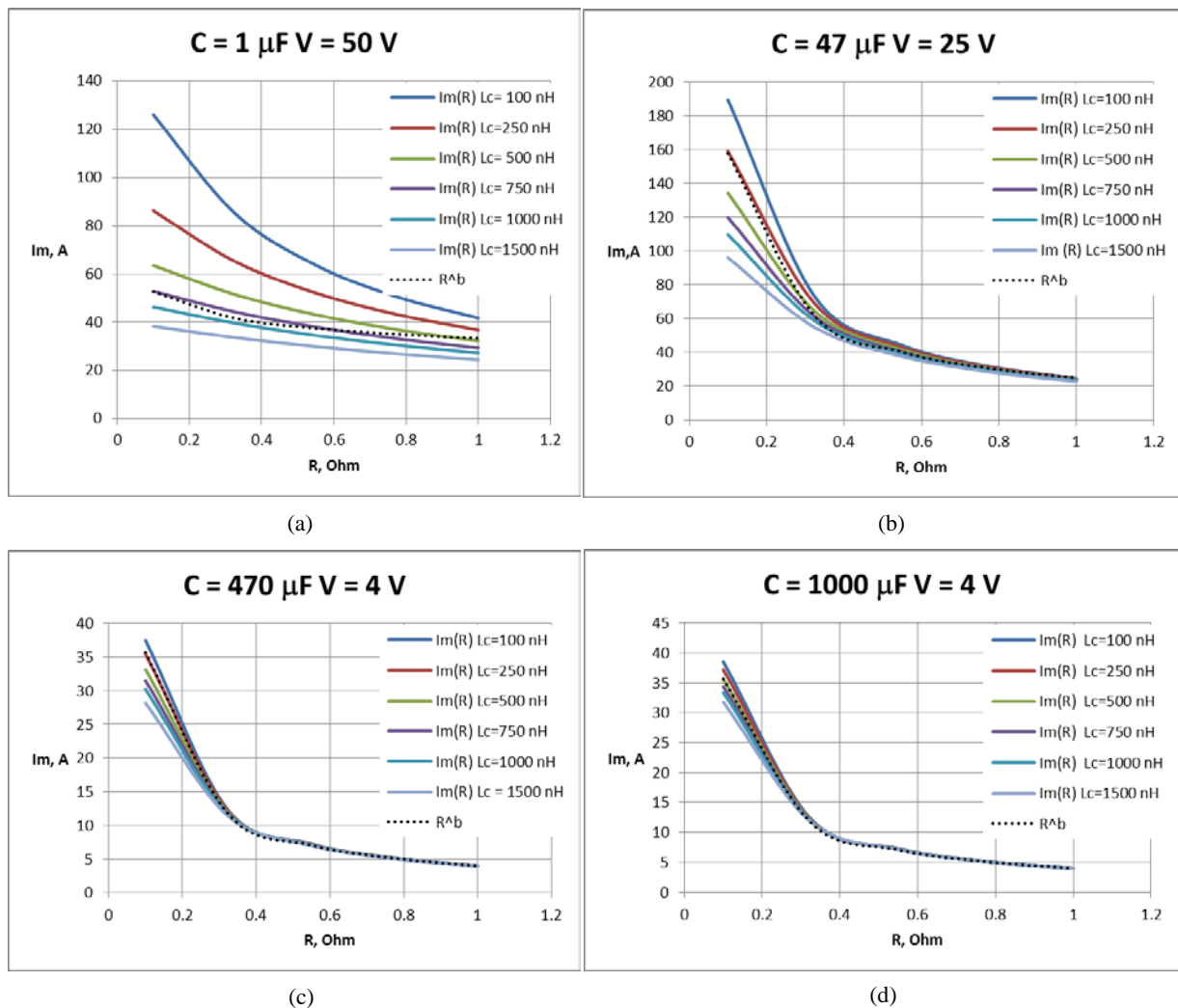

Figure 4. Relationship between amplitude of current spike and circuit resistance at different circuit inductance during surge current testing of 1 µF (a), 47 µF (b), 470 µF (c) and 1000 µF (d) capacitors.
The black dotted line shows approximations with the power law

It should be mentioned here that at small capacitance transients can be underdamped and current and voltage can exhibit oscillations. The critical inductance, at which transients became underdamped can be find from following equation [3]:

$$L_{cr} \leq \frac{C(R_c + ESR)^2}{4} - ESL. \tag{3}$$

The results of calculations of L_{cr} at different capacitance are shown on Fig. 5.

It is seen that at small circuit resistance and capacitance it is almost impossible to achieve underdamped conditions of transients. For example, at circuit resistance $R_c = 0.1$ Ohm and capacitance $C = 1$ µF the critical inductance $L_{cr} = 10$ nH. In practice, testing circuits more often would have circuit inductance $L_c > 150$ nH [3]. The relationship between the overvoltage across the capacitor and circuit resistance at different capacitance and circuit inductance are shown on Fig. 6. As the relationship $I_m(R)$, relationship between overvoltage and circuit resistance can be approximated by the power law. But in this case such approximation would be rougher.

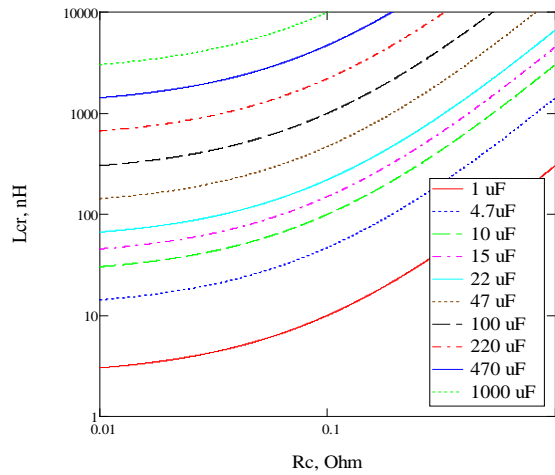*Figure 5.* The relationship between critical inductance L_{cr} and circuit resistance R_c at different capacitance
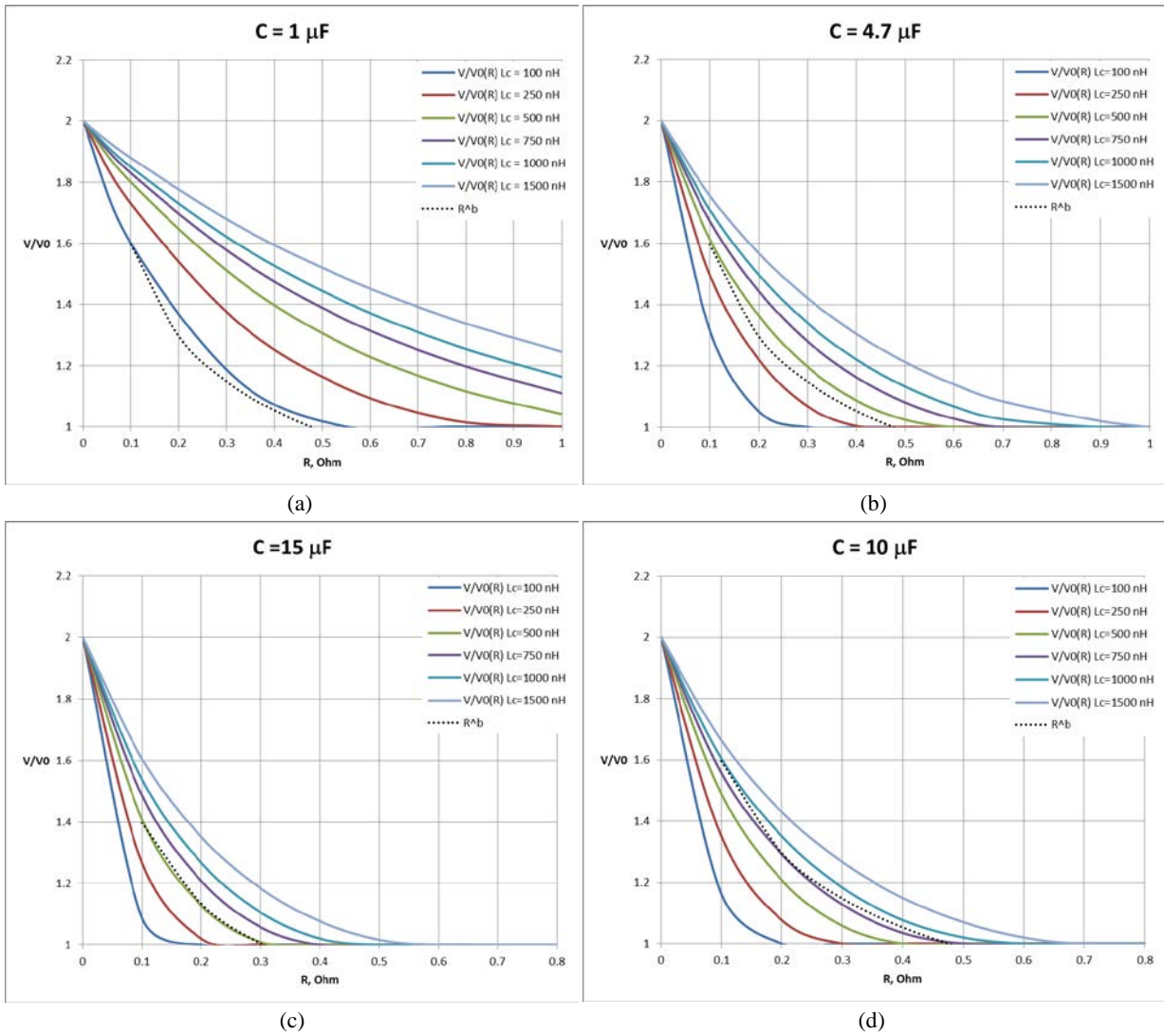

Figure 6. The relationship between overvoltage across the capacitor and circuit resistance at different circuit inductance during surge current testing of 1 µF (a), 4.7 µF (b), 10 µF (c) and 15 µF (d) capacitors. The black dotted line shows approximations with the power law

168

Theoretical maximum overvoltage across the capacitor is equal to $2V_0$ at circuit resistance $R_c = 0$. In this case sustained electrical oscillations will occur. For the range of circuit inductance 100–1500 nH at $R_c = 0.1$ Ohm oscillations can be observed at capacitance up to ~ 100 μF, whereas at $R_c = 1$ Ohm transients become overdamped at the capacitance $C > 10$ μF. Thus, circuit resistance significant reduces the probability and value of overvoltage. Capacitors of smaller values more often suffer from overvoltage. In this case, failure mechanisms of capacitors with small and high values can be different. The duration of overvoltage also is of value and can significantly effect on the probability of breakdown. Capacitors can be exposed to several spikes of overvoltage at high enough inductance. Teverovsky in [3] suggested that it may be necessary to develop the special method of testing to establish the capability of tantalum capacitors to withstand impact of short spikes of overvoltage. It is may be a challenge because it is quite difficult to keep values of circuit inductance and resistance in the narrow range. From the other hand, during charging the capacitor is exposed to joint effects of current spike and voltage rise. To develop such testing method it is necessary to take into account all these factors. Obviously, this issue requires further investigations.

CONCLUSION

Circuit resistance R_c and inductance L_c have a significant influence on surge current conditions. Even slight variations of R_c and L_c can lead to significant changes of the amplitude of current spike, spike width, the rate of current rise di / dt and the rate of voltage rise dV / dt. All this changes influence on the probability of surge current failure. Moreover, such variations of surge current conditions can produce different failure mechanisms. In this case it is quite difficult to achieve reliable and reproducible evaluation of performance of tantalum capacitors under surge current conditions. Calculations show that at R_c above ~ 0.4 Ohm the effect of circuit resistance and inductance on amplitude of current spike is less significant. May be it is reasonable to determine the allowable resistance of surge current testing circuit in narrower range, for example, between 0.4 Ohm and 1 Ohm. But in this case surge current conditions would be less stressful. To guarantee the reliable operating of tantalum capacitors in surge current conditions, an appropriate derating must be applied [2].

Another problem that deserves attention is the possible oscillations during surge current testing. Overvoltages which develop at underdamped conditions of transients can reach values up to $2V_0$. It is reasonable to assume that failure mechanisms in the presence and absence of overvoltages across the capacitor would be different. Note that capacitors with small values would be more likely exposed to overvoltages. The probability of occurrence of overvoltage decreases as the circuit resistance increases and circuit inductance decreases. For achieving reproducible testing all possible measures to decrease circuit inductance must be taken. The length of wires must be as short as possible and all elements of testing circuit must be with a very low inductance.

REFERENCES

1. A. Teverovsky, "Scintillation and Surge Current Breakdown Voltages in Solid Tantalum Capacitors," IEEE Transactions on Dielectrics and Electrical Insulation, vol. 16, pp. 1134–1142, 2009.

2. A. Teverovsky, "Derating of surge currents for tantalum capacitors," in ESA 1st International Symposium "Space Passive Component Days", (Noordwijk, The Netherlands, 2013), Available: https://escies.org/download/webDocumentFile?id=60981.

3. A. Teverovsky, "Effect of inductance and requirements for surge current testing of tantalum capacitors," in CARTS'06, the 26th Symposium for Passive Components, (Orlando, FL, 2006), pp. 363–384.

4. B.I. Sibgatullin, V.K. Barsukov, "Calculation and simulation of transients during charging of tantalum capacitors," in Young scientists – to accelerate scientific and technological progress in the XXI century: Conference Proceedings, (Izhevsk, 2015), pp. 883–889.

5. E.K. Reed, J.L. Paulsen, "Impact of circuit resistance on the breakdown voltage of tantalum chip capacitors," Proceedings of the CARTS, pp. 150–156, 2001.

Development of the Diagnostic Complex for the Analysis of Thermal Degradation of Semiconductor Structures

A.A. Skvortsov, M.V. Koryachko, V.P. Chortov, P.A. Skvortsov

Mechanics of Materials Department, Moscow State University of Mechanical Engineering (MAMI),
Moscow, Russia
E-mail: skvortsovaa@outlook.com

Abstract. The present work was aimed at development of a diagnostic complex for studying the thermal degradation of metallization systems of semiconductor structures. The method consists of decoding the oscillogram $U(t)$ of the test structures during the passage through them of current pulses of different shape. The proposed method allows to detect the initial stages of melting in the metal-semiconductor systems.

Keywords: a semiconductor structure, metallization systems and contacts, the thermal degradation, diagnostic complex

INTRODUCTION

It is known that the reliability of semiconductor devices is determined by the reliability of the interconnects and contacts of metal-semiconductor. Reducing of the size of the p-n junctions contributes to local thermal overheating and accelerates degradation of the devices [1-5]. Therefore, the aim of this work is the development and creation of the diagnostic complex for the analysis of thermal degradation of semiconductor structures.

METHODOLOGY

The study of systems of metallization and contacts was carried out on the designed test structures (Fig. 1) by using the oscillograms $U(t)$ in the process of passing a single current pulse of different shapes.

The experimental setup (Fig. 2) was allowed to pass the current pulses of various shapes through the investigated samples. The duration of current pulses was set by a generator, and the amplitude was determined by the pulse shaper. It provided the following parameters: the current was up to 150 A, the load resistance was no more than 0.5 Ω; maximum pulse duration was not less than 1.5 ms.
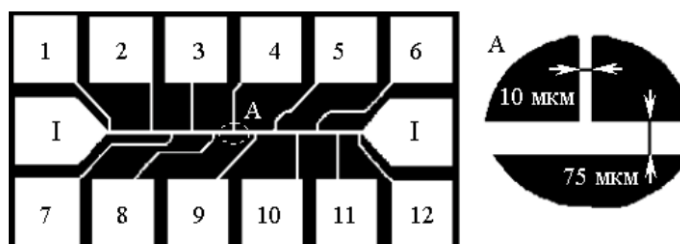
Figure 1. View of test structure with 12 potential and 2 current "I" contacts.
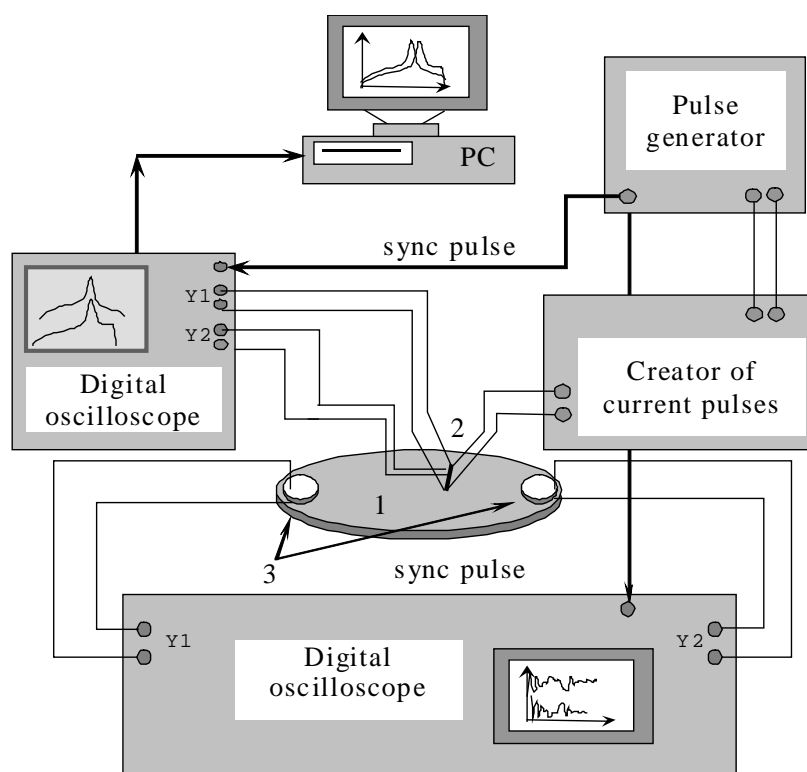Inset A: fragment of the test structure, 21 times increase

Figure 2. Structure of the experimental setup for research of thermal modes of operation, defect formation and thermally induced flexural vibrations in semiconductor structures under pulse current influences:
1 – single crystal silicon plate; 2 – test structure; 3 – piezoelectric sensors

The current that passed through the investigated test structure was determined by a calibration curve, which was received from the reference resistors. For registration of mechanical vibrations arising due to the surface thermal shock, piezoelectric transducers were used. They were located on the plate. The signal from them was also registered by oscilloscope. The electrical signal from the test structure was received from probes. Observation of the conductive paths was done by using the probe which was connected with the microscope digital eyepiece.

ANALYSIS OF EXPERIMENTAL RESULTS

Experimental study of heat regimes by using the diagnostic complex was carried out on test structures with aluminum film [6, 7].
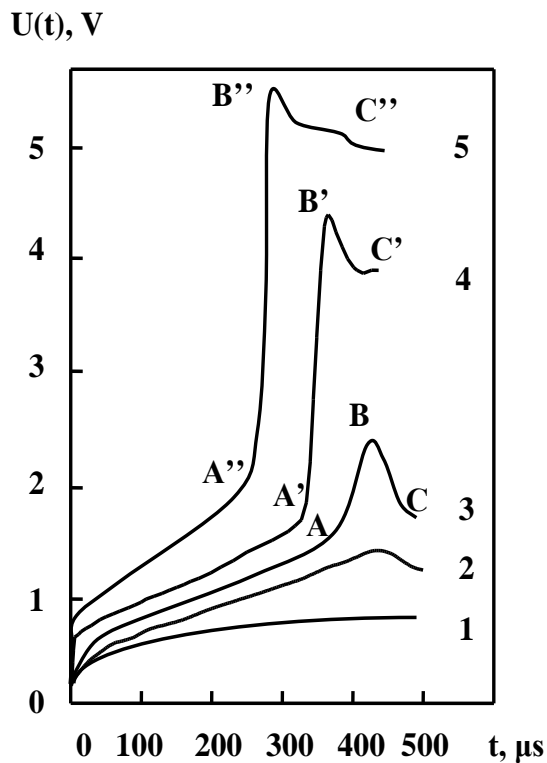
U(t), V

Figure 3. Voltage waveforms $U(t)$ (probes 1–12) during the passage of a current pulse through the aluminum metallization track lying on silicon. The pulse duration $\tau_i = 500$ μs, the amplitude j (A/m²): **1** – $4.5 \cdot 10^{10}$; **2** – $4.5 \cdot 10^{10}$ (contact melting, without melting Al); **3** – $5.2 \cdot 10^{10}$ (contact melting, partial melting Al); **4** – $4.5 \cdot 10^{10}$ and **5** – $4.5 \cdot 10^{10}$ (complete melting Al)

A monotonic increase of $U(t)$ at short times t after the pulse inclusion is associated with the heating of a thin film of metal and is determined by the heat removal mode in the semiconductor plate (Fig. 3). By using this setup the beginning of the phase formation on structures was recorded. It is associated with a fast increase of potential as a result of Al melting (when the temperature is 661 °C, AB, A'B', A''B'' in Fig. 3). Further decrease of $U(t)$ is associated with contact melting at the boundary of aluminum-silicon (melting point of eutectic Al-Si is 577 °C) and the extension of the conductive layer (Fig. 3, plots of BC, B'C', B''C'').

The increase in current density up to values of $j \sim 8 \cdot 10^{10}$ A/m² accelerates full melting of test structures. At the same time the processes of melting ($j > 5 \cdot 10^{10}$ A/m² and pulse durations $\tau_i \leq 300$ μs) dominate over the contact melting in the metallization systems. The presence of layers SiO_2 or Si_3N_4 of thickness ~ 0.1 μm on some of the plates prevents the development processes of contact melting.

The formation of melted areas had a random nature. After turning off the pulse, the melted areas crystallized. The fragment of structure after the passage of the current pulse is shown in Fig. 4. There are visible crystallized areas with a well-defined crystallization front. His form reflects temperature heterogeneity on the aluminum track width.
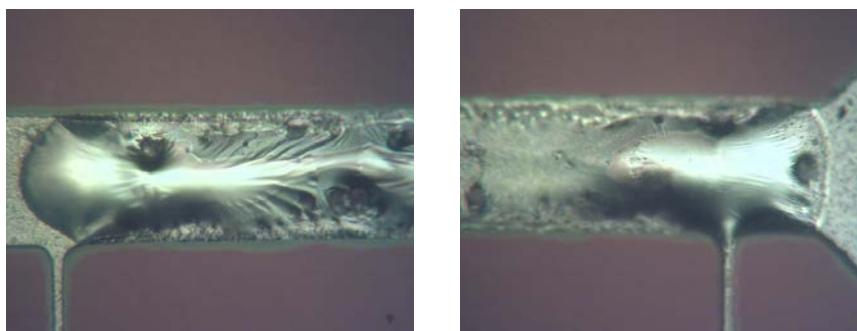
Figure 4. Photographs of a fused fragment of the test structure after passing of a rectangular current pulse with amplitude $j = 6 \times 10^{10}$ A/m² and duration $\tau_i = 300$ μs

Conclusion

Thus, the work describes the methodology of studying the processes of thermal degradation of the metallization systems and contacts. The basic mechanisms for moving interphase boundaries are associated with the heat generation at the interface of solid and liquid phases under conditions of thermal shock generated by a rectangular current pulse. The

proposed method allows to analyze the length of the molten zone after pulsed current effects and to predict the safe operating area of metallization systems on silicon.

REFERENCES

1. B. Lu, G. Gautier, D. Valente, B. Morillon, D. Alquier, "Etching optimization of post aluminum-silicon thermomigration process residues", Microelectronic Engineering, vol. 149, pp. 97–105, January 2016.

2. M. Zhang van Soestbergen, A. Mavinkurve, R.T.H. Rongen, K.M.B. Jansen, L.J. Ernstb, "Theory of aluminum metallization corrosion in microelectronics", Electrochimica Acta, vol. 55, No. 5. pp. 5459–5469, 2010.

3. C.-K. Hu, J. Ohm, L. M. Gignac, C. M. Breslin, S. Mittal, "Electromigration in Cu(Al) and Cu(Mn) damascene lines", Journal of Applied Physics, vol. 111, p. 093722, 2012.

4. H. Xiong, Z. Huang , P. Conway, "Effects of stress and electromigration on microstructural evolution in microbumps of three-dimensional integrated circuits", IEEE Transactions on Device and Materials Reliability, vol. 14, iss. 4, pp. 995–1004, 1 December 2014.

5. A.A. Skvortsov, A.M. Orlov, S.M Zuev, "Diagnostics of degradation processes in the metal-semiconductor system", Russian Microelectronics, vol. 41, iss. 1, pp. 31–40, January 2012.

6. A.A. Skvortsov, S.G. Kalenkov, M.V. Koryachko, "Phase transformations in metallization systems under conditions of nonstationary thermal action," Technical Physics Letters, vol. 40, iss. 9, pp. 787–790, 1 September 2014.

7. A.A. Skvortsov, S.M. Zuev, M.V. Koryachko, V.V. Glinskiy, "Thermal shock in metallization systems on silicon and the degradation of metallization systems and contacts," Microelectronics International, 2016, in press.

Ordering the Numeric Sequence of Image Pixels at Lossless Compression

V. Smirnov [1], A. Korobeynikov [2]

Dept. Software, Kalashnikov Izhevsk State Technical University, Izhevsk, Russian Federation
E-mail: [1] drolbs@gmail.com, [2] kav33@inbox.ru

Abstract. The present paper describes approach to building the ordered sequence of image pixels at lossless compression. This approach comprises the methods of supplementary virtual pixels, cascade fragmentation, and code book. Virtual pixels are added to split image into randomly-sized fragments. The cascade fragmentation method makes it possible to limit the number of stored start values to one. The code book method allows to minimize the search of subimage optimal bypass, the search algorithm complexity attaining $O(N^2)$. The numeric parameters such as the number of bypass options and time required to define optimal bypass are given for 6×6 image.

Keywords: lossless image compression, optimal bypass, code book, cascade fragmentation

INTRODUCTION

Paper [1] discusses building the image pixels bypass path based by the way of minimizing the costs of differential coding of pixels values employing the Little's algorithm. One disadvantage of the method is the long time of building the optimal bypass: approximately 1 minute for 16×16 image [1]. This can be explained by combinatorial explosion of the number of possible bypasses caused by increased image size. Hence, obtaining the optimal bypass for large-sized images is not feasible.

The present paper considers splitting the image into numerous fragments of equally small size. Subsequently, the optimal bypass is found for each fragment. The resulting fragments bypasses are to be joined in order to get the bypass of the complete image.

To implement the proposed method the following problems are to be solved:

1. Building optimal bypass for randomly-sized images which might be not multiple of fragment size.

2. Finding a method of joining image fragments bypasses.

3. The task of building bypass path for image fragment pixels is to be divided into subtasks: compiling the code book of all possible bypasses and searching the optimal bypass within their scope.

VIRTUAL PIXELS

Virtual pixels: splitting the image sized $N{\times}M$ into fragments sized $n{\times}m$ gives two areas: one containing complete fragments and another made up of incomplete fragments (Fig. 1). The number of pixels in the incomplete fragments area is found by formula:

$$K_{Mn} = \sum_{i=0}^{M-1}\left[N - (N/n)\cdot n\right] + \sum_{j=0}^{N-1-(N-(N/n)\cdot n)}\left[M - (M/m)\cdot m\right] , \qquad (1)$$

where «/» is the integer division operation.

True pixels   Virtual pixels
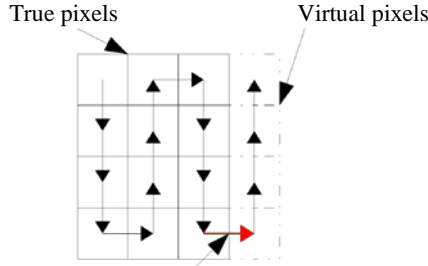
Transition between true and virtual pixels

Figure 1. A fragment containing true and virtual pixels

In order to build image bypass in the incomplete fragments area it is required to add such number of virtual pixels to the image (fig. 1) that the following condition is satisfied:

$$\begin{cases} M\%m = 0 \\ N\%n = 0 \end{cases} , \qquad (2)$$

where «%» stands for modulo operation.

Virtual pixels are not to be stored and represented in the compressed image, however they are used to build bypass of the fragmented image. Values attached to all virtual pixels are the same and they are many-fold the maximum values of true pixels.

Building the optimal bypass of a fragment consisting of virtual and true pixels is special in regard that only the true pixels values are taken into account:

$$min\left(\sum_{i\in V}\sum_{j\in V}c_{ij}\cdot x_{ij}\right) = min_{\partial}\left(\sum_{i\in V_{\partial}}\sum_{j\in V_{\partial}}c_{ij}\cdot x_{ij}\right) +$$

$$+ min_{M}\left(\sum_{i\in V_{M}}\sum_{j\in V_{M}}c_{ij}\cdot x_{ij}\right) + c_{kl}\cdot x_{kl} , \qquad (3)$$

where $x_{ij} \in \{0,1\}$ is binary variable representing the (i, j); $x_{ij} = 1$ edge if it belongs to the bypass and $x_{ij} = 1$ edge otherwise; i and j vertices are matrix pixels of image fragment; (i, j) edges are transitions between i and j *vertices*; $c_{ij} = |z_i - z_j|$ weights is the module of values difference for pixels joined by the edge (vertices), V_M and V_{∂} are subsets of vertices of all virtual and true pixels correspondingly; min_M and min_{∂} is the minimum sum of all virtual and true pixels correspondingly; $c_{kl}\cdot x_{kl}$ is the transition between true pixel k and virtual pixel l. Assuming that $c_{kl}\cdot x_{kl} = \infty$, the number of transitions between true and virtual pixels cannot exceed one and all virtual pixels have the same value.

176

Let us simplify the formula:

$$min\left(\sum_{i\in V}\sum_{j\in V}c_{ij}\cdot x_{ij}\right)=min_{\partial}\left(\sum_{i\in V_{\partial}}\sum_{j\in V_{\partial}}c_{ij}\cdot x_{ij}\right).$$

(4)

CASCADE FRAGMENTATION OF IMAGE

Having built the bypass of each fragment we next need to record the value of start pixel and the numeric sequence of bypass delta-code [1]. The number of image fragments (0 level) is found with the formula:

$$K_{\phi}=[(N/n)+ORD((N\%n)>0)]\cdot[(M/m)+ORD((M\%m)>0)],$$

(5)

where «ORD» is the operation of converting the Boolean number into {0, 1}.

The number of start elements is supposed to be equal to the number of fragments K_{Φ}. To avoid storing redundant data the matrix of start elements is generated (level 1). Thus obtained matrix is further split into fragments and optimal bypasses are found for them. The image cascade fragmentation (Fig. 2) goes on until the condition is met:

$$N\cdot M\le n\cdot m,$$

(6)

where N and M denote the size of the matrix, consisting of start vertices belonging to the previous fragmentation level.
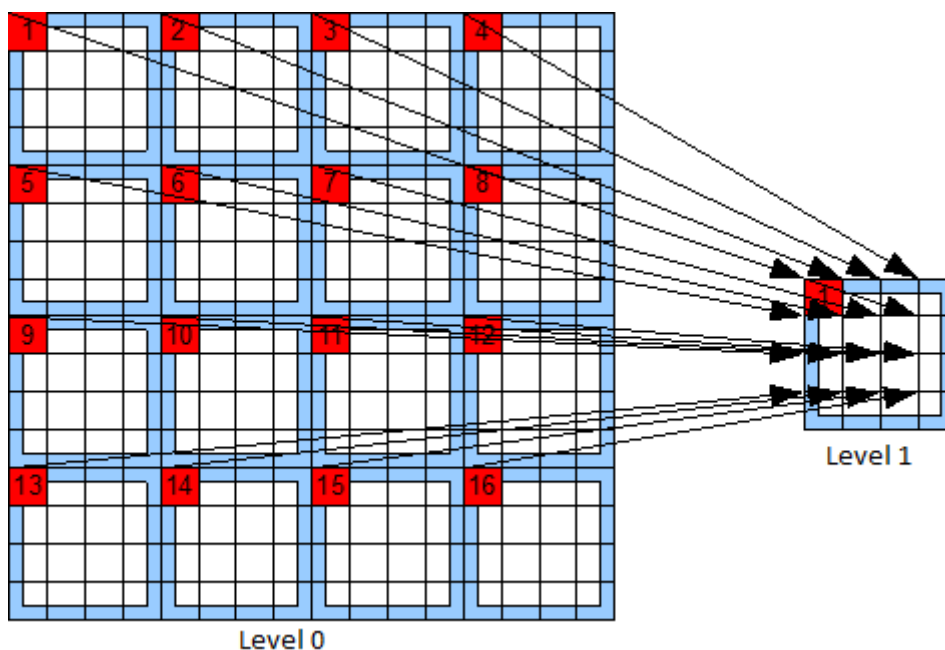

Figure 2. Cascade splitting of 16×16 image into 4×4 fragments

Recording the source image bypass starts with the last fragmentation level. For the last level matrix the value of its start vertex is recorded (the storage capacity of 1 byte is required for the range of pixels values $z_i = \{0, …, 255\}$), delta-code for its bypass [1] and also bypass path code. This information provided, the recorded matrix, i.e. the values of all its vertices, can be reconstructed. Thus, there is no need to store the values of fragments start vertices when recording the lower fragmentation levels.

Let us exemplify the recording of the image matrix bypass given in Fig. 2:

$$z_1; D^1{}_1; O^0{}_1; D^0{}_1; O^0{}_1; D^0{}_2; O^0{}_2; ...; D^0{}_{16}; O^0{}_{16};$$

where z_i is the value of start vertex; $D^s{}_i$ and $O^s{}_i$ are delta-code and bypass path code of fragment on s level with start vertex i correspondingly.

IMAGE FRAGMENT BYPASS

The novelty of the optimal image bypass method was checked against the sources [3–6]. The image fragment represented by the pixels values matrix $z_i \in (0,255)$ (Fig. 3) serves as the source data. Pixels matrix bypass can be any possible path beginning at the start cell and passing through all the cells just once. The task of searching optimal bypass is the special case of the Traveling Salesman problem. Similar to the Traveling Salesman problem the start vertex is given (upper left corner), although bypass is not limited to the start vertex return condition (Fig. 5). To solve the problem the weighted graph of the image is built (Fig. 4) [2]:

$$G(V,E) = \{i \in V, j \in V, (i,j), c_{ij} = \infty \mid (i,j) \notin E, c_{ij} \neq \infty \mid (i,j) \in E\}, \qquad (7)$$

where i and j are matrix pixels; edges (i,j) are transitions between i and j vertices; weights $c_{ij} = |z_i - z_j|$ is module of values difference for pixels (vertices) joined by an edge. To reduce the calculating costs of the algorithm only the vertices corresponding to the matrix pixels and neighboring them either vertically or horizontally are joined by edges. For the rest (non-neighboring) vertices there are no edges on the graph and $c_{ij} = \infty$.

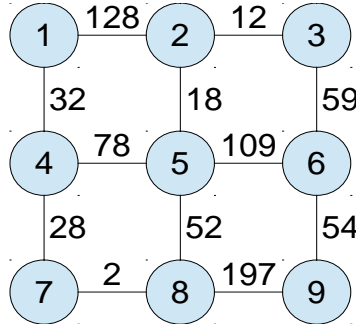**Figure 3.** Sample pixels matrix for 3×3 image

Figure 4. Sample image representation as weighted graph
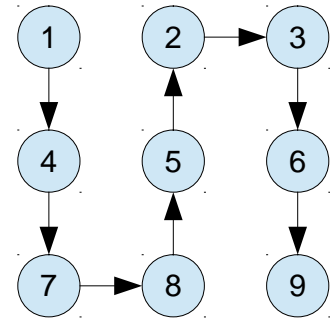
Figure 5. Sample bypass of image pixels

The graph bypass is limited by conditions (8) and (9):

$$|O| = |V| - 1 \qquad (8)$$

$$\forall i \in V; \sum_{j \in V} x_{ij} \in \{1,2\} \qquad (9)$$

where $x_{ij} \in \{0,1\}$ is the binary variable representing the (i,j); $x_{ij} = 1$ edge, provided the edge belongs to the bypass, and $x_{ij} = 0$ otherwise, $|O|$ stands for the length of the bypass.

The optimality of the bypass is evaluated as the minimum sum of bypass edges weights:

$$\min\left(\sum_{i \in V} \sum_{j \in V} c_{ij} \cdot x_{ij}\right) \qquad (10)$$

Limitations for the graph bypass given in formulae (8) and (9) result in dead-end bypass paths failing to embrace all vertices. Such paths are not the sought ones, however they are considered at the stage of possible bypasses search.

The task should be divided into subtasks:

1. building all possible graph bypasses by conditions (8) and (9);

2. searching the optimal bypass according to criterion (10).

BYPASSES CODE BOOK

The subtask of building possible bypasses depends not on the edges weights c_{ij} but the structure and size of the graph solely. For a given graph all bypasses can be defined once and the obtained results can be stored later in a certain data structure such as the code book (bypass paths list). The use of the code book will allow to eliminate the task of searching all possible bypass options including the calculation of dead-end bypasses; this will save the time of optimal bypass search.

Bypass code book is the data structure having the form of oriented tree and storing the numbered bypasses of the given graph. The root node of the tree is the start vertex of the graph bypass. The internal nodes are the intermediate vertices of the bypassed graph. The number of siblings of non-terminal nodes varies from 1 to 3 and depends on the graph vertex which can have from 2 to 4 incident edges. The bypass is closed by the vertex represented as the terminal node in the tree. Data stored in the node has the following structure:

```
struct tree{
    int ind;
    tree *left, *middle, *right;
    long bRange, eRange;}
```

where *ind* is the number of bypass, *bRange*, *eRange* are numbers of all bypasses falling within *bRange* to *eRange* range and having common vertices up to the given node.

With help of the code book method the problem of the optimal bypass search is confined to evaluating the cost of bypass against all other bypasses stored in the book and subsequently choosing the least costly bypass.

EFFICIENCY OF THE APPLIED METHOD

An image patch has been tested representing a square matrix with pre-set size of 6×6. The time of searching optimal bypass is defined as the difference between two time measurements, one taken at search start, and another upon its completion. Branch and bound method was used for optimal bypass search. The PC in the experiment had the following configuartion: CPU T2080 1.73GHz, RAM DDR PC-3200 1024 Mb. For image sized 6×6 the code book contained 22144 various bypasses. Time of discovering the optimal bypass without the use of code book amounted to 626.766 s and with the pre-compiled book – 0.016 s. Algorithm complexity without the use of code book comes to $O(2^N)$ and with the book – $O(N^2)$.

CONCLUSION

To eliminate the bypasses number combinatory explosion problem the optimal bypass has to be built for the fragments of finite size.

Adding virtual pixels to the image allows splitting the randomly-sized image into fragments of equal size.

To join image fragments bypasses the cascade splitting of image into fragments of uniform size has been offered.

The proposed method of optimal image bypass search applying the code bypass book reduces the search time considerably.

Efficiency tests for the method revealed that compilation of the book represents the most time-consuming task at this.

The time of calculating the optimal bypass can be shortened by using a more efficient method in place of all bypass options search: branch-and-bound method, dynamic programming or parallel computation based on *OpenCL* or *CUDA* technologies.

REFERENCES

1. V.S. Smirnov, A.V. Korobeynikov, "The application of the Little's algorithm for minimizing the costs of coding image bypass at lossless compression," in Information systems in industry and education: Young researchers' collected papers, (Izhevsk, 2010), pp. 165–171.

2. F.A. Novikov, Discrete mathematics for programmers. Students' manual, SPb.: Piter, 2005.

3. D. Vatolin, A. Ratushnyak, M. Smirnov, V. Yukin, Methods of data compression. Archivers make-up, image and video, Moscow: Dialogue-MIFI, 2003.

4. W.B. Pennebaker and J.L. Mitchell, JPEG: Still Image Data Compression Standard, New York : Van Nostrand Reinhold, 1992.

5. D. Taubman and M. Marcellin, JPEG2000 Image Compression Fundamentals, Standards and Practice, New York: Springer Science+Business Media New York, 2002.

6. D. Duce, Portable Network Graphics (PNG) Specification, 8.2 chapter, 2003, unpublished.

Optimization of Circuit Parameters for the EMA Sensor Excitation

V.A. Strizhak, R.R. Khasanov, N.V. Moskvin, A.V. Pryakhin

Kalashnikov Izhevsk State Technical University, Izhevsk, Russia
E-mail: pmkk@istu.ru, beif@mail.ru, mikta93@mail.ru

Abstract. The paper presents the analysis of excitation pulses of the electromagnetic acoustic (EMA) transducer for rod stocks. The requirements to the key component of the node of excitation are stated. The transient processes in the system are simulated. The experimental results are given.

Keywords: generator for transducers, simulation of electronic assemblies

INTRODUCTION

The Pump Rods Acoustic Flaw Detector (PRAFD) is applicable for the wave guided acoustic nondestructive testing method to control bar solids with the diameter of 15–36 mm [1, 2]. The next step in evolution of this flaw detector could be utilization of a contactless acoustic signal receiver.

The use of contactless electromagnetic-acoustic (EMA) transducers possesses the following significant operational benefits:

- the control is possible via an air gap instead of liquids and also available in high temp conditions;
- EMA transducers are not subject to wear;
- testing results are not dependent upon either misalignment of the transducers relative to the surface of the object or possible rust, scale, paint or dirt on the product surface. The main disadvantages of EMA transducers are low conversion index [4] and a significant increase of the acoustic probe impulse in a shadow area. Therefore, it is necessary to increase the efficiency of acoustic pulses excitation and to diminish transient disturbances on the system device receiver along with utilizing complex systems of extracting information on noise background [5].

This would require a development of new sensors and some electronic circuit modification [3]. Optimization of the generator circuit elements would allow to adapt the radiator to the Russian standard GOST 13877-96 to the bar stock.

1. DESCRIPTION OF THE GENERATOR BLOCK DIAGRAM

The node responsible for probe impulse and the oscillating system is formed by the following components of the electrical circuit (Fig. 1): Switch K, Condenser C, ballast resistor R2 and the sensor with inductance L. The System is configured for 50 kHz frequency. The optimization aim is to obtain the maximum field momentum in the emitter in the form of a coil L.
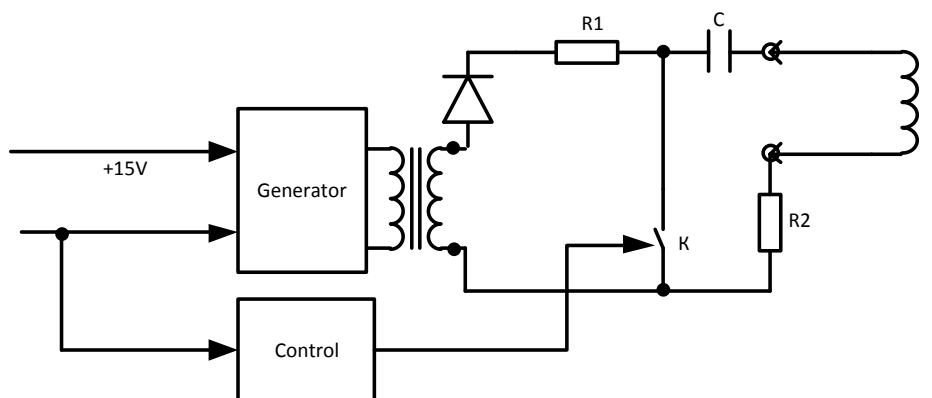

Figure 1. PRAFD Generator Block Diagram

The field momentum is proportional to the product of current in coil I by the number of turns of the coil N ($I*N$). The limiting element in the circuit is maximum current in the switch. Unfortunately, the market for the key elements to solve the problem is not very wide now.

The use of a common IGBT transistor as a high-voltage (over 200 V) switch is limited by current (less than 30 A). A typical solution is a thyristor with a reverse conductivity. The market for these devices is growing at a rate of 10–12 % per year [5]. In contrast to the IGBT transistor, the thyristor control does not require significant energy.

A typical high-frequency pulse thyristor provides the pulse current $I = 100$ A in the open state, a constant voltage $U = 500$ V in the closed state and the current slew rate $dI/dt = 1300$ A/µs in the open state.

The main circuitry feature of the sensor is a nonlinear decrease of the inductance L depending on the number of coil turns at different frequencies. The change in inductance along with the frequency decrease is due to electromagnetic properties of the core.

2. MATHEMATICAL ANALYSIS

The system analysis is done using MathCad software with the following parameters: the voltage on the coil at the moment of the key closing corresponds to the voltage in the capacitor that is $E = 350$ V, the resonance frequency is 50 kHz. The voltage on the coil U and current I in a transient oscillatory process is calculated by the classic formulas (1):

$$U = \frac{E}{\omega_0 \sqrt{LC}} \cdot e^{\delta t} \cdot \sin(\omega_0 t + a\tan\frac{\omega_0}{\delta}), I = \frac{E}{\omega_0 L} e^{\delta t} \sin(\omega_0 t + \pi), \qquad (1)$$

where L is the coil inductance, C is the capacity of the driving condenser, R is the total ohmic resistance of all circuits involved, including circuits connecting the coil, δ – damping factor of the system (2), ω_0 – cyclic frequency of the oscillatory process (2).

$$\delta = \frac{R}{2L}, \quad \omega_0 = \sqrt{\frac{1}{LC} - \frac{R^2}{4L^2}}. \tag{2}$$

The voltage and current on the coil in a transient oscillatory process are damped sinusoids, angularly shifted relative to each other.

Damping of the oscillating system is influenced by the effective resistance R. During the analysis it is necessary for the damping to be significant, not to increase the shadow area (the area in which the control process is not yet possible due to the probe pulse, RNP is the Reverberation-Noise Performance). The size of the shadow area is defined at 600 µs that is about 1m for the speed of an ultrasonic wave $V = 5200$ m/s (the movement of the acoustic pulse from a transducer and back).

The recommended rejection level is set at the value 0.5 %. These parameters can be used to estimate the minimum resistance in the oscillatory system. Let us set RNP values to be $Trhx = 400$ µs and the level $Urhx = 0.1$ %.

The active resistance of the coil depends on the number of coils and is calculated according to the resistance of 1 meter of Ø 0.49 – 93 mω/m copper wires and the diameter of the mandrel. The resistance of the supply cable 1.5 m with a copper core size-due-section of 0.5 (0.32) mm^2 is about 107 (165) mOhm. The resistance of the open key is 35 mOhm. Thus, the minimum circuit value of active resistance is estimated in the system, $R_{min} = 143$ (200) + 7.9 N mOhm, where N is the number of turns. Based on the required RNP duration for a transient oscillatory process, it is possible to calculate the minimum resistance R for a coil with N turns:

$$Rrhx = -\ln(Urhx)\frac{2LN}{Trhx}, \tag{3}$$

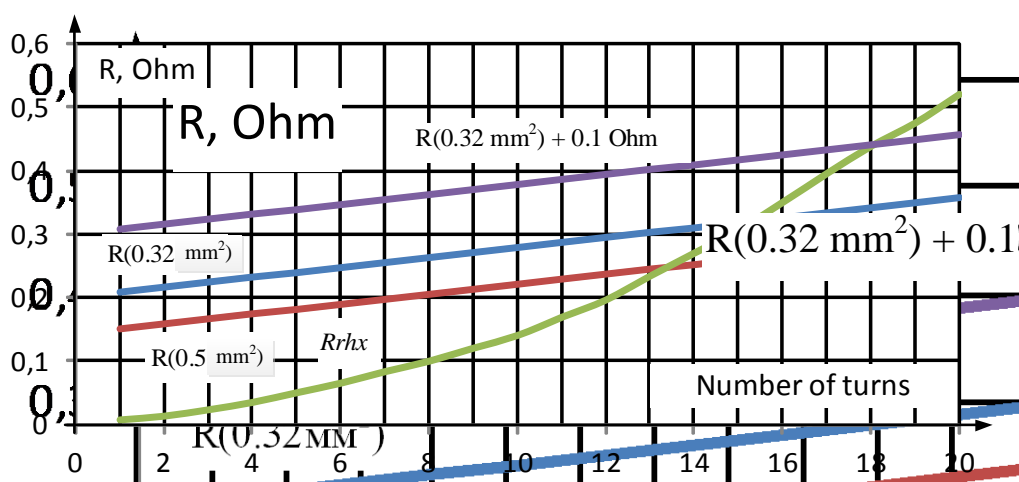where LN is the inductance of the coil with N turns.

Figure 2. Minimum resistance values in the oscillatory system

Fig. 2 shows the values of active resistance minimum in the oscillatory system at the cross-sections of copper conductors of 0.5 (0.32) mm^2 with lead wire and minimum resistance calculated from the required duration RNP. Thus, the minimum resistance in the system should be increased only if there are 14 or more turns.

3. THE SIMULATION RESULTS

The simulation results are presented in the graph (Fig. 3). The value *IN* at different internal resistance values has maxima at different numbers of coil turns.

The decrease of the resistance leads to an increase of the maximum current in the system and greater value of *IN*. Unfortunately, the system is restricted by the maximum resultant current *I* passing through the switch.

Application of new editions of triodes by the IXYS company (for example, MCC 310-08 model has 9.2 kA at a 800 V voltage mode) could be a perspective one [6].
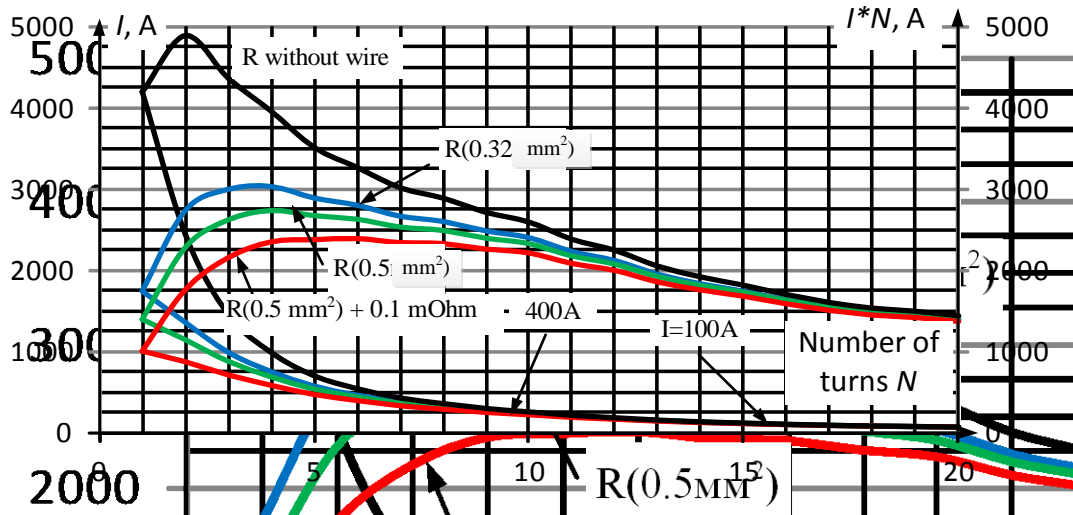

Figure 3. Maximum currents and the product of the current by the number of turns depending on the number of turns of the coil

The oscillator circuit assembled with the ballast resistor is 0.1 Ohm and the 7 turns' coil showed the pulse current *I* = 200 A at pulse voltage *U* = 150 V (Fig. 4). The results obtained on the oscilloscope AKIP-4115/4A, probe HP9258-x100-1500V. The shadow area defined with RNP was about 250 μs at 0.5 %.
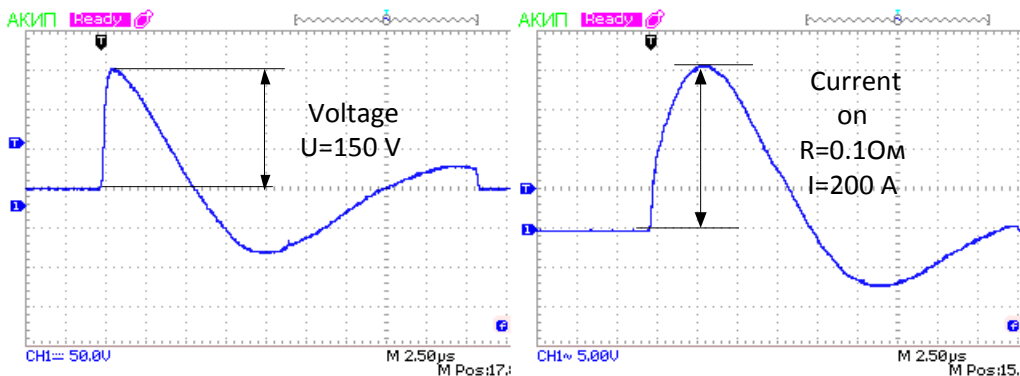

Figure 4. The maximum current and the product of the current by the number of turns depending on the number of turns of the coil

The disadvantage of this method of calculation is the lack of consideration of the capacitor internal resistance and the presence of the core (object of control) with non-linearity and saturation capability.

CONCLUSION

The analysis of EMA sensor excitation for the purpose of obtaining the maximum field momentum allows to design a laboratory bench in order to continue the research by a contactless EMA method with the use of Pump Rods Acoustic Flaw Detectors, implementing the wave guided acoustic method of nondestructive testing.

REFERENCES

1. O.V. Muravyova, V.V. Muravyev, V.A. Strizhak, E.N. Kokorina, M.A. Leiferman, "The Real sensitivity of the input acoustic control rods-blanks in the manufacture of springs" In the NDT world, No. 1 (59), pp. 52–60, 2013.

2. G.A. Budenkov, O.V. Nedzvetskaya, N. Kokorin and V.A. Strizhak, "Experience of acceptance of acoustic control and strengthening sucker rods for servicing," In the NDT world, No. 4, p. 14, 2007.

3. R.R. Khasanov, A.V. Pryakhin, V.A. Strizhak, "Modification of the generator of probing pulses of the detector ADNS," in Instrumentation Engineering in the XXI century – 2014. Integration of science, education and production (Izhevsk, November, 12–14, 2014), 2015, pp. 214–246.

4. V.A. Strizhak, A.V. Pryakhin, S.A. Obukhov, A.B. Efremov, "Informational-measuring system excitation, reception, registration and processing of signals of electromagnetic acoustic transducers," Intelligent systems in manufacturing, vol. 1, pp. 243–250, 2011.

5. B. Green, O. Holger, "How technological innovation can give new life to the thyristors in the twenty-first century," World electronic components, 2014, No. 1, pp. 44–47.

R-C-NR Structure Based on MOSFET

P. Ushakov, A. Shadrin

Kalashnikov Izhevsk State Technical University, Izhevsk, Russia
E-mail: leolektor@gmail.com

Abstract. Paper presents one of the possible realizations of the R-C-NR-network with distributed parameters which is based on metal-oxide-semiconductor field-effect transistor (MOSFET). Device structure is proposed, device operation and layers description are presented. The model of the new device is developed.

Keywords: RC-network, R-C-NR, distributed parameters, MOSFET, admittance matrix

INTRODUCTION

RC-networks with distributed parameters are intended for different analog signal processing operations, particularly can be used for fractional-order devices realization. Fractional-order devices, whose impedance have non-integer frequency dependency, are currently researched and developed for more advanced modelling of the complex dynamic processes.

Lately the RC-networks are successfully fabricated using *thick film technology*, where single layers are created in the form of films deposited onto the dielectric substrate. This technology allows fabricating circuits with different parameters, which, however, cannot be changed after the fabrication during using by electrical way. And it limits the functionality of the circuits. General disadvantages of the film technology, such as inability to implement qualitative active components and low integration scale, also restrict their applications.

Promising task is implementation of such networks in semiconductor technology, which makes it possible to place them in integrated circuit together with other analog and digital circuits with high density. Currently the most popular technology is complementary metal-oxide-semiconductor (CMOS), especially for processors and other logical devices fabrication. Therefore perspective basis to implement RC-networks is MOSFET-structure.

PROPOSAL AND Y-MATRIX OF R-C-NR NETWORK

Use of MOSFET as RC distributed element is known [1]. The basic idea is to use distributed gate capacitance and channel resistance of the MOSFET. In this case the device acts as simple RC circuit with distributed parameters, and channel resistance can be tuned by voltage connected to the gate. This principle is used for MOSFET-based implementation of low-pass filters [2], high-pass filters [3], and other frequency-selective circuits [4].

In this paper another idea is proposed – to use not only distributed channel resistance, but also gate distributed resistance, which is, of course, also presented in MOSFET because of non-zero polisilicon sheet resistance.

Proposed structure is depicted on Fig. 1a, which represents the depletion mode MOSFET consisting of polysilicon layer (gate), gate-oxide layer and the channel. Actually, the structure implements R-C-NR network with distributed parameters, where r, c, Nr are per unit length (PUL) parameters: gate resistance, gate-to-channel capacitance and channel resistance, respectively. Fig. 1b shows device symbol, where: terminal 5 represents "bulk" of the transistor and is intended for tune N – ratio between top and bottom resistances; 1, 2 – gate terminals; 3, 4 – drain and source terminals.
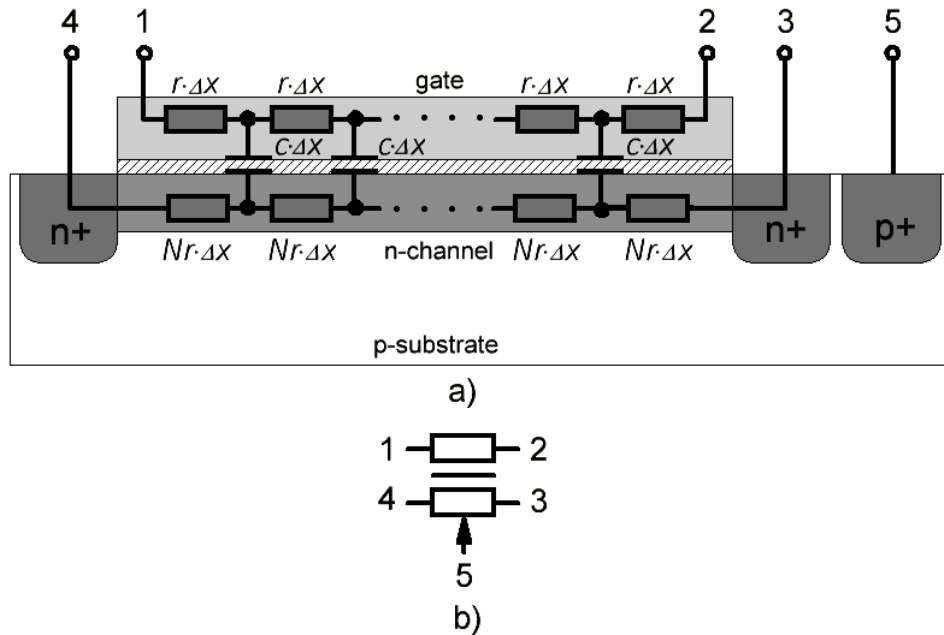

Figure 1. R-C-NR network with distributed parameters: cross section (a); symbol (b)

For modelling of the device conventional CAD could be used, but current MOSFET models don't represent distributed character of layers parameters, so they can't be used for this purpose. Thus, it is necessary to develop new model, which is able to be useable for modelling of the proposed structure.

Y-matrix (or nodal admittance matrix) of four-terminal system can be considered as the model. To derive the equations let's divide the structure into elementary sections of length Δx (Fig. 1a), and parameters are determined by used MOSFET. To derive parameters mentioned above classical MOSFET operation equations will be used [5, 6].

Top level resistance is determined by sheet resistance of the polysilicon R_s, channel length L and channel width W:

$$R = \frac{R_s \cdot L}{W}.$$

(1)

PUL resistance of the top layer in this case equals to:

$$r = \frac{R_s}{W}.$$

(2)

Some parameters depend on the operation mode of transistor, such as channel resistance and gate-to-channel capacitance. Transistor in triode region acts as a resistor controlled by

bias voltage, and the gate-to-channel capacitance as well as channel resistance are uniform over all channel length. So the linear mode is more preferable to R-C-NR network implementation. Following expressions will be derived with assumption that MOSFET operates in *linear mode*.

Next expression represents the PUL channel resistance of the MOSFET:

$$Nr = \frac{1}{\mu_n \cdot C_{ox} \cdot W \cdot \left(V_{gs} - V_{th}\right)}, \tag{3}$$

where μ_n – electrons mobility, C_{ox} – capacitance of the oxide layer, V_{gs} – gate-to-source voltage, V_{th} – threshold voltage.

To get N parameter let's divide (3) by (2):

$$N = \frac{1}{\mu_n \cdot C_{ox} \cdot R_s \cdot \left(V_{gs} - V_{th}\right)}. \tag{4}$$

Due to the body-effect the threshold voltage depends on substrate potential as following:

$$V_{th} = V_{th0} + \gamma \left(\sqrt{|2\varphi_F + V_{sb}|} - \sqrt{2|\varphi_F|} \right), \tag{5}$$

where V_{th0} – zero-biased threshold voltage ($V_{sb} = 0$), γ – body-effect coefficient, φ_F – electrostatic potential of the substrate (determined by technology), V_{sb} – source-to-bulk voltage. It means that channel resistance is affected by the voltage; therefore, R-C-NR network parameters can be changed by voltage connected to the substrate.

Gate-to-channel capacitance is determined by size, mode of operation and technology factors of the transistor. For linear mode transistor we can calculate the capacitance as:

$$C = WLC_{ox}. \tag{6}$$

To get PUL capacitance let's divide it by L:

$$c = WC_{ox}. \tag{7}$$

Thus, PUL conductivity of the oxide layer equals to:

$$y = j \cdot \omega \cdot c. \tag{8}$$

Now having all per unit length parameters of the layers, admittance matrix can be observed as [7]:

$$[Y] = \frac{1}{(1+N)R} \begin{vmatrix} \dfrac{\theta}{th\theta} + N & \dfrac{-\theta}{sh\theta} - N & \dfrac{\theta}{sh\theta} - 1 & \dfrac{-\theta}{th\theta} + 1 \\[2mm] \dfrac{-\theta}{sh\theta} - N & \dfrac{\theta}{th\theta} + N & \dfrac{-\theta}{th\theta} + 1 & \dfrac{\theta}{sh\theta} - 1 \\[2mm] \dfrac{\theta}{sh\theta} - 1 & \dfrac{-\theta}{th\theta} + 1 & \dfrac{\theta}{th\theta} + \dfrac{1}{N} & \dfrac{-\theta}{sh\theta} - \dfrac{1}{N} \\[2mm] \dfrac{-\theta}{th\theta} + 1 & \dfrac{\theta}{sh\theta} - 1 & \dfrac{-\theta}{sh\theta} - \dfrac{1}{N} & \dfrac{\theta}{th\theta} + \dfrac{1}{N} \end{vmatrix}, \tag{9}$$

where θ – propagation constant equals to:

$$\theta = \gamma \cdot L = \sqrt{(1+N) \cdot r \cdot y} \cdot L = \sqrt{j \cdot \omega \cdot \left(R_s \cdot C_{ox} + \frac{1}{\mu_n \cdot \left(V_{gs} - V_{th}\right)} \right)} \cdot L. \tag{10}$$

CONCLUSION

The model of semiconductor one-dimensional R-C-NR network based on MOSFET was developed, which makes it possible to research, simulate and design analog semiconductor circuits, particularly with fractional-order devices using. Model was derived using conventional MOSFET equations. Benefit of proposed structure is using of distributed gate resistance as additional element, which can be used for R-C-NR distributed network implementation. This network is tunable due to voltage dependency of channel-resistance, it means ratio between R and NR resistances can be changed by voltage. This feature is very useful for tunable analog filter realization.

REFERENCES

1. J. Khoury, Y. Tsividis, M. Banu, "Use of transistor as a tunable distributed RC filter element," Electron. Lett., vol. 20, pp.187–188, Feb. 1984.

2. A. Kielbasinski, "Another simple transistor-only lumped-distributed tunable low-pass filter," in 9th International Conference Electronics, Circuits and Systems, 2002, pp. 197–200.

3. V. Pirajnanchai, J. Nakasuwan, N. Songthanapitak, K. Janchitrapongvej, "High frequency transistor-only high pass filter," in Proceedings of 2005 International Symposium on Intelligent Signal Processing and Communication Systems, December, 13–16, 2005, pp. 701–704.

4. Pu Lih-Jiuan, P. Tsividis, "Transistor-only frequency-selective circuits," IEEE Journal of Solid-State Circuits, vol. 25, No. 3, pp. 821–832, June 1990.

5. J.R. Baker, Circuit design, layout, and simulation, Published: Wiley-IEEE Press, 3rd Edition, 2010, p. 1208.

6. T.C. Carusone, D.A. Johns, W.M. Kenneth, Analog integrated circuit design, Published: Wiley, 2nd Edition, p. 822, 2011.

7. W.W. Happ, P.S. Castro, "Distributed Parameter Circuit Design Techniques," NEC Proc., vol. 17, pp. 44–70, 1961.

The Laser Engraving in Decorative Processing of Organic Glass

A.V. Usoltseva

Kalashnikov Izhevsk State Technical University, Izhevsk, Russia
E-mail: Ajieksa_oo@mail.ru

Abstract. Conducted work on development of a methodology for setting the modes of the laser engraving in decorative processing of plexiglass under uncertainty characteristics of the material used and of providing multiple choice of possible combinations of operating modes. Used the results from the mathematical analysis and the expert survey. The study derived a universal laser engraving for various brands of organic glass to provide a stable contour cutting, highly contrasting dark view of paintings and patterns, the necessary adhesion during filling of the image dye.

Keywords: plexiglass, organic glass, engraving, laser technology, laser engraving

Plexiglass is modern, functional and aesthetically pleasing material, which has many useful properties, natural beauty, and the made from it products are popular and have demand in the most various spheres of human activity. It is widely used in industrial production, medicine, Commerce, advertising, in complying with such finishing works, etc.

Primary brand of Plexiglass, used in industrial manufacturing, is a technical organic glass marks top and TON (GOST 17622-72, THE 2216-271-05757593-2001), which is a plasticized and plastifici) polymer of methyl methacrylate produced by the method of block polymerization, (formula [- $CH_2C(CH_3)(COOCH_3)$ -]n). Plexiglass is produced by the form of transparent sheets with a perfectly glossy surface on both sides, translucent, colorless or colored, including smoky, opaque white, black, any color. It is widely used in machine tool, machinery, automotive, instrumentation and other industries, when you perform exterior jobs [1].

Due to the high aesthetic requirements to the surface, low mechanical strength, the presence of internal stresses, the treatment of the Plexiglas causes some difficulties. High attractiveness of the products of Plexiglas attached to laser processing, including gravity field and cutting. Throught to the creation of reliable and low cost laser equipment in the 70–80s of the last century was reappear a new technology of industrial – it is the laser materials processing technology. This allows changeover to flexibly change applied to the product image at the maximum use of the material.

Compared with other types of engraving: cutting, grinding, cutting, striking, abrasive blast the graving, physic-chemical, ultrasonic, electric-arc, electron-ion laser engraving has a some of significant advantages. Laser engraving does not require high staff qualification, used for contactless processing of blanks, there are no internal stresses, is obtained a smooth and stable contour cutting, highly contrasting dark view of paintings and patterns, a minimum

radius of rounding of corners cutting (0.1–0.3 mm), it is possible to apply simultaneous engraving and cutting material, there is no positioning error, there is no additional processing.

Organic glass is superior to most numbers of plastics by its extreme transparency, differing light transmission in a wide range, including ultraviolet, visible and part of near infrared region of the spectrum. For light transmission in the visible region of the spectrum, it is second only to quartz glass, letting in almost 100 % of visible light. This makes good paintability plexiglass in various colors. Apply the ability to pass ultraviolet rays Plexiglas is superior to ordinary silicate glass, some yielding quartz glass.

Choosing between the modes of laser processing for work by organic glass to produce an acceptable result arise some the numbers of peculiarities caused by the uncertainty of material properties and the many variability combinations of the selected technological regimes. The most common method of action in these cases is using of all modes a working material which will be used to manufacture real products. The disadvantage of this methodology is unreasonable use of a large amount of working material, or some numbers of the products, the service life of laser equipment, time to conduct these works and the compilation of the test programs.

The aims of this study is to develop methods of setting the modes of the laser engraving in decorative processing of organic glass under uncertainty characteristics of the material used and of providing multiple choice of possible combinations of operating modes. To solve this problem we use the theory of probability, mathematical statistics, mathematical modeling, theory of random functions.

The main physical parameters of the laser which determine the effects of quantum energy on a test sample are the length of the generated waves, the energy flux density, exposure time and the angle of incidence of the laser beam [3].

The relationship between the modes of the laser engraving and optical properties of organic glass in General can be described by the following formula:

$$R\,(Y_1,\,Y_2,\,\ldots,\,Y_i) = f\,\{R_i\,(X_1,\,X_2,\,\ldots,\,X_i)\},$$

where R – parameters of laser engraving, R_i – parameter changes of the optical properties of Plexiglas, $X_1, X_2, \ldots, X_i$ – types of the optical properties of Plexiglas, $Y_1, Y_2, \ldots, Y_j$ – levels of laser engraving, i – number of the optical properties of Plexiglas, j – number of levels of the modes of laser engraving, f – the function that links physical parameters of the laser.

Often the laser engraving should be applied to the finished product when the brand Plexiglas, from which it is made, is unknown. The existence of correlations between the optical properties of Plexiglas and microstructure, chemical compositions and physic-mechanical properties of Plexiglas can be represented by the expression.

$$R_i\,(X_1,\,X_2,\,\ldots,\,X_i) = \gamma\,(Z_1,\,Z_2,\,\ldots,\,Z_k),$$

where R_i – is changing the parameters of the optical properties of Plexiglas, $X_1, X_2, \ldots, X_i$ – types of the optical properties of Plexiglas, i – number of the optical properties of Plexiglas, $Z_1, Z_2, \ldots, Z_k$ – the characteristics of the microstructure, chemical composition and physic-mechanical properties of Plexiglas, k – the number of microstructure characteristics, chemical composition and physic-mechanical properties of Plexiglas.

Any random function can be centered, that is, lead to a form when its mathematical expectation is equal to zero. Therefore further displayed only centered elementary random functions.

Using the method of canonical decomposition of random function pre-suppose as a sum of so called elementary of random functions:

$$W\,(x) = V\,\beta(x),$$

where $W(x)$ – is a random function, V – normal random variable, $\beta(x)$ – is regular (nonrandom) function.

Assuming that the deviation of density, hardness, heat resistance, thermal conductivity, viscosity, heat capacity, softening temperature, temperature of combustion have a normal (or Gaussian) distribution, conduct a simulation of normal random variable based on Central limit theorem:

$$V = \mu + \sigma(\textstyle\sum_{i=1}^{12} P_i - 6),$$

where μ – the mean of normal distribution, σ – standard deviation, P – random base number, for the generation which used the gene-operator random numbers [4].

Ordinary (non-random) function $\beta(x)$ describe the dependence of the transmittance (light transmission, %) in the ultraviolet, visible and near infrared spectral regions on the wavelength of optical radiation.

To determine analytical expressions applied the method of interpolation and extrapolation using the approximation least-squares adjustment with condition:

$$F = \textstyle\sum_{i=1}^{n} (y_i - \beta(x_i))^2 \to \min,$$

where F is the minimized function, y_i – an empirical point of statistical dependence, $\beta(x_i)$ – analytical functional dependence.

For directional transmission, when the dispersion can be not included, the luminous flux incident on the sample, divided into three components: reflected, absorbed and missed. Assuming that the reflected flux in all varieties of Plexiglas is 5–7 %, missed flux is calculated according to the obtained expressions. The difference between the energy of the incident flow and the reflected and missed streams will allow us to calculate the energy absorbed substance used for heating.

To select wavelength of laser radiation used for the light transmission dependence on the wavelength. The definition of this functional dependence was conducted on the basis of the obtained and the literature cited in the statistical data (Figures 1 and 2).
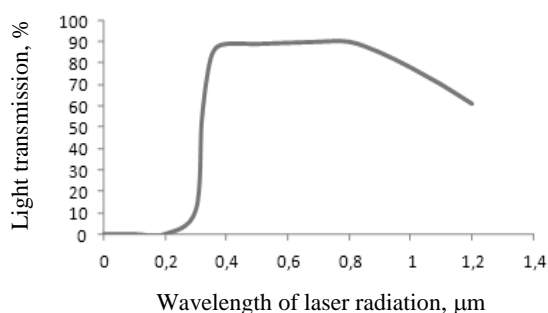

Figure 1. Chart based light transmission of the wavelength of the radiation to the PMMA block, plasticized by addition of DBP
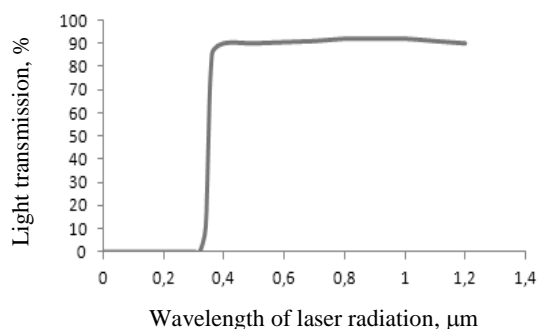

Figure 2. Chart based light transmission of the wavelength of radiation for unplasticized PMMA stabilized by addition of FS

On the basis of the conducted studies the approximation polynomial function of second order:

$$\beta(x) = -194.57x^2 + 296.97x - 19.961,$$

$$\beta(x) = -127{,}41x^2 + 249.33x - 25.76,$$

where $\beta(x_i)$ – analytical functional dependence of transmittance on wave length of optical radiation, x – wavelength optical radiation.

The obtained expression describes the boundary values of the changes of light transmission of Plexiglas, while changing the wavelength of the laser radiation. The most optimal for the case in question is a CO_2 laser, the emission wavelength of 10.6 μm, controlled by the computer. Selected for engraving laser engraver Speedy series of companies Trotec (Austria) using the software CORELDRAW, JOBCONTROL.

Analysis and expert survey showed that to obtain the most clear and high-contrast images to obtain a depth of penetration of laser radiation in an organic glass of 0.3–0.5 mm is enough to obtain a stable contour cutting, highly contrasting dark view of paintings and patterns, the necessary adhesion during filling of the image dye.

Given the functional relations between the modes of operation of the laser system, the maximum absorption of light energy by organic glass, optimum performance, set the modes of laser engraving:

• Laser output power of 11.4 Watts.
• Laser engraving speed of 27.0 cm/h.
• Resolution of 500 dpi.
• Pulse frequency 1000 Hz.
• The diameter of the focused laser beam on the material is 0.1 mm.
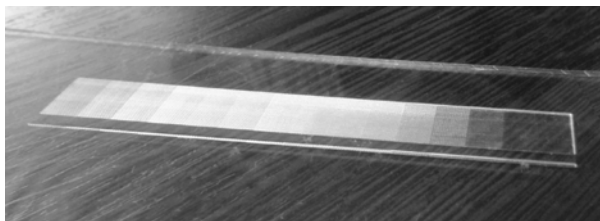• The angle of incidence of the laser beam 90°.

Figure 3. Half-tone wedge from white to black

To check the correctness of application of the developed methodology for setting the modes of interaction of laser radiation with a Plexiglas reproduce halftone wedge [5] from white to black, Figure 3 when changing the laser output power from 2 to 12 W, the laser engraving speed from 10 to 180 cm/s, resolution from 100 to 1000 dpi, the frequency of pulses from 500 to 1000 Hz, the diameter of the focused laser beam on the material from 0.05 to 1.0 mm the angle of incidence of the laser beam from 45 to 900, and combinations of these modes.

The practical significance of the work is determined by the developed proposals applicable to the solution of actual tasks of the job of laser engraving for decorative processing of organic glass with a lot of variants of implementations in the face of uncertainty of the material used. Promising the continuation of works in relation to other materials.

REFERENCES

1. V.N. Serov, Polymeric optical materials, publisher NOTES, 2015.

2. S. Litvinenko, Technology engraving, Kiev: Stained glass workshop, 2006.

3. A.G. Grigor'yants, A.A. Sokolov, Laser technique and technology, vol. 4, Laser processing of non-metallic materials: Textbook for universities, Ed. by A.G. Grigoryants, M: Higher school, 1988.

4. V.P. Usoltsev, Russian Patent No. 1226451 (23 April 1986).

5. GOST 24930-81. (1981). Half-tone wedge for a facsimile apparatus.

6. V.A. Usoltseva, V.P. Usoltsev, "Features of laser engraving leather goods" in Instrumentation Engineering in XXI Century – 2014. Integration of Science, Education and Production (Russia, Izhevsk, November, 12–14, 2014), 2015, pp. 522–524.

Wearable Electronics for Efficiency Increase of Prevention and Diagnosis of Ecologically Caused Diseases

A.N. Varnavsky

Ryazan State Radio Engineering University, Ryazan, Russia
E-mail: varnavsky_alex@rambler.ru

Abstract. The paper describes the use of wearable electronics and applications for smartphones to increase prevention and diagnosis of the environmentally caused diseases. This is achieved through collection, storage and accounting of environmental information personalized for each user. It is suggested to compare this information with dynamics of individual's functional state of the regulatory systems determined by the result of the analysis of heart rate variability.

Keywords: environmentally caused diseases, prevention, diagnostic, portable wearable electronics, smart phone, a neural network, a personalized account

INTRODUCTION

According to statistics about 85 % all diseases of modern people are related to unsatisfactory conditions of environment. Total contribution of ecological factor in population mortality is estimated on level 4–5 % and takes third place after general and social factors. Environmental pollution in cities increases the number of residents with chronic diseases of lung, heart, brain, endocrine and urogenital system, metabolism [1, 2]. Symptoms and diseases related to air pollution are chronical cough, phlegm allocation, infectious lung diseases, lung cancer, heart diseases and heart attack. For example, long contact with environment intoxicated exhaust gas of cars causes general organism weakening – immunodeficiency [3].

Environmentally caused diseases are diseases that develop among the population of any territory under the influence on people bad environmental factors and revealed by typical for this causal factor symptoms and syndromes or another nonspecific deviations provoked to ecologically negative factors [4, 5].

To increase effectiveness of diagnostics and treatment of several diseases (cardiovascular, endocrine, respiratory systems, brain and other) it's necessary to know whether the disease is a result of influence of negative ecological factors on the human, i.e. whether it is environmentally caused disease.

It should be noted that currently city environmental services carry out condition monitoring of urban air by automatic stations of air pollution control and mobile environmental laboratories. In the best case and not for all cities this information is available

in the public domain (e.g., on www.mosecom.ru). However, the environmental information related to the influence of negative factors on the individual is not defined and accordingly is not used for a personalized assessment and individual's condition prediction, support of diagnosis, prevention and treatment of ecologically caused diseases.

It is possible to suggest a new direction in development and use of wearable electronics and mobile technologies to improve the efficiency of solving the problem of prevention and diagnosis of the environmentally caused diseases.

The aim of this work is to develop a system based on wearable electronics and smart phone software to support the prevention and diagnosis of the environmentally caused diseases of the individual.

In the work the following tasks are solved:

1. Prediction of air pollution in the points of the city based on neural network model.

2. Development of conception of portable wearable electronics to increase effectiveness of the prevention and diagnosis of environmentally caused diseases the individual by assessing the concentration, the duration of negative impact of polluted air.

3. Issuing recommendations for prevention of environmentally caused diseases the individual by analyzing the accumulated evaluation and comparison with the results of the analysis of heart rate variability.

USE OF WEARABLE ELECTRONICS IN THE SYSTEM OF ECOLOGICAL MONITORING OF AIR OF URBAN ENVIRONMENT

The block diagram of the developed system for ecological monitoring consists of the following elements: air pollution sensors, meteoconditions sensors, transmitters, receivers, switchboard, server, smartphone, portable wearable electronics, client's application (Fig. 1).
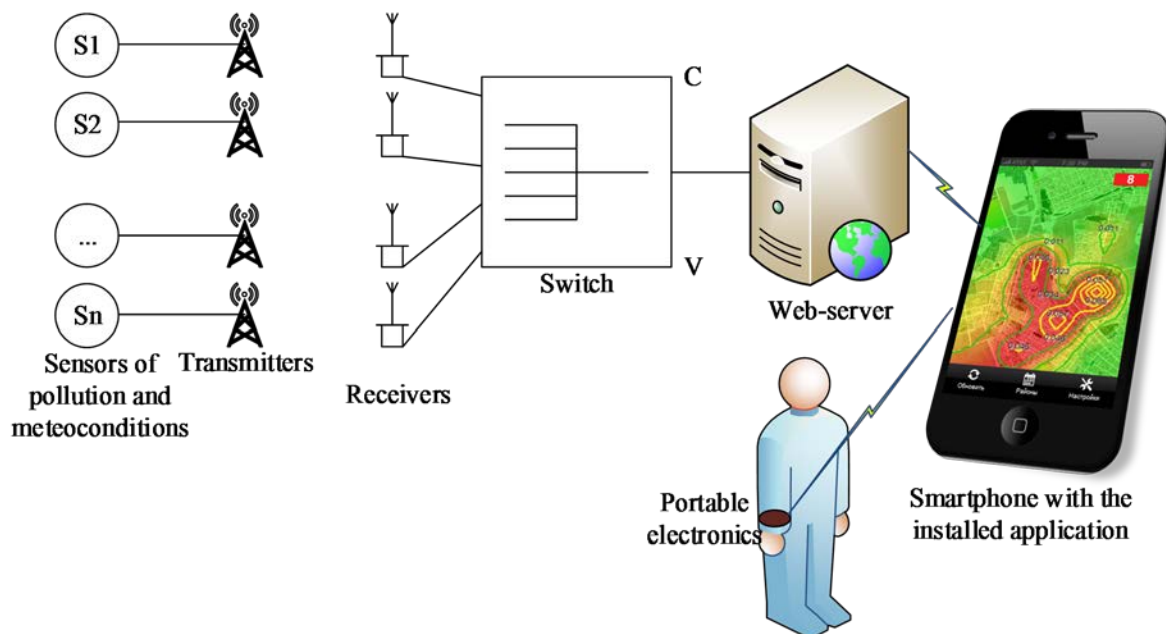

Figure 1. The block diagram of the developed system of ecological monitoring

The sensors connected to the corresponding transmitters define information about the current values of air pollution and meteoconditions at a specific point in the city and wireless transmit it to the receivers connected via the switchboard to the server. The server processes the received information and forecasts air pollution value in other points of the city. The server has Internet connection. In this way, the developed client's application which is

installed on the user's smartphone gets the access to information on air pollution and its forecast in city's districts [6]. The task of mobile application is collection of environmental and biomedical information for the individual, their comparison and output the results. The task of wearable electronics is assessment of the environmental situation at the location of the user and signal receiving to analyze heart rate variability and their transfer to the user's smartphone.

Neural Network Model of Forecasting of Air Pollution

Now for assessment and forecasting of air pollution at various points of the city various empirical analytical models are used, such as the regular models of services GO, standard models based on the OND-86 model, Paskuilla-Gifford's model, model of IAEA, etc. [7]. Such models of forecasting the spread of pollutants in the atmosphere suppose existence of complex systems of the analytical equations describing dynamics of impurity distribution. Processes of pollution distribution are random, badly reproducible and possess unsteadiness which complicates the analytical description. All the existing models and techniques accept assumptions of constancy of meteoconditions that contradicts reality. The features accounting of atmosphere pollution process in the conditions of incomplete meteodata and data about pollution sources can be achieved by applying neural network models of forecasting [8].

The main advantage of artificial neural networks is the ability to learn on the basis of the available expeditious selection. Besides, the trained neural networks can be trained in addition, using constantly arriving actual data about pollution and meteoconditions.

As input variables are selected wind speed (U, m/s), wind direction (W, °), air temperature (T, °C), pollutant concentration (C_p, mg/m^3). The realization of neural network model was enabled in the program Matlab using the Neural Network Toolbox appendix.

Eight types of neural networks were analyzed: a cascade network with direct distribution of a signal and the return distribution of a mistake; a network with direct distribution of a signal and the return distribution of a mistake; a network with delay and the return distribution of a mistake; the generalized regression network; a radial basic network with a zero mistake; a radial basic network with the minimum number of neurons; Elman's network with the return distribution of a mistake.

To determine the effectiveness of the studied neural networks the mean square mistake was used average by quantity of output variables of a neural network and counted on the basis of the predicted and real values of test selection on a formula:

$$E = \frac{1}{N \cdot K} \sum_{i=1}^{K} \sum_{j=1}^{N} \left(q_{ij}^r - q_{ij}^p \right)^2, \tag{1}$$

where q_{ij}^r – value i of an output variable neural network for j of the training or test example; q_{ij}^p – the predicted i value of an output variable neural network for j of the training or test example; N – quantity of examples in the training or test selection; K – quantity of output variables of a neural network.

While creating a model, based on calculation results of the mean square mistake, the choice of an optimum configuration of a neural network for the task was carried out. It was selected the learning algorithm by the Levenberg-Markar's method and a cascade network with direct distribution of a signal and the return distribution of a mistake with 11 neurons is chosen. The structure of the chosen network displayed in the software Matlab is presented in Fig. 2.
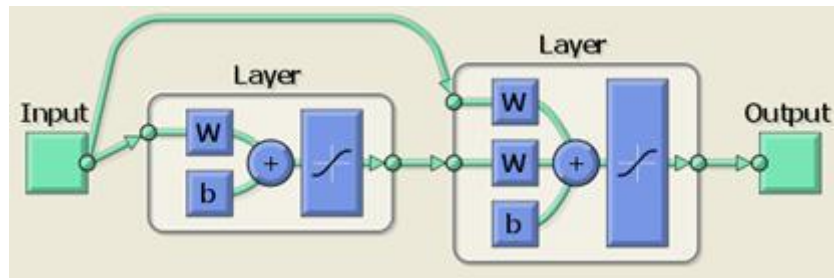
Figure 2. Structure of a cascade network with direct distribution of a signal
and the return distribution of a mistake

The structure displaying input and output parameters of a neural network for forecasting of pollutants distribution in atmospheric air is presented in Fig. 3 [8].

This neural network model is put in the program for forecasting air pollution in the developed system of environmental monitoring.
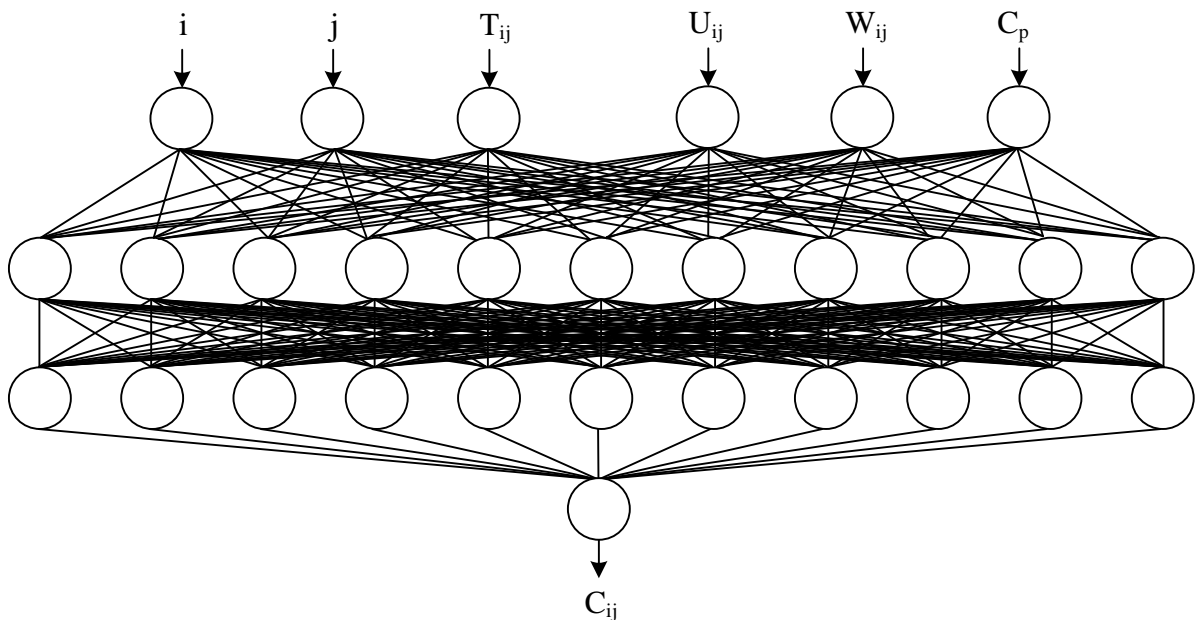

Figure 3. Structure of a neural network for forecasting pollutant distribution in air:
U – wind speed, m/s, W – wind direction, °; T – air temperature, zs; C_p – pollutant concentration, mg/m^3;
C – the concentration of the pollutant calculated on neural network model, mg/m^3; i, j – coordinates of points

IMPACT ASSESSMENT OF THE POLLUTED AIR ON THE INDIVIDUAL

The value of influence depends on the following factors:
- pollutant type;
- pollutant concentration;
- influence durations;
- the volume of the inhaled air (physical activity of the person).

To estimate risk of ecologically caused diseases it is necessary to estimate the pollutant influence level and a condition of regulatory systems of the person. It is possible to offer the following principle of prevention of ecologically caused diseases for the specific person. This principle is based on the fact that the mobile application installed on the smartphone carries out not only display of ecological information, but also in the background its continuous collection, account and storage. In parallel there should be a definition of physical activity of the person. Due to this it will be possible to estimate during the day the concentration value,

duration and volume of the inhaled air. After receiving such data for a time interval (day/week/month), based on the use of the developed indistinct model it is possible to conclude about whether there is a risk of developing of ecologically caused pathology, and if necessary to take certain measures to change a food allowance, a way of life, etc. At emergence, existence and an exacerbation of any disease it will be possible to conclude about whether a cause of pathology is the effect of negative ecological factors, how it is better to carry out the process of treatment of such disease, how to achieve permanent remission. The condition of regulatory systems can be estimated, for example, by the result of the analysis of heart rate variability of the person.

Thus, it is possible to offer the following algorithm to realize this approach.

1. Obtaining the predicted value of air pollution level at a point of location of the person.

2. Assessment of physical activity of the person.

3. Accumulation of the predicted values of air pollution level and physical activity of the person.

4. Assessment of influence of the polluted air.

5. Assessment of a condition of regulatory systems.

6. Forecasting of health change, need of prevention and treatment.

The value assessment of negative impact can be received based on the use of the developed fuzzy logic model which allows to connect the impact level on the person the polluted air with a pollutant concentration, contact duration with this air, breath frequency, weight and human height.

The possibility of accumulation of statistical ecological data allows use them together with control devices and forecasting of a person condition, diagnostics, prevention and treatment. For example, it is possible to carry out creation of a states ladder based on a heart rate variability analysis and to perform comparison and analysis of changes in person's condition and his adaptation process to the received ecological information (Fig. 4).
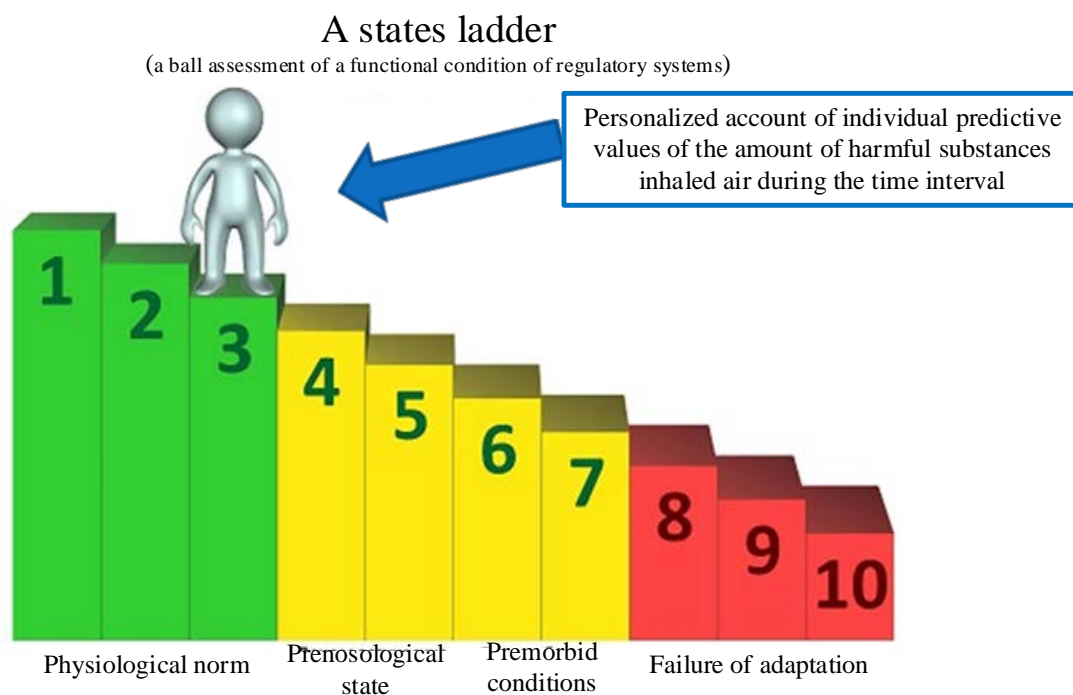

Figure 4. The accounting of ecological information in the analysis of a state ladder

The principle of dynamics comparison of a ball assessment of a functional condition of regulatory systems to the value of air pollution can be shown in Fig. 5. Here the chart 1

presents a case when eventually there is a growth of ball estimates of a functional condition of regulatory systems, i.e. there is development of diseases. At the same time points there is a growth of contact with the polluted air. From this it is possible to conclude that there is a high probability that the reason of deterioration of the person condition and pathology development is air pollutants, and the disease is ecologically caused. Chart 2 also shows the case of growth of ball estimates of a functional condition of regulatory systems, i.e. development of diseases. However, growth of negative impact of the polluted air in this case was not observed. Respectively it is possible to conclude that probability that the reason of deterioration of the person condition and pathology development is air pollutants, is small, and the disease is not ecologically caused. This fact can be used to increase the efficiency of treatment or prevention of the arising disease.
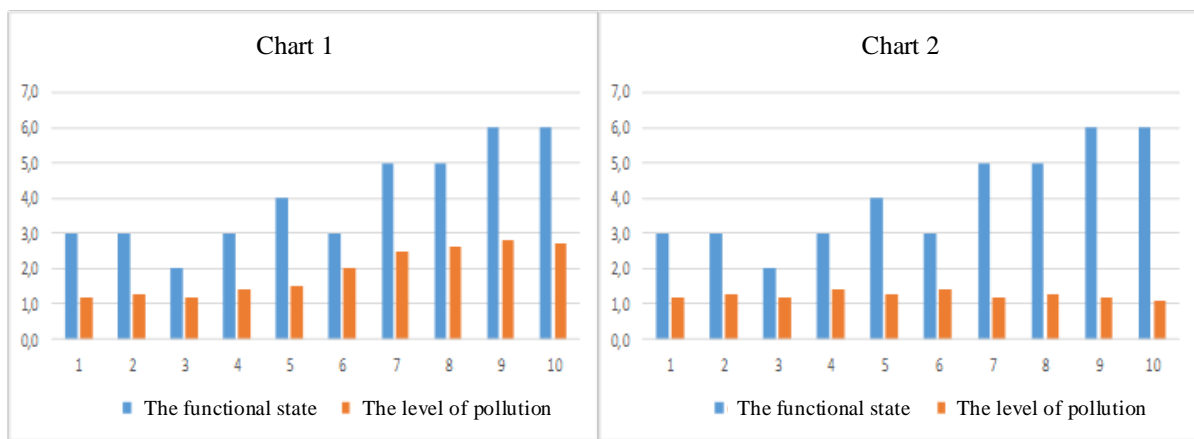

Figure 5. Principle of comparison of a ball assessment of a functional condition
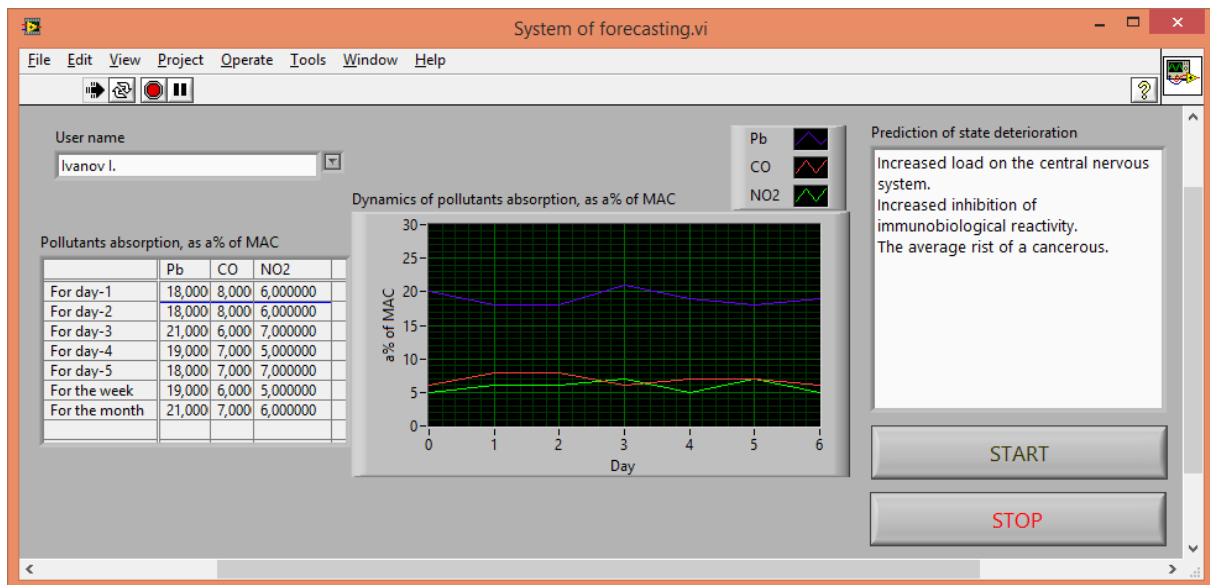of regulatory systems to air pollution value

Figure 6. The developed automated system forecasting of diseases emergence risk
based on statistical data of contact with the polluted air for time interval

Using sensors and data acquisition card USB-6008 in LabView was created a virtual device which present the demonstration version of the developed automated system for the personified support process of diagnostics, prevention and treatment of ecologically caused

pathologies on the basis of the accounting of individual predictive values of volume of the inhaled polluted air per time interval (Fig. 6) [9].

CONCLUSION

In work was suggested the structure of ecological monitoring system of air space of the city a key element of which is the client application installed on the smartphone of the user and which is carrying out obtaining the forecast air pollution in a point of location of the user. Due to this it is suggested the principle of prevention and diagnosis of ecologically caused diseases based on the fact that the mobile application performs in the background continuous collection, account and storage of ecological information. Due to this it will be possible to estimate during the day the concentration value, duration and volume of the inhaled air during time interval. Based on this information it is possible to conclude about necessarily of prevention and diagnosis of ecologically caused diseases. It is also offered to compare this information with dynamics of a condition of regulatory systems estimated by the results of the analysis of heart rate variability.

The use of the developed system and smartphones application will allow:

1. to quickly get information about air pollution in a point of location of the user and in other districts of the city, in contrast to information from city services through the internet in a number of cities;

2. to increase efficiency of prevention and diagnosis of ecologically caused diseases of the individual.

REFERENCES

1. A. Bolsherotov, "The evaluation system of ecological safety of construction", Moscow: Publishing Association Building universities, p. 216 , 2010,

2. T. Khoruzhaya, "Assessment of environmental hazard", Moscow: "Book service", 2002.

3. V. Korobkin, "Ecology", Rostov on Don: Phoenix, 2003.

4. Y.P. Gichev, "To questions of classification of environmentally induced human diseases for the study of influence of pollution in the health," Siberian Medical Journal, No. 1, pp. 36–41, 1996.

5. V.A. Baturin, D.E. Urbanovich, N.V. Efimova, A.B. Stolbov, "Using mathematical modelling in identification of ecologically stipulated diseases," Bulletin ESSC SB RAMS, No. 8, pp. 11–14, 2005.

6. A. Varnavsky, A. Fochkin, "The use of mobile devices for monitoring of urban air pollution," in Proceedings of the International Youth Scientific School "Modern bioengineering and nuclear-physical technologies in medicine", (Saratov, 2012), pp. 153–156.

7. S. Zamay, O. Yakubailik, Model evaluation and forecasting of air pollution from industrial emissions in the information-analytical system of environmental services of a large city: study guide, Publisher: Krasnoyarsk, 1998.

8. A.N. Varnavskiy, N.K. Plugotarenko, "Application of neural networks to build prediction model of urban air pollution," Electronic scientific journal «Engineering Journal of Don», No. 4 (part 2), 2012, URL: http://ivdon.ru/magazine/archive/n4p2y2012/1351.

9. A. Varnavsky, "The forecasting system to support personalized diagnosis, prevention and treatment of environmentally mediated diseases," in Proceedings of the III All-Russian Extramural Conference for Young Scientists, students and pupils (Saratov, 2013), pp. 95–100.

Justification of the Scheme of Ultrasound Processing of Inner Spherical Surface of Quartz Resonators of Solid-State Vibratory Gyroscopes

I.V. Zlobina [1], N.V. Bekrenev [2]

[1] Candidate of Technical Sciences, assistant professor of the Department of Technical Mechanics and Machine Details, Yuri Gagarin Saratov State Technical University, Saratov, Russian Federation
E-mail: irinka_7_@mail.ru
[2] Ph.D. of Technical Sciences, Head of the Department of Technical Mechanics and Machine Details, Yuri Gagarin Saratov State Technical University, Saratov, Russian Federation
E-mail: nikolaj.bekrenev@yandex.ru

Abstract. the scheme of final processing of thin-walled spherical surface` details of navigational instruments made of quartz or fused quartz using ultrasound oscillations, which amplitude and frequency provides a uniforn cutting speed at the sphere surface without using complex kinematics of tool movement is justified.

Keywords: navigational instruments, fused quartz, ultrasound, resonator, precision

INTRODUCTION

Among the perspective tools of flying objects` navigation, including spacecraft, there are solid-state vibratory gyroscopes (SSVG). The main unit of SSVG is resonator. It has such constructional peculiarities as the usage of fused quartz or quartz; presence of cylinder stem on inner and outer surfaces of hemispherical forms; small thickness of the walls (1–2 mm); high demands to the precision of the form and to the quality of the surface (form`s deviations are not more than 0.3 µm, roughness Ra ≤ 0.04 µm). The most complicated technological operations in the process of making the resonator are morphogenesis and final polish of the inner and outer spheres which are bounded in central part by cylinder stems.

Processing of spherical surfaces by already known methods is multioperational grinding and succeeding polish with special tools. Herewith high firmness and fragility of the material lead to fractures formation which length exceeds the abrasive grain of the tool by 3 sizes. This layer disturbs the stable work of SSVG and decreases the set resource. The layer with fractures is removed by multi transitional polish. the mentioned above demands the increasing of the allowance for polish and causes the growth of technical cycle` duration. Kinematics of sphere grinding and sphere polish includes the combination of rotary and reciprocating movements of the tool [1].

The change of the speeds and velocities sign causes dynamic loads, and presence of the stem in the center of inner hemisphere makes the exclusion of tool`s hit almost impossible. It leads to the appearance of overvoltages, which lead to early damage of the resonator. There

also exists a danger of stem trimming by the tool. The exclusion of tool swinging leads to unevenness of surface taking off because of the difference of speeds at resonator`s sections.

The usage of casting, stamping or additive technologies which don't demand dimensional accuracy. The usage of free ball grinding which makes chaotic movements when it is influenced by the energy of ultrasound oscillations of the pressed waveguide which is effectively used in final processing of stamps` surfaces in bearing manufacturing, for example, is almost unperformable to the SSVG resonator because the center of hemisphere is occupied by the stem.

Thereby the existing technological methods don`t allow a stable receiving of the demanded characteristics of resonator in mass production conditions.

RESULTS AND DISCUSSION

We have performed the research [2], where we have found the dependence of the length and concentration of fractures on the surface layer of fragile materials to the amplitude of ultrasound oscillations of the tool and we have shown the ability of high-performance processing with minimal defectiveness at the expense of decreasing the amplitude by the criterion of fractures' length acceptable and increasing oscillation frequency to the level which provides the necessary taking off intensity.

Taking into consideration the research data for solving the SSVG resonator processing task with the demanded quality and precision we offer to use the following approach.

It is offered to perform the processing only with rotation of the product at the minimal speed without tool swinging, which excludes the hitting loads and the danger of the resonator`s stem trimming. The offered scheme of SSVG resonator processing is shown at the Fig. 1.
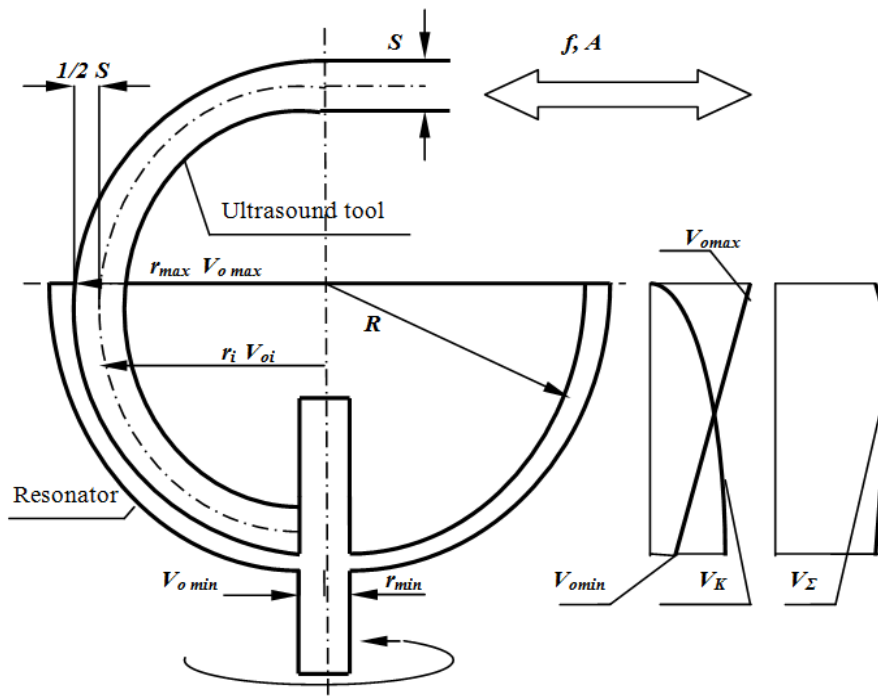

Figure 1. Scheme of SSVG resonator ultrasound processing:
V_0 – speed of resonator rotating; V_K – speed of tools oscillations; V_Σ – total speed; R – radius of the resonator sphere; r_i, r_{min}, r_{max} – current, minimum and maximum rotation radiuses; S – thickness of the tool; f and A – frequency and amplitude of oscillations

For alignment of speeds diagram, and consequently- taking the material off the surface, it is offered to give the tool a special profile of ultrasound oscillations, which amplitude and frequency are chosen according to the conditions of non-excess, which was defined by specifications, of the fractured layer' depth. The shape of the tool provides the distribution of speed oscillation which in combination with speed rotation diagram provides the alignment of speed on the whole processed surface and, consequently, stabilizes the taking off.

To make the distribution of the tools oscillation speed at resonator sections, perpendicular to its axis of rotation, reverse to the distribution of peripheral speed at the surface of the inner sphere of the resonator, which length of generatrix is obviously equals the quarter of sphere circumference radius R, a quarter of ultrasound oscillation wavelength i.e. $1/4\lambda$ should be put on it. This is a necessary condition of performing an equal taking off the material and accuracy of processing without swinging movements and tool's rotation. In this case there will be followed the condition: at $V_0 = max \rightarrow V_K = min$ and at $V_0 = min \rightarrow V_K = max$. The diagram of total speed at the sphere surface will be comparatively uniform, i.e. the total speed at the generatrix length is approximately equal. This will provide the uniformity at different sections of the processed surface. Herewith it is necessary to view the oscillations wavelength at the medium section of the tool, which curvature radius will be different from the radius of resonator`spherical surface in a half of tool`s thickness.

To find the ultrasound frequency which provides the given condition, we'll use a known formula [3]:

$$f = \frac{C}{\lambda}, \tag{1}$$

where f – resonance frequency of ultrasound oscillations; C – velocity of sound in the tool's material, λ – oscillations wavelength.

Considering the mentioned above, we have an equality:

$$\frac{1}{4}\lambda = \frac{1}{4}2\pi R_t, \tag{2}$$

where R_t – radius of tool's curvature.

In the calculation it is necessary to consider the distribution of ultrasound at the axis of the tool which has the length S. I.e. the radius of curvature R_t will be $1/2S$ smaller than sphere radius. Considering this after transformation we`ll get the formula for finding the tool's wavelength of oscillations:

$$\frac{1}{4}\lambda = \frac{\pi}{4}(R - S)_t. \tag{3}$$

If inside the resonator there is a cylinder stem with radius r_{min}, then in calculating the wavelength in the tool it is necessary to consider decreasing of sphere generatrix' length at Δl, which owing to comparative smallness of the stem radius can be equal: $\Delta l = r_{min}$, i.e. the formula (3) transforms into:

$$\frac{1}{4}\lambda = \left[\frac{\pi}{2}(R - S) - r_{min}\right]. \tag{4}$$

After transformations and substitution (4) in (1) we'll get a formula for finding the tool's oscillations frequency depending on the sizes of the main parts of resonator:

$$f = \frac{C}{2\pi(R - S) - 4r_{min}}. \tag{5}$$

Based on joint viewing of the known dependencies of finding peripheral speed of the product through its diameter and the number of turnings and also the average speed of ultrasound oscillations, equalling $V_0 = V_K$ in all the sections of resonator perpendicular to axis of its rotation, we'll get a formula for finding the number of resonator turnings at its ultrasound processing:

$$n = \frac{1200 fA(1 - \frac{r_{min}}{R})}{\pi R \cos(arc \sin \frac{r_{min}}{R})}, \tag{6}$$

where A – amplitude of tool's oscillations.

As the task of final formation of SSVG resonator consists not only of providing the accuracy of the shape and decreasing the dynamic loads, as mentioned above, but in decreasing the sizes of fracture formation area as well, in formula (6) it is necessary to consider maximum meaning for oscillations amplitude at the criterion of fracture formation.

In formula [3] we`ve got the formula for maximum meaning of oscillations amplitude causing fracture formation in amorphous materials:

$$A_M = \frac{[\sigma]e^{\delta x}}{E}, \tag{7}$$

where δ – coefficient of ultrasound wave attenuation; E – elastic modulus; $[\sigma]$ – breaking point of the material's compression; x – depth of fracture distribution.

After substitution of (7) into (6) we'll finally get a formula for the resonator's number of turnings:

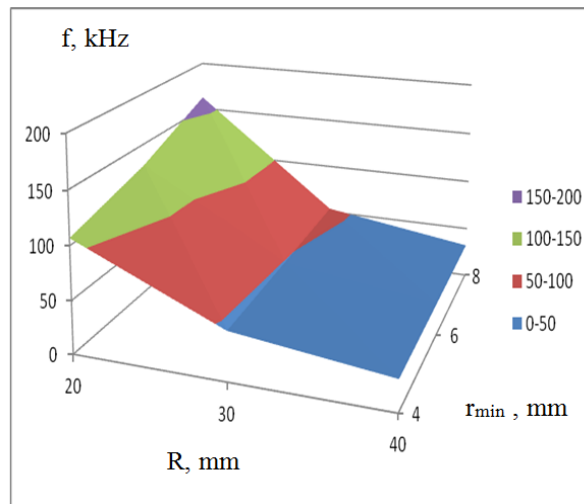$$n = \frac{1200 f [\sigma](1 - \frac{r_{min}}{R})e^{\delta x}}{\pi RE \cos(arc \sin \frac{r_{min}}{R})}. \tag{8}$$

Figure 2. Dependence of tool's oscillations frequency f from sphere radiuses R and resonator's stem r_{min}
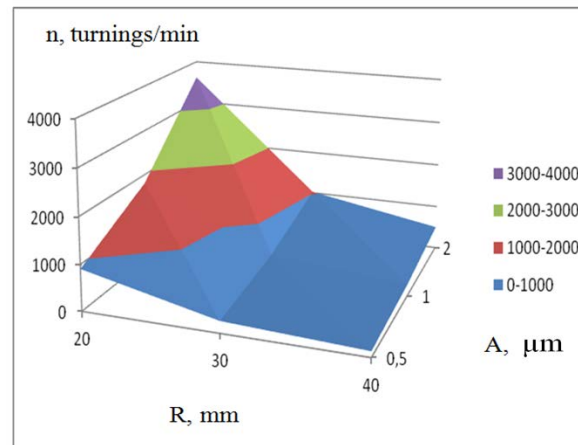
Figure 3. Dependence of tools number of turnings *n* from its oscillations amplitude *A* and resonator's sphere radius *R* at r_{min} = 6 mm

Below at Fig. 2 and 3 there are the results of the calculations of the demanded tool frequencies *f* and the number of resonator`s turnings *n* for its different sizes. As the basic material of the tool the alloy D16T was taken. the velocity of sound distribution in it is *C* = 5000 m/s. For different conditions of fracture formation the meanings of oscillations amplitude *A* 0.5; 1.0 and 2.0 µm were defined.

It can be seen that resonator's sphere radius influences on the tool oscillations frequency mostly. The stem`s radius influences significantly less, especially at big sizes of sphere.

At small sphere radiuses transverse sizes of stem mostly decrease the sphere generatrix' length, and so the tool's oscillations wavelength. With sphere radiuses less than 40 mm, the demanded oscillations frequencies get further the range of ultrasound technological frequencies. That is why, in case of making compact resonators, for manufacturing them according to the offered technology it is necessary to make special ultrasound generators. Thus for developing SSVG at present time, which has the resonator sizes bigger than 30 mm, it is possible to use serial generators with the frequency of output signal 22 and 44 kHz. Some frequency deviation from the calculated frequencies in this case will lead to a non-significant decrease of processing performance, which is allowed in the conditions of experimental producing SSVG for working off the resonator's construction and its production technology, and also for its subsequent small-scale and mass production.

For justifying the rational processing scheme, regimes and construction of the tool we have performed solid-state modeling of resonator's vibratory stability at different schemes of processing final-cell analysis of stress-strain state of resonator and the tool, the shape of the tool has been optimized.

CONCLUSION

Experimental working off the offered scheme has shown that, comparing to the existing schemes of sphere grinding, the number of resonators which have the deviation from sphericity less than 0.3 µm after processing, increased almost in 1.4 times (75–80 % binstead of 54–60 %). Herewith the depth of fractured layer decreased by 35-50 %. It has decreased the time of final polish for its excretion by more than 2 times. It will allow a stable receiving of SSVG with drifting indicators of heightened accuracy and to provide the demanded output of valid products and products' lifetime specified.

Thereby we generally have proved the principal possibility of SSVG resonators processing by the simple kinematic scheme with product`s rotation and corresponding ultrasound oscillations of definite dependences of frequency and amplitude mentioned above.

For processing most of the known resonators with sphere radius more than 30 mm the following regimes can be recommended: rotational frequency of 200–500 turnings/min, tool's oscillations frequency 0.5–1 µm. Herewith the existing ultrasound generators production models with output voltage frequency of 22–44 kHz can be used.

REFERENCES

1. N.V. Bekrenev, R.S. Velikanov, O.A. Dudareva, Ceramics and glass-ceramic in instrumentation. Properties. Processing workflow. Tools: tutorial, edited by prof. V.N. Lyasnikov, Saratov: Gagarin State Technical University, 2006.

2. N.V. Bekrenev, I.V. Zlobina, A.P. Petrovsky, "Low-defective ultrasound processing of the parts of navigational instruments from firm, fragile materials of non-uniform structure," SSTU Bulletin, No. 4 (77), pp. 97–103, 2014.

3. B.M. Brzhozovsky, N.V. Bekrenev, Ultrasound technological processes and equipment in Mechanical Engineering and Instrumentation, Saratov: SSTU, 2009.